UNIVERSITY OF CALIFORNIA, SAN DIEGO

Bioinspired Design: Magnetic Freeze Casting

A dissertation submitted in partial satisfaction of the
requirements for the degree Doctor of Philosophy

in

Materials Science and Engineering

by

Michael Martin Porter

Committee in charge:

Professor Joanna McKittrick, Chair
Professor Shengqiang Cai
Professor Olivia Graeve
Professor Marc Meyers
Professor Robert Sah

2014

The Dissertation of Michael Martin Porter is approved, and it is acceptable in quality and form for publication on microfilm and electronically:

_____

_____

_____

_____

_____
Chair

University of California, San Diego

2014

TABLE OF CONTENTS

LIST OF FIGURES

LIST OF TABLES

ACKNOWLEDGEMENTS

The research presented in this dissertation was partially supported by the following awards and grants: Ceramics Program Grant, 1006931, National Science Foundation; Kunzel/Powell Fellowship, Jacobs School of Engineering; Gordon Fellowship, Gordon Engineering Leadership Center; ARCS Scholarship, Achievement Rewards for College Scientist Foundation. I would especially like to thank my advisors Joanna McKittrick and Marc Meyers for their much appreciated financial support, workspace, and guidance throughout the course of my Ph.D. work. I would also like to thank my committee members, Robert Sah, Shengqiang Cai, and Olivia Graeve, for their suggestions and support. I am grateful for all of my coauthors, collaborators, colleagues, and undergraduate students that helped make this work possible. Most importantly, I appreciate the continued support and encouragement from my family, William, Susan, and Gregory Porter, my grandparents, John and Betty Porter and James and Sarah Radcliffe, and my fiancé, Lydia Lundgren.

I also acknowledge S. Jin (UCSD), C. Lauve (UCSD), J.V. Agnew (UCSD), E. Cory (UCSD), R. Anderson (UCSD), N. Delson (UCSD), J. Tustaniskyj (UCSD), A. Almutairi (UCSD), E.E. Novitskaya (UCSD), M.I. Lopez (UCSD), S. Wasko (UCSD), S. Lee (UCSD), M. Jaremko (UCSD), J. Yu (University of Hawaii), P.-Y. Chen (National Tsing Hua University), Y.-S. Lin (San Diego State University), and E.A. Olevsky (San Diego State University) for their insightful discussions and assistance with experimental procedures, equipment fabrication, and administrative work. In particular, I am very grateful to A. Tomsia (Lawerence Berkeley National Laboratory) for generously opening his laboratory to our group and demonstrating the freeze casting process.

Chapter 2, in part, is published as a review article in *American Ceramic Society Bulletin* with co-author J. McKittrick of UCSD. The dissertation author is the first author of this work.

Chapter 3, in part, is published as a review article in *JOM* (2012 ISI Impact Factor: 1.053) and co-authored by M.A. Meyers, and J. McKittrick of UCSD. The dissertation author is the first and corresponding author of this work.

Chapter 4, in full, is published and featured on the back cover of *Advanced Functional Materials* (2012 ISI Impact Factor: 9.765), and co-authored by R. Imperio, M. Wen, M.A. Meyers, and J. McKittrick of UCSD. The dissertation author is the first and corresponding author of this work.

Chapter 5, in full, is published in *Materials Science and Engineering: A* (2012 ISI Impact Factor: 2.108), and co-authored by M. Yeh, J. Strawson, T. Goehring, S. Lujan, P. Siripasopsotorn, M.A. Meyers, and J. McKittrick of UCSD. The dissertation author is the first and corresponding author of this work.

Chapter 6, in full, is currently under peer review for publication in *Composites Part A: Applied Science and Manufacturing* (2012 ISI Impact Factor: 2.744), and co-authored by L. Meraz, A. Calderon, H. Choi, A. Chouhan, L. Wang, M.A. Meyers, and J. McKittrick of UCSD. The dissertation author is the first and corresponding author of this work.

Chapter 7, in part, will be revised and submitted for publication in *Materials Today* (2012 ISI Impact Factor: 6.071), and co-authored by A. Bahadur of Bruker Biospin and M.A. Meyers, and J. McKittrick of UCSD. The dissertation author is the first and corresponding author of this work.

VITA

2014 Ph.D. Materials Science and Engineering
University of California, San Diego, La Jolla, CA
Dissertation: *Bioinspired design: magnetic freeze casting*
Advisors: Prof. Joanna McKittrick, Prof. Marc A. Meyers | GPA: 4.0/4.0

2010 M.S. Biological Engineering
University of Hawai'i at Mānoa, Honolulu, HI
Thesis: *In situ crystallization of native poly(3-hydroxybutyrate) granules in varying environmental conditions* | Advisor: Prof. Jian Yu | GPA: 3.9/4.0

2007 B.S. Engineering Science and Mechanics
Virginia Polytechnic Institute and State University, Blacksburg, VA
Minor: *Mathematics* | Advisor: Prof. Jack Lesko | GPA: 3.7/4.0

HONORS & AWARDS

2014 Cover, *Advanced Functional Materials*, article featured on back cover
2014 Gordon Fellowship, Gordon Engineering Leadership Center, UCSD
2013 Editors' Choice, *Acta Biomaterialia*, 1 of 5 articles selected
2013 NSF Innovation Corps Award, von Liebig Entrepreneurism Center, UCSD
2013 ARCS Scholarship, Achievement Rewards for College Scientists Foundation
2013 Featured Research in *Popular Science*, *Scientific American* and 100+ more
2013 Honorable Mention Poster Award, Jacobs School of Engineering, UCSD
2013 Image of the Day, *National Science Foundation* and *The Scientist*
2013 Best Student Paper Award, Society of Experimental Mechanics
2011 Kunzel/Powell Fellowship, Jacobs School of Engineering, UCSD
2011 Golden Key Research Grant, Golden Key International Honour Society
2010 Best Student Paper Award, BioEnvironmental Polymer Society
2007 Featured Research in *Prism Magazine*, *Design News* and 15+ more
2006 Hampton Roads Scholarship, Society of American Military Engineers

PUBLICATIONS

Journal Articles

1. Porter M.M., Meraz L., Calderon A., Choi H., Chouhan A., Wang L., Meyers M.A., McKittrick J. (2014). "Torsional properties of helix-reinforced composites fabricated by magnetic freeze casting." *Composites Part A: Applied Science and Manufacturing.* (under review, submitted 13 Feb 2014)
2. Porter M.M., Imperio R., Wen M., Meyers M.A., McKittrick J. (2013). "Bioinspired scaffolds with varying pore architectures and mechanical properties." *Advanced Functional Materials*. (doi: 10.1002/adfm.201302958) - Back Cover, Apr 2014
3. Porter M.M., Novitskaya E.E., Castro-Ceseña A.B., Meyers M.A., McKittrick J. (2013). "Highly deformable bones: unusual deformation mechanisms of seahorse armor." *Acta Biomaterialia*. 9(6): 6763-6770. (doi: 10.1016/j.actbio.2013.02.045) - Editors' Choice, Oct 2013
4. Porter M.M., McKittrick J., Meyers M.A. (2013). "Biomimetic materials by freeze casting." *JOM*. 65(6): 720-727. (doi: 10.1007/s11837-013-0606-3) - Cover of *Materials News*, Fall 2013
5. Porter M.M., Yeh M., Strawson J., Goehring T., Lujan S., Siripasopsotorn P., Meyers M.A., McKittrick J. (2012). "Magnetic freeze casting inspired by nature." *Materials Science and Engineering: A*. 556: 741-750. (doi: 10.1016/j.msea.2012.07.058) - 7 citations, including *Science*
6. Porter M.M., Yu J. (2011). "Monitoring the in situ crystallization of native biopolyester granules in *Ralstonia eutropha* via infrared spectroscopy." *Journal of Microbiological Methods*. 87(1): 49-55. (doi: 10.1016/j.mimet.2011.07.009)
7. Porter M.M., Yu J. (2011). "Crystallization kinetics of poly(3-hydroxybutyrate) granules in different environmental conditions." *Journal of Biomaterials and Nanobiotechnology*. 2(3): 301-310. (doi: 10.4236/jbnb.2011.23037)

Book Chapters

8. Porter M.M., Lee S., Tanadchangsaeng N., Jaremko M.J., Yu J., Meyers M.A., McKittrick J. (2013). "Porous hydroxyapatite-polyhydroxybutyrate composites fabricated by a novel method via centrifugation." *Mechanics of Biological Systems and Materials*. B.C. Prorok et al. (Ed.): New York, Springer, 5: 63-71. (doi: 10.1007/978-1-4614-4427-5_10) - SEM Best Student Paper Award, Mar 2013

9. Yu J., Porter M.M., Jaremko M.J. (2013). "Generation and utilization of microbial biomass hydrolysates in recovery and production of poly(3-hydroxybutyrate)." *Biomass Now - Cultivation and Utilization*. M.D. Matovic (Ed.): New York, InTech: 33-48. (doi: 10.5772/52940)

Conference Proceedings

10. Chou P.C., Porter M.M., McKittrick J., Chen P.-Y. (2014). "Vapor deposition polymerization as an alternative method to enhance the mechanical properties of bio-inspired scaffolds." *Advances in Bioceramics and Biotechnologies II: Ceramic Transactions*. 247: 3-12.

11. Manilay Z., Nguyen V., Novitskaya E., Porter M.M., Castro-Ceseña A.B., McKittrick J. (2014). "Structural differences between alligator pipehorse and bay pipefish tails." *Advances in Bioceramics and Biotechnologies II: Ceramic Transactions*. 247: 57-64.

12. Yang W., Nguyen V., Porter M.M., Meyers M.A., McKittrick J. (2014). "Structural characterization and compressive behavior of the boxfish horn." *Advances in Bioceramics and Biotechnologies II: Ceramic Transactions*. 247: 105-112.

13. Lee S., Porter M.M., Wasko S., Lau G., Chen P.-Y., Novitskaya E.E., Tomsia A.P., Almutairi A., Meyers M.A., McKittrick J. (2012). "Potential bone replacement materials prepared by two methods." *MRS Proceedings*, 1418. (doi: 10.1557/opl.2012.671)

14. Porter M.M., Yu J. (2010). "Crystallization of poly(3-hydroxybutyrate) granules under changing environmental conditions." *Polymers and the Environment: Emerging Green Technologies and Science*, Toronto: BioEnvironmental Polymer Society. - BEPS Best Student Paper Award, Oct 2010

15. Yu J., Porter M.M. (2009). "In vivo crystallization of polyhydroxybutyrate for polymer recovery and purification." *8th World Congress of Chemical Engineering*, Montreal: Canadian Society for Chemical Engineering.

ABSTRACT OF THE DISSERTATION

Bioinspired Design: Magnetic Freeze Casting

by

Michael Martin Porter

Doctor of Philosophy in Materials Science and Engineering

University of California, San Diego, 2014

Professor Joanna McKittrick, Chair

Nature is the ultimate experimental scientist, having billions of years of evolution to design, test, and adapt a variety of multifunctional systems for a plethora of diverse applications. Next-generation materials that draw inspiration from the structure-property-function relationships of natural biological materials have led to many high-performance structural materials with hybrid, hierarchical architectures that fit form to function. In this dissertation, a novel materials processing method, magnetic freeze casting, is introduced

to develop porous scaffolds and hybrid composites with micro-architectures that emulate bone, abalone nacre, and other hard biological materials. This method uses ice as a template to form ceramic-based materials with continuously, interconnected microstructures and magnetic fields to control the alignment of these structures in multiple directions. The resulting materials have anisotropic properties with enhanced mechanical performance that have potential applications as bone implants or lightweight structural composites, among others.

CHAPTER 1:

AN INTRODUCTION TO BIOLOGY FOR ENGINEERS

1.1. Bioinspired design

Nature is the ultimate experimental scientist, having billions of years of evolution to design, test, and adapt a variety of multifunctional systems for a plethora of diverse applications. Learning from biological systems (i.e., natural materials and organisms), then applying modern engineering techniques to emulate these systems, scientists and engineers from a wide range of interdisciplinary fields develop surprisingly creative solutions to complex engineering problems. This process of engineering design inspiration and scientific discovery is broadly defined here as "**bioinspired design**."

The origins of this field date back to the late 1950's and early 1960's. In 1957, Otto Schmitt, a polymath, coined the term "**biomimetics**," which is now defined in the Merriam-Webster dictionary as:

> *The study of the formation, structure, or function of biologically produced substances and materials (as enzymes or silk) and biological mechanisms and processes (as protein synthesis or photosynthesis) especially for the purpose of synthesizing similar products by artificial mechanisms which mimic natural ones* [1].

This is not to be confused with the traditional field of "**bioengineering**," defined as:

> *The biological or medical application of engineering principles or equipment [or] the application of biological techniques (as genetic recombination) to create modified versions of organisms (as crops)* [1].

Later, in 1960, Jack Steele of the US Air Force coined the term "**bionics**," defined as:

> *A science concerned with the application of data about the functioning of biological systems to the solution of engineering problems* [1].

However, following popularization of the bionic man from the American television series, "The Six Million Dollar Man," the term *bionics* lost its appeal in the scientific community. Also, the term *biomimetics* suggests that scientists and engineers simply "mimic" natural systems to develop new technologies. On the contrary, the vast majority of these technologies are not copied, but rather, inspired by observations of the natural world. One of the most famous examples of this is Velcro®, which was invented by George de Mestral in 1941, and later patented in 1955, after plucking several burdock burrs off his dog's fur [2]. Following observation of the burdock burr under a microscope, de Mestral discovered the hook-and-loop mechanism - the inspiration for his invention (refer to Figure 1.1). Therefore, the title of this dissertation, *Bioinspired Design,* is a more accurate description of this multidisciplinary field of science and engineering.

Figure 1.2 contains a simple diagram illustrating the synergetic relationship between engineering and biology. That is, not only can engineers learn from biological systems to inspire novel engineering technologies - *i.e.*, *bioinspiration*, but scientists can also apply engineering methods to further explore biological phenomena - *i.e.*, *bioexploration*. For example, the gecko's tail was found by to be an active appendage in locomotion [3]. This scientific discovery came to light after engineers designed and tested a wall climbing robot, mimicking the gecko, finding that an artificial tail was necessary to act as a counterbalance for stability [4]. This example, presented as a TED talk in February 2009, inspired Robert Full, an integrative biologist at the University of

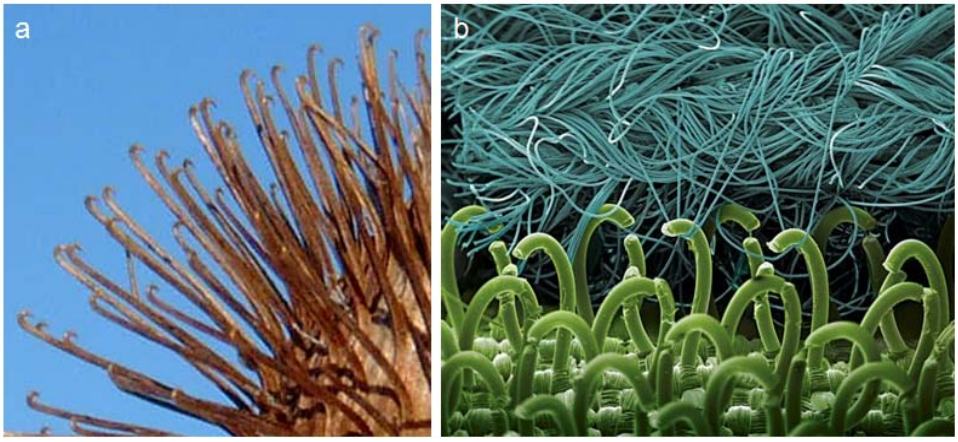

Figure 1.1. (a) Image of a burdock burr; **(b)** scanning electron micrograph of the hook-and-loop mechanism of Velcro. Images taken from [5, 6].

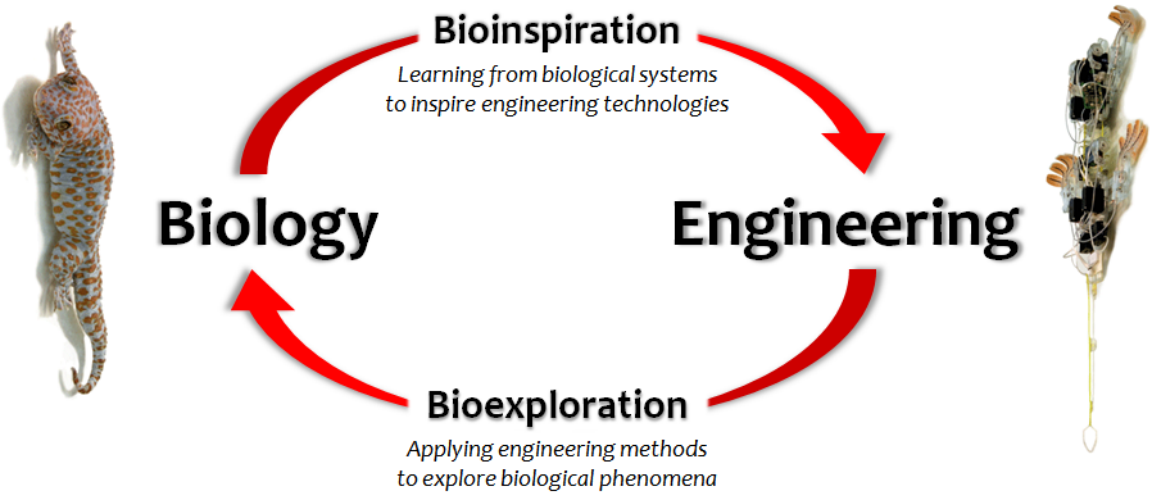

Figure 1.2. The synergetic relationship between biology and engineering, illustrating the processes of *bioinspiration* and *bioexploration* through the gecko-inspired, wall climbing robot. Adapted from Robert Full's definition of biomutualism [4]. Images taken from [7].

California, Berkeley, to coin the term "**biomutualism**," defined as:

> *An association between biology and another discipline where each discipline reciprocally advances the other [and] collective discoveries emerge beyond any single field* [4].

Although there are many examples of *bioinspiration* and *bioexploration* in the literature [8-13], the concepts and design methods involved are not well defined across the biological and engineering sciences. It seems the bottleneck, limiting the flow of knowledge between disciplines, is the difference in terminology and research methods commonly used in biology and engineering. Therefore, many engineering research groups have put forth considerable effort to investigate biological phenomena from an engineering point of view [8-55]. These groups have contributed significantly to the advancement of both engineering and biology, creating a vast "dataset" of biological knowledge using modern engineering techniques to investigate and present their findings in terms engineers can understand.

Other groups [56-65] have taken a different approach, using abstraction and linguistics as foundations to build bridges across disciplines. These groups [56-65] have identified several functional analogies that link common biological activities to engineering functions. For example, an engineer may use the functional term "clean" to devise a solution to a problem where, for optimal performance, a structure, surface, or device may need to be free from external dust, fluids, microorganisms, etc. [58]. Biologists, on the other hand, may not always use the term "clean" to describe systems that perform these tasks [58]. Instead, biologist may use terms such as "remove," "eliminate," or "kill" to describe biological systems that clean [58]. This lack of translation between disciplines makes research in bioinspired design difficult for

engineers not familiar with biology. Thus, several databases and search engines have emerged as attempts to bridge the gap between biology and engineering: BioTRIZ (biotriz.com), BioOnline (biology-online.org), and AskNature (asknature.org). Although their effectiveness is highly controversial, those attempts to link biology and engineering have gained considerable attention in recent years. For instance, AskNature.org is an online "catalog of nature's solutions to human design challenges [66]," maintained by the B Corporation, Biomimicry 3.8, which is sponsored by several legitimate engineering organizations, including Autodesk.

Regardless, the most exciting path through the bioinspired design process is, perhaps, an adventitious approach. This approach requires engineers to observe biological systems directly [64]. Then, rather than relying on complicated abstraction or functional analogies to devise new technologies, engineers can see for themselves the ingenious design of the complex, yet elegant, biological world. Through direct observation, it becomes apparent that several fundamental biological design principles emerge (detailed the following Section). Using those principles, engineers can begin to *learn from Nature* to develop more fundamental design methods, materials, and mechanical devices that draw inspiration from the vast array of highly-optimized biological solutions.

1.2. Learning from nature

Although inspiration from biology is not a new concept (e.g., flying machines inspired by birds were first conceptualized by Leonardo Da Vinci in 1488 and later realized by the Wright brothers in 1903 [67]), the rise of nanotechnology in the 1960's made it possible to design and fabricate an array of advanced functional materials and

mechanical devices inspired by nature [68]. These materials and devices, broadly defined here as bioinspired systems, emulate one or more of the basic principles that provide biological systems their efficient, life-friendly designs and highly-optimized properties (i.e., mechanical, electrical, optical, thermal, chemical, etc.). Nearly all natural biological systems follow six fundamental design principles (adapted from [9, 10, 12, 13, 67, 69, 70]):

1. *Depend on **water** for existence;*
2. *Produced & decomposed in **cyclic, life-friendly** processes (~300 K, ~1 atm);*
3. *Made up of locally available **organic (soft) & inorganic (hard)** building blocks (C, N, O, H, Ca, P, S…), resulting in a vast array of **hybrid** systems;*
4. ***Self-assembled** from the bottom up;*
5. *Able to grow, self-repair, adapt & evolve, **fitting form to function**;*
6. *Designed with **hierarchical** structures for efficiency and multifunctionality.*

The human body provides excellent examples of these design principles at work (see Figure 1.3). The musculoskeletal system (Figure 1.3a) is a multifunctional system that depends on water to grow and operate, composed of hierarchical materials that fit form to function [71]. The system combines both hard (skeleton) and soft (muscles) materials to achieve the multiple functions that allow organisms to perform daily activities. These materials are composed of locally available building blocks, self-assembled from the bottom up in life-friendly conditions. The hierarchical organization of, not only the materials that make up the system (bone and muscle), but also the different levels at which the two components interact, provides organisms an efficient biomechanical framework for body support and locomotion.

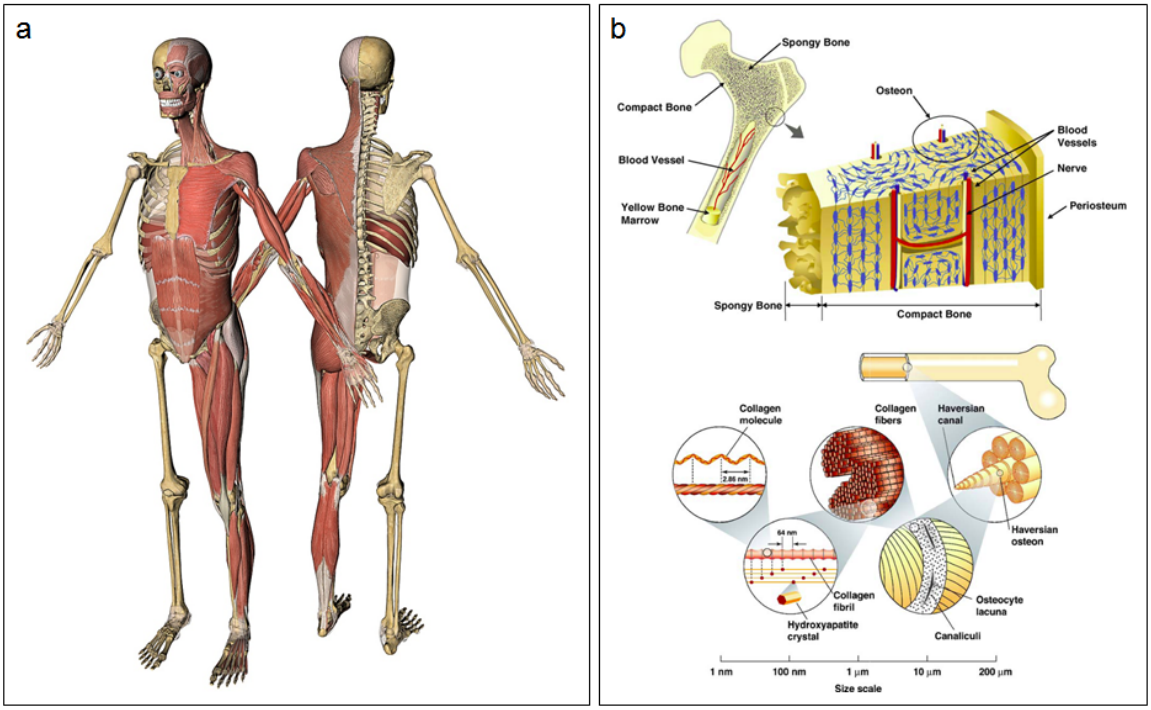

Figure 1.3. Illustrations of **(a)** the musculoskeletal system and **(b)** the hierarchical structure of bone. Images taken from [72, 73].

Looking further, bone is a multifunctional material that provides body support, joint movement, and blood flow, as well as the production and storage red and white blood cells and minerals [28]. It is a hybrid composite material composed of water, inorganic minerals (i.e., hydroxyapatite) and organic proteins (i.e., collagen), hierarchically structured from the nano- to macro- scales [28]. Figure 1.3b shows the hierarchical organization of bone (described in more detail in the following chapter) [72]. This intricate organization of both hard (minerals) and soft (proteins) constituents provides bone with its exceptional strength and toughness, while allowing it to be highly porous to reduce weight and permit fluid flow.

Research in bioinspired design has led to the development of novel, high-performance engineering technologies that mimic or draw inspiration from natural biological systems. For instance, many bioinspired materials that mimic bone are stronger, tougher, and more lightweight - ideal for applications ranging from bioactive tissue replacements to lightweight structural composites [74-84]. In addition to bioinspired materials, there is also an assortment of bioinspired structures, devices, and robotics [17, 18] that draw inspiration from biological structures (e.g., buildings inspired by termite mounds [85]), mechanisms (e.g., light-harvesting devices inspired by photosynthesis [86]), and organisms (e.g., flying robots inspired by insects [87]). The ultimate goal of bioinspired design is to allow engineers to, not only mimic or draw inspiration from natural systems, but also use the six principles listed above as design guidelines to develop more high-performance and environmentally sustainable technologies.

1.3. What to expect?

In this dissertation, the invention of a novel materials processing method, *Magnetic Freeze Casting*, is revealed as an example of a bioinspired design. First published in *Materials Science and Engineering: A*, Porter et al. [88] demonstrated the use of magnetic fields to align ceramic particles during the freeze casting process. The inspiration behind this method came from the quest to engineer bioinspired materials with designer architectures that emulate the microstructural anisotropy and mechanical properties of bone, abalone nacre, and other hard biological materials. To provide sufficient background, Chapter 2 introduces selected bioinspired materials relevant to

appreciate the novelty and potential application of this work. Chapters 3-4 provide a comprehensive review of different freeze casting techniques developed to date, including those investigated by Porter et al. [89], featured on the back cover of *Advanced Functional Materials*. Chapters 5-7 elucidate magnetic freeze casting as an advanced materials processing method to fabricate bioinspired materials with aligned microstructures and enhanced mechanical properties. Finally, the future of magnetic freeze casting is discussed in Chapter 8, as this research will continue beyond the scope of this dissertation. Chapters 2-7 are adapted from six manuscripts, published, currently under review or in progress [88-92].

CHAPTER 2:

BIOINSPIRED MATERIALS

2.1. Introduction

Biological materials science focuses on the structure-function-property-processing paradigm, a common theme in materials science, that governs the performance of natural materials [93]. Most research in the area of bioinspired materials is directed toward the development of functional materials inspired by the latter four principles, presented in Chapter 1: *hybrid systems*, *self-assembly*, *fitting form to function, and hierarchical structures*. A few examples of functional materials inspired by nature include:

- Resilient fibers inspired by spider silk [94-96];
- Self-assembled and mineralized fibers inspired by collagen [97-99];
- Wet and dry adhesives inspired by mussel byssus and gecko toes [39, 100];
- Hydrodynamic and antifouling surfaces inspired by shark skin [101-104];
- Antireflective films inspired by butterfly wings and insect eyes [105-108];
- Fiber optics inspired by sponge spicules [14, 15, 106, 109, 110];
- Self-cleaning surfaces and paints inspired by the lotus leaf [23, 111, 112];
- Self-healing composites inspired by bone and vascular networks [113-115];
- Stimuli responsive materials inspired by sea cucumbers [21, 116];
- Electro-active and shape memory materials inspired by muscles [117-120];
- Cellular solids inspired by bone [121-124];
- Tough ceramics and composites inspired by abalone nacre [75, 80, 84].

Of those listed above, the work presented in the remainder of this dissertation is directed toward the development of cellular solids, tough ceramics, and hybrid composites inspired by bone, abalone nacre, and other structural biological materials. These materials may be useful for a variety of applications ranging from load-bearing bone implants and lightweight structural composites to separation filters and catalyst supports [90].

2.2. Learning from bone and nacre

Why learn from bone and nacre? Well, bone and nacre are both natural ceramic-based materials, containing small fractions of organic matter, that exhibit extraordinary mechanical properties, given their lightweight composition of locally available elements (Ca, P, C, O, H) [8-10, 12, 27, 31]. Bone and nacre are stiff, strong and tough - mechanical properties, which are generally considered mutually exclusive [46]. Figure 2.1 contains Ashby plots comparing the mechanical properties of bone and nacre to several other natural materials [13]. As seen in the plots, these materials are surprisingly tough, considering their low density, high strength and stiffness. The reason for this unusual combination of properties stems from their hybrid, hierarchical design, self-assembled from the molecular level up, resulting in anisotropic architectures. The diagrams shown in Figure 2.2 contain images illustrating the structural hierarchy of bone and nacre [43, 52].

Bone is generally composed of ~65 wt.% hydroxyapatite ($Ca_{10}(PO_4)_6(OH)_2$) minerals embedded in an organic matrix of type I collagen (refer to Figure 2.2a) [27, 52, 125]. It exists in two main forms: cortical (or compact) and cancellous (or spongy)

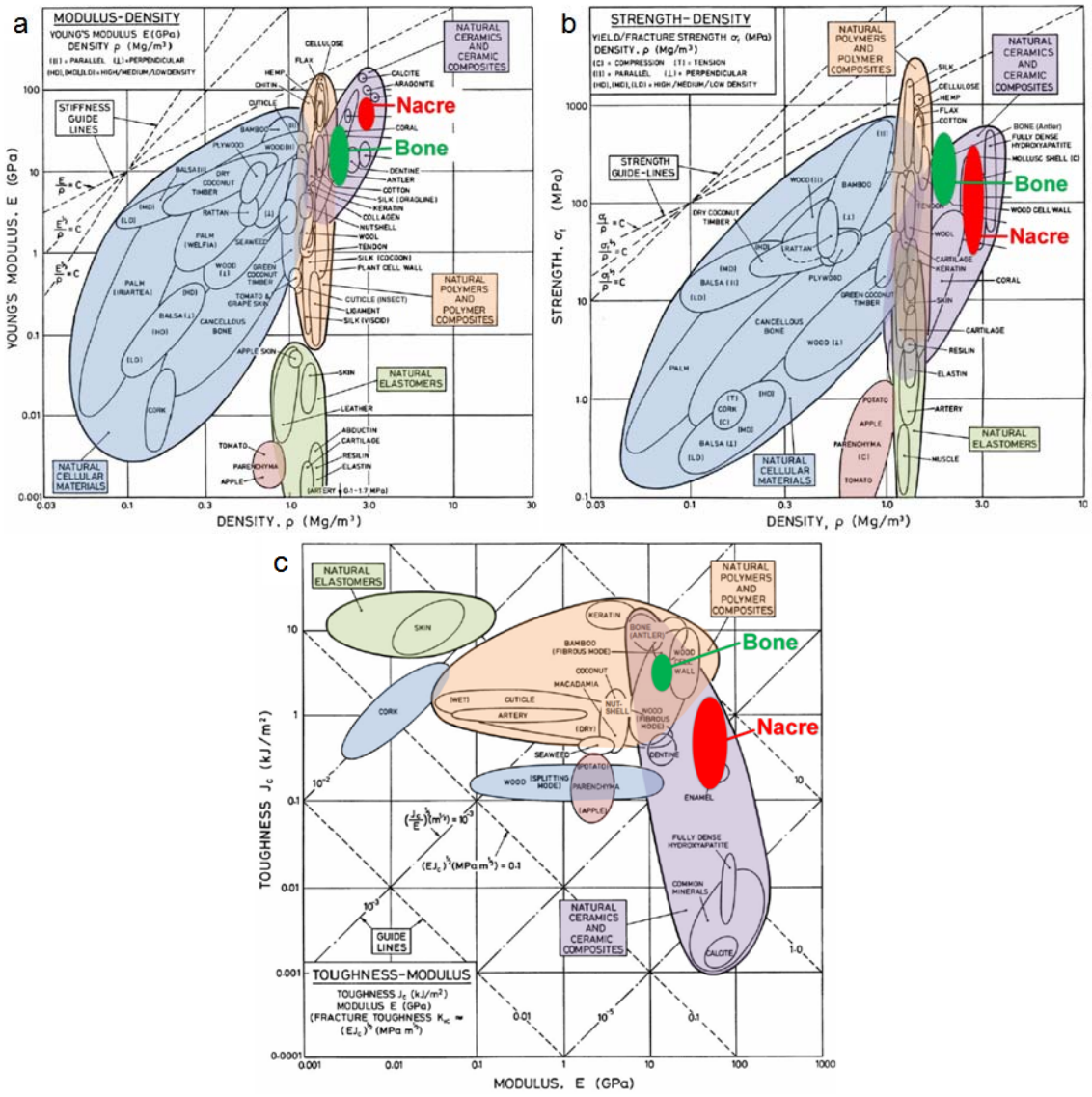

Figure 2.1. Ashby plots comparing the mechanical efficiency of natural materials: **(a)** Young's modulus versus density; **(b)** strength versus density; **(c)** toughness versus modulus. The highlighted green and red regions correspond to bone and nacre, respectively. The light colored regions correspond as follows: blue - natural cellular materials; green - natural elastomers; orange - natural polymers and polymer composites; purple - natural ceramics and ceramic composites. Adapted from [13].

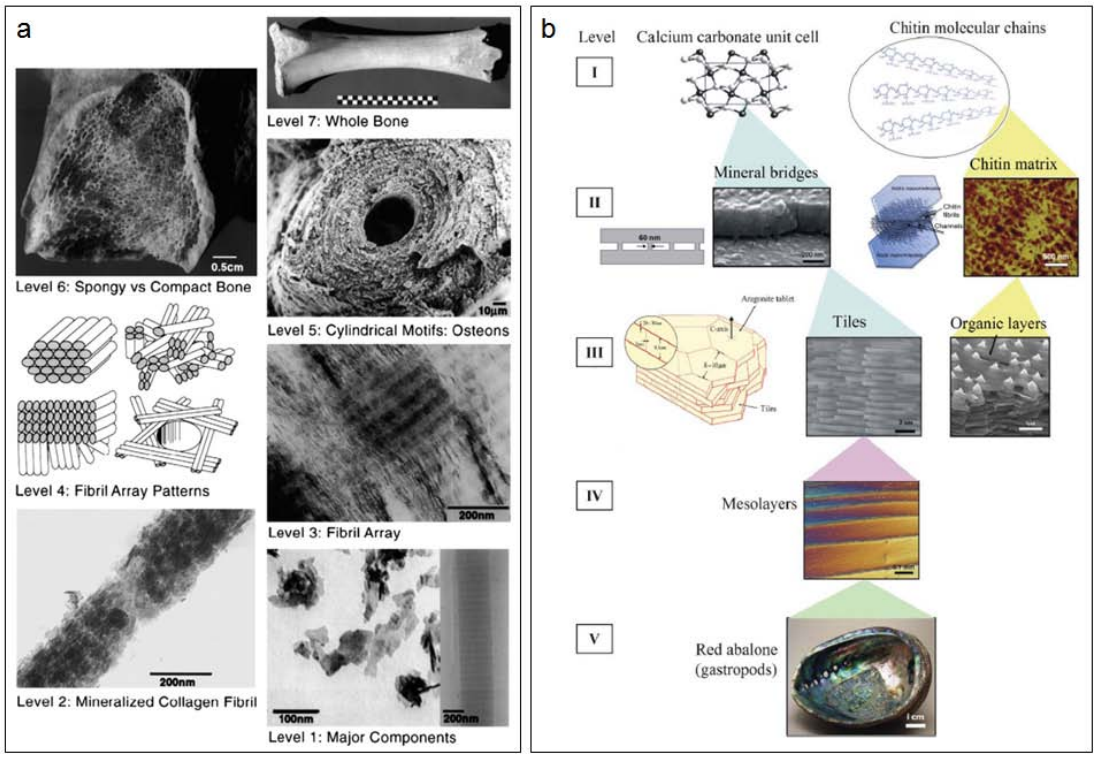

Figure 2.2. Hierarchical structure of **(a)** bone and **(b)** nacre. Taken from [43, 52].

[27, 52, 125]. At the microstructural level, cortical bone is composed of osteons, which consist of dense (5-10% porosity) concentrically oriented lamellar sheets that surround small vascular channels (Haversian canals) and lacuna spaces ~10-50 μm in diameter [126, 127]. These lamellar sheets are ~3-7 μm thick, arranged in a twisted plywood architecture, where the fibers making up each lamellae are oriented at different angles [38, 52]. Each fiber is composed of several mineralized collagen fibrils ~100 nm in diameter and ~5-10 μm in length [38]. Each fibril consists of tropocollagen proteins and periodically spaced hydroxyapatite minerals with a characteristic periodicity of ~67 nm [128]. Cancellous bone, on the other hand, is an open porous cellular solid (75-85% porosity), consisting of trabecular struts that surround large pores ~100-500 μm in

diameter [126, 129]. Although morphologically similar to cortical bone at the submicron-level, cancellous bone contains flat lamellar sheets, rather than cylindrical osteons [130]. Interestingly, the growth of bone (cortical and cancellous) is mediated by mechanical loading (i.e., bone grows in response to stress), which results in heterogeneous compositions and mechanical properties that vary across species with location, age, sex, and physiology [38]. And, although not widely accepted, recent studies have confirmed that the organic proteins and inorganic minerals in bone are continuously interconnected [125, 131-133].

In comparison to bone, nacre exhibits superior mechanical properties, primarily due to its lack of porosity. Nacre is composed of ~95 wt.% crystalline aragonite ($CaCO_3$) platelets (or tiles) embedded in an organic matrix of chitin (refer to Figure 2.2b) [35, 40]. Organization of the inorganic platelets and organic matrix is most commonly described as a "brick-and-mortar" structure, where stacked aragonite platelets, ~0.5 μm thick by ~8-10 μm wide, are the "bricks" and organic layers, ~20-50 nm thick, are the "mortar" [35, 134]. Connecting the platelets are mineral bridges ~25-55 nm thick [135, 136]. The platelets have a characteristic surface roughness due to asperities ~50 nm wide and ~30 nm high [137]. However, the platelets are not discrete tiles dispersed in a continuous organic matrix. Like bone, the organic and inorganic constituents are continuous, interpenetrating phases that grow concurrently [135, 138]. Additional growth bands, corresponding to periods of growth interruption, are composed of organic layers ~20 μm thick, which separate mesolayers ~300 μm wide [40, 138].

Several mechanisms across different length scales contribute to the excellent strength and toughness of bone and nacre [11, 38, 44, 46, 134, 137, 139-141]. In bone,

extrinsic toughening mechanisms occur behind the crack tip at length scales typically >1 μm [38, 46]. These include crack deflection and twisting around osteons, uncracked-ligament bridging, collagen-fibril bridging, and constrained microcracking [38]. Intrinsic toughening mechanisms in bone occur ahead of the crack tip at length scales typically <1 μm [38, 46]. These include hidden length sacrificial bonding, microcracking, fibrillar sliding, and molecular uncoiling [38]. In nacre, the brick-and-mortar structure deflects crack propagation, leading to failure via delamination, tile pull-out or tile fracture [139]. As stress accumulates through the structure, the organic matrix dissipates energy, acting as a tough viscoelastic glue [134, 137]. The mineral bridges resist inter-tile shearing (tile pull-out) and tensile failure (tile fracture), acting as reinforcing struts that provide nacre its strength and stiffness [134, 137]. The surface asperities shield against excessive sliding between adjacent platelets, further reinforcing nacre against fracture mechanisms, such as delamination or tile pull-out [134, 137]. Other proposed toughening mechanisms in nacre, include platelet interlocks (waviness) as well as the rotation, sliding, and organic bridging between nanograins [11, 139, 141].

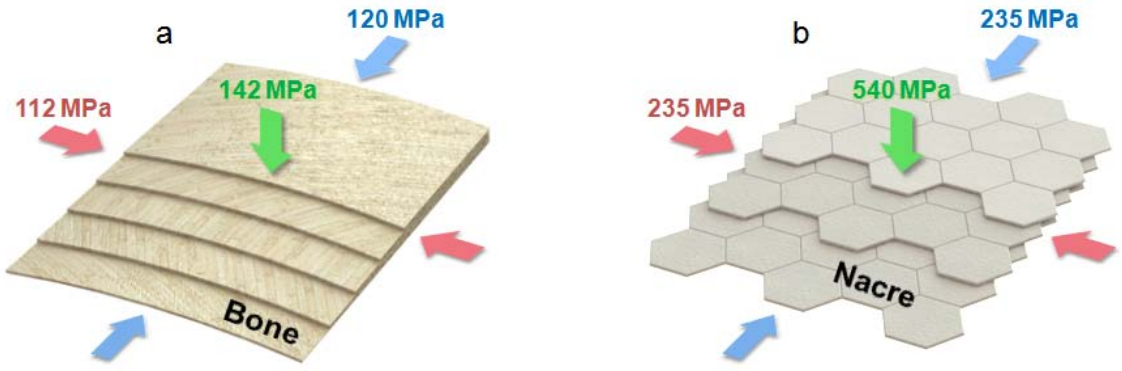

Figure 2.3. Microstructural anisotropy and compressive strengths for **(a)** lamellar bone and **(b)** abalone nacre. Mechanical properties taken from [25, 142].

On a more fundamental level, the microstructural anisotropy found in lamellar bone and nacre provide these materials their high compressive mechanical properties. As seen in Figure 2.3a, the microstructure of lamellar bone consists of several layers (or lamellae) of directionally aligned fibers that are oriented in successive rotations of ~30° [143]. This "twisted-plywood" structure, similarly observed in many hard biological materials [51, 55, 144-147], is commonly referred to as a Bouligand structure, after the discovering scientist, Y. Bouligand [148]. Figure 2.3b shows a schematic of the brick-and-mortar architecture found at the microstructural level in nacre. This organization of successive layers is a consequence of the nucleation and growth of aragonite crystals, leading to the formation of tiles aligned about the *c*-axis [138, 149]. The high, yet anisotropic, compressive strengths, shown in Figure 2.3, are directly related to the orientation, alignment, and uniformity of the layered microstructures in bone and nacre.

2.3. Engineering bioinspired materials

Learning from the strengthening and toughening mechanisms in found in nature, scientists and engineers now understand that most hard biological materials develop hybrid, hierarchical structures for optimal mechanical performance [8]. Emulating the intricate organization of the molecular, nano, micro, and macro structures found in nature may be the key to developing more high-performance synthetic materials [8]. With advanced synthetic material constituents (e.g., alumina (Al_2O_3), zirconia (ZrO_2), polymethylmethacrylate (PMMA), epoxy, etc.), rather than the relatively weak constituents found in nature (i.e., hydroxyapatite (HA), aragonite ($CaCO_3$), collagen, chitin, etc.), it becomes possible to engineer bioinspired materials with hybrid,

hierarchical architectures that outperform their biological counterparts. That is, following the rule of mixtures, it is obvious that the global mechanical properties (X) of a hybrid composite material are dependent on the properties (X_i) and fractions (ϕ_i) of its individual parts (i) [150]:

$$X = \sum \phi_i X_i. \tag{2.1}$$

However, most biological materials do not follow the rule of mixtures, exhibiting higher than expected mechanical properties [8]. For instance, two common modes of failure in platelet-reinforced composites are platelet fracture (brittle failure) and platelet pull-out (ductile failure) [48, 150]. In bone and nacre, the interfacial adhesion between the stiff inorganic platelets and ductile organic matrix are optimized, such that ductile failure occurs just before the point of brittle failure [48, 151]. This adaptation, in conjunction with their structural hierarchy, provides bone and nacre extremely high flaw tolerance and fracture toughness [48, 151] - better than that of most synthetic materials. As a result, much research has been dedicated to the development of multiscale models that predict the mechanical properties of natural and synthetic materials with hybrid, hierarchical architectures [131, 152-156]. Following these principles, bioinspired materials are expected to perform *better than predicted*, as well.

2.4. Bioinspired ceramic-based materials

Drawing inspiration from hard biological materials, many research groups have engineered, in the past decade, extremely strong, stiff, and tough ceramic-based materials [48, 74, 75, 80-84, 124, 151, 157-161]. Figure 2.4 shows images of several materials

fabricated by different processing techniques inspired by nature to produce thin films (a-e), porous scaffolds (f-j), or bulk composites (k-o). Table 2.1 compares the properties of bone and nacre with these selected bioinspired materials.

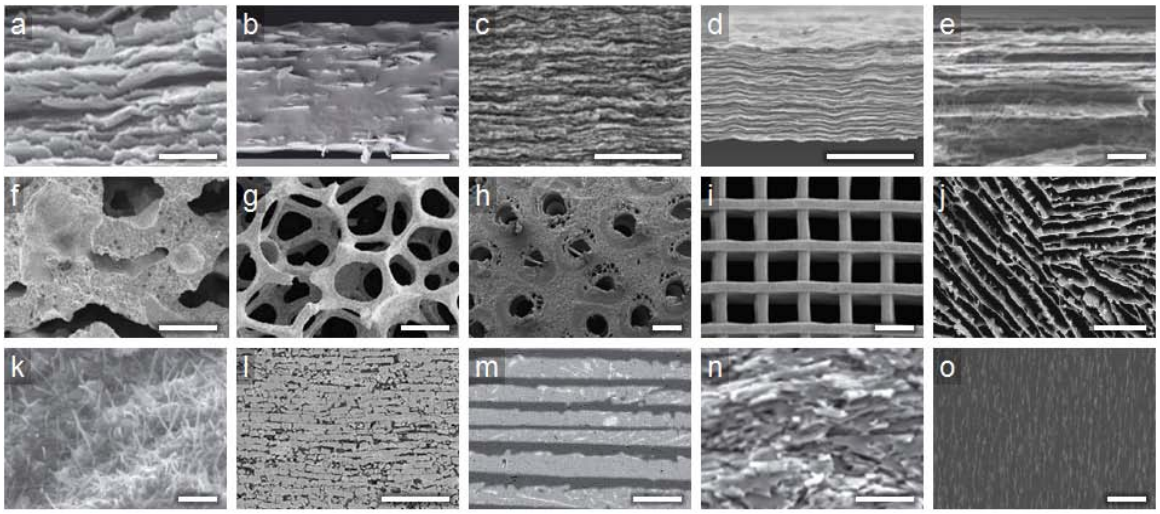

Figure 2.4. Images of several bioinspired **(a-e)** thin films, **(f-j)** porous scaffolds, and **(k-o)** bulk composites fabricated by different materials processing methods. **Thin films: (a)** layer-by-layer deposition [158]; **(b)** spin-coating [151]; **(c)** vacuum filtration [162]; **(d)** solution casting [163]; **(e)** fiber stretching and hot pressing [164]. **Porous scaffolds: (f)** direct foaming [165]; **(g)** polymer sponge replication [166]; **(h)** wood templating [167]; **(i)** 3D printing [160]; **(j)** freeze casting (ice templating) [76]. **Bulk composites: (k)** colloidal mixing and spark plasma sintering [161]; **(l)** freeze casting and polymer infiltration [84]; **(m)** freeze casting and metal infiltration [82]; **(n)** freeze casting and pressurized sintering [80]; **(o)** magnetic alignment and resin casting [83]. Scale bars: (a) 500 nm; (b) 10 µm; (c) 10 µm; (d) 10 µm; (e) 10 µm; (f) 500 µm; (g) 500 µm; (h) 500 µm; (i) 200 µm; (j) 150 µm; (k) 1 µm; (l) 100 µm; (m) 50 µm; (n) 10 µm; (o) 40 µm. Images correspond to Table 2.1, adapted from [76, 80, 82-84, 151, 158, 160-167].

Table 2.1. Structural and mechanical properties of bone and nacre compared to selected bioinspired thin films, porous scaffolds, and bulk composites fabricated by different materials processing methods. Data taken from [76, 80, 82-84, 141, 151, 158, 160-174].

	Material Composition	Total Porosity (%)	Young's Modulus (GPa)	Ultimate Strength (MPa)	Ultimate Strain (%)	Fracture Toughness ($MPa \cdot m^{1/2}$)
Natural Materials						
Bone (cancellous) [a]	HA/collagen	> 30*	0.001-0.5	0.2-116^{C}	0.3-3	---
Bone (cortical) [b]	HA/collagen	< 30*	6-28	10-172^{T} 106-283^{C} 157-238^{B}	0.9-2	2-11
Abalone nacre [c]	$CaCO_3$/chitin	---	10-147	3-170^{T} 235-540^{C} 177-197^{B}	0.2-2	3-9
Thin films [d]						
Podsiadla et al. [158]	MTM/PVA	---	106	400^{T}	0.33	---
Bonderer et al. [151]	Al_2O_3/chitosan	---	9.6	315^{T}	21	---
Walther et al. [162]	MTM/PVA	---	45.6	248^{T}	0.9	---
Li et al. [163]	GO/PVA	---	10.4	189^{T}	2.67	---
Cheng et al. [164]	CNT/Epoxy	---	107	1600^{T}	---	---
Porous Scaffolds [e]						
Almirall et al. [165]	HA	51-66	---	1.2-4.3^{C}	---	---
Kim et al. [166]	ZrO_2	74-92	---	1.6-35^{C}	---	---
Tampieri et al. [167]	HA	70-85	---	2.5-4^{C}	---	---
Fu et al. [160]	Glass	60-80	---	40-136^{C}	---	---
Deville et al. [76]	HA	47-64	---	16-145^{C}	---	---
Bulk Composites [f]						
Estili et al. [161]	Al_2O_3/CNT	---	---	404^{B}	---	4.62
Munch et al. [84]	Al_2O_3/PMMA	---	---	210^{B}	---	5.1
Launey et al. [82]	Al_2O_3/Al/Si	---	---	328^{B}	---	8.3
Bouville et al. [80]	Al_2O_3/SiO_2/CaO	---	290	470^{B}	---	6.2
Libanori et al. [83]	Al_2O_3/Epoxy	---	16.6	180^{B}	---	2.56

* Classification of bone porosity taken from [169].

[a] All data for proximal tibia; Young's modulus and ultimate compressive (C) strengths taken from [170]; ultimate strain to failure taken from [174].

[b] Young's modulus, ultimate strain to failure, and ultimate tensile (T), compressive (C), and bending (B) strengths taken from [173]; fracture toughness taken from [171].

[c] Young's modulus, fracture toughness, and tensile (T) and compressive (C) strengths taken from [141]; bending (B) strength taken from [172]; ultimate strain to failure taken from [168].

[d] All data are recorded as the highest reported values for Young's modulus, ultimate tensile (T) strength, and ultimate strain to failure.

[e] All data are recorded as a range of values for the total porosity and ultimate compressive (C) strength.

[f] All data recorded as the highest reported values for Young's modulus (flexural modulus), ultimate bending (B) strength (flexural strength), and fracture toughness for crack initiation.

2.4.1. Thin films

Thin films that draw inspiration from nacre have led to the development of many bottom-up fabrication techniques, in which a variety of chemical, physical, electrical, or mechanical forces are exploited to drive the assembly of synthetic building blocks [175, 176]. These methods include various processing techniques via layer-by-layer self-assembly [151, 157, 158, 177-179], biomineralization [180-182], centrifugation [183], evaporation or vacuum filtration [159, 162, 184-188], solution casting [163, 189, 190], chemical bath or electrophoretic deposition [191-197], ion beam sputtering [198, 199], and morphosynthesis [200].

Of these, a few methods stand out [151, 157, 158, 162, 163] (refer to Figures 2.4a-e and Table 2.1). In 2003, Tang et al. [157] reported one of the first significant attempts to develop nacre-like films by depositing sequential layers of montmorillonite (MTM) clay platelets and polyelectrolytes, polydiallydimethylammonium (PDDA), through a surfactant-mediated self-assembly approach. The resulting films [157] exhibited ultimate tensile strengths (up to 109 MPa) and Young's moduli (up to 13 GPa) similar to that of nacre and lamellar bone, respectively. Years later, Podsiadlo et al. [158] adopted a similar layer-by-layer approach to fabricate MTM/polyvinyl alcohol (PVA) nanocomposites that closely resemble the brick-and-mortar microstructure of nacre (see Figure 2.4a). These multilayer composites [158] are optically transparent and have an unsurpassed stiffness compared to similar nanocomposite films (see Table 2.1). Bonderer et al. [151] developed Al_2O_3/chitosan films with more ductility and flaw tolerance than prior works [157, 158], with observed ultimate tensile strains up to 21% (see Figure 2.4b and Table 2.1). These composites [151] were developed sequentially, through a bottom-

up spin-coating technique. Using an alternative, eco-friendly method via vacuum filtration (i.e., paper-making), Walther et al. [162] fabricated high strength-high stiffness MTM/PVA composites with varying optical transparencies as well as gas barrier and fire-resistant properties (see Figure 2.4c and Table 2.1). More recently, Li et al. [163] and Cheng et al. [164] developed carbon-based composite films with extraordinary mechanical properties (see Table 2.1). Graphene oxide (GO)/PVA composite films (see Figure 2.4d) were fabricated by Li et al. [163] via a simple solution casting method [163]. In addition to their outstanding mechanical properties, the GO/PVA films showed excellent electrical conductivity and biocompatibility, making them promising candidates for tissue engineering applications [163]. Flattened double-walled carbon nanotube (FDWCNT)/epoxy composites developed by Cheng et al. [164] exhibited extremely high tensile strength and stiffness (see Figure 2.4e and Table 2.1). These remarkably high mechanical properties were obtained by aligning and cross-linking the FDWCNT/epoxy composites through a sequential process via fiber stretching, functionalizing, and hot pressing [164].

Regardless of the outstanding mechanical properties and special functionalities, thin films are, in fact, thin (<<1 mm) and not practical for many applications. Therefore, considerable effort has been put forth to develop bulk materials (i.e., porous scaffolds and hybrid composites) inspired by bone and nacre.

2.4.2. Porous scaffolds

Porous scaffolds that mimic bone are ideal for tissue engineering applications, such as load-bearing bone implants that promote tissue ingrowth, or other applications

requiring a combination of high porosity and reasonable mechanical strength [79, 123, 201]. Many different methods to emulate the trabecular architecture of cancellous bone have been reported [127, 129, 202-219], including direct foaming (Figure 2.4f) [165] and polymer sponge replication (Figure 2.4g) [166]. However, mimicking cancellous bone is not ideal for load-bearing applications due to its high porosity, near isotropic structure, and poor mechanical properties (see Table 2.1). Instead, highly anisotropic scaffolds with unidirectionally aligned pores have shown great potential for load-bearing applications [76, 160]. An interesting method developed by Tampieri et al. [167] utilizes the unidirectional porosity of wood as a template to fabricate anisotropic hydroxyapatite scaffolds, following a series of chemical treatments (see Figure 2.4h). Although they [167] obtained optimal pore sizes (100-300 μm) required for the migration and proliferation of osteoblasts (bone synthesizing cells), the mechanical properties obtained are quite poor when compared to other unidirectionally porous scaffolds (refer to Table 2.1) [76, 160].

With the introduction of additive manufacturing (or 3D printing), a variety of porous scaffolds with designer architectures are now possible. In recent years, this technique has gained tremendous attention throughout the medical industry as an efficient means to develop customizable scaffolds for biomedical implants [74, 124, 160, 220]. Figure 2.4i shows an image of an anisotropic scaffold 3D printed from bioactive glass [160]. This 3D-printed scaffold, having a porosity of 60%, exhibits a compressive strength (136 MPa) within the range of cortical bone and a compressive modulus (2 MPa) within the range of cancellous bone (refer to Table 2.1) [160]. Because this scaffold is

fabricated from bioactive glass and the pore sizes are 200-500 μm, it is ideal for osseointegration (bone ingrowth) [126].

Other 3D printed scaffolds for tissue engineering applications show great promise [74, 221]. However, the mechanical properties of 3D printed parts are dependent on the formation and resolution of the layers (with the highest resolutions approaching ~10 μm). Ultimately the interface between layers is the weakest point of the structure, which may lead to catastrophic crack initiation, propagation, and subsequent failure. Thus, 3D printing is not the most economical means to develop high-performance scaffolds, due to its high cost, high energy consumption, extended fabrication times, limited material availability, restricted workspace, and poor material properties. Until additive manufacturing technologies improve, other methods to fabricate high-strength, porous scaffolds are more desirable.

Alternatively, freeze casting (or ice templating) is simple and convenient method to fabricate porous scaffolds with excellent mechanical properties [90, 121, 222]. Figure 2.4j shows a representative image of a hydroxyapatite scaffold formed by freeze casting, while Table 2.1 shows a range of compressive strengths and porosities for scaffolds freeze cast by Deville et al. [76]. This method is quite adaptable and will be discussed in more detail in the following chapters.

2.4.3. Bulk composites

Bulk composites are, quite possibly, the most versatile and high-performance bioinspired materials of those discussed, due to their large macrostructures and general scalability. Several different methods have been explored to fabricate bulk ceramic-based

composites, including: polymer-controlled mineralization [223-225], lithography [226-228], slip casting [229], gel casting [230, 231], freeze casting [75, 80, 84], particulate or fiber reinforced resin casting [81, 83, 232, 233], extrusion and roll compaction [234], and hot pressing or sintering [80, 84, 161, 235]. Other promising techniques leading to ceramic-based composites with enhanced mechanical properties, include: infiltrating ceramic scaffolds with polymers or metals or aligning ceramic microstructures with external forces. Polymer or metal infiltration techniques can be classified as melt immersion [236, 237], solvent evaporation [233, 238-241], *in situ* polymerization [75, 82, 84, 126, 242-244], particle centrifugation [218], and chemical vapor deposition [245-247]. Alignment of ceramic microstructures can be accomplished via mechanical force [80, 84], thermal processing [80, 84], ice templating [75, 80, 82, 84], or magnetic fields [81, 83].

Table 2.1 compares the flexural strength and fracture toughness for crack initiation of several high-toughness Al_2O_3-based composites [80, 82-84, 161]. Estili et al. [161] mixed Al_2O_3 nanoparticles with multi-wall carbon nanotubes (MWCNT) in a colloidal suspension before spark plamsa sintering to densify the composites (see Figure 2.4k). Extremely high flexural strengths and fracture toughness up to 404 MPa and 4.62 $MPa \cdot m^{1/2}$, respectively, were observed in these composites [161]. For the following three materials presented in Table 2.1, Munch et al. [84], Launey et al. [82], and Bouville et al. [80], utilized freeze casting with different post processing techniques to fabricate extremely strong and tough Al_2O_3-based materials. Munch et al. [84] infiltrated polymethylmethacrylate (PMMA) into freeze cast scaffolds after pressurized sintering to make composites that resemble a brick-and-mortar microstructure (Figure 2.4l). Launey

et al. [82] use a similar method to infiltrate molten Al-Si alloys into freeze cast scaffolds (see Figure 2.4m), resulting in a much higher flexural strength (up to 328 MPa) and unsurpassed toughness (up to 8.3 $MPa \cdot m^{1/2}$). However, the polymeric phase in the Al_2O_3/PMMA composites or the metallic phase in the Al_2O_3/Al/Si composites may be undesirable for certain applications, such as high-temperature work environments. For that reason, Bouville et al. [80] developed $Al_2O_3/SiO_2/CaO$ composites by freeze casting and subsequent pressurized spark plasma sintering (see Figure 2.4n), which exhibit the highest combination of strength (470 MPa) and toughness (6.2 $MPa \cdot m^{1/2}$), yet to be reported for a pure ceramic material. These freeze casting methods rely on the controlled growth of ice crsytals to align the microstructures of these materials [80, 82, 84]. The outstanding combinations of strength and toughness result from this intricate microsturctural alignment, which provides these materials several fracture resistant mechanisms, similar to that of bone and nacre [80, 82, 84].

In a different technique, Erb et al. [81] and Libanori et al. [83] (see Figure 2.4o) used low magnetic fields to align Al_2O_3 platelets in polymer matrices. The aligned microstructures increased the flexural modulus, strength, and fracture toughness significantly compared to that of identical composites without magnetic alignment [83]. However, these composites are still limited by the low achievable volume fraction and discontinuity of ceramics platelets embedded in a continuous polymer matrix.

2.5. Inspiration from biology

Mimicking the microstructural features and anisotropic organization of bone, nacre, and other hard biological materials has led to more lightweight, stronger, tougher,

and robust functional materials for a variety of applications (see Table 2.1) [76, 80, 82-84, 151, 158, 160-167]. In all of the methods previously discussed, the thin films, porous scaffolds, and bulk composites were selected because they mimic, or draw inspiration from, one or more of the nano/microstructural features that provide bone and nacre their extraordinary mechanical properties.

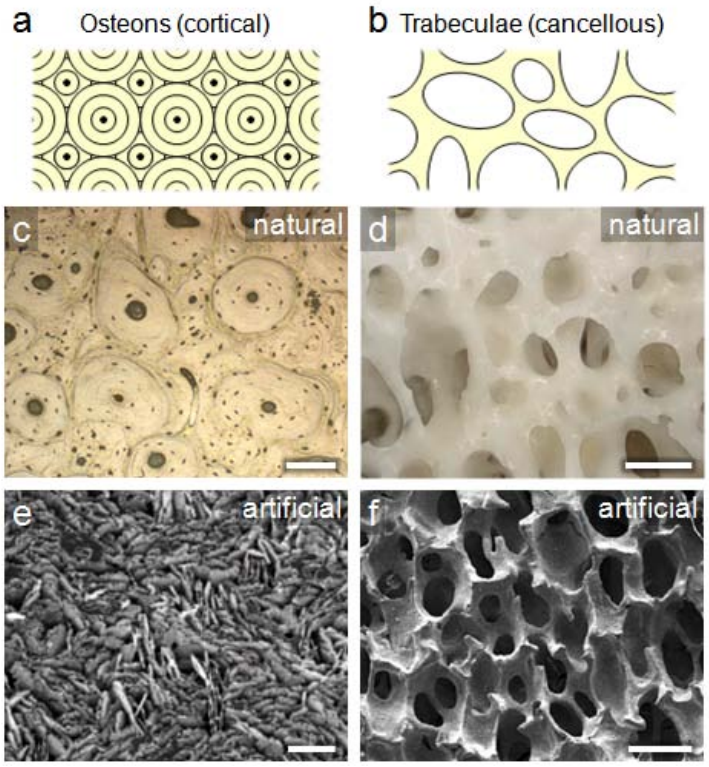

Figure 2.5. Images of natural (top) and artificial (bottom) bone materials: **(a-b)** schematics of osteonal and trabecular bone architectures; **(c)** natural osteons found in cortical bone (credit: E. Novitskaya); **(d)** natural trabecular struts found in cancellous bone; **(e)** artificially aligned microstructures mimicking the architecture of osteonal bone [81, 248]. **(f)** artificially produced scaffold mimicking the architecture of trabecular bone [249]. Scale bars: (c) 100 µm, (d) 500 µm, (e) 20 µm, (f) 500 µm. Adapted from [81, 249].

Figure 2.5 shows two artificial materials inspired by bone that mimic the microstructures of osteons (Figure 2.5a,c) and trabeculae (Figure 2.5b,d). The artificial osteon-like architecture shown in Figure 2.5e was fabricated by Erb et al. [81, 248], using magnetic fields to control the directional alignment of Al_2O_3 platelets in a polyurethane resin. The resulting particulate composites exhibited enhanced stiffness, strength, hardness, wear resistance, and localized reinforcement similar to that of natural cortical bone [81, 248]. The artificial trabecular scaffold shown in Figure 2.5f was fabricated by Yang et al. [249] using a modified method that combined freeze gel casting and the polymer sponge technique [249-251]. In this method, a polyurethane foam was placed in a mold containing a HA/TBA-based slurry, then unidirectionally frozen [249]. After complete solidification, the frozen constructs were lyophilized to remove the frozen solvent and heat-treated to burn-out the sacrificial polyurethane sponge [249]. After sintering, the highly porous (55-95%) trabecular scaffolds had large pore sizes of 180-360 μm and reasonable compressive strengths of 1-7 MPa [249], comparable to that of natural cancellous bone (refer to Table 2.1).

Figure 2.6 juxtaposes schematics and micrographs of natural abalone nacre (Figure 2.6a-h) with various bioinspired materials that mimic the microstructural features of nacre (Figure 2.6i-l). In the first column of Figure 2.6 (a, e, i), the strong and tough ceramics developed by Bouville et al. [80] are compared to that of natural nacre. Not only, did they [80] obtain extremely high mechanical properties (refer to Table 2.1), but they also mimicked nearly all of the microstructural features of nacre on equivalent length scales, including: the brick-and-mortar architecture, platelets, mineral bridges and surface asperities. The next three columns of Figure 2.6 (b-d, f-h, j-l) compare natural and

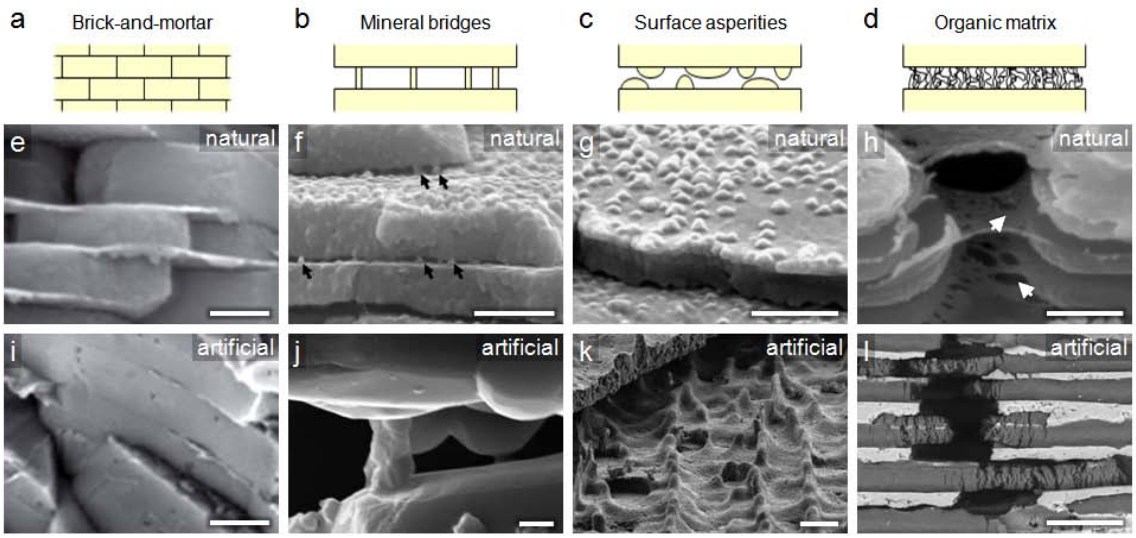

Figure 2.6. Schematics and images of different architectures in natural (top) and artificial (bottom) nacre materials: **(a, e, i)** brick-and-mortar, **(b, f, j)** mineral bridges, **(c, g, k)** surface asperities, and **(d, h, l)** organic matrix. Scale bars: (e) 500 nm, (f) 500 nm, (g) 500 nm, (h) 1 µm, (i) 500 nm, (j) 500 nm, (k) 10µm, (l) 25 µm. The natural micrographs were taken from [40, 80, 137]. The artificial micrographs were all developed by different freeze casting techniques, taken from [80, 84, 243].

artificial mineral bridges, surface asperities, and organic matrices [84, 243]. The artificial mineral bridges and surface asperities were fabricated by freeze casting [84], while the artificial organic matrix was produced by infiltrating a polymer into a freeze cast scaffold [243]. Although all of these features occur on different length scales in the natural and artificial materials (on the order of ~50 nm for the natural and ~500-5000 nm for the artificial), their mechanical functions are the same [84, 243]. The mineral bridges and surface asperities add strength and stiffness, resisting against tensile fracture and intertile shearing. The organic matrix adds toughness, dissipating energy that accumulates between adjacent lamellae under stress.

In all of these examples (Figures 2.5 and 2.6) [80, 81, 84, 243, 249], different processing techniques were used to synthesize materials that mimic various structural features of bone and abalone nacre, leading to outstanding mechanical properties that either match or surpass those of their natural counterparts. In this dissertation, a combination of these methods was employed to develop ceramic-based porous scaffolds and bulk composites with highly anisotropic architectural alignment and enhanced mechanical properties.

Figure 2.7 provides a general overview of the methods: (a) freeze casting, (b) magnetic alignment, and (c) polymer infiltration. First, as previously mentioned, freeze casting is an efficient means to fabricate porous ceramic scaffolds with unidirectionally align pores, parallel to the direction of ice growth (Figure 2.7a). Second, applying magnetic fields during the freeze casting process leads to a second order of microstructural alignment, parallel to the magnetic field (B) direction (Figure 2.7b). Third, infiltration the bi-aligned porous scaffolds with a second phase (e.g., polymer) leads to bulk hybrid composite materials with designer architectures and enhanced mechanical properties (Figure 2.7c). Representative micrographs of materials fabricated by the different techniques are shown in Figures 2.7d-f. The specific details of the magnetic freeze casting technique and the resulting architectural alignment and mechanical performance of these materials obtained to date are discussed in further detail in the following chapters.

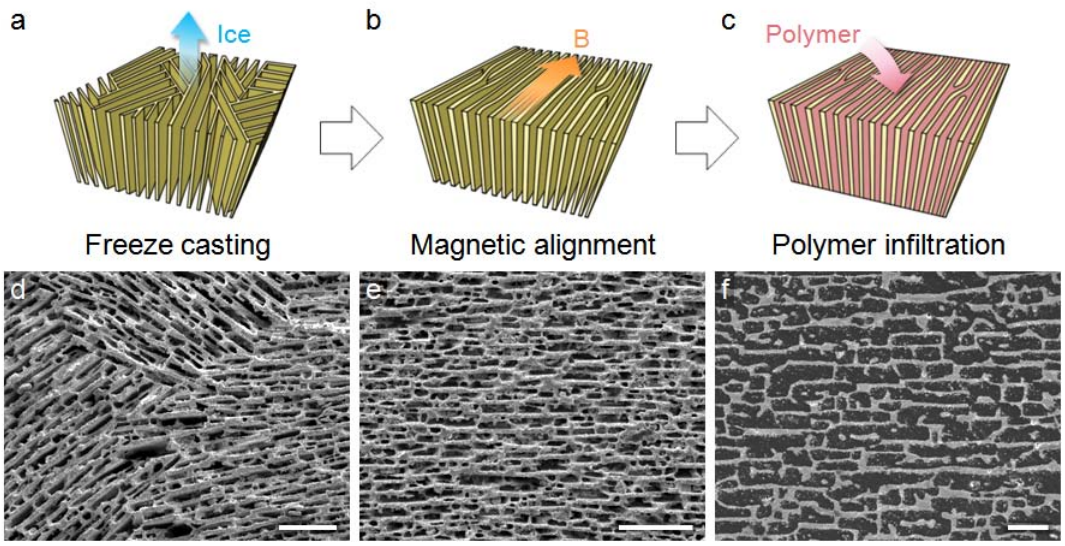

Figure 2.7. Schematics of the **(a)** freeze casting, **(b)** magnetic alignment, and **(c)** polymer infiltration methods to produce ceramic-based porous scaffolds and hybrid composites. **(d-f)** Representative micrographs of ZrO_2 scaffolds (d-e) and ZrO_2-epoxy composites (f) fabricated by the respective techniques, shown above. All scale bars are 100 µm.

2.6. Acknowledgements

Chapter 2, in part, is published as a review article in *American Ceramic Society Bulletin* and co-authored by J. McKittrick of UCSD.

CHAPTER 3:

FREEZE CASTING: A REVIEW

3.1. Introduction

Synthetic materials inspired by nature often posses one or more characteristics that mimic their biological counterparts. Whether form or function, bioinspired materials arise from the study and observation of various biological phenomena [8, 9]. Many structural biological materials, such as bone and abalone nacre, have evolved to be lightweight, strong and tough [9, 10]. Their exceptional mechanical properties are a product of their intricate structural organization, anisotropy, and architectural hierarchy from the nano- to macro-scale [8-10]. In recent years, a variety of different "bottom-up" and "top-down" materials processing methods, ranging from self-assembly [157, 163, 186] and layer-by-layer deposition [151, 158] to nanolithography [226, 252] and 3-D printing [160, 253, 254], have been explored to mimic the microstructural characteristics of different biological materials. Of those, freeze casting is a relatively simple and inexpensive technique to fabricate bulk porous materials and hybrid composites of near net shapes. Reviews by Deville [121], Gutierrez et al. [255], Qian et al. [256], and Li et al. [222] provide excellent overviews of general freeze casting topics, including the processing principles, materials, structures, properties, and applications. This chapter provides a review of freeze casting as is relates to different materials and processing modifications inspired by nature.

Freeze casting, also known as ice templating or freeze gelation, is commonly used to form ceramic components with controllable porosity. Because freeze casting is a

physical process, it can be used to fabricate a variety of polymeric, metallic, ceramic, and composite materials [121, 222, 255, 256]. The fabrication of materials formed by freezing was first introduced in 1908 by Lottermoser [257] and Bobertag et al. [258]. In 1954, modern day freeze casting was described by Maxwell et al. [259] as a way to cast intricately shaped objects from refractory powders. However, it was not until 2001 when Fukasawa et al. [260, 261] described freeze casting as a way to fabricate ceramic materials with complex pore architectures and controllable porosity. In 2006, Deville et al. [75] introduced the methods of freeze casting porous ceramics and subsequent infiltration of polymers or metals to develop hybrid composites inspired by bone and nacre. Using this technique, Munch et al. (2008) [84] developed hybrid inorganic-organic composites that mimic the brick-and-mortar structure of nacre, yielding a toughness more than 300 times (in terms of energy) that of their individual constituents. Since, freeze casting has become a popular field of research in the processing of bioinspired porous ceramics and hybrid composites - the main focus of this review.

The typical materials processing steps involved in freeze casting porous ceramic structures combine "bottom-up" and "top-down" approaches. Figure 3.1 shows a phase diagram of water, illustrating the processing path of (a) slurry preparation and mixing, (b) freeze casting, (c) lyophilizing, and (d) sintering. First, ceramic powders are mixed into a liquid slurry consisting of a freezing vehicle (e.g., liquid solvent), dispersant (e.g., surfactant), and binder (e.g., long-chain polymer) (Figure 3.1a). A variety of freezing vehicles have been investigated, including water, camphene, camphor-naphthalene, and tert-butyl alcohol (TBA) [121]. Water is the most commonly used solvent in freeze casting because of its availability, ease of use (e.g., slurry preparation at room

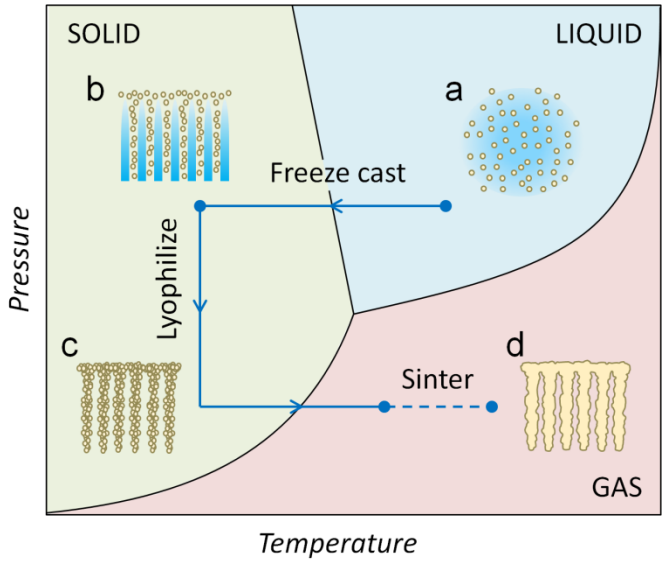

Figure 3.1. Phase diagram of water showing the path of processing steps involved in freeze casting porous ceramics: **(a)** slurry preparation and mixing; **(b)** freezing casting; **(c)** lyophilizing; **(d)** sintering. Adapted from [121].

temperature), low price and environmental friendliness. The dispersant is added to the slurry to prevent aggregation and flocculation of the ceramic particles during freezing [262]. The binder is added to act as a sort of glue, preventing collapse of the green bodies after lyophilization [263, 264]. Before freezing, the slurry is homogenized, usually by ball-milling, to sufficiently disperse the ceramic powders, and in many cases, grind the powders into finer particles [260, 261]. Second, the liquid slurry is poured into a mold and frozen (Figure 3.1b). Solidification of the freezing vehicle occurs in the direction of the temperature gradient, forming columnar channels of frozen solvent crystals. To prevent air bubbles from forming unwanted voids during solidification, the liquid slurry is usually degassed (or de-aired) prior to freezing [260, 261]. Third, the frozen sample is lyophilized (or freeze dried) to sublimate the frozen liquid phase (Figure 3.1c). The

resulting pores of the freeze-cast scaffolds after freeze drying are direct replicas of the frozen solvent crystals that form channels in the direction of the temperature gradient [121]. An economical alternative to lyophilization is freeze-photocuring-casting [265], where photo-curable monomers are added to the slurry as sacrificial binders. After freezing, the freeze-cast microstructure is fixed by photo-initiated polymerization, allowing it to be dried in ambient conditions [265]. Fourth, the dried green body is sintered to partially densify and strengthen the porous ceramic constructs (Figure 3.1d). During or prior to this stage, the fugitive organic phases (i.e., dispersants and binders) are removed from the scaffolds with heat. The final sintered scaffolds are composed of a continuous network of dense ceramic walls that surround interconnected channels with open porosity [266].

There is a wide range of potential applications for porous ceramics fabricated by freeze casting. Bioinspired applications, such as potential bone replacements [75-78, 89, 126, 249, 267-283] and hybrid composites (upon infiltration of a second phase) [75, 82, 84, 242, 243, 284-286] are most encouraging and are the primary focus of this review. However, more traditional applications [121, 222, 255, 256], such as separation filters and insulators, may also benefit from the ability to cast ceramic materials into complex shapes with designer porosity. Other potential applications include, but are not limited to, sensors, electrodes, catalyst supports, fuel cells, and piezoelectric devices [121, 222, 255, 256].

3.2. Solidification theory

The theory behind freeze casting was recently explicated by Zhang et al. [287], Deville et al. [288-290], and Wegst et al. [78]. The process of freeze casting ceramics depends on the rheological properties and thermodynamics of the colloidal suspension [78, 253, 262-264, 283, 288, 291-294]. The slurry viscosity depends on the type of liquid carrier and the type and concentration of dispersants, binders, solid loadings (e.g., ceramic particles) and any other additives. As with any colloidal system, sedimentation of the particles is affected by the force of gravity, buoyancy, slurry viscosity and particle size, while the particle-liquid interactions are controlled by van der Waals forces, hydrogen bonds, and electrostatic forces [78].

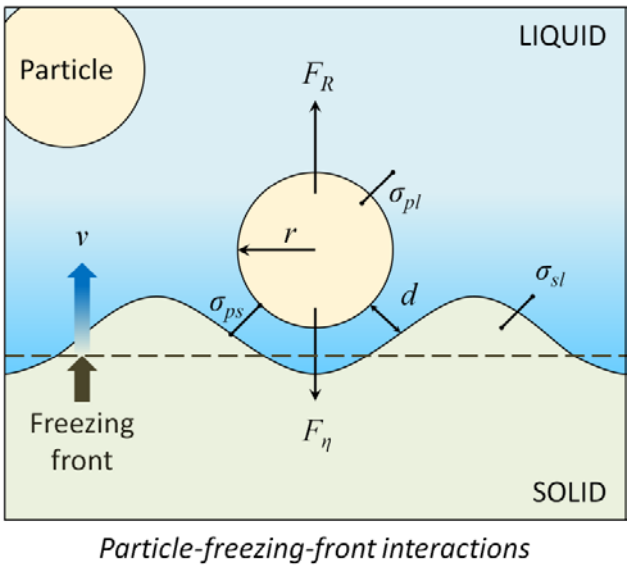

Figure 3.2. Particle-freezing-front interactions, where a particle of radius r separated from the solid-liquid interface by a liquid film of thickness d experiences a repulsive force F_R and an attractive force F_η. Balancing the forces, a critical freezing front velocity v_{cr} can be calculated, above which the particles will be engulfed and trapped, and below which the particles will be rejected and pushed ahead by the solid-liquid interface. Adpated from [78].

Figure 3.2 contains a diagram of the interactions present at the particle-freezing-front interface [78]. Instabilities (or undulations) at the freezing-front occur due to Brownian diffusion of the particles leading to constitutional supercooling, which drives the nucleation and growth of well-ordered, interconnected frozen solvent crystals (e.g., ice crystals) [288]. During freezing, ceramic particles are pushed between and trapped within the frozen solvent (refer to Figure 3.1b). The velocity of the freezing-front governs the phenomena of particle entrapment and rejection. A critical velocity at which the particles are trapped or rejected is derived from the thermodynamic free energy of the system [78]:

$$\Delta\sigma_0 = \sigma_{ps} - \left(\sigma_{pl} + \sigma_{sl}\right) \tag{3.1}$$

where $\Delta\sigma_0$ is the free energy of the system, and σ_{ps}, σ_{pl}, and σ_{sl} are the surface energies between the particle-solid, particle-liquid, and solid-liquid interfaces, respectively (see Figure 3.2). If the energy of the particle-solid interface is lower than the sum of the energies at the particle-liquid and solid-liquid surfaces, then the system free energy is negative ($\Delta\sigma_0 < 0$), resulting in particle entrapment [78]. If the system free energy is positive ($\Delta\sigma_0 > 0$) the particle is rejected [78]. The repulsive force (F_R) and attractive force (F_η) experienced by a particle close to the freezing-front are primarily due to van der Waals interactions and viscous drag at the solid-liquid interface, respectively. These forces are expressed in terms of the particle radius r and the liquid layer thickness d, and determine the fate of a particle close to the approaching solid-liquid interface [78]:

$$F_R = 2\pi r\Delta\sigma_0\left(\frac{a_0}{d}\right)^n \tag{3.2}$$

$$F_\eta = \frac{6\pi\eta v r^2}{d} \tag{3.3}$$

where a_0 is the mean distance between molecules in the liquid layer, n is an exponential correction value typically in the range of 1 to 4 [287, 295, 296], η is the dynamic viscosity of the liquid, and v is the velocity of the freezing-front. Consequently, the critical velocity (v_{cr}) of the freezing-front, which governs particle entrapment and rejection, is derived by equating the repulsive and attractive forces [78]:

$$v_{cr} = \frac{\Delta\sigma_0 d}{3\eta r}\left(\frac{a_0}{d}\right)^n. \tag{3.4}$$

When the solidification velocity is above the critical velocity ($v > v_{cr}$), the particles are entrapped by the approaching freezing-front, while a solidification velocity below the critical velocity ($v < v_{cr}$) results in the particles being rejected and pushed ahead of the freezing-front. Consequently, the architecture of the pores or channels etched out by the freezing vehicle depends on a balance of particle entrapment and rejection. Empirically, it was found that the spacing and thickness of the lamellar walls of porous ceramics freeze cast with water are dependent on the velocity of the freezing front [75, 297]. As the velocity of the freezing-front increases, the lamellar spacing (λ) decreases:

$$\lambda \propto \frac{1}{v^m} \tag{3.5}$$

where m is dependent on the particles size [297]. Likewise, increasing the freezing-front velocity decreases the thickness of the lamellar walls, as seen in Figure 3.3 [75]. The freezing-front velocity and temperature gradient of a colloidal suspension can be precisely controlled by regulating the freezing rate and temperature of the cold-finger

surface(s) in a freezing device. As a result, the pore size and lamellae thickness may be finely tuned for specific applications.

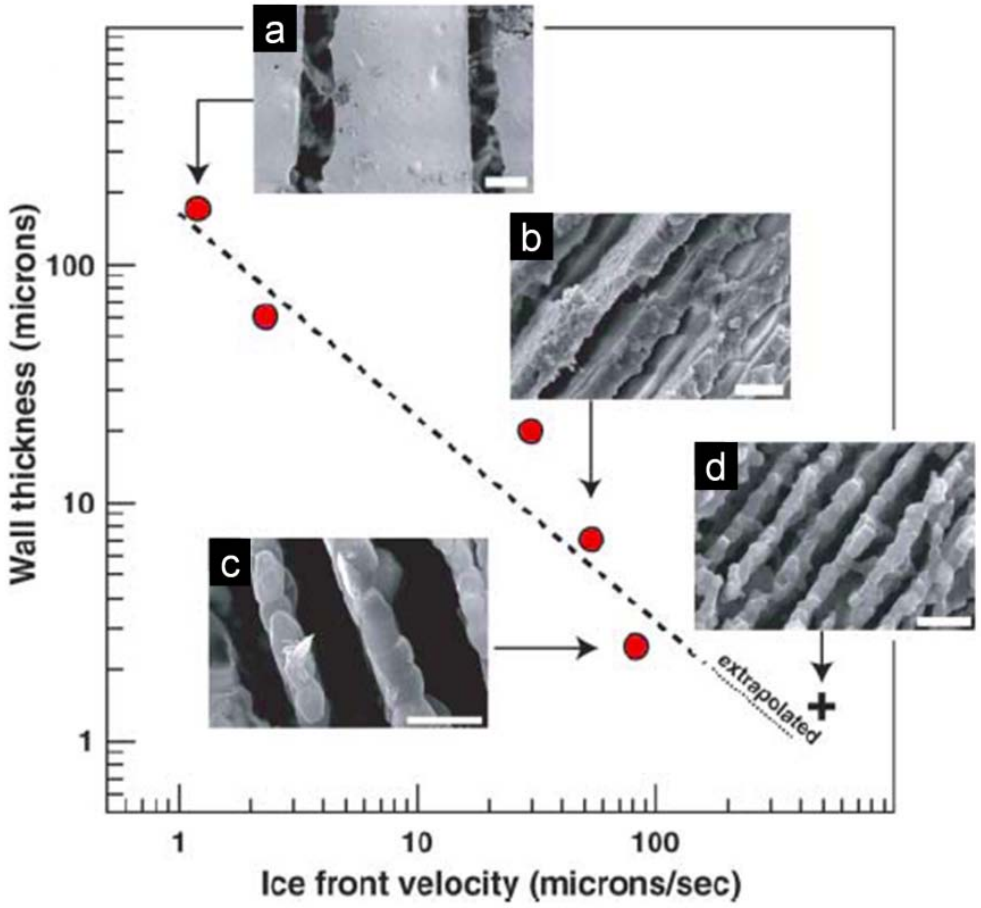

Figure 3.3. Effect of the solidification rate on the wall thickness of lamellae for alumina scaffolds cast with water. **(a-d)** Micrographs of representative scaffold cross-sections parallel to the freezing-front [75]. Scale bars: (a) 50 µm; (b) 10 µm; (c) 5 µm; (d) 5 µm. Adapted from [75].

3.3. Slurry properties

3.3.1. Freezing vehicles

In addition to the freezing-front velocity (i.e., solidification rate) and temperature gradient, the slurry properties have a tremendous impact on the resulting architecture and mechanical performance of freeze-cast scaffolds. Because the pore shape and size are direct replicas of the frozen solvent crystal structures, selection of an appropriate freezing vehicle (or liquid carrier) is of upmost importance. Four different solvents commonly used in freeze casting are water, camphene, tert-butyl alcohol, and camphor-naphthalene [121]. The solidification temperature, viscosity, and volume change of each solvent vary and are most responsible for the resulting pore morphology (see Table 3.1). Figure 3.4 shows micrographs of scaffolds cast with the different solvents. As seen in the images, ceramics cast in water have lamellar pore structures (Figure 3.4a) [76], while ceramics cast in camphene have cellular structures (Figure 3.4b) [298], camphor-naphthalene have dendritic structures (Figure 3.4c) [299], and tert-butyl alcohol have prismatic structures (Figure 3.4d) [300].

3.3.2. Ceramic powders

Other factors that affect the microstructure of freeze-cast scaffolds are the solid loading (Figure 3.5a) and particle size (Figure 3.5b) of the ceramic powders. The solid loading is a measurement of the initial slurry concentration of solid material (i.e., ceramic powder). Empirically, porosity was found to be linearly dependent on the solid loading, where increasing the solid loading decreases the porosity (Figure 3.5a) [291, 297]. The minimum and maximum limits of solid loading range from approximately 5 to 60 vol%

Table 3.1. Characteristics of different solvents used in freeze casting and the resulting pore morphology [121].

Solvent	Water	Camphene	Naphthalene-Camphor	Tert-butyl alcohol
Solidification temperature	0°C or lower, depending on slurry composition	44–48 °C	Naphthalene: 80 °C Camphor: 180 °C Eutectic: 31 °C	25.3 °C 8 °C for the slurry
Typical slurry preparation temperature	RT	60 °C	60 °C	RT
Viscosity	1.78 mPa.s at 0°C	1,4 mPa.s at 47 °C	Naphthalene: 0,91 mPa.s at 80 °C Camphor: 0,63 mPa.s at 180 °C	
Volume change associated to solidification	9 %	–3.1 %	Negative. Depends on the composition.	2 %
Vapor pressure in solid state	0,1 kPa at –20 °C	2 kPa at 55 °C	Naphthalene: 0,13 kPa at 52 °C Camphor: 0,13 kPa at 41 °C	6.4 kPa at 40 °C
Usual sublimation conditions	Freeze-dryer, trap at –50 °C or –85 °C	Room temperature and atmospheric pressure	Room temperature and atmospheric pressure	85 °C, atmospheric pressure
Pores morphology	Lamellar channels	Dendritic channels	Dendritic channels or dense, depending on the composition	Prismatic channels
Environmental friendliness (Hazard Codes)	–	Highly flammable (F)	Highly flammable (F), harmfull (Xn), dangerous for the environment (N)	Highly flammable (F), harmfull (Xn)
Price	–	100€/kg	40€/kg	300€/kg
Comments	Very strong anisotropy of surface tension, leading to the formation of lamellar ice crystals		Inhibition of particles rejection with the eutectic composition (no residual porosity)	Freeze-gelcasting with acrylamide. High strength of green body.

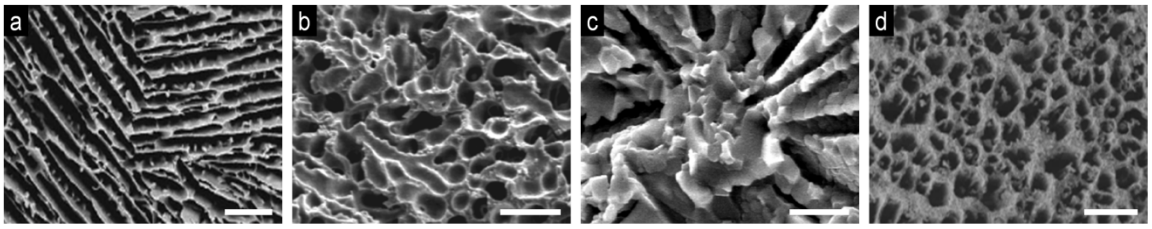

Figure 3.4. Effect of different freezing vehicles on pore architecture: **(a)** hydroxyapatite/water, resulting in lamellar pores [76]; **(b)** alumina/camphene, resulting in cellular pores [299]; **(c)** alumina/camphor-naphthalene, resulting in dendritic channels [298]; **(d)** lead zirconate titanate/tert-butyl alcohol, resulting in prismatic pores [300]. Scale bars: (a) 150 µm; (b) 50 µm; (c) 10 µm; (d) 200 µm. Adapted from [76, 298-300].

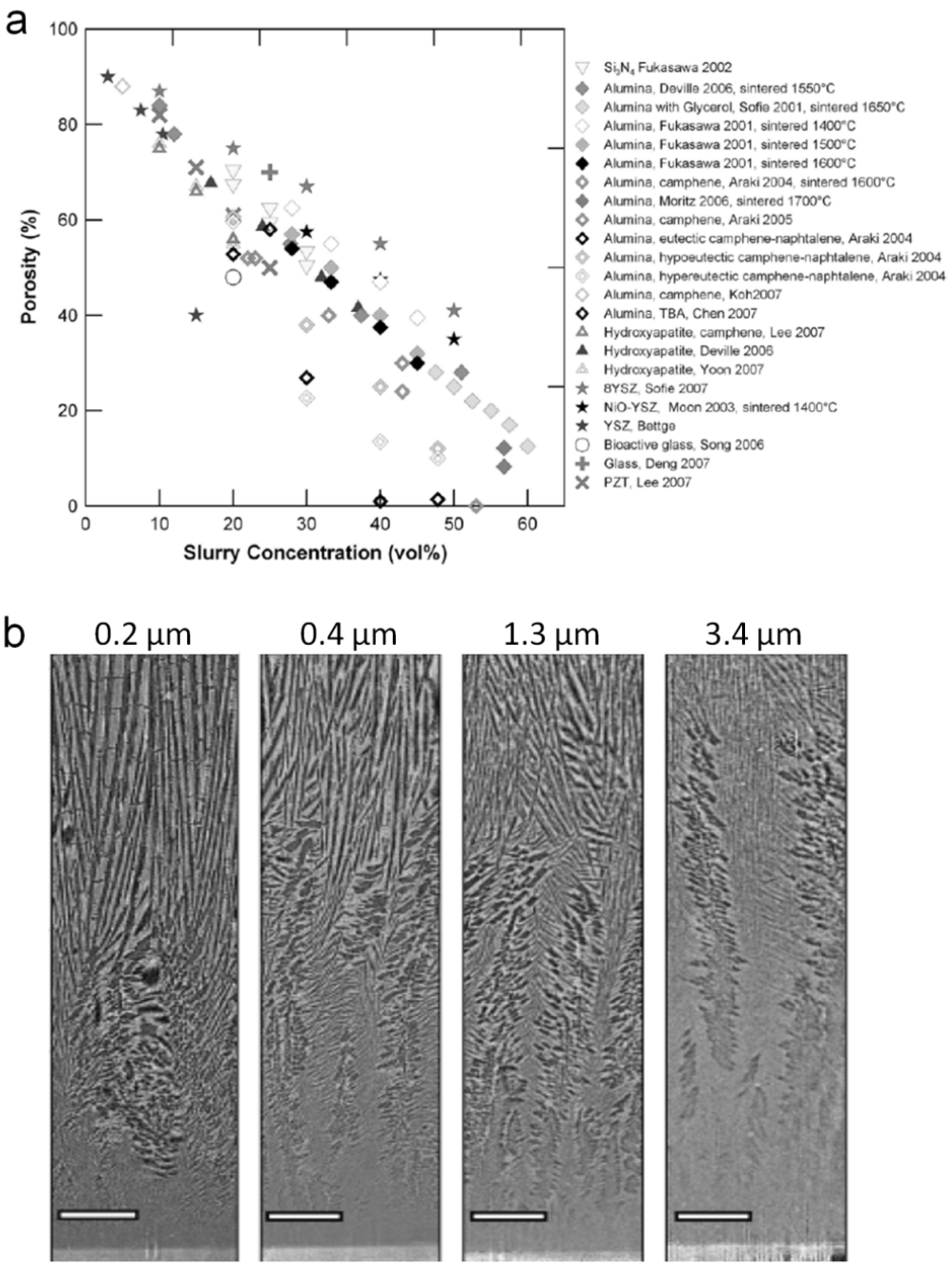

Figure 3.5. (a) Effect of solid loading on the porosity of different freeze-cast scaffolds from literature [121]. **(b)** Effect of particle size on the evolution of lamellar ice crystals in aqueous suspensions of alumina particles. From left to right, as the particle size increases a larger structural gradient in the vertical cross-sections of the resulting scaffolds is observed. The ice growth direction is from the bottom up [301]. Scale bars: 250 µm. Adapted from [121, 301].

[291]. Below 5 vol% the dried scaffolds are very fragile and tend to crumble, while above 60 vol% the scaffolds become too densely packed and lose their signature pore architecture.

The pore size, surface roughness, and homogeneity of freeze-cast scaffolds are, in part, affected by the initial particle size of the ceramic powders. Deville et al. [301] proposed that the initial particle size controls the nucleation of ice crystals, where the surfaces of the particles act as nucleation sites. That is, smaller particles have more surface area, and therefore, more nucleation sites than larger particles, allowing the nucleation and growth of ice crystals at higher temperatures [301]. As a result, the degree of supercooling in slurries with smaller particles is lower, leading to a slower freezing-front velocity in the initial instants of solidification, increasing the homogeneity of well-ordered lamellar ice crystals (Figure 3.5b) [301]. The surface roughness of the lamellar walls is also a product the particle size. Scaffolds fabricated with small particles less than the size of the ice crystals have uniform microstructures that directly replicate the intricate dendritic features of the tiny ice crystals [121, 222]. Secondary dendrites that grow perpendicular to the primary dendrites create a characteristic surface roughness and, in some cases, bridges connecting adjacent lamellae [75]. Large particles, on the other hand, can impede the growth of ice dendrites and do not replicate the tiny dendritic features of the growing ice crystals [121, 222]. Thus, scaffolds fabricated with particle sizes larger than the solvent crystals may have low surface roughness and non uniform, heterogeneous microstructures.

Other more recent studies have investigated the freezing behavior of different geometries and bi-modal size distributions of colloidal particles [302-305]. These include the freezing of spherical particles, platelets, rods, wires, and various distributions of each. Hunger et al. [305] was the first to demonstrate the effect of bimodal particle size distributions on the formation of lamellar walls. In the same work [305], it was shown that freeze casting can be used as an efficient means to force the self-assembly of ceramic platelets, closely mimicking the geometric arrangement of tiles in abalone nacre. Later, Bouville et al. [302, 303] developed a similar method to self-assemble ceramic platelets during the freezing process. In both instances, high aspect ratio ceramic platelets were aligned with their long axis parallel to the lamellar walls formed by freeze casting. Figure 3.6 shows schematics and micrographs of the walls formed by freezing different particles.

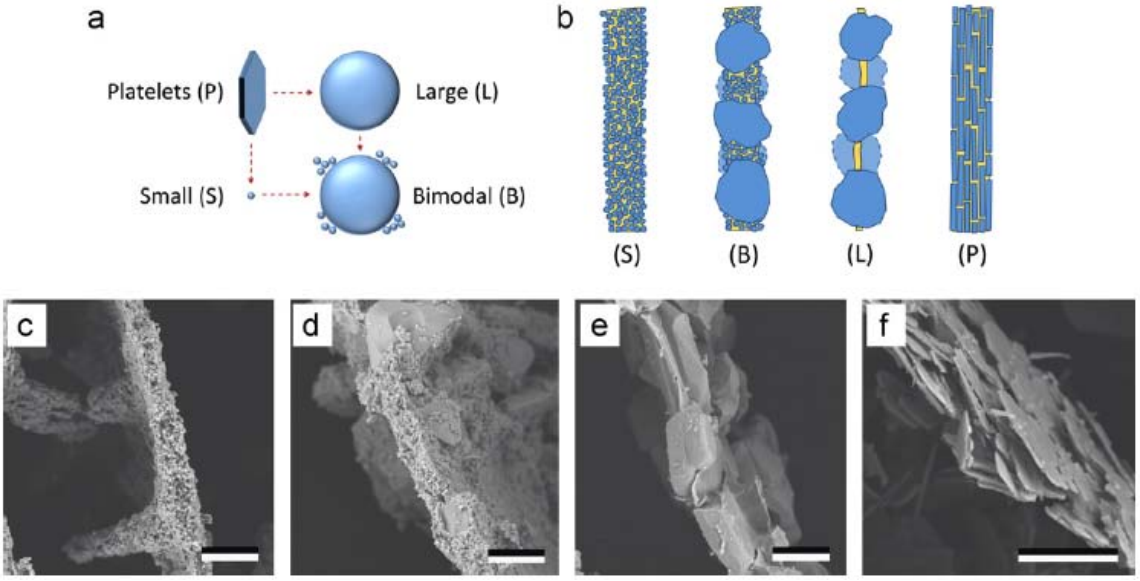

Figure 3.6. (a-b) Schematics of the different particle shapes and sizes as well as the architectures of the corresponding lamellar walls formed by freezing. **(c-f)** Micrographs of lamellar walls freeze cast with: **(c)** small particles; **(d)** bimodal particles; **(e)** large particles; **(f)** platelets. Scale bars not given. Taken from [305].

3.3.3. Additives

The pore architecture, bridge density, and surface roughness of freeze-cast scaffolds can be modified by changing the slurry properties with various additives. Figure 3.7 shows the effects of additives on the microstructures of different scaffolds (adapted from [306]). Properties such as the eutectic temperature, viscosity, pH, osmotic pressure, and surface tension influence the freezing behavior of the solvent [78, 262-264, 283, 288, 291-294, 306]. Munch et al. [306] demonstrated this by adding a variety of common liquid modifiers to alter the eutectic phase diagram of aqueous suspensions of alumina particles. The resulting scaffolds showed varying degrees of inter-lamellar bridging, smooth and rough surfaces, and cellular and lamellar pore architectures (see Figure 3.7a-d, j-m). Fu et al. [77] used glycerol and dioxane to alter the lamellar microstructures of hydroxyapatite (HA) scaffolds cast with water (Figure 3.7e). Adding 60 wt% dioxane resulted HA scaffolds with cellular microstructures, few ceramic bridges, and low surface roughness (Figure 3.7f) [77]. Adding 20 wt% glycerol resulted in dendritic microstructures with dense ceramic bridging, and high surface roughness (Figure 3.7g) [77]. Other additives explored by Porter et al. [89] include isopropanol, which results in elongated lamellar pores with thick ceramic bridges and smooth surfaces (Figure 3.7h); and sodium hydroxide, which increases the pH of the slurry resulting in enlarged cellular pores with a high density of bridging and rough, dendritic surfaces (Figure 3.7i).

Systematic studies on rheological properties, such as pH and viscosity, have shown strong correlations to the microstructure and mechanical properties of HA scaffolds [283]. Soluble polymers such as polyethylene glycol (PEG) and polyvinyl alcohol (PVA) are commonly used as plasticizers, having an effect on the degree of

constitutional supercooling [263, 264]. Altering the concentration of PEG and PVA can significantly affect the pore size and secondary dendrite spacing [263, 264]. Zirconium acetate, a salt with unique ice-structuring properties similar to ice-structuring proteins found in nature, binds to the surface of ice via hydrogen bonding [307]. At a critical concentration, zirconium acetate limits the incorporation of water molecules into the growing ice crystals, resulting in faceted polyhedral structures (Figure 3.8) [307]. Although several additives have been investigated yielding different slurry properties and freezing conditions, more work is needed to fully characterize the underlying mechanisms that lead to changes in the freezing behavior of solvents modified with additives.

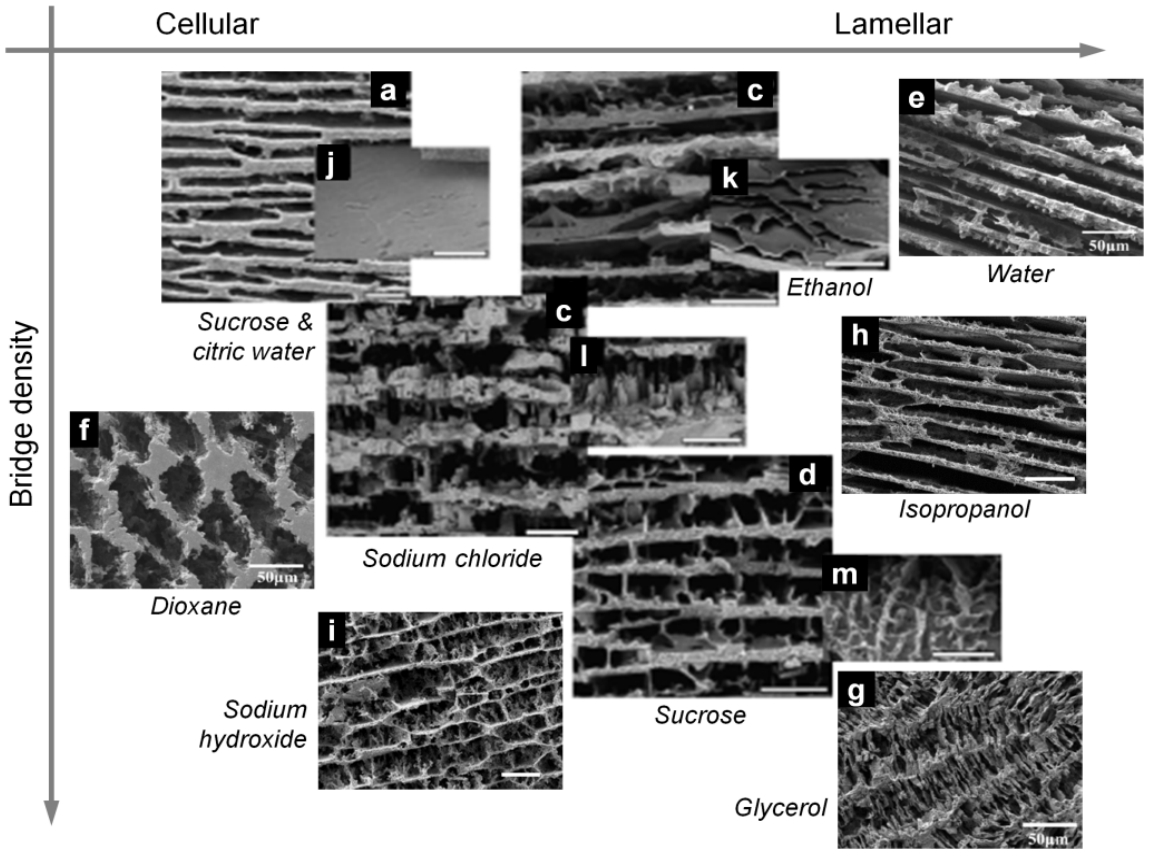

Figure 3.7. Effect of different additives on the pore architecture, bridge density, and surface roughness: **(a)** alumina and 10 wt% sucrose in citric water (pH 2.5), resulting in cellular pores with smooth surfaces [306]; **(b)** alumina and 4 wt% ethanol, resulting in lamellar pores with smooth surfaces [306]; **(c)** alumina and 4 wt% sodium chloride, resulting in sharp-faceted lamellae surfaces [306]; **(d)** alumina and 4 wt% sucrose, resulting in lamellar pores with microscopic roughness [306]; **(e)** hydroxyapatite and water, resulting in lamellar pores [77]; **(f)** hydroxyapatite and 60 wt% dioxane, resulting in cellular pores [77]; **(g)** hydroxyapatite and 20 wt% glycerol, resulting in dendritic pores [77]. **(h)** titania and 9 wt% isopropanol, resulting in elongated lamellar pores [89]; **(i)** titania and sodium hydroxide (pH 12), resulting in cellular pores with dense bridging [89]; Insets **(j-m)**: details of surface roughness [306]. Adapted from [77, 89, 306]. Scale bars: (a) 50 µm; (b) 100 µm; (c) 50 µm; (d) 100 µm; (e) 100 µm; (f) 50 µm; (g) 50 µm; (h) 50 µm; (i) 50 µm; (j) 50 µm; (k) 100 µm; (l) 100 µm; (m) 100 µm.

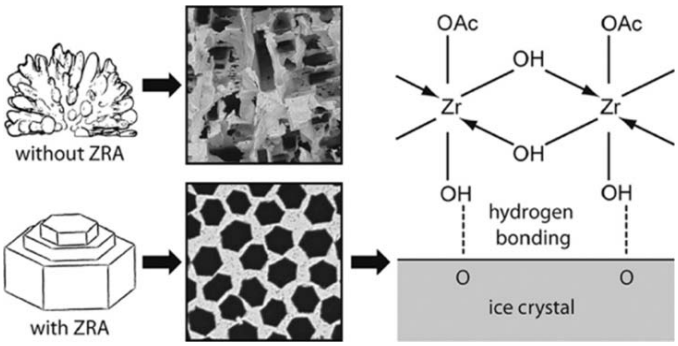

Figure 3.8. Ice-structuring mechanism for zirconium acetate (ZRA) resulting in faceted polyhedral pore morphologies [307]. Taken from [307].

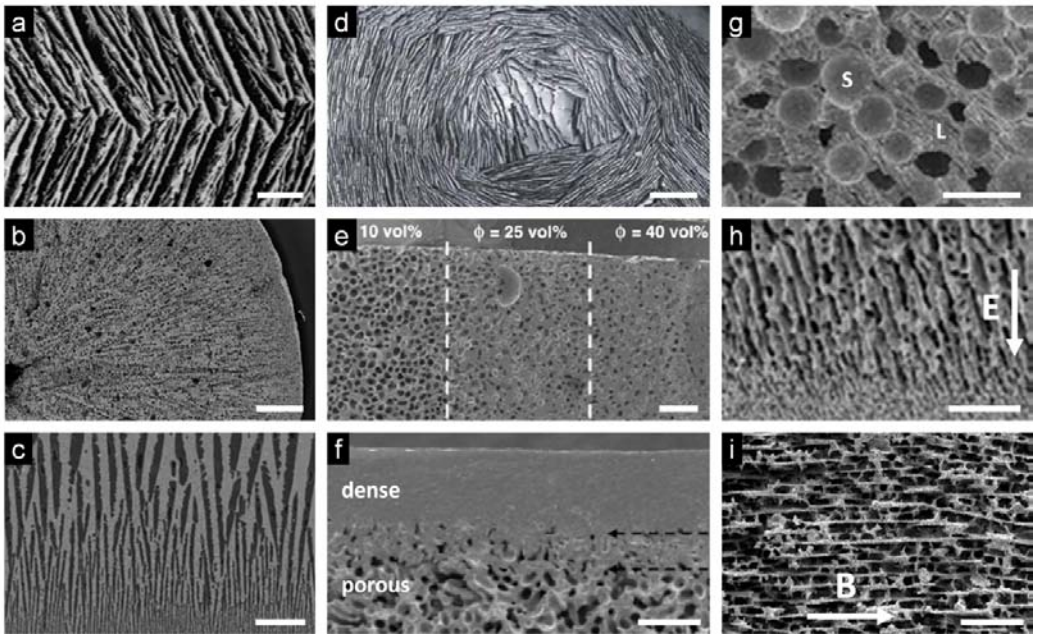

Figure 3.9. Effect of different freeze casting techniques on pore architecture and alignment: **(a)** double-sided cooling, resulting in tilted lamellae at the interface of opposing freezing fronts [297]; **(b)** radial cooling, resulting in radially aligned pores [275]; **(c)** freeze-tape-casting, resulting in functionally graded pores [189]; **(d)** surface patterning, resulting in concentrically aligned pores [75]; **(e)** sequential solid loading, resulting in porosity gradients [270]. **(f)** solvent evaporation, resulting in dense/porous bi-layered regions [308]; **(g)** pore-forming agents, resulting in large spherical (S) pores and small lamellar (L) pores [309]; **(h)** electric fields applied parallel to the freezing direction, resulting in dense/porous bi-layers (arrow indicates direction of electric field) [310]; **(i)** magnetic fields applied perpendicular to the freezing direction, resulting in pore alignment in multiple directions (arrow indicates direction of magnetic field) [92]. Adapted from [75, 88, 189, 270, 275, 297, 308-310]. Scale bars: (a) 200 µm; (b) 1 mm; (c) 50 µm; (d) 500 µm; (e) 1 mm; (f) 100 µm; (g) 500 µm; (h) 50 µm; (i) 100 µm.

3.4. Freezing conditions

3.4.1. Directional cooling

Uniaxial freezing, where a single freezing surface (or cold-finger) is used to freeze a liquid ceramic slurry, is the most common method used to cast porous ceramics with unidirectional pore alignment. Several variations of directional freezing, such as double-sided cooling (Figure 3.9a) and radial cooling (Figure 3.9b), have successfully aligned pore channels in multiple directions. Double-sided cooling consists of two cold-fingers at opposing ends, enabling the temperature gradient to be more precisely controlled [297, 311, 312]. Radial cooling is performed by freezing the outer perimeter of a cylindrical mold [275, 308, 313]. This, in turn, creates a radial temperature gradient from the outer surface to the center of a cylindrical sample resulting in radially aligned pore channels [275, 308, 313]. Freeze-tape-casting is a variation of freeze casting that results in thin ceramic substrates with functionally graded acicular pores, as shown in Figure 3.9c [189]. In this method, a thin layer (or slip) of ceramic slurry is fed across a freezing bed that promotes unidirectional solidification in the tape-casting direction [189, 314, 315].

Another technique used to control the directional alignment of pores is surface patterning [75, 84]. Deville et al. [75] and Munch et al. [84] showed that patterning the freezing surface in a uniaxial freezing device leads to directional alignment of pores, not only in the direction of the temperature gradient, but also perpendicular to the freezing direction as replicates of the patterned surfaces. Figure 3.9d shows a micrograph of concentrically aligned pores perpendicular to the freezing direction made by surface patterning [75].

However, surface patterning has never been replicated [316]. Thus, Bouville et al. [80] developed a method known as flow freezing to further align the pore channels perpendicular to the ice growth direction. In this method, a ceramic slurry flows across a freezing surface, forming two thermal gradients in the solution [80, 316]. Recently, this method (in combination with other freezing and post processing techniques) led to the development of the strongest, toughest synthetic ceramics (composed of 100% ceramic materials) yet to be reported [80].

3.4.2. Gradient loading and pore formers

Other modifications to freeze casting that yield gradient porosities and varied pore morphologies include techniques such as sequential solid loading [270], solvent evaporation [317, 318], and pore-forming [249-251, 309, 319, 320]. Jung et al. [270] used sequential solid loading to create titanium scaffolds with a gradient in porosity and pore size. This simple method used camphene as the freezing vehicle to solidify slurries sequentially with decreasing solid contents of 40, 25, and 10 vol% [270]. The resulting scaffolds had well bonded layers with different porosities of 10, 25, and 40%, as seen in Figure 3.9e. Koh et al. [318] fabricated dense/porous bi-layered ceramics with camphene, by exposing the top surface of the slurry to air, while freezing the bottom surface. This allowed for the controlled evaporation of camphene; thereby, producing a gradient of solids that resulted in scaffolds composed of a dense top layer (due to evaporation) and a porous bottom layer (due to directional solidification) (Figure 3.9f) [318]. Sacrificial pore-forming agents may also be used to create complex pore architectures with varied pore shapes and sizes [249-251, 309, 319, 320]. In this method, sacrificial pore formers,

such as polymer beads, sponges or salts, are added to the slurry before freezing [249-251, 309, 319, 320]. After lyophilization, the dried green bodies are either heated to burn-out the fugitive polymer phase or immersed in a solvent to leech-out the fugitive salts [249-251, 309, 319, 320]. Figure 3.9g shows a HA scaffold fabricated by freezing with a polymethylmethacrylate (PMMA) pore-forming agent [309]. The final microstructure is composed of two pore shapes and sizes - large, spherical pores formed by PMMA particles and small, lamellar pores formed by ice (see Figure 3.9g) [309].

3.4.3. Electric and magnetic fields

The concepts of adding electric fields and magnetic fields to conventional freeze casting processes have recently been introduced, respectively, by Zhang et al. [310] and Porter et al. [88]. Zhang et al. [310] applied electric fields parallel to the freezing direction of uniaxially frozen alumina slurries. The negatively charged alumina particles migrated toward the anode, creating a concentration gradient of solids in the direction of the applied electric field [310]. Increasing the voltage (15-90 V) of the electric field, increased the dense layer thickness of the dense/porous bi-layered ceramics [310]. Figure 3.9h shows a micrograph of an alumina scaffold fabricated under an electric field, where the arrow indicates the direction of the electric field (E), which is parallel to the ice growth direction. In a more recent study, Preiss et al. [311] investigated the use of electrophoretic deposition with double-sided cooling to form a graded pore structure in zirconia toughened alumina ceramics.

Porter et al. [88] applied a weak magnetic field (0.12 T) perpendicular to the freezing direction of uniaxially frozen ceramic slurries (discussed in more detail in the

following chapters). Briefly, using magnetite nanoparticles as the magnetic attractant, various concentrations of magnetite were mixed with nonmagnetic ceramic powders (i.e., HA, zirconia, alumina, and titania) [88]. The HA, zirconia, and alumina scaffolds showed biphasic material properties [88]. The titania scaffolds showed homogeneous distributions of magnetite, aligned pore channels and enhanced mechanical properties parallel to the magnetic field, perpendicular to the freezing direction [88]. Figure 3.9i shows a micrograph of a titania-magnetite scaffold fabricated under a static magnetic field, where the arrow indicates the direction of the magnetic field (B), and the ice growth direction is out of the page.

3.5. Post processing

3.5.1. Sintering

Prior to lyophilization, freeze-cast scaffolds may be sintered to densify and strengthen the porous constructs [266]. Sintering is commonly used to manufacture ceramic objects by heating powders to a temperature just below the melting point of the material. When compacted ceramic powders are sintered, the atoms in the powder particles are excited and may diffuse across the particle boundaries. This allows the particles to coalesce, resulting in a densified structure with reduced porosity [321]. Sintering in an open air furnace is most commonly utilized for freeze-cast materials; however, spark plasma sintering has been shown to increase manufacturing efficiency by lowering the sintering temperature and increasing the heating rate, passing an electric current through the sample [274, 322, 323]. Figure 3.10 shows micrographs of titania scaffolds sintered in air at different temperatures [unpublished work]. As the sintering

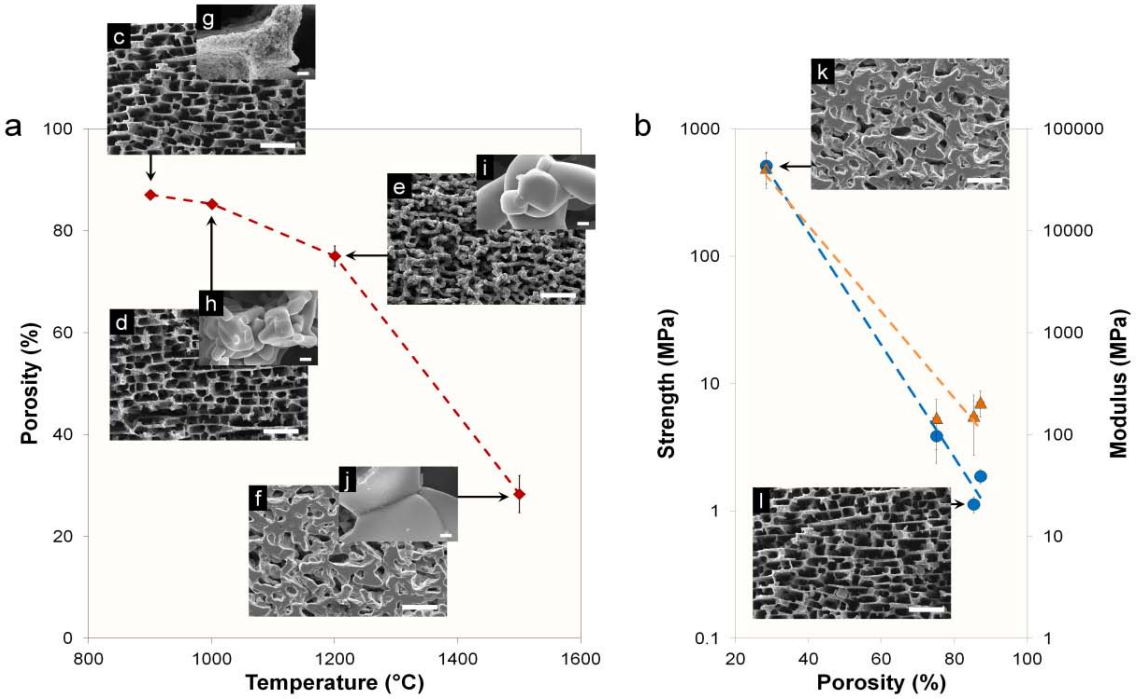

Figure 3.10. Effect of sintering temperature on the porosity, microstructure, and lamellar wall density (insets g-j) of titania scaffolds sintered for 3 hrs with heating and cooling rates of 2°C/min. Plots of **(a)** porosity versus temperature and **(b)** compressive mechanical properties versus porosity at **(c, l)** 900°C; **(d)** 1000°C; **(e)** 1200°C; **(f, k)** 1500°C. Scale bars: (c-f, k, l) 50 µm; (g-j) 2 µm. [unpublished work]

temperature increases, the ceramic bodies shrink and the apparent porosity decreases (Figure 3.10a). Consequently, the mechanical properties are enhanced with increasing temperature (Figure 3.10b) due to the densification of lamellar walls (see Figure 3.10g-j) [266]. However, microstructural changes (refer to Figure 3.10c-f) and decreased porosity may be undesirable for specific applications [266]. Therefore, it is important to determine the optimal sintering profile of the ceramic scaffolds to control the delicate balance of these mutually exclusive properties (i.e., mechanical properties and porosity).

Another variation of the sintering technique is hot-pressing or pressurized sintering [80, 84]. In this method, a sacrificial low molecular weight polymer (e.g., wax)

is infiltrated into the porous scaffolds before sintering [80, 84]. Then, during the heating process, pressure is applied to the scaffold to collapse the pores, resulting in aligned microstructures with very little to no porosity [80, 84]. This variation of sintering has led to the development of tough ceramic composites with extremely high volume fractions of the ceramic phase, similar to that of abalone nacre [80, 84].

3.5.2. Infiltration techniques

To fabricate hybrid composites, liquid polymers or metals may be infiltrated into the porous ceramic scaffolds [75, 82, 84, 243]. Figure 3.11 shows a schematic of this process and micrographs of a zirconia scaffold infiltrated with epoxy [90]. The resulting composites are composed of bi-continuous, interpenetrating networks of the two constituent phases with very little to no porosity. Different polymer infiltration techniques used to impregnated ceramic scaffolds include melt immersion [236, 237], solvent evaporation [233, 238-241], *in situ* polymerization [75, 82, 84, 126, 242-244], particle centrifugation [218], and chemical vapor deposition [245-247]. *In situ* polymerization is the most popular method used to infiltrate polymers, in which a liquid monomer and catalyst are forced into the pores of a ceramic scaffold, typical under vacuum, and subsequently polymerized. The zirconia-epoxy composite shown in Figure 3.11d was fabricated in this manner. The benefit of this technique is that the low viscosity of the liquid monomers allows the polymer precursors to easily flow into the intricate micro-porosity of the scaffolds, completely filling the open pores. Such interpenetrating, bi-continuous composites are generally stronger and tougher than composites having a randomly dispersed ceramic phase of equal concentration [84]. This enhanced

mechanical performance is attributed to the complex architectural hierarchy and strong interactions between the two phases.

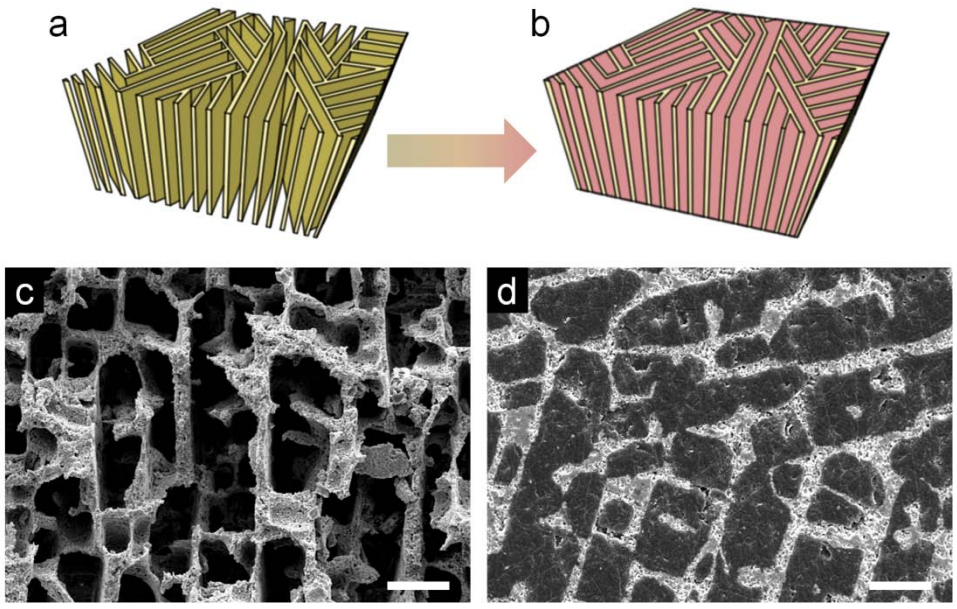

Figure 3.11. (a-b) Schematic of before (a) and after (b) polymer infiltration, where yellow represents the ceramic scaffold and pink represents the polymer phase. **(c-d)** Micrographs of zirconia scaffolds before (c) and after (d) infiltration with epoxy, where zirconia is the light phase and epoxy is the dark phase in (D) [90]. Scale bars: 20 µm.

3.6. Bioinspiration

3.6.1. Bone-inspired materials

Referring to Chapter 2, freeze casting can also lead to bioinspired materials with osteonal and trabecular microstructures. Mimicking these microstructural features may lead to better, more robust and functional materials for bone implants and tissue engineering [324]. Figure 3.12 shows two artificial freeze-cast materials that mimic the microstructures of an osteon (Figure 3.12c) and trabecular scaffold (Figure 3.12d). As previously mentioned, the osteon-like scaffold shown in Figure 3.12c was fabricated by freeze casting on a concentrically patterned surface [75] and the artificial trabecular scaffold shown in Figure 3.12d was fabricated by Yang et al. [249] using a modified method that combined freeze gel casting and the polymer sponge technique [249-251].

An alternative approach to freeze casting bone-like materials is to mimic the mechanical properties of bone. While cancellous bone is generally highly porous and lacking in mechanical strength, cortical bone has exceptional mechanical properties with compressive strengths of 106-283 MPa and Young's moduli of 6-28 GPa (refer to Table 2.1) [126, 142]. However, matching the mechanical properties of natural bone for tissue engineering applications is a difficult task. Effective bone replacements should be biocompatible, have an interconnected porosity to allow bone ingrowth, and exhibit proper strength and stiffness [126]. To accomplish these goals, much research has focused on the development of porous scaffolds made from hydroxyapatite, the primary mineral constituent of natural bone. Deville et al. [76] showed that freeze casting can be used to make hydroxyapatite scaffolds with an interconnected porosity and high compressive strengths up to 145 MPa (Figure 3.13a-b). Compared to other

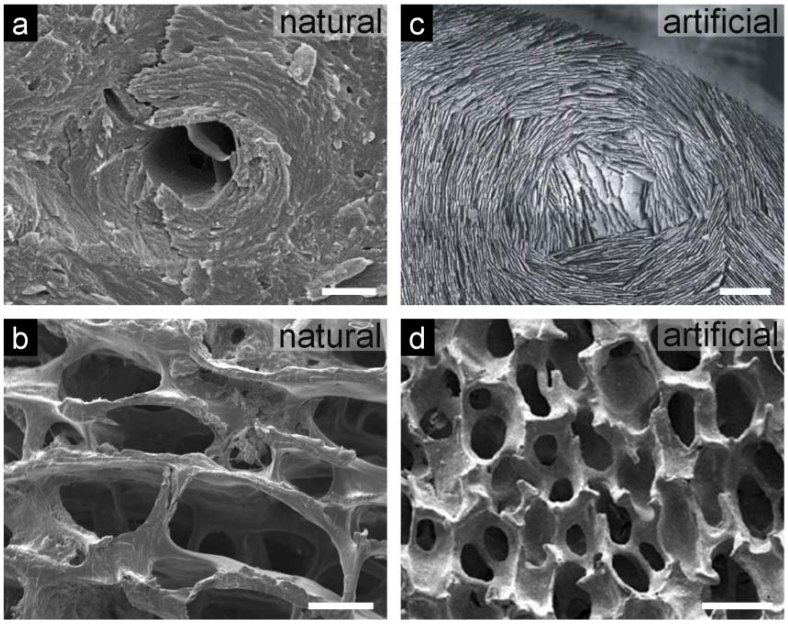

Figure 3.12. Micrographs of natural (left) and artificial (right) bone materials: **(a)** a natural osteon found in cortical bone (credit: E. Novitskaya); **(b)** a natural cancellous bone scaffold (credit: E. Novitskaya); **(c)** an artificial freeze cast scaffold that mimics the architecture of an osteon [75]. **(d)** an artificial freeze cast scaffold that mimics the architecture of cancellous bone [249]. Scale bars: (A) 50 μm; (B) 500 μm; (C) 500 μm; (D) 50 μm. Adapted from [75, 249].

hydroxyapatite scaffolds reported in literature [127, 129, 202-217], the intricate hierarchical architecture and directional alignment of the lamellar walls make these scaffolds nearly four times as strong in compression (see Figure 3.13a) [76].

For significant bone ingrowth to occur, it was determined that implant scaffold porosity must have an interconnection size of at least 50 μm [325]. The hydroxyapatite scaffolds made by Deville et al. [76] (Figure 3.13a-b) were shown to have lamellar pores 10-50 μm wide (see Figure 3.13b); just large enough to allow bone ingrowth [75, 76]. Fu et al. [269] proved that hydroxyapatite scaffolds fabricated by freeze casting are able to support the proliferation of pre-osteoblastic cells (MC3T3-E1) *in vitro* (Figure 3.13c-d).

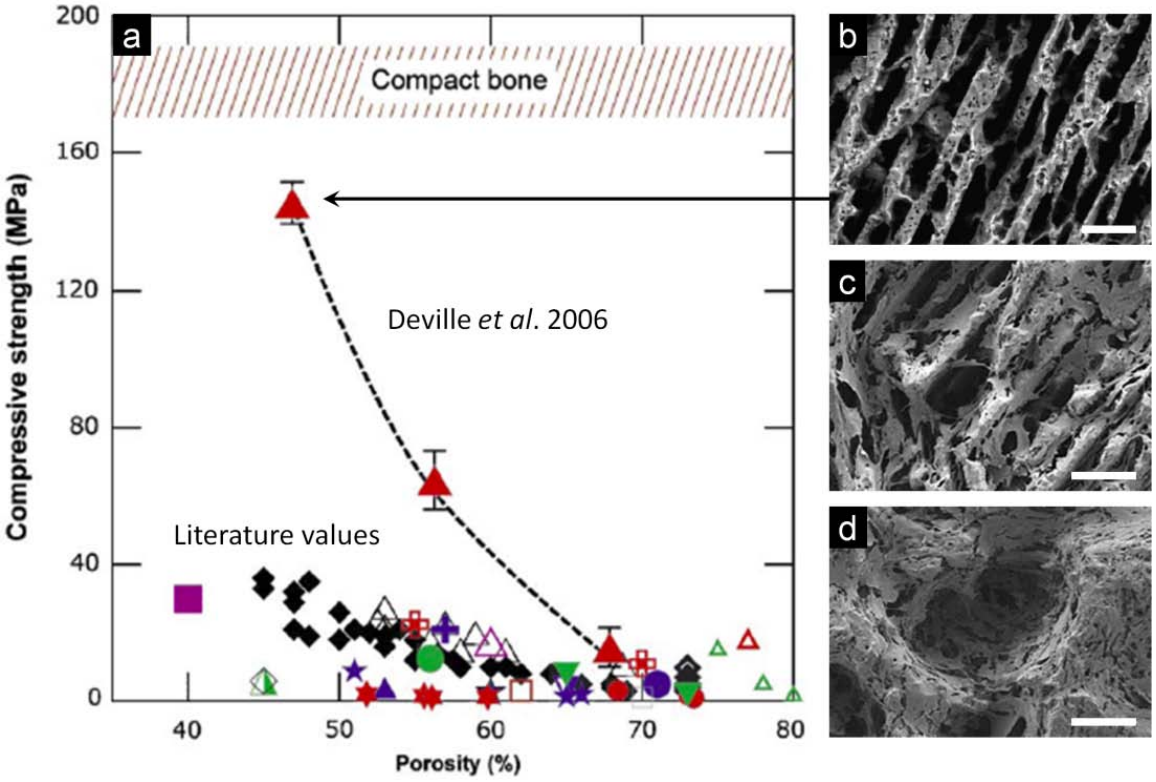

Figure 3.13. (a) Maximum compressive strength of freeze cast hydroxyapatite scaffolds versus porosity [76]; **(b)** hydroxyapatite scaffold with compressive strength of 145 MPa and 47% porosity [76]; **(c-d)** pre-osteoblastic cell (MC3T3-E1) morphology on freeze cast scaffolds with lamellar (c) and cellular (d) architectures after culturing for 6 days [269]. Scale bars: (b) 50 µm; (c) 100 µm; (d) 100 µm. Adapted from [76, 269].

By investigating two types of pore architectures - lamellar pores ~25 µm wide (Figure 3.7e and 3.13c) and cellular pores ~100 µm in diameter (Figure 3.7f and 3.13d) - it was demonstrated that the scaffolds with cellular pores showed far better cell proliferation, differentiation, and migration [269]. This response is most likely due to the pore size being large enough to support the cells, rather than the morphology of the pores themselves, as the optimal pore size for significant bone ingrowth is considered to be 75-100 µm [326].

While large pores and high porosity are desirable to promote bone ingrowth in freeze-cast materials, filling the pores with another phase, such as a biocompatible metal [82] or biodegradable polymer [126], may significantly enhance the mechanical performance of these implants. Such hybrid composites may be useful for total bone replacements, where bone ingrowth is not possible due to injury or disease [126]. Infiltration with a biodegradable polymer, such as polylactic acid (PLA), may also prove beneficial, allowing the polymer phase to degrade over time so that porosity is created *in situ* to promote new bone ingrowth [75, 126]. Preliminary results by Lee, Porter, et al. [126] introduced this concept.

3.6.2. Nacre-inspired materials

Figure 3.14a-b show images of abalone nacre, which was fractured to illustrate the mechanisms of tile pull-out (Figure 3.14a) and biopolymer tearing and stretching (Figure 3.14b) [243]. These unique micromechanics and microstructural architectures make nacre one of the toughest, lightweight ceramic materials known, having a fracture toughness of 8 ± 5 MPa·m$^{1/2}$ [149]. Tomsia, Ritchie and coworkers (Lawrence Berkeley National Laboratory) have developed lightweight composite materials by freeze casting and subsequent polymer infiltration that mimic the design principles of nacre (Figure 3.14c-f) [84, 243]. Mimicking the architecture and toughening mechanisms of nacre may lead to novel hybrid composites that far surpass the mechanical performance of traditional structural components for applications ranging from bone tissue engineering to aerospace and automotive industries.

Figure 3.14 compares micrographs of natural abalone nacre (Figure 3.14a-b) with two types of ceramic-polymer (alumina-polymethylmethacrylate (Al_2O_3-PMMA)) composites fabricated by freeze casting (Figure 3.14c-f) [243]. As seen in the images, the artificial composites have similar "brick-and-mortar" structures as natural nacre. The lamellar composites (Figure 3.14c-d) were fabricated by freeze casting alumina scaffolds with water, followed by sintering and subsequently infiltrating PMMA precursors to initiate *in situ* polymerization, as previously described (refer to Figure 3.11) [84, 243]. The brick-and-mortar composites (Figure 3.14e-f) were also fabricated, initially, by freeze casting alumina scaffolds. However, an intermediate hot-press processing step using a sacrificial binder was employed prior to sintering to collapse the lamellar walls of the scaffolds and create a denser brick-like structure before subsequent polymer infiltration [84, 243]. The resulting artificial composites had uniform microstructures with a ceramic phase of ~36 vol% for the lamellar architectures and ~80 vol% for the brick-and-mortar architectures [84, 243].

Although the size scales of the artificial lamellar and brick-and-mortar composites are different from that of natural nacre (see Figure 3.14), the flexural strength and fracture toughness of the composites exceed that of nacre (Figure 3.15a-b) [75, 84, 243]. Furthermore, the crack-growth fracture toughness (K_{Ic}) of the artificial composites is much greater than that of homogeneous composites composed of PMMA containing randomly dispersed alumina nanoparticles (Figure 3.15b) [84]. Compared to natural nacre, the superior mechanical properties observed in the artificial nacre-like composites are, in part, due to the use of high-performance engineering materials (e.g., alumina and

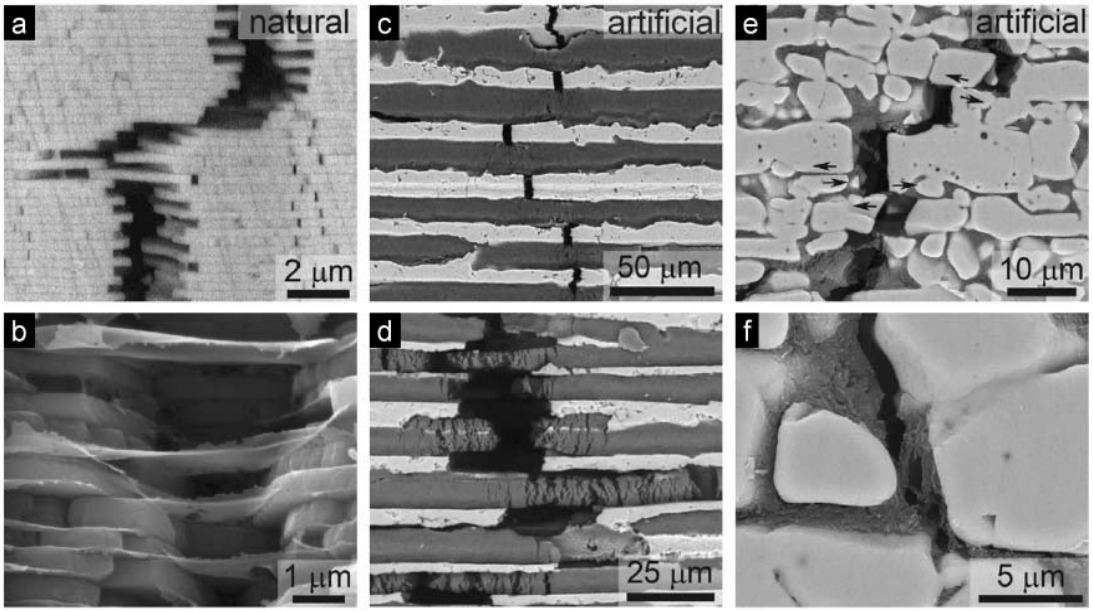

Figure 3.14. Micrographs of natural (left) and artificial (right) nacre materials: **(a-b)** natural abalone nacre; **(c-d)** artificial lamellar composite that mimics the architecture of nacre; **(e-f)** artificial brick-and-mortar composite that mimics the architecture of nacre [243]. Adapted from [84, 243].

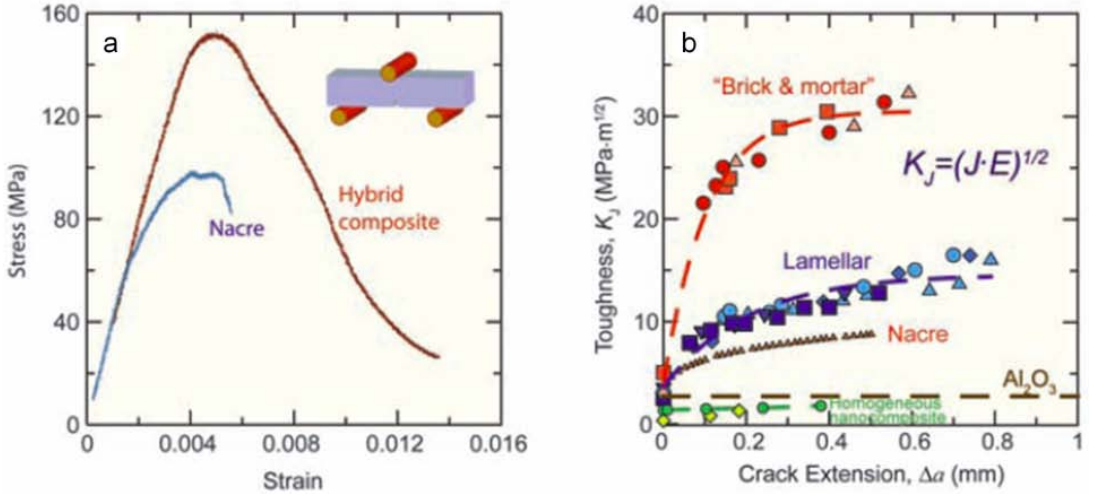

Figure 3.15. Mechanical response of artificial hybrid composites that mimic nacre: **(a)** bending stress-strain comparison of artificial lamellar composite (hybrid composite) and natural hydrated nacre; **(b)** toughness (R-curve) comparison of artificial brick-and-mortar and lamellar composites with natural nacre and homogeneous nanocomposites consisting of randomly dispersed nanoparticles. All composites were composed of Al_2O_3 and PMMA constituents [84]. Adapted from [84].

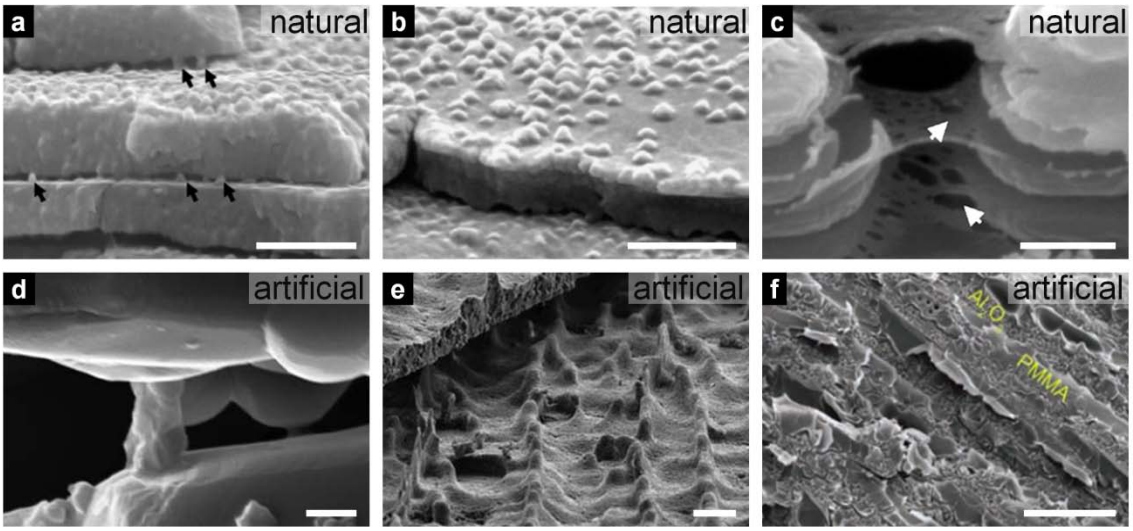

Figure 3.16. Micrographs of **(a-c)** natural and **(d-f)** artificial (Al_2O_3-PMMA) nacre showing **(a, d)** mineral bridges (black arrows) [40, 84], **(b, e)** surface asperities [84, 137] and **(c, f)** the organic matrix (white arrows) [84, 137]. Scale bars: (D) 500 nm; (E) 500 nm; (F) 1 µm; (G) 600 nm; (H) 10 µm; (I) 5 µm. Adapted from [40, 84, 137].

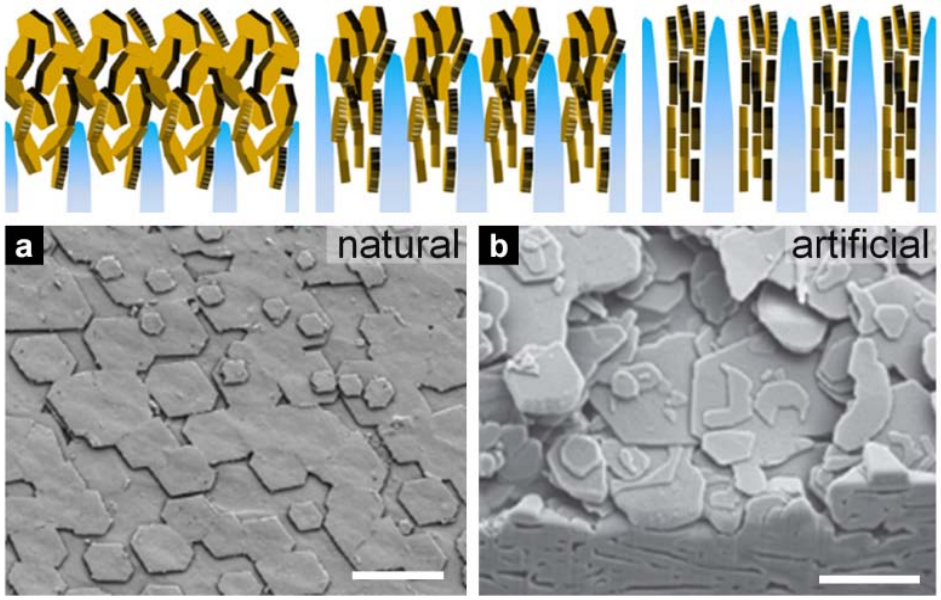

Figure 3.17. Platelet self-assembly by freeze casting inspired by nacre: **(top)** schematic of platelet self-assembly during freeze casting, where the platelets align by shear with their long dimension parallel to the freeze direction [305]; **(a)** natural abalone nacre showing platelet forming layers [327]; **(b)** artificial platelets self-assembled by freeze casting [305]. Scale bars: (a) 10 µm; (b) 5 µm. Adapted from [305, 327].

PMMA), rather than the relatively weak constituents that makeup natural nacre (i.e., aragonite and chitin). The bi-continuous interpenetrating networks of the ceramic and polymer phases, along with the anisotropic directional alignment induced by freeze casting, enhances the strength and toughness of these hybrid composites.

Other nano-/micro-scale toughening mechanisms observed in natural nacre have been emulated by freeze casting (Figure 3.16). Nacre primarily relies on three intrinsic toughening mechanisms: mineral bridges, surface asperities, and the organic matrix (Figure 3.16a-c) [40, 134, 137]. As shown previously in Figure 3.7, the density and thickness of mineral bridges and the surface roughness of lamellar walls can be finely tailored by changing the slurry properties with additives. Figure 3.16d-f show magnified micrographs of a single mineral bridge connecting two adjacent lamellae and surface roughness asperities of freeze-cast scaffolds [84]. The third, and perhaps most important, toughening mechanism is the organic matrix [137]. For instance, the tensile strength in abalone nacre (perpendicular to the layered structure) is 3-4 MPa, compared to that of deproteinized nacre having a strength of ~0.325 MPa [135]. Even though the organic matrix accounts for only 5 vol% of nacre, when it is removed the strength of nacre is reduced by ~92% [135]. Munch et al. [84] demonstrated the importance of the organic matrix in the freeze-cast hybrid composites described in Figure 3.14 and 3.15, by chemically grafting PMMA to the alumina surfaces (Figure 3.16f). Chemical grafting promoted strong covalent bonding between the two phases, which resulted in increased strength and fracture toughness for both the lamellar and brick-and-mortar composites [84, 243]. This is a significant feat because failure of hybrid composites typically occurs at the interface of the constituents by interfacial shear and delamination [285, 286].

More recently, the effect of lamellar layer thickness and ceramic volume fraction on the mechanical properties and thermal conductivities of similar hybrid composites were investigated by Dutta et al. [285] and Chen et al. [242], respectively. Dutta et al. [285] synthesized silica-epoxy composites with staggered architectures by freeze casting to investigate the effect of varying inorganic contents and aspect ratio (ratio of length to width of ceramic layers) on mechanical properties. It was discovered that the aspect ratio of the ceramic phases plays a superior role in contributing to the overall strength and toughness of the hybrid composites. Chen et al. [242] found that the thermal conductivity of freeze-cast Al_2O_3-PMMA composites is higher with higher inorganic content and in the direction along to the lamellar layers than across the layers. Tailoring the thermal conductivity of hybrid composites may be useful for various applications in medicine and electrochemistry [242].

Another interesting use of freeze casting that was inspired by nacre is the development of platelet self-assembly by Hunger et al. [328]. Figure 3.17 shows a schematic of platelet self-assembly, where thin alumina platelets align with their long dimension parallel to the freezing direction by viscous shear flow and shear forces caused by the growing ice crystals [328]. Compared to natural nacre (Figure 3.17a), the lamellae of these artificial freeze-cast scaffolds (Figure 3.17b) have a very similar architecture. The additional level of structural organization that was introduced by the alignment of platelets resulted in a higher toughness, yield strength, and Young's modulus when compared to scaffolds prepared by the same method with spherical particles [328].

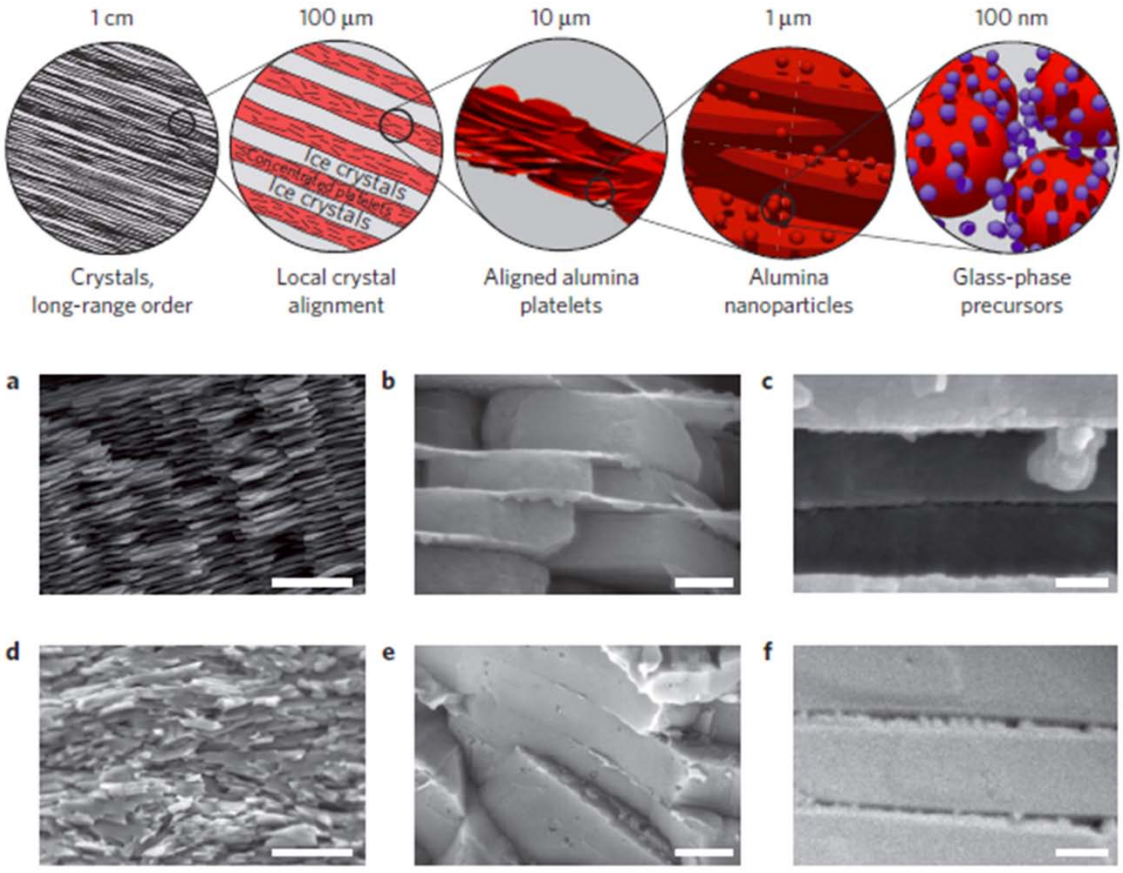

Figure 3.18. (top) Design strategy of nacre-like materials developed by Bouville et al. [80]. Micrographs of **(a-c)** natural nacre and **(d-f)** artificial nacre at equivalent length scales. Scale bars: (a,d) 10 µm; (b,e) 500 nm; (c,f) 250 nm. Adapted from [80].

Utilizing the this concept of platelet self-assembly, along with several other techniques (i.e., flow freezing, bimodal particles, and pressurized spark plasma sintering), Bouville et al. [80] developed pure ceramic materials that outperform nacre in terms of strength and toughness (refer to Table 2.1). This was achieved by mimicking the hierarchical design strategy of nacre on equivalent length scales (see Figure 3.18). Rather than infiltrating a polymeric or metallic phase, a bimodal distribution of glass and alumina nanoparticles were bi-directionally frozen with alumina platelets via flow

freezing. After lyophilization, the porous constructs were spark plasma sintered under pressure to collapse the pores and form nano-bridges between the platelets. The glass precursor was then melted to fill the remaining porosity, taking the role of the organic phase. Figure 3.18a-f juxtapose the hierarchical structure of the natural (a-c) and artificial (d-f) nacre on equivalent length scales.

3.7. Conclusions

Natural structural materials, such as bone and nacre, are excellent examples of how microstructure and architectural organization across multiple length scales influence mechanical properties. Mimicking the various strengthening and toughening mechanisms observed in nature lead to the development of novel lightweight, high-performance materials. Freeze casting is a popular method to fabricate biomimetic materials that emulate the microstructural features of natural biological materials. Intricate microstructural control of porous scaffolds and hybrid composites is possible by altering the slurry properties and freeze conditions during the freeze casting process. A variety of post processing techniques can also be employed to further enhance the mechanical performance of freeze cast materials. Bioinspired applications for freeze casting include hybrid inorganic-organic composites for structural components that mimic nacre and porous ceramic scaffolds for bone replacements that mimic bone.

3.8. Acknowledgements

Chapter 3, in part, is published as a review article in *JOM* and co-authored by M.A. Meyers, and J. McKittrick of UCSD.

CHAPTER 4:

BIOINSPIRED SCAFFOLDS WITH VARYING PORE ARCHITECTURES AND MECHANICAL PROPERTIES

4.1. Introduction

Attempts to replicate the microstructures of biological materials, such as bone and nacre, have long been the focus of intense study due to their robust mechanical properties and moderate density, despite being comprised of relatively weak constituents [8]. This combination of properties is advantageous for the aerospace, automotive, and, especially, biomedical industries, with the possibility of fabricating synthetic bone replacements [8, 75, 84, 90]. The microstructure of bone is highly anisotropic and requires specific levels of open porosity for the presence of living tissues, cells, and fluids [52]. An ideal bone replacement should have an open porosity and mechanical properties similar to those of natural bone [329]. However, a common challenge in manufacturing porous structures is maintaining desired levels of compressive strength and stiffness while generating specific levels of open porosity with optimal pore morphologies.

Freeze casting is a fabrication method that allows for fine microstructural control during the synthesis of porous ceramic scaffolds or hybrid composites (upon infiltration of a second phase) with physical and mechanical properties similar to natural bone [75, 84, 90]. It involves directionally freezing a liquid slurry comprised of a solvent, ceramic powder, dispersant and binder (the latter two are for even particle distribution and green body integrity, respectively) [90]. After freezing, the solvent crystals are sublimated by freeze drying, resulting in lamellar pore channels that are direct replicas of the frozen

solvent. Afterwards, the ceramic scaffold is sintered to partially densify and strengthen the porous construct.

Numerous studies have been conducted using different ceramic powders and liquid solvents with observed changes in the microstructure and compressive behavior of various ceramic scaffolds fabricated by freeze casting [90, 121, 222]. The overall porosity of a scaffold is directly dependent on the amount of solid loading in the slurry, while the pore size and morphology can be controlled by changing the processing conditions [330]. Microstructural properties, such as the composition and thickness of lamellar columns, amount of bridging between the columns, surface roughness and pore geometry are some of the most important mechanisms that affect the mechanical performance [84, 330]. Several works have analyzed these structural parameters, which may be induced by the addition of soluble additives, such as polyethylene glycol (PEG) [264], polyvinyl alcohol (PVA) [263], sucrose, ethanol, sodium chloride [306], glycerol, dioxane [77], and zirconium acetate [307]. Many soluble additives generate significant changes in the pore size and morphology, as they have an observed effect on the solidification temperature, freezing-front velocity, and crystal formation in the liquid slurry [77, 263, 264, 306, 307]. For example, different chemical additives were found by Munch et al. [306] to alter the solidification temperature of the slurry. Regardless of the obvious architectural differences, the spacing of the pores was directly related to the freezing-front velocity, independent of the additives used [306]. Similarly, Deville et al. [307] showed that the evolution of pores is dependent on the growth velocity and driving force of crystal formation, through the use of various ice-structuring compounds. The

pore structures in these works were shown to be cellular, lamellar, columnar, faceted, dendritic, hopper, or polyhedral in nature [77, 304, 306, 307].

Rheological properties of freeze cast slurries have also been shown to influence the pore morphology of the resulting scaffolds without changing their overall porosity. Parameters such as the viscosity and pH influence the dispersion homogeneity and stability of ceramic particles in aqueous solutions [262, 283, 294]. During the freezing process particles are either rejected or entrapped by the approaching freezing front - a function of the thermodynamic free energy of the system and constitutional supercooling, as described by Wegst et al. [78] and Deville et al. [288]. Therefore, to avoid significant particle agglomeration and/or segregation during the freezing process, it is important to determine the optimal viscosity and pH of the slurry for a desired pore morphology [283]. Different types and concentrations of dispersants have been added to significantly lower the slurry viscosity for better defined pore structures [262, 283, 294]. Likewise, the pH can be adjusted so that the electric potential of the colloidal solution is stable [283, 294]. Along with other processing parameters, including the freezing rate and sintering conditions, these liquid properties are easily controlled and have a profound effect on the final pore architecture and resulting mechanical performance [76, 262, 266]. Finely-tailored pore architectures can be designed for specific applications, for example osteogenesis or bone ingrowth, by utilizing a variety of liquid additives.

Here we demonstrate the effect of slurry viscosity, pH, and alcohol concentration on the structural and mechanical properties associated with porous TiO_2 scaffolds, which are promising and relatively untested ceramic constructs produced by freeze casting. To the best of our knowledge, Ren et al. [315, 331, 332] and Porter et al [88]. provide the

only other reports on freeze cast TiO_2 to date. Although it has been shown that TiO_2 is a suitable material for freeze casting porous anisotropic scaffolds [88], the structural and mechanical properties of TiO_2 freeze cast with various liquid additives has not yet been reported. Altering the viscosity, pH and alcohol concentration may allow for the modification of the porous microstructures to meet the criteria of various applications, specifically by altering the pore size and shape without changing the overall porosity. This is the first empirical analysis on the effect different rheological properties in the liquid slurry (i.e., viscosity, pH, alcohol concentration) have on the microstructure and mechanical properties of freeze cast TiO_2. Unlike other works that investigate the slurry viscosity by altering the concentration of dispersants [262, 283, 294], we use equal concentrations of a soluble polymer (PEG) with varying molecular weights or varying concentrations of a liquid additive (isopropanol alcohol (IPA)) to change the liquid properties of the ceramic slurries. Quantitative measurements of the porosity, pore morphology, lamellar architecture, and compressive mechanical properties of the freeze cast scaffolds are systematically compared for each of the conditions investigated. A simplified analysis of Euler buckling is used to describe the principal failure mechanisms of these scaffolds when subjected to compressive loading.

4.2. Materials and methods

4.2.1. Sample preparation

Aqueous slurries of 10 vol.% TiO_2 (Sigma Aldrich, St. Louis, MO) powders (100-200 nm) were mixed with 1 wt.% PVA (Alfa Aesar, Ward Hill, MA) and 1 wt.% of an ammonium polymethacrylate anionic dispersant, Darvan® 811 (R. T. Vanderbilt

Company, Inc. , Norwalk, CT). Three sets of aqueous slurries with different rheological properties were investigated by changing the following parameters:

(1) *viscosity* - controlled by adding 1 wt.% of PEG (Alfa Aesar, Ward Hill, MA) with varying molecular weights (0-20,000);

(2) *pH change* - controlled by adding small amounts of 1M HCl or NaOH (Fisher Scientific Inc., Waltham, MA) to respectively decrease or increase the slurry pH (2-12);

(3) *alcohol concentration* - controlled by adding isopropanol alcohol (IPA) (J.T. Baker, Center Valley, PA) of varying concentrations (0-30 vol.%).

The slurries with varying pH and alcohol concentration also contained 1 wt.% PEG with a molecular weight of 10,000. All slurries were ball milled in an alumina grinding medium for 24 hrs, followed by degassing under low vacuum for 10-20 min. Approximately 10 mL of the degassed slurries were poured into a PVC mold and frozen at a constant rate of 10 °C/min using a custom built freeze casting device, as previously described [88]. After freezing, the samples were removed from the mold with a hydraulic press and lyophilized in a bench-top freeze dryer (Labconco, Kansas City, MO) at -50°C and 350 Pa for 72 hr. The porous green constructs were then sintered in an open air furnace for 3 hr at 1000 °C with heating and cooling rates of 2 °C/min.

4.2.2. Slurry properties

The pH of the aqueous slurries containing TiO_2 were measured with Alkacid pH test ribbons (Fisher Scientific Inc., Waltham, MA). The viscosity of the aqueous solutions were measured before adding the TiO_2 powders using a Gilmont® falling ball viscometer

(No. 2) with a glass ball (Thermo Fisher Scientific Inc., Waltham, MA). The viscosities (μ, mPa·s) of the solutions were measured at 18 °C and calculated by Equation 4.1:

$$\mu = K(\rho_b - \rho_l)t \tag{4.1}$$

where K = 3.3 is the viscometer constant, ρ_b = 2.53 g/mL is the density of the glass ball, ρ_l is the measured density of the liquid, and t is the measured time of descent of the glass ball in min.

4.2.3. Material characterization

X-ray diffraction (XRD) with a Miniflex II XRD machine (Rigaku, Woodlands, TX) confirmed that the crystal structures of all the TiO_2 scaffolds transformed from anatase before sintering to rutile after sintering at 1000 °C.

Scanning electron microscopy (SEM) images were taken at 15 kV on a Philips XL30 field emission environmental scanning electron microscope (FEI-XL30, FEI Company, Hillsboro, OR). For SEM preparation the samples were sputter-coated with iridium using an Emitech K575X sputter coater (Quorum Technologies Ltd., West Sussex, UK).

The relative density (ρ_{rel}) and porosity (ϕ) of the scaffolds were measured by mass (m) and volume (V) with respect to that of fully dense TiO_2 (ρ_{TiO_2} = 4.26 g/cm^3), as shown in Equations 4.2 and 4.3:

$$\rho_{rel} = \frac{\rho}{\rho_{TiO_2}} = \frac{m/V}{\rho_{TiO_2}} \tag{4.2}$$

$$\phi = (1 - \rho_{rel}) \times 100\% \tag{4.3}$$

where $\rho = m/V$ is the measured sample density. The average (± standard deviation) porosities of the scaffolds were calculated from eight samples each.

Figure 4.1 shows a representative image of the different structural features and measurements taken to characterize the microstructures of each scaffold. The average pore size, geometry, lamellar thickness and interlamellar spacing of the scaffolds were measured from scanning electron micrographs using ImageJ software (National Institutes of Health, Bethesda, MD). To measure the pore size, the thresholds of the micrographs were adjusted equally such that the region of interest (i.e., pore area) could be selected and calculated from the major and minor axes of a fitted ellipse with an equivalent area and aspect ratio approximated by the software. The pore area (A_p) reported here is the average (± standard deviation) pore area calculated from the elliptic major (a) and minor (b) axes from 40 selected pores each:

$$A_p = \frac{\pi}{4} ab. \tag{4.4}$$

The pore aspect ratio (χ_p) is a measure of the pore morphology and was calculated from the major (a) and minor (b) axes as follows:

$$\chi_p = \frac{a}{b}. \tag{4.5}$$

The lamellar thickness (t) of the scaffold walls was averaged from 40 selected linear measurements each. The interlamellar spacing (λ) of the scaffold walls, which is equivalent to the minor axis ($\lambda = b$) noted above, is inversely proportional to the freezing front velocity (v), following the power law [297]:

$$\lambda \sim \frac{1}{v^n} \tag{4.6}$$

where n is related to the colloidal particle size and should be equal for all experiments reported here. Therefore, it can be assumed that changes in the lamellar thickness and interlamellar spacing of the scaffolds are caused by the different slurry properties, which may affect the freeze front velocity.

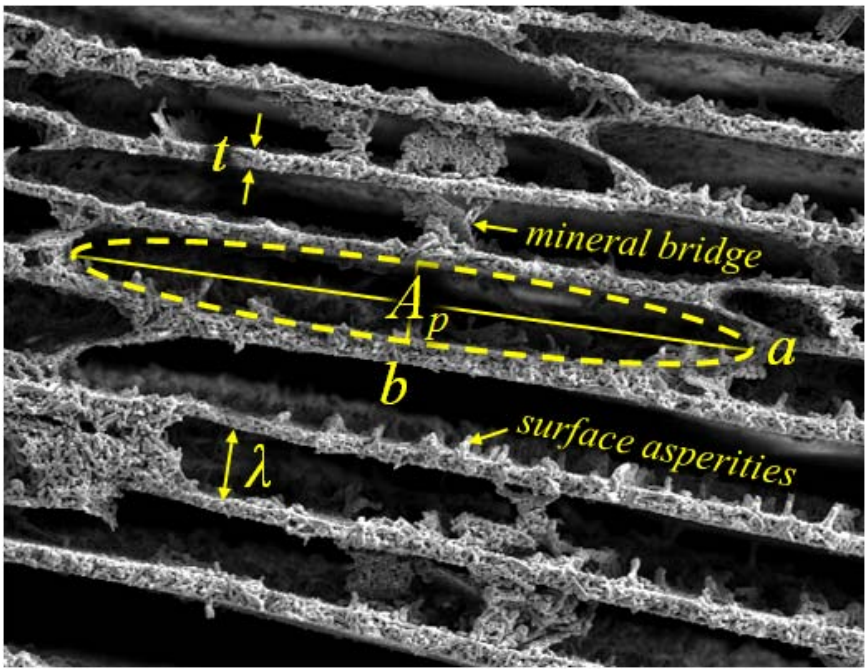

Figure 4.1. Representative image of a freeze cast TiO_2 scaffold illustrating the different microstructural features and measurements: *mineral bridges* connecting adjacent lamellar walls; *surface asperities* creating a characteristic wall roughness; fitted ellipse (dashed line) - pore area (A_p), major axis (a) and minor axis (b); interlamellar spacing ($\lambda = b$), and lamellar thickness (t).

4.2.4. Mechanical testing

Compression testing of the scaffolds was performed in an Instron materials testing machine (Instron 3342, Norwood, MA) with a 500 N load cell at a crosshead velocity of 0.005 mm/sec. The scaffolds were cut into small samples of approximately 5 x 5 x 5 mm^3 and compressed in the longitudinal, ice growth direction. To ensure testing of the homogeneous region and avoid the high-density regions of the scaffolds (i.e., the outer perimeter and the bottom 5 mm of the scaffold [297]), the samples were cut from the central core of the scaffolds (10 x 10 mm^2) between 5-30 mm from the bottom. The ultimate compressive strength and Young's modulus were determined from the maximum stress and the linear slope of the stress-strain curves, respectively. The average (± standard deviation) strength and modulus of the scaffolds were calculated from eight samples from each processing condition.

4.3. Results and discussion

4.3.1. Viscosity

Adding PEG to the freeze cast slurries and increasing its molecular weight increased the viscosity of the slurries without changing the overall porosity of the scaffolds (see Table 4.1). However, the different molecular weights of PEG added to the slurries resulted in variations in pore area, surface roughness, lamellar bridging, and channel alignment. These structural parameters were observed to have a pronounced effect on the mechanical properties. Figures 4.2 and 4.3 compare, respectively, SEM images and the structural and mechanical properties of the scaffolds fabricated with varying slurry viscosities. During freezing, ice crystal formation generated successive

Table 4.1. Slurry properties (viscosity, pH), pore morphology (porosity, pore area, major and minor axes, aspect ratio, lamella thickness), and compressive mechanical properties (strength, modulus) of TiO_2 scaffolds freeze cast with 1 wt.% polyethylene glycol (PEG) of varying molecular weight (MW).

PEG (MW)	0	2,000	10,000	20,000
Viscosity, (mPa·s)	1.44 ± 0.02	1.50 ± 0.03	1.63 ± 0.02	1.75 ± 0.02
pH	~7	~7	~7	~7
Overall porosity, (%)	82.1 ± 0.9	82.8 ± 0.3	83.2 ± 0.1	83.7 ± 0.4
Pore area, (μm^2)	465 ± 234	302 ± 54	234 ± 36	531 ± 82
Pore major axis, (µm)	37 ± 32	30 ± 15	29 ± 14	49 ± 28
Pore minor axis, (µm)	16 ± 9	13 ± 5	10 ± 3	14 ± 4
Pore aspect ratio,	2.36	2.33	2.74	3.52
Lamella thickness, (µm)	3.69 ± 1.85	4.06 ± 2.86	2.54 ± 1.27	2.87 ± 1.67
Strength, (MPa)	4.4 ± 0.3	6.1 ± 0.4	6.7 ± 0.2	3.0 ± 0.4
Modulus, (MPa)	309 ± 125	616 ± 194	662 ± 162	327 ± 123

* All data shown as average ± standard deviation.

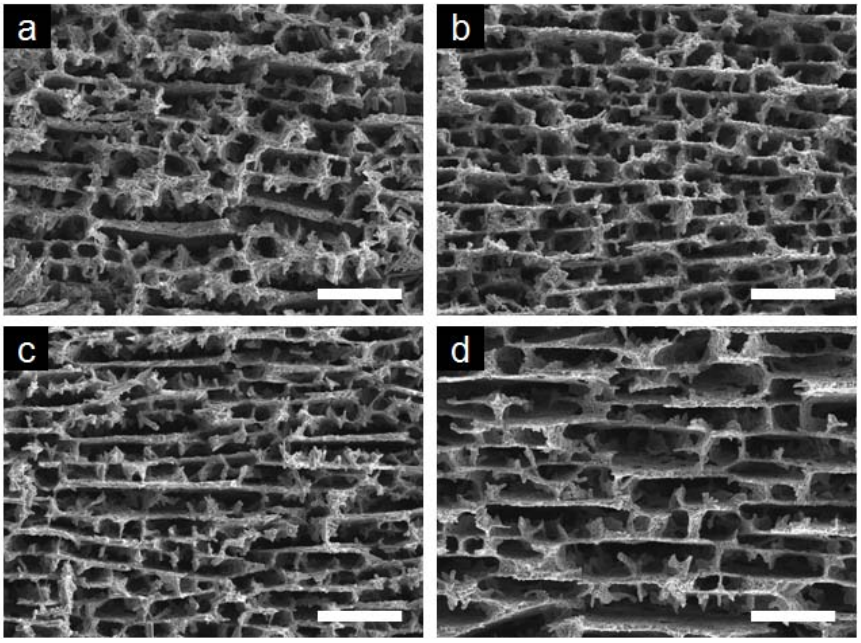

Figure 4.2. Scanning electron micrographs of TiO_2 scaffolds freeze cast with 1 wt.% polyethylene glycol (PEG) of varying molecular weight (MW) and solution viscosity: **(a)** 0 wt% PEG, 1.44 mPa·s; **(b)** 2000 MW, 1.50 mPa·s; **(c)** 10,000 MW, 1.63 mPa·s; **(d)** 20,000 MW, 1.75 mPa·s. Scale bars: 50 µm.

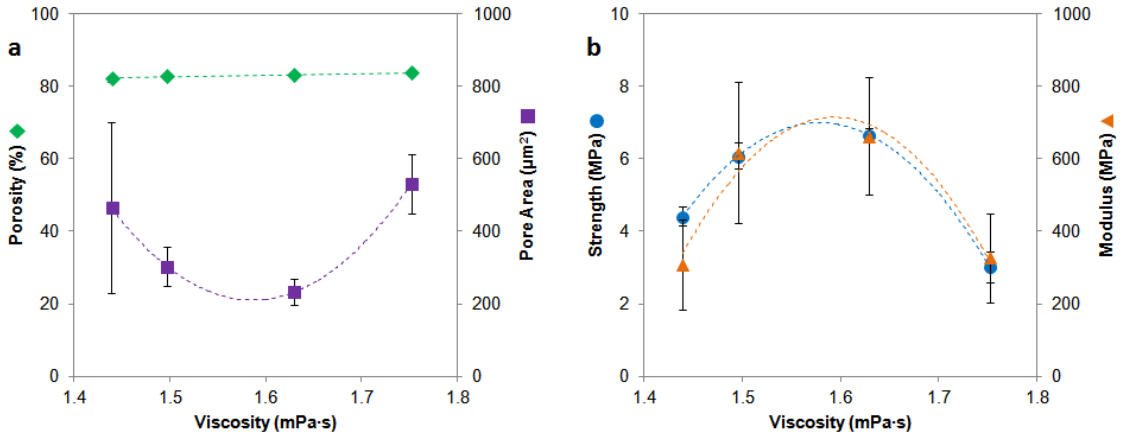

Figure 4.3. Comparison of **(a)** porosity (green, diamonds), pore area (purple, squares), **(b)** compressive strength (blue, circles), and compressive modulus (orange, triangles) for TiO_2 scaffolds freeze cast with varying viscosity by addition of polyethylene glycol (PEG) with different molecular weights.

layers of scaffolding along the ice growth direction (out of the page, Figure 4.2). Secondary dendrites produced irregularities in the scaffolds as the solidification front progressed, resulting in characteristic surface roughness, similar to PEG experiments reported by Pekor et al. [264]. Referring to Figure 4.3a, a slight variation in the pore area (200-600 μm^2) was observed, while the overall porosity (~85%) of the scaffolds remained constant. The pore channels in the scaffolds made with no PEG are cellular with less homogeneous alignment, higher surface roughness, and dense mineral bridging (see Figure 4.2a). Conversely, the pore channels in the scaffolds made with the highest molecular weight PEG are more homogeneously aligned with lower surface roughness and less mineral bridging (see Figure 4.2d).

Although, the addition of PEG initially lowers the freezing temperature of water-PEG solutions to below 0°C, increasing the viscosity (with higher molecular weight

PEG) increases the freezing temperature of the PEG-modified slurries. Figure 4.4 contains a diagram of expected thermal profiles for different water-PEG solutions at the solid-liquid interface (i.e., freezing front). As seen in the diagram, the region of constitutional supercooling is greater for solutions with higher molecular weights, and thereby, higher viscosities. This increase in viscosity leads to a larger amount of constitutional supercooling, ΔT [333]:

$$\Delta T \sim \frac{A}{\lambda} \tag{4.7}$$

where A is a materials constant and λ is the lamellar spacing, which is directly related to the local curvature of instabilities at the solid-liquid interface. Constitutional supercooling occurs when the applied thermal gradient in the liquid (G^L) is less than the equilibrium thermodynamic temperature of the liquid (refer to Figure 4.4) [334]:

$$G^L < \frac{v}{D}(T^{liq} - T^{sol}) \tag{4.8}$$

where v is the freezing front velocity, D is the mass diffusivity of the liquid, T^{liq} is the equilibrium liquidus temperature, and T^{sol} is the equilibrium solidus temperature. When no supercooling exists in the solution, the solid-liquid interface is considered stable and planar [334]. At low viscosity the amount of supercooling is small, leading to a slow freezing front velocity and the growth of cellular ice crystals [334]. In contrast, a larger region of supercooling at higher viscosity leads to a faster freezing front velocity and the formation of dendritic ice crystals [334]. Therefore, scaffolds made from the slurry with the lowest viscosity (~1.50 mPa·s) contain smaller cellular pore structures (Figure 4.2b), while those made from the highest viscosity (~1.75 mPa·s) contain larger lamellar pores

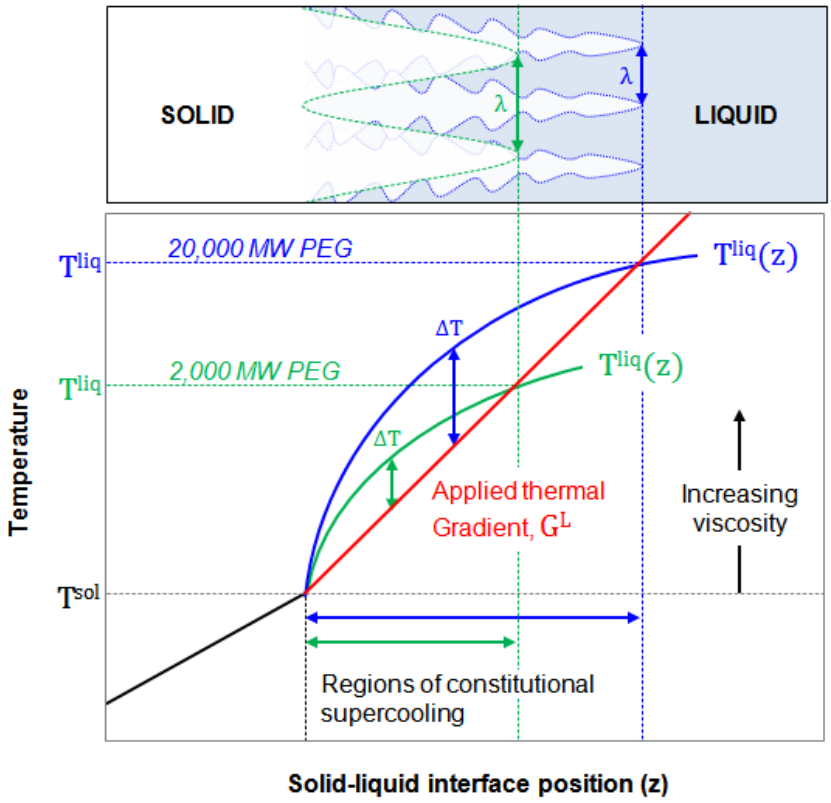

Figure 4.4. Thermal profiles of water-PEG solutions as a function of the position across the solid-liquid interface. The blue curve represents PEG solutions with a high molecular weight (e.g., 20,000) and higher freezing temperature, resulting in columnar dendritic-like structures. The green curve represents PEG solutions with a low molecular weight (e.g., 2,000) and lower freezing temperature, resulting in more cellular-like structures. The diagram above illustrates the transition from cellular (green) to dendritic (blue) crystal structures. The two curves in the diagram illustrate that there is a larger region of constitutional supercooling, $\Delta T \sim \frac{A}{\lambda}$, for water-PEG solutions with higher viscosities, resulting in finer instabilities.

(Figure 4.2d). If the viscosity is increased even further (beyond ~2 mPa·s), the dendritic crystals should become finer, resulting in a reduced lamellar spacing. This phenomenon is discussed in more detail in Section 3.3, where the addition of IPA increases the viscosity beyond ~2 mPa·s.

Referring to Figure 4.3, both the compressive strength and modulus are inversely related to the pore area. An optimal viscosity of ~1.6 mPa·s leads to a minimum pore area and maximum compressive mechanical properties. Beyond this point (~1.6 mPa·s), the pore area increases as the viscosity increases. This is likely due to the tendency of TiO_2 particles interacting with the longer-chain PEG molecules to aggregate as they are rejected by the solidification front. The smaller, more homogenous pore channels (Figure 4.2b and 4.2c) with low aspect ratios (~2.5) displayed the highest compressive strength (~6 MPa) and modulus (~600 MPa) at a liquid viscosity of ~1.6 mPa·s. This observed structure-property relationship agrees with hypotheses presented by Hunger et al. [330], suggesting that decreased lamellar spacing and reduced aspect ratio lead to enhanced mechanical performance. For this reason, 1 wt.% PEG with a molecular weight of 10,000 (~1.6 mPa·s) was added to all of the slurries of the remaining experiments, detailed in the following sections.

4.3.2. pH change

In contrast to changes in viscosity, variations in the pH of the slurries had a more significant effect on the pore area (200-4000 μm^2) of the microstructures, while the overall porosity (~85%) remained constant (Table 4.2). The slurries with changing pH showed nearly equal viscosities (Table 4.2). Figure 4.5 compares SEM micrographs of the scaffolds made from slurries at pH 2, 7, and 12. Figure 4.6 compares the porosity, pore area, and compressive mechanical properties of scaffolds made from slurries at different pH levels. As seen in Figure 4.5**,** the channel lengths, widths, and general morphologies vary considerably with changing pH. At low pH (~2) the lamellar surfaces

have a coarse roughness and low density of bridging, due to the increased spacing and thickness of lamellae. This results in a large variation in pore area (refer to error bars, Figure 4.6a). It appears that a low pH induces more elongated pores, with aspect ratios of ~5 (see Table 4.2). As the pH increases from 2 to 7 the pore area reduces significantly from values of 4000 μm^2 at pH 2 (Figure 4.5a) to 250 μm^2 at pH 7 (Figure 4.5b). At neutral pH a fine network of pores evolves from tiny homogeneously distributed ice crystals. As the pH increases from 7 to 12 there is only a slight increase in the pore area, approaching values of 1000 μm^2 at pH 12 (Figure 4.5c). A high pH has only moderate effects on lamellar wall spacing, thus allowing some bridging of the walls.

In agreement with Zhang et al. [283], there was a significant variation in the pore architecture at different pH levels. However, the dispersion of particles in the suspension seemed stable at all pH levels, resulting in well-defined pore structures. The presence hydrogen, hydronium, or hydroxide groups may decrease the solidification temperature in the solvent, thereby slowing the ice crystal growth velocity [297], similar to the effect of ice-structuring compounds investigated by Deville et al. [307]. The resulting effect of a decreased freezing front velocity is the presence of larger, faceted pores in the lamellar microstructure as the region of constitutional supercooling is smaller and water molecules are more slowly incorporated into the ice crystals, causing an increase in their average size and aspect ratio [307].

Similar to the viscosity experiments, the compressive mechanical properties follow a loose inverse relationship with the pore area, with strengths ranging from 4-10 MPa and stiffnesses ranging from 200-800 MPa. The highest strength (~9 MPa) and

stiffness (~600 MPa) occur in scaffolds with the lowest pore area (~200 μm^2) and aspect ratio (~2) at pH ~8.

Table 4.2. Slurry properties (viscosity, pH), pore morphology (porosity, pore area, major and minor axes, aspect ratio, lamella thickness), and compressive mechanical properties (strength, modulus) of TiO_2 scaffolds freeze cast with varying pH by adding various concentrations of HCl or NaOH to increase or decrease the pH of the slurry, respectively.

HCl or NaOH (M)	0.036 (HCl)	0.024 (HCl)	0.012 (HCl)	0.002 (NaOH)	0.004 (NaOH)	0.006 (NaOH)
Viscosity, (mPa·s)	1.59 ± 0.04	1.66 ± 0.02	1.60 ± 0.03	1.61 ± 0.03	1.59 ± 0.02	1.62 ± 0.04
pH	~2	~4	~6	~8	~10	~12
Overall porosity, (%)	85.5 ± 0.6	83.7 ± 1.2	84.5 ± 0.2	84.0 ± 0.4	84.8 ± 0.3	85.7 ± 0.1
Pore area, (μm^2)	3332 ± 492	1673 ± 561	544 ± 145	186 ± 47	351 ± 111	929 ± 126
Pore major axis, (μm)	154 ± 92	97 ± 90	57 ± 38	23 ± 13	36 ± 27	64 ± 33
Pore minor axis, (μm)	28 ± 7	22 ± 8	12 ± 5	10 ± 5	12 ± 5	18 ± 5
Pore aspect ratio,	5.59	4.45	4.77	2.15	2.94	3.47
Lamella thickness, (μm)	17.73 ± 9.43	12.12 ± 6.66	6.32 ± 3.40	3.13 ± 2.76	3.86 ± 2.25	5.13 ± 2.71
Strength, (MPa)	4.8 ± 0.8	6.6 ± 0.5	5.4 ± 0.4	9.5 ± 0.4	7.2 ± 0.6	7.1 ± 0.8
Modulus, (MPa)	301 ± 54	415 ± 52	442 ± 80	621 ± 229	496 ± 77	582 ± 174

* All data shown as average ± standard deviation.

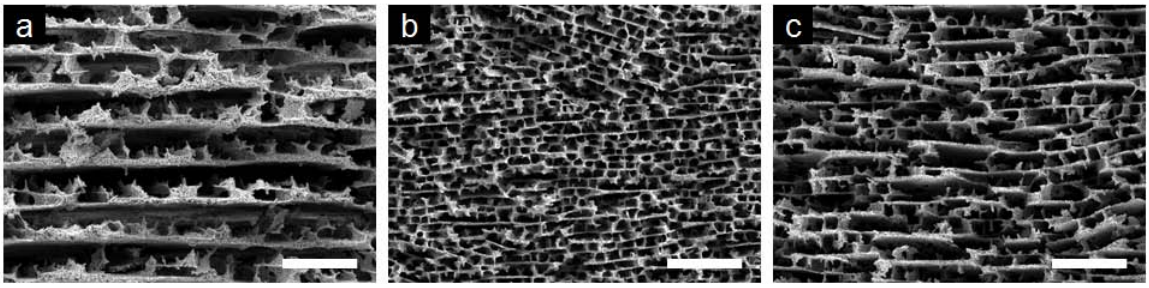

Figure 4.5. Scanning electron micrographs of TiO_2 scaffolds freeze cast with varying pH: **(a)** pH 2; **(b)** pH 7; **(c)** pH 12. Scale bars: 100 μm.

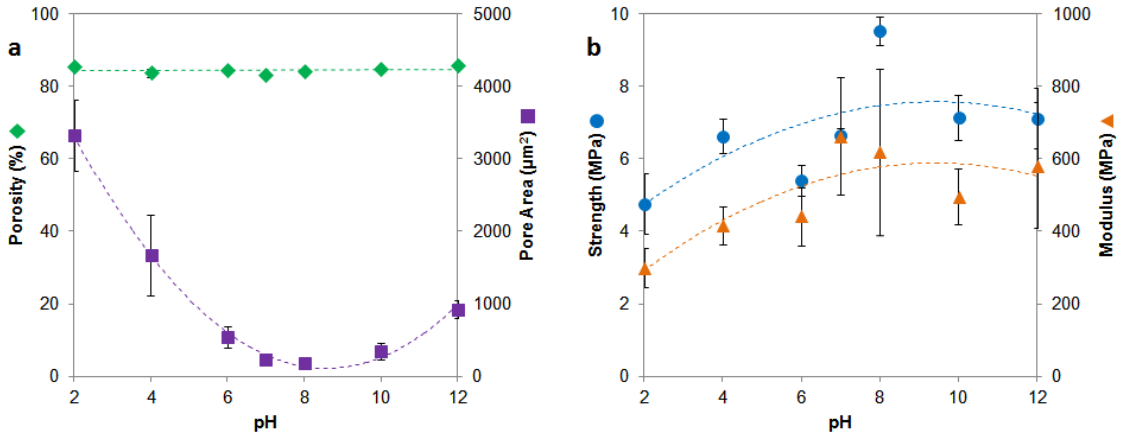

Figure 4.6. Comparison of **(a)** porosity (green, diamonds), pore area (purple, squares), **(b)** compressive strength (blue, circles), and compressive modulus (orange, triangles) for TiO_2 scaffolds freeze cast with varying pH.

4.3.3. Alcohol concentration

Modification of alcohol (IPA) concentration in the slurries generated scaffolds that are vastly different from those freeze cast with changing viscosity and pH. Figures 4.7 and 4.8 show SEM images and plots, respectively, of the structural and mechanical properties of the scaffolds freeze cast with increasing concentrations of IPA. The addition of IPA to the slurries increased the viscosity significantly; however, the pH remained neutral (~7) (see Table 4.3). As seen in Figure 4.7a, the pore area increases dramatically, then slowly decreases as the alcohol concentration is further increased. In comparison, scaffolds freeze cast with changing viscosity and pH had more boxy, rectangular pores (Figure 4.2 and 4.5), while the addition of alcohol led to more elongated pore channels (Figure 4.7) with high aspect ratios, up to ~10 (Table 4.3). Furthermore, scaffolds freeze cast with IPA showed some extent of finer periodic surface features (see Figure 4.7). The

different pore morphologies coincide with an increase of the maximum pore area and aspect ratio, respectively, to ~6000 μm^2 and ~10 for IPA-modified slurries, compared to ~4000 μm^2 and ~5.5 for pH-modified slurries, and ~600 μm^2 and ~3.5 for viscosity-modified slurries. As the alcohol concentration was increased beyond 5 vol.% there is very little change in the porosity, compressive strength and stiffness. However, the dramatic increase in viscosity above ~2 mPa·s (see Table 4.3) led to finer instabilities in the solid-liquid interface, resulting in smaller pore sizes and reduced lamellar spacing (refer to Figure 4.4).

The maximum pore area observed at 5 vol.% IPA is likely due to an interaction between IPA and water that favors crystallization, producing large elongated pore channels (Figure 4.7c). Similar to observations made by Munch et al. [306] for ethanol, the antifreeze properties of IPA lower the solidification temperature and increase the viscosity significantly, which slows the freezing front velocity [335]. Furthermore, water-IPA mixtures are believed to form clathrate hydrate structures [335, 336], in which the 'guest' IPA molecules are trapped by hydrogen bonding within an organized lattice of 'host' water molecules. Figure 4.9 shows a phase diagram of the water-IPA system taken from Aladko et al. [335]. As seen in the diagram, the concentrations of IPA used in this work (0-30 vol.% or 0-37 wt.%; red dots) all fall along the region corresponding to the clathrate structure: IPA-$5H_2O$. These clathrate hydrates, crystallized at temperatures below -50 °C, are composed of tetragonal unit cells (a = 0.640 nm, c = 1.116 nm) [335]. The unit cells are folded into layers where the hydroxyl groups of the guest IPA molecules displace one of the water molecules in the lattice, leading to the elongated c-axis over that of the cubic clathrate [335]. Thus, the formation of these crystalline

Table 4.3. Slurry properties (viscosity, pH), pore morphology (porosity, pore area, major and minor axes, aspect ratio, lamella thickness), and compressive mechanical properties (strength, modulus) of TiO_2 scaffolds freeze cast with varying concentrations of isopropanol alcohol (IPA).

IPA (vol.%)	0	1	5	15	30
Viscosity, (mPa·s)	1.63 ± 0.02	2.18 ± 0.06	2.05 ± 0.05	3.04 ± 0.03	4.67 ± 0.10
pH	~7	~7	~7	~7	~7
Overall porosity, (%)	83.2 ± 0.1	84.6 ± 0.2	84.8 ± 0.2	83.1 ± 0.3	78.9 ± 1.1
Pore area, (μm^2)	234 ± 36	2330 ± 556	4876 ± 1153	2778 ± 188	612 ± 146
Pore major axis, (µm)	29 ± 14	158 ± 106	244 ± 197	170 ± 69	72 ± 44
Pore minor axis, (µm)	10 ± 3	19 ± 7	25 ± 7	21 ± 3	11 ± 4
Pore aspect ratio,	2.74	8.46	9.61	8.17	6.67
Lamella thickness, (µm)	2.54 ± 1.27	6.72 ± 4.04	15.71 ± 12.85	10.39 ± 6.62	4.53 ± 2.62
Strength, (MPa)	6.7 ± 0.2	3.3 ± 0.3	0.7 ± 0.1	1.3 ± 0.3	1.0 ± 0.2
Modulus, (MPa)	662 ± 162	263 ± 55	90 ± 38	176 ± 51	132 ± 38

* All data shown as average ± standard deviation.

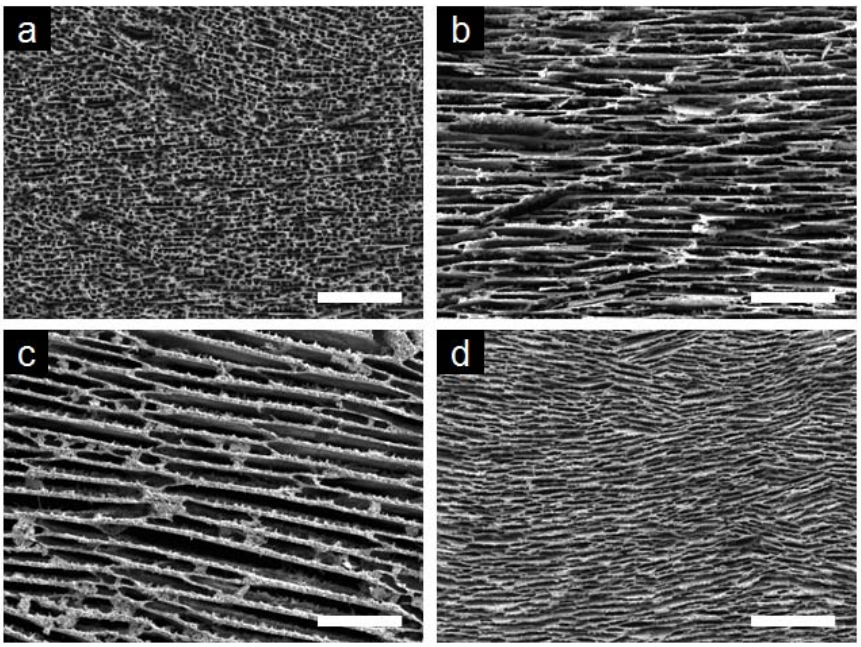

Figure 4.7. Scanning electron micrographs of TiO_2 scaffolds freeze cast with varying concentrations of isopropanol alcohol (IPA): **(a)** 0 vol.%; **(b)** 1 vol.%; **(c)** 5 vol.%; **(d)** 30 vol.%. Scale bars: 200 µm.

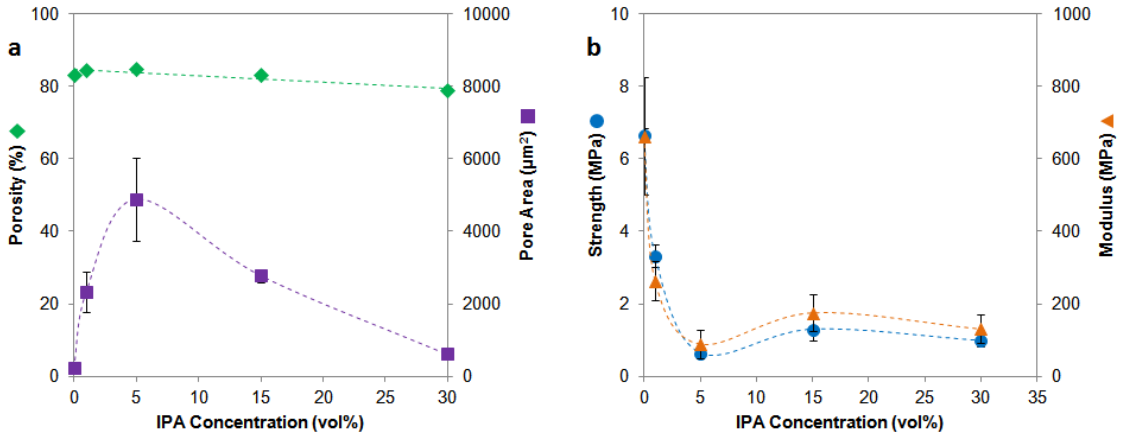

Figure 4.8. Comparison of **(a)** porosity (green, diamonds), pore area (purple, squares), **(b)** compressive strength (blue, circles), and compressive modulus (orange, triangles) for TiO_2 scaffolds freeze cast with varying isopropanol alcohol (IPA) concentrations.

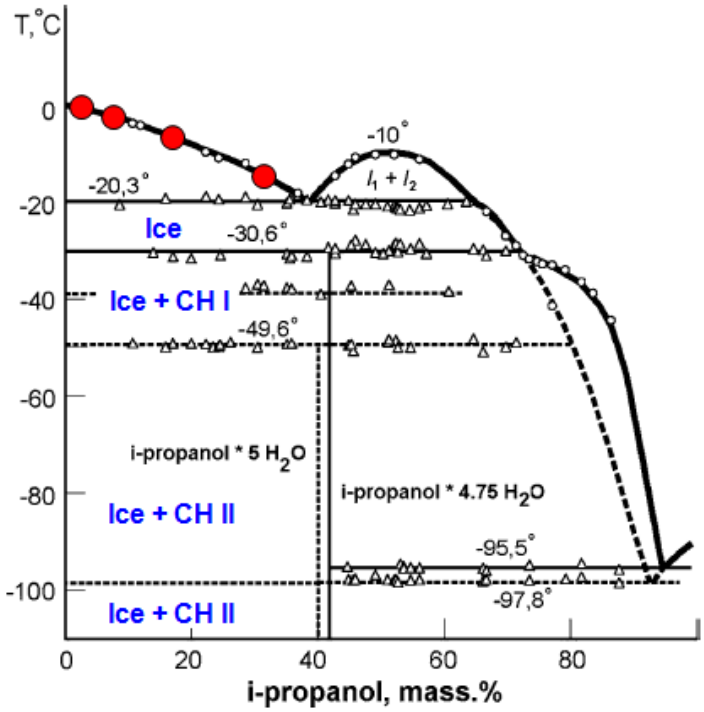

Figure 4.9. Phase diagram of the water-IPA system. The red dots represent the initial freezing points of the experiments carried out in this work for IPA concentrations of 0-30 vol.% (corresponding to 0-37 wt.% of the water-IPA solutions). The different mixtures of crystal structures existing in this system are shown in blue: ice, hexagonal (a = 0.452 nm, c = 0.736 nm); clathrate hydrate I (CH I), cubic (a = 1.256 nm); clathrate hydrate II (CH II), tetragonal (a = 0.640 nm, c = 1.116 nm). Adapted from [335].

clathrate hydrates significantly increases the viscosity. The pore structures observed in Figure 4.7 must, therefore, be replicas of clathrate-like structures that form with the addition of IPA. Based on experimental results, an optimal concentration of IPA is likely to exist around 5 vol.%, where the formation of these layered or elongated hydrates seems most favorable.

The ranges of strength from 0.5-6.5 MPa and modulus from 100-800 MPa show that the dramatic increase in pore area and aspect ratio significantly reduces the compressive mechanical properties (see Figure 4.8). The changing pore morphologies resulting from changes in alcohol concentration reduce the mechanical performance of the scaffolds by a factor of ~5; in contrast to the mechanical reduction by factors of ~2 and ~1.5 for the pH change and viscosity experiments, respectively. The decline in mechanical properties observed with the addition of alcohol (Figure 4.8b) may be due to the semi-uniform alignment and elongation of lamellar walls, which allow cracks to propagate through more easily as lamellae buckle under compression. Conversely, the smaller pore channels generated with no addition of alcohol (Figure 4.7a) distribute the load more evenly across the scaffold, putting less stress on each lamellae. Therefore, in agreement with Section 3.1, and as suggested by Hunger et al. [330], smaller, low aspect ratio pores result in higher compressive properties by resisting the buckling of lamellar microstructures and subsequent crack propagation.

4.3.4. Microstructure and mechanical properties

Figures 4.10 and 4.11 compare the lamellar thickness, pore area, aspect ratio, and compressive mechanical properties of all the scaffolds freeze cast with varying viscosity,

pH, and alcohol concentration. As expected, a linear relationship between the pore area and lamellar thickness exists for all slurry conditions, despite the additive used (Figure 4.10). Obviously, at equal porosity, the pore area must increase as the lamellar thickness increases. The slight discrepancy between the pH change and alcohol concentration data, seen in Figure 4.10, is most likely due to the fact that water-IPA mixtures may form clathrate hydrate structures [335, 336], increasing the apparent pore sizes for respective lamellar thicknesses. Although the solidification time was not measured in this study, the lamellar thickness, and consequently the pore size, are expected to exhibit a similar direct correlation to the freezing front velocity as reported by Munch et al. [306]. According to this work, the use of ethanol as an additive led to increased lamellar spacing, which is related to its relatively low solidification temperature, lengthening the phase to which the liquid and crystallized solid can coexist [306]. Our use of IPA as an additive provides evidence for this point, given that IPA-modified slurries resulted in larger pore areas and aspect ratios compared to scaffolds fabricated with varying viscosity or pH change. The low solidification temperature and the presence of intermolecular interactions (such as hydrogen bonding with IPA or increased local concentrations of additives due to the crystallization of water and clathrate hydrates) may affect the thermal properties of the newly-crystallized solid interface, as explained by Wegst et al. [78]. Therefore, it is reasonable to assume that the different additives used to modify the rheological properties of the liquid slurries changed the temperature profile at which constitutional supercooling occurs, resulting in different freezing front velocities and consequent pore morphologies.

While no clear, comprehensive trend relating the lamellar thickness or pore area to the mechanical performance of the scaffolds was observed, a fairly strong empirical

correlation between the pore aspect ratio and the compressive properties was found (see Figure 4.11). As seen in the plot (Figure 4.11a), both the strength and modulus show a rapid decay as the pore aspect ratio increases. As mentioned earlier, these results agree with Hunger et al. [330]: a decreased lamellar spacing (i.e., pore minor axis) and decreased pore aspect ratio lead to enhanced mechanical properties. This decreasing trend can be attributed to, not only the possibility for crack formation and growth due to local buckling of lamellar walls, but also the semi-uniform alignment of pore channels that distribute the load evenly across several lamellae. Moreover, an increased number of mineral bridges would decrease the apparent pore area and aspect ratio, yielding higher compressive mechanical properties. In response to compressive loading, mineral bridges prevent Euler buckling by hindering crack propagation through parallel lamellae [306]. Hence, the smaller and more uniform (i.e., low aspect ratio) the pores, the higher the mechanical properties - a function of the mechanisms that arrest local buckling of lamellae and subsequent crack propagation.

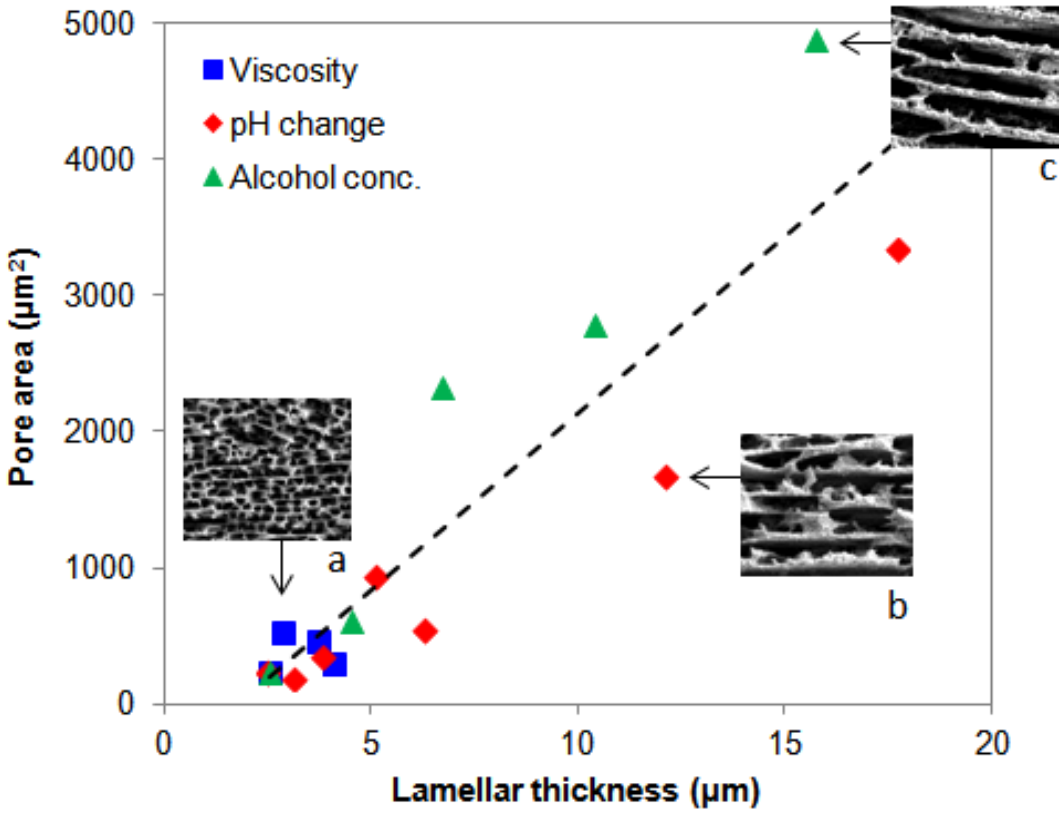

Figure 4.10. Comparison of TiO_2 scaffolds freeze cast with varying viscosity (blue, squares), pH change (red, diamonds), and alcohol concentration (green, triangles), illustrating an increasing trend for pore area versus lamellar thickness. Representative SEM images of TiO_2 scaffolds: **(a)** 10k PEG MW, pH 7, 0 vol.% IPA; **(b)** 10k PEG MW, pH 4, 0 vol.% IPA; **(c)** 10k PEG MW, pH 7, 5 vol.% IPA. SEM images are 250 µm wide.

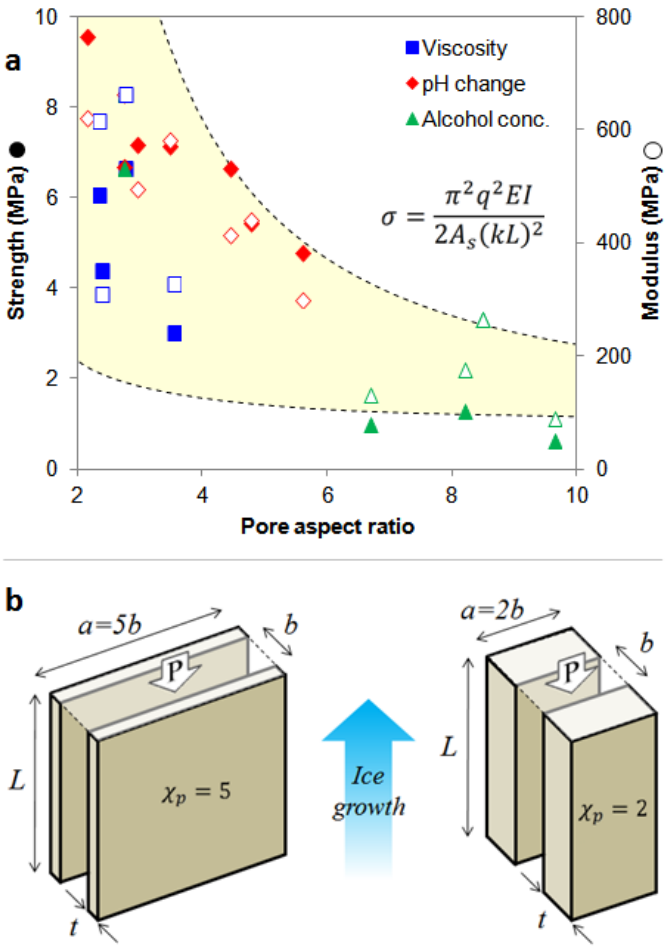

Figure 4.11. (a) Comparison of the compressive mechanical properties versus pore aspect ratio of TiO_2 scaffolds freeze cast with varying viscosity (blue, squares), pH change (red, diamonds), and alcohol concentration (green, triangles). Solid markers correspond to compressive strength measurements, while hollow markers correspond to compressive modulus measurements. The decreasing quadratic trend shown in yellow is determined by the modified Euler buckling equation shown (σ), where the area moment of inertia (I) is a function of the pore aspect ratio (χ_p) (refer to Equations 4.9-4.13).

(b) Representative schematic drawings used to describe the simplified Euler buckling analysis (refer to Equations 4.9-4.13), where two lamellar walls of equal length (major axis) a, thickness t and height L, separated by a pore width (minor axis) b, are subjected to a compressive load P applied parallel to the height L. For the analysis, it is assumed that the representative specimens have constant lamellar wall heights (L = 500 µm), pore widths (b = 15 µm), and equal lamellar cross-sectional areas ($A_s = at$), but different pore aspect ratios (for example - left image: χ_p = 5; right image: χ_p = 2). For the range plotted above (yellow region), the lamellar wall cross-sectional area (A_s) was varied from 250 µm^2 to 1500 µm^2, which incorporates the majority of experimental measurements.

4.3.5. Euler buckling analysis

To further elucidate the effect of the aspect ratio on the local Euler buckling of the scaffolds, an analytical expression relating the compressive strength (σ) to the pore aspect ratio (χ_p) can be derived. Two idealized schematic representations are shown in Figure 4.11b to illustrate this phenomenon. This simplified model ignores the effect of mineral bridges and surface asperities. Keeping the total amount of material (i.e., lamellar wall cross-sectional area, $A_s = at$) and pore width (minor axis, b) constant, the pore aspect ratio can be increased by increasing the lamellar wall length (major axis, a) and correspondingly decreasing the lamellar wall thickness (t) (refer to Figure 4.11b). The Euler equation has the form [337]:

$$P = n^2 \frac{\pi^2 q^2 EI}{(kL)^2} \tag{4.9}$$

where P is the compressive load, n is the order of deflection (in our case, $n = 1$), E is the Young's modulus, I is the area moment of inertia, k is dependent on the geometry of the ends (in our case, $k = 0.5$ for fixed ends), and L is the lamellar wall height. In order to incorporate experimental unknowns, such as the internal wall porosity and surface roughness, an empirical factor q , dependent on the lamellar wall properties, was added into Equation 4.9. From the parallel axis theorem, the area moment of inertia is determined to be:

$$I = 2 \times \left(\frac{at^3}{12} + \frac{A_s}{4}(b+t)^2 \right). \tag{4.10}$$

By substituting $A_s = at$ and $\chi_p = a/b$ into Equation 4.10 and rearranging the variables, the area moment of inertia can be rewritten as a function of the pore aspect ratio (χ_p) in terms of the constants A_s and b:

$$I = \frac{2}{3}\frac{A_s^3}{b^2}\left(\frac{1}{\chi_p}\right)^2 + A_s^2\left(\frac{1}{\chi_p}\right) + \frac{A_s}{2}b^2. \tag{4.11}$$

The maximum compressive stress is $\sigma = P/2A_s$ and can be written as:

$$\sigma = \frac{\pi^2 q^2 EI}{2A_s(kL)^2}. \tag{4.12}$$

Finally, substituting in the area moment of inertia given by Equation 4.11 into the stress relation above, the maximum compressive stress is expressed as a function of the pore aspect ratio:

$$\sigma = \frac{\pi^2 q^2 E}{(kL)^2}\left(\frac{A_s^2}{3b^2}\left(\frac{1}{\chi_p}\right)^2 + \frac{A_s}{2}\left(\frac{1}{\chi_p}\right) + \frac{b^2}{4}\right). \tag{4.13}$$

To fit this modified Euler buckling equation (Equation 4.13) to the experimental data plotted in Figure 4.11a, several assumptions were made according to Figure 4.11b. First, the lamellar wall height and pore width (minor axis) were kept constant (equal to the averages of experimental measurements) at values of L = 500 μm and b = 15 μm, respectively. The Young's modulus of pure TiO_2, E = 270 GPa [338], the geometric constant of k = 0.5, and the empirical correction factor of q = 0.02 were used to represent the stiffness and geometry of the lamellar walls. By setting the lamellar wall cross-sectional area equal to a range of 250 μm^2 < A_s < 1500 μm^2, which incorporates the majority of experimental measurements, and plotting the stress (σ) as a function of the

pore aspect ratio (χ_p), the quadratic trend shown in Figure 4.11a (yellow region) fits the experimental data quite well. Therefore, a simple modified Euler analysis incorporates the principal effects, suggesting that the primary failure mechanism in the TiO_2 scaffolds is local buckling followed by tensile cracking. The low value of q is an indication that the existing internal wall porosity and surface roughness introduce flaws that decrease the maximum stress considerably.

4.4. Conclusions

The effects of polyethylene glycol (PEG) viscosity, pH, and isopropanol alcohol (IPA) concentration on freeze cast TiO_2 scaffolds are compared. Porous ceramic scaffolds are achieved with varied properties such as pore size, coarse/fine surface features, alignment and spacing of lamellar walls, as well as bridging between pore channels. Relationships between porosity, lamellar thickness, pore morphology, compressive strength and modulus for each of these methods are reported. Altering the different slurry properties did not change the overall porosities of the scaffolds, but changed the pore morphologies significantly. In general, it is observed that smaller pore areas and aspect ratios provided increased strength and stiffness. A simplified analysis of Euler buckling predicts this trend in agreement with experimental results, where the strength of the scaffolds decreases as the aspect ratio of the pores increases, following a quadratic dependency.

The control of structure and mechanical properties achieved through the methods delineated above presents a bright potential for the creation of tailored scaffolds for bone replacement. The biocompatibility of TiO_2 is excellent and it is known to promote

osteointegration. The control of pore size and aspect ratio is essential for cellular scaffolding and thus the methodology presented herein is eminently applicable for biomaterials. Applications needing a predefined porosity as well as requiring specified pore dimensions can be fulfilled by modifying the processing parameters of a freeze cast slurry. These parameters are readily available for control in the laboratory: its combination with TiO_2 may provide a base scaffolding compatible with biological materials and organisms.

4.5. Acknowledgements

Chapter 4, in full, is published in *Advanced Functional Materials* and co-authored by R. Imperio, M. Wen, M.A. Meyers, and J. McKittrick of UCSD.

CHAPTER 5:

MAGNETIC FREEZE CASTING INSPIRED BY NATURE

5.1. Introduction

A common unifying theme in the study of natural materials is the presence of anisotropy and architectural hierarchy over multiple length scales [8-10]. This type of directional order allows biomaterials to be lightweight, high strength, and multifunctional [13]. Abalone nacre and bone, for instance, are structural materials with exceptional mechanical properties designed for body support; and, impact resistance in the case of nacre, or blood flow and joint movement in the case of bone [28, 339]. These properties result from highly ordered, structural alignment in multiple directions across several length scales. In the field of bio-inspired design, many new technologies to fabricate high-performance, multifunctional materials that mimic the nano-/micro-structural features of natural materials are being explored with varying success.

Of these, freeze casting has become a most promising new technique to fabricate porous ceramic scaffolds [121, 222]. Potential applications range from bone replacements [76, 77, 329] and tough hybrid composites (upon infiltration of a second phase) [75, 82, 84, 243], to separation filters, insulators, catalyst supports, or piezoelectric devices [222, 279, 298, 340, 341]. Freeze casting of ceramics is a physical process in which an aqueous slurry composed of a solid phase (e.g., ceramic powder) and a fugitive liquid carrier (e.g., water) is directionally frozen in a mold, then sublimated to remove the frozen liquid phase, and finally sintered to partially densify and strengthen the green constructs [78, 121, 222]. During the freezing process, ceramic particles are pushed between and trapped

within growing lamellar ice crystals [78, 121, 222]. The thermodynamics that govern the phenomena of particle rejection and entrapment are explicated by Wegst *et al.* [78] and Deville *et al.* [288], where constitutional supercooling drives instabilities (or undulations) in the freezing front that lead to the nucleation and growth of well-ordered, interconnected ice channels. Intricate microstructural features, such as surface roughness, wall thickness, pore geometry and inter-lamellar bridging, may be controlled by altering the slurry properties or changing the freezing direction and solidification kinetics [76, 77, 253, 262, 266, 275, 294, 297, 306, 308, 312, 313, 342]. An inherent drawback of these scaffolds is their lack of strength and stiffness transverse to the direction of ice growth. That is, the outstanding mechanical properties usually celebrated in these materials only exist in a single uniaxial direction, parallel to the freezing direction [306]. For many applications, this may not be problematic. However, applications such as bone replacements or tough hybrid composites that require substantial mechanical performance in multiple directions may not be well-suited by conventional freeze casting.

Some attempts to introduce greater microstructural control have been previously reported. Fu *et al.* [77] and Munch *et al.* [306] used additives, such as glycerol, dioxane, ethanol or sucrose, to modify the microstructure (e.g., lamellar or cellular) and surface roughness (e.g., smooth or dendritic) of freeze-cast scaffolds by changing the eutectic phase diagram of the colloidal suspensions. Munch *et al.* [306] showed that patterning the freezing surface can manipulate the long-range ordering of ice lamellae by controlling the initial direction of nucleation. Zhang *et al.* [310] fabricated dense/porous bilayered ceramics by applying an electric field during freezing. Moon *et al.* [313], Macchetta *et al.* [275], and Koh *et al.* [308, 342] demonstrated the concept of radial cooling to construct

porous ceramics with radial channel alignment. Regardless, none of these modifications have been shown to significantly enhance the mechanical properties in planes normal the ice growth direction. New additions to conventional freeze casting techniques that may align microstructural features and increase the strength and stiffness in multiple directions are still of great interest.

One mechanism commonly used to align small-scale materials, such as carbon nanotubes or ferrous nanoparticles, is an external magnetic field [343-349]. Magnetic fields are particularly useful in materials fabrication when physical barriers, such as the walls of a mold, restrict the manipulation of materials through direct contact. In ceramics processing, high magnetic fields (> 10 T) have been shown to control the texture of feeble magnetic ceramics, such as HA, Al_2O_3, or TiO_2 [350-356]. Unfortunately, high magnetic fields are produced by special superconducting magnets that are infeasible in most laboratories due to their high cost, high energy consumption, and safety concerns [345]. In contrast, small magnetic particles such as magnetite (Fe_3O_4) are known to aggregate into linear-chain clusters in the direction of relatively weak magnetic fields (< 1 T) [347, 349, 357]. Mashkour *et al.* [345] showed that it is possible to align cellulose fibers doped with Fe_3O_4 using a permanent magnet with a field strength < 0.18 T. Using this concept, low magnetic fields may align the complex microstructures in freeze-cast ceramics containing small amounts of Fe_3O_4.

Inspired by the helicoidal structure of the narwhal tusk, an external rotating magnetic field was applied to a conventional freeze cast system for the first time. A permanent neodymium magnet and cast iron flux path distributors were used to direct a magnetic field perpendicular to the ice growth direction. Porous scaffolds with structural

alignment in both the longitudinal (i.e., ice growth direction) and transverse (i.e., magnetic flux direction) planes were fabricated from nonmagnetic ceramic powders mixed with small amounts of Fe_3O_4 nanoparticles. The compressive mechanical properties of the scaffolds were measured in directions perpendicular and parallel to the magnetic flux path and freezing directions. This work introduces the novel concept of magnetic freeze casting and explains its potential as a simple, low cost processing method to fabricate porous, anisotropic ceramic scaffolds with a hierarchy of architectural alignment in multiple directions.

5.2. Materials and methods

5.2.1. Magnetic freeze casting setup

Samples were prepared using a custom built freeze cast unit and rotating permanent magnet. Figure 5.1 shows a picture of the magnetic freeze casting setup. The freeze cast unit consists of a copper cold finger immersed in a liquid nitrogen bath. A band heater and thermocouple linked to a PID controller are attached to the copper cold finger in order to control the cooling rate of the copper surface at the bottom of a polyvinyl chloride (PVC) mold with a 20 mm inner diameter. The rotating permanent magnet is constructed from a 1.32 T neodymium rare earth magnet, grade N42 ($2.5 \times 10 \times 10$ cm^3) (Applied Magnets, Plano, TX). Two cast iron channel arms, threaded stainless steel rods, and cast iron flux path distributors are attached to the neodymium magnet to direct and concentrate the magnetic flux path through the PVC mold perpendicular to the ice growth direction (Z-axis). The magnetic field strength can be varied from 0-0.15 T by adjusting the distance of the flux path distributors with the threaded rods. The permanent

magnet device was hung by a vertical aluminum shaft connected to a 3 V, 1.6 A, 233 oz-in geared bipolar stepper motor (RobotShop Inc., Swanton, VT), controlled by an electronic user interface, Arduino Uno-R3 (SparkFun Electronics, Boulder, CO), capable of rotating the magnet 0.05-0.50 rpm about the Z-axis. Finite element models (FEM) of the magnetic flux path distributions were developed using the software, FEMM 4.2 (David Meeker, Waltham, MA).

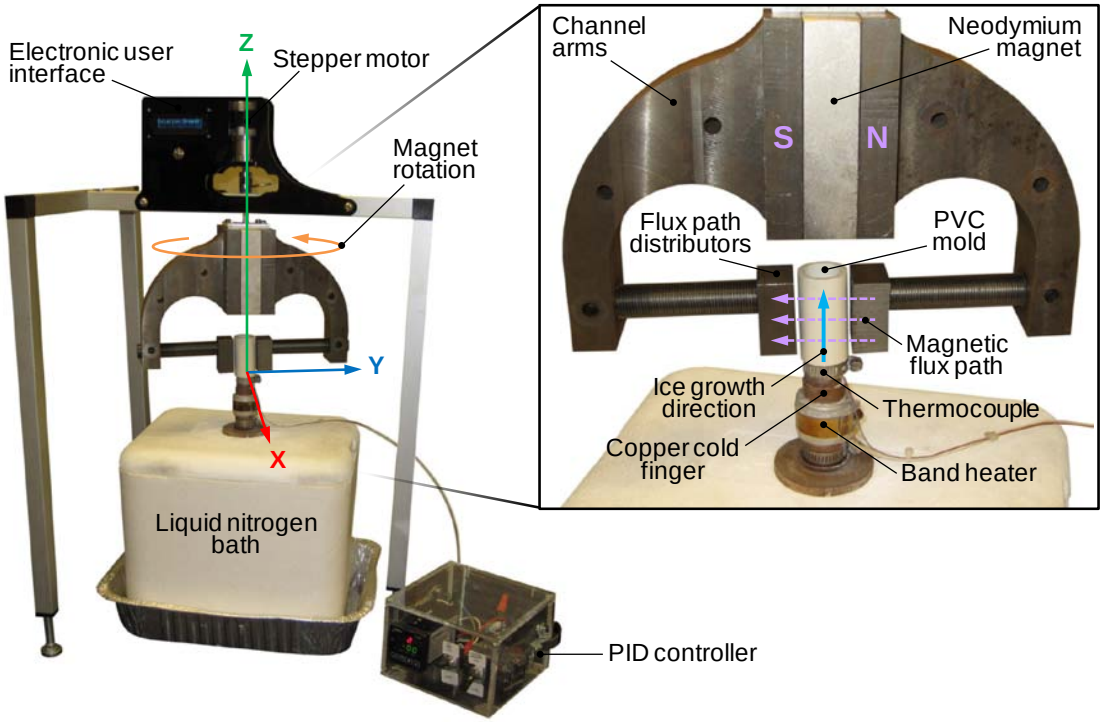

Figure 5.1. Magnetic freeze casting setup, illustrating the magnet rotation, ice growth, and magnetic flux path directions. The direction normal to the ice growth (Z-axis) and magnetic flux path (Y-axis) directions is represented by the X-axis.

Table 5.1. Properties of ceramic powders, as received. Information reported by manufacturers unless otherwise noted.

	Magnetite (Fe_3O_4)	Hydroxyapatite (HA)	Zirconia (ZrO_2)	Alumina (Al_2O_3)	Titania (TiO_2)
Crystal system[a]	Cubic	Hexagonal	Monoclinic	Hexagonal	Tetragonal
Density (g/cm^3)	4.95	3.15	5.89	4.00	4.26
Molar mass (g/mol)	231.53	502.31	123.22	101.96	79.87
Particle size (μm)[b]	<0.05	1-3	0.2-0.5	2-5	0.2-0.5

[a] Crystal systems confirmed by XRD measurements.
[b] Particle sizes measured from SEM micrographs.

5.2.2. Sample preparation

Aqueous slurries of 10 vol% HA (Trans Tech, Adamstown, MD), ZrO_2 (Sigma Aldrich, St. Louis, MO), Al_2O_3 (Sigma Aldrich, St. Louis, MO), or TiO_2 (Sigma Aldrich, St. Louis, MO) powders were mixed with varying concentrations of 0-9 wt% (0-8 vol% of the total solids) Fe_3O_4 nanoparticles (Sigma Aldrich, St. Louis, MO). Table 5.1 shows the physical properties of the ceramic powders, as received. All slurries contained 1 wt% of each: organic binders, polyethylene glycol (PEG) (Alfa Aesar, Ward Hill, MA) and polyvinyl alcohol (PVA) (Alfa Aesar, Ward Hill, MA), and an ammonium polymethacrylate anionic dispersant, Darvan® 811 (R. T. Vanderbilt Company, Inc. , Norwalk, CT). The slurries were ball milled in an alumina grinding medium for 24 hours, followed by degassing under low vacuum for 10-20 min. Approximately 10 mL of the degassed slurries were poured into the PVC mold and frozen at a constant rate of 10°C/min. Samples were frozen under three different magnetic field conditions: (1) no magnetic field; (2) a static magnetic field of 0.12 T; and (3) a rotating magnetic field of 0.12 T at 0.05 rpm. After freezing, the samples were removed from the mold with a hydraulic press and lyophilized in a bench-top freeze dryer (Labconco, Kansas City, MO)

at -50°C and 350 Pa for 72 hr. The porous green constructs were then sintered in an open air furnace for 3 hr at predetermined temperatures of 1300°C for HA and ZrO_2, 1500°C for Al_2O_3, and 900°C for TiO_2 with heating and cooling rates of 2°C/min.

5.2.3. Material characterization

The relative density (ρ_{rel}) and porosity (ϕ) of the scaffolds were measured by mass (m) and volume (V) with respect to that of a fully dense material of equal composition (ρ'), as shown in Equations 5.1 and 5.2:

$$\rho_{rel} = \frac{\rho}{\rho'} = \frac{m/V}{\gamma\rho'_{Fe_3O_4} + (1-\gamma)\rho'_{host}} \tag{5.1}$$

$$\phi = (1 - \rho_{rel}) \times 100\% \tag{5.2}$$

where $\rho = m/V$ is the measured sample density, $\rho'_{Fe_3O_4}$ and ρ'_{host} are the densities of fully dense Fe_3O_4 and host ceramic (HA, ZrO_2, Al_2O_3, or TiO_2), respectively, and the γ is the weight fraction of Fe_3O_4. The average pore sizes and channel widths of the scaffolds were measured using ImageJ software.

Energy-dispersive X-ray spectroscopy (EDX) was performed with a Philips XL30 field emission environmental scanning electron microscope (FEI-XL30, FEI Company, Hillsboro, OR). The samples were coated with iridium using an Emitech K575X sputter coater (Quorum Technologies Ltd., West Sussex, UK). Elemental mapping and analyses were performed at 20 kV using an Oxford EDX attachment and Inca software.

X-ray diffraction (XRD) was performed with a Miniflex II XRD machine (Rigaku, The Woodlands, TX) to confirm the crystal systems of the as-received ceramic

powders (Table 5.1) and characterize the crystal structures of the TiO_2 scaffolds before and after sintering.

5.2.4. Micro-computed tomography

Two TiO_2 scaffolds containing 3 wt% Fe_3O_4, made with (1) no magnetic field and (2) a rotating magnetic field of 0.12 T at 0.05rpm, were scanned on a micro-computed tomography (μCT) unit, Skyscan 1076 (Skyscan, Kontich, Belgium). The scaffolds were positioned inside a Styrofoam tube and imaged at 9 μm isotropic voxel size, applying an electric potential of 70 kVp and a current of 200 μA, using a 1 mm aluminum filter. A beam hardening correction algorithm was applied during image reconstruction. Images and 3D rendered models were developed using Skyscan's Dataviewer and CTVox software.

5.2.5. Microscopy

Optical microscopy images were taken with a VHX-1000 digital microscope system equipped with a CCD camera (KEYENCE Corporation, Osaka, Japan).

Scanning electron microscopy (SEM) images were taken at 10 kV on a Philips XL30 field emission environmental scanning electron microscope (FEI-XL30, FEI Company, Hillsboro, OR). For SEM preparation the samples were sputter-coated with iridium using an Emitech K575X sputter coater (Quorum Technologies Ltd., West Sussex, UK).

5.2.6. Mechanical testing

Compression testing of the TiO_2 scaffolds was performed on an Instron machine (Instron 3342, Norwood, MA) with a 500 N load cell at a crosshead velocity of 0.005 mm/sec. The scaffolds were cut into small samples of approximately $5 \times 5 \times 5$ mm^3 and tested in three orthogonal directions (see Figure 5.1): (1) ice growth direction (Z-axis); (2) magnetic flux path direction (Y-axis); and (3) transverse direction (X-axis). To ensure testing of the homogeneous region and avoid the high-density regions of the scaffolds (i.e., the outer perimeter and the bottom 5 mm of the scaffold [297]), the cubic samples were cut from the center core of the scaffolds (10×10 mm^2) between 5-30 mm from the bottom. The compressive ultimate strength and Young's modulus were determined from the maximum stress and the linear slope of the stress-strain curves, respectively.

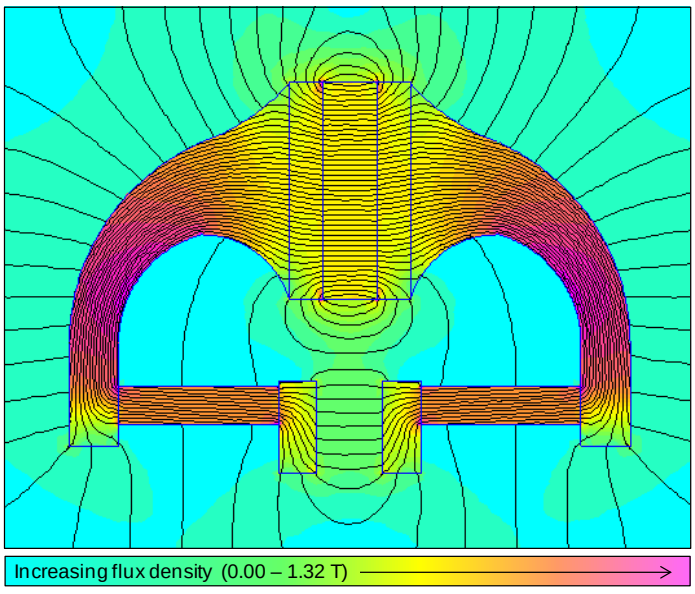

Figure 5.2. Finite element model (FEM) showing the magnetic flux path and density distributions through the permanent magnet apparatus shown in Figure 5.1. According to the legend (bottom), the highest flux density is shown in purple, while the lowest flux density is shown in light blue.

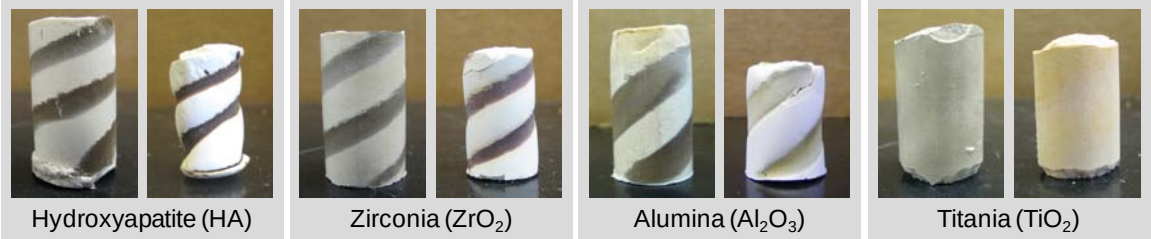

Figure 5.3. Images of different ceramic scaffolds containing 3 wt% (~3 vol%) Fe_3O_4 nanoparticles made with a rotating magnetic field of 0.12 T at 0.05 rpm. Left images of each scaffold were taken after lyophilizing and before sintering. Right images were taken after sintering for 3 hr at predetermined temperatures of 1300°C for HA and ZrO_2, 1500°C for Al_2O_3, and 900°C for TiO_2. All scaffolds before sintering were 20 mm in diameter.

5.3. Results and discussion

5.3.1. Freezing under magnetic fields

Directing a magnetic field through the ceramic slurries perpendicular to the ice growth direction was accomplished by channeling the field through the flux path distributors seen in Figure 5.1. Figure 5.2 shows a 2D finite element model (FEM) illustrating the magnetic field lines and density throughout the permanent magnet system. Measurements of the magnetic field strength using a Gauss meter and observations of the field direction using iron filaments in a clear test tube confirmed that the magnetic field through the PVC mold in the experiments described here was 0.12 T and normal to the freezing direction.

Figure 5.3 shows images of freeze-cast HA, ZrO_2, Al_2O_3, and TiO_2 with 3 wt% (~3 vol%) Fe_3O_4 frozen at 10°C/min under a rotating magnetic field of 0.12 T at 0.05 rpm. As seen in the images, the HA, ZrO_2, and Al_2O_3 scaffolds showed two distinct phases of the host ceramic (HA, ZrO_2, Al_2O_3) and Fe_3O_4 when fabricated under the

influence of the external field. The TiO_2 scaffolds, on the other hand, did not show separate ceramic phases, suggesting that the Fe_3O_4 nanoparticles were well distributed and absorbed into the TiO_2 scaffold. Additionally, the Fe_3O_4 phase of the HA, ZrO_2, and Al_2O_3 scaffolds seemed to densify and deform the macrostructures after sintering (Figure 5.3, right images).

5.3.2. Biphasic properties of HA, ZrO_2, and Al_2O_3 scaffolds

Figure 5.4 shows elemental mappings of the iron (Fe) concentration in sintered HA, ZrO_2, Al_2O_3, and TiO_2 scaffolds containing 3 wt% Fe_3O_4 made with a static magnetic field of 0.12 T. As seen in the elemental maps, gradients of varying Fe concentrations were observed in the HA, ZrO_2, and Al_2O_3 scaffolds (Figure 5.4a-c). Alternatively, Fe in the TiO_2 scaffold was evenly distributed throughout (Figure 5.4d). Table 5.2 shows measured concentrations of Fe and the host elements (Ca, P, Zr, Al, Ti, O) of each scaffold taken from Figure 5.4. The *Fe_3O_4-rich region* was measured at the edges of the scaffolds closest to the poles of the external magnetic field, while the *Fe_3O_4-poor region* was measured at the center of the scaffolds away from the poles of the external field. It is apparent that the Fe concentrations in the Fe_3O_4-rich and Fe_3O_4-poor regions of the TiO_2 scaffold were nearly equal. However, the highest concentrations of Fe in the HA, ZrO_2, and Al_2O_3 scaffolds were located at the edges (Fe_3O_4-rich region), closest to the poles of the external magnetic field.

Table 5.2. Elemental analysis of sintered HA, ZrO_2, Al_2O_3, and TiO_2 scaffolds containing 3 wt% (~3 vol%) Fe_3O_4 made with a static magnetic field of 0.12 T, showing the concentration (wt%) of iron (Fe) and host elements (Ca, P, Zr, Al, Ti, O) in the Fe_3O_4-rich (edge) and Fe_3O_4-poor (center) regions of the scaffolds.

	Hydoxyapatite (HA)		Zirconia (ZrO_2)		Alumina (Al_2O_3)		Titania (TiO_2)	
	element	*wt %*	*element*	*wt %*	*element*	*wt %*	*element*	*wt %*
Fe_3O_4-rich region	Fe	5.78	Fe	8.27	Fe	7.83	Fe	1.64
	Ca	36.56	Zr	61.29	Al	47.40	Ti	61.07
	P	15.83	O	30.44	O	44.77	O	37.29
	O	41.82	---	---	---	---	---	---
Fe_3O_4-poor region	Fe	0.08	Fe	0.20	Fe	0.33	Fe	1.61
	Ca	45.89	Zr	71.17	Al	51.69	Ti	61.65
	P	15.29	O	28.62	O	47.98	O	36.74
	O	38.73	---	---	---	---	---	---

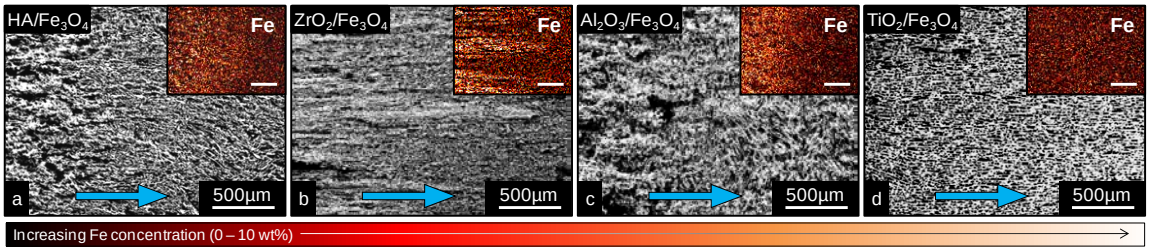

Figure 5.4. Elemental mapping of iron (Fe) concentration in sintered **(a)** HA, **(b)** ZrO_2, **(c)** Al_2O_3, and **(d)** TiO_2 scaffolds containing 3 wt% (~3 vol%) Fe_3O_4 made with a static magnetic field of 0.12 T. According to the legend (bottom), the highest concentration of Fe is shown in white, while the lowest concentration of Fe is shown in black. Images were taken in the transverse XY-plane, perpendicular to the direction of ice growth. The magnetic field direction is shown with blue, horizontal arrows. All scale bars are 500 µm.

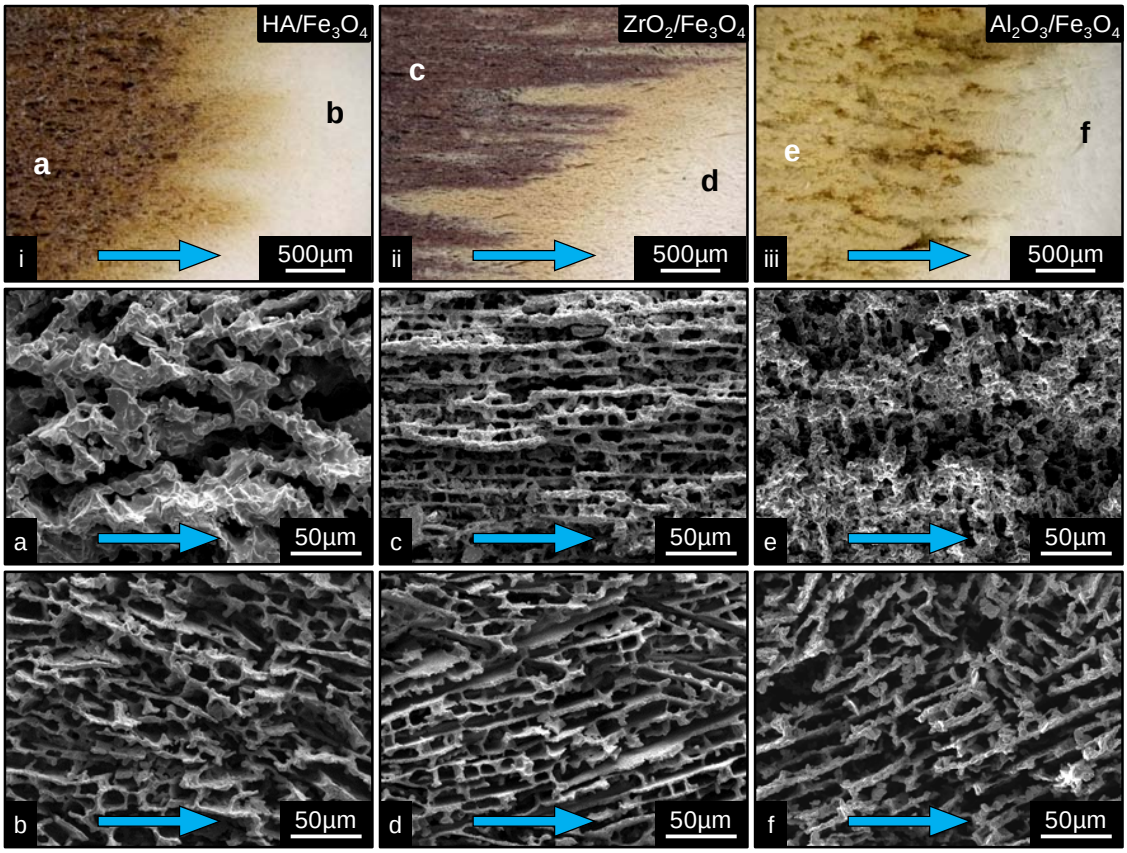

Figure 5.5. From left to right, micrographs of sintered HA, ZrO_2, and Al_2O_3 scaffolds containing 3 wt% (~3 vol%) Fe_3O_4 made with a static magnetic field of 0.12 T. **(i-iii)** Optical images of the different scaffolds showing the Fe_3O_4 phase transitions. **(a, c, e)** Magnified SEM images of the Fe_3O_4-rich regions. **(b, d, f)** Magnified SEM images of the Fe_3O_4-poor regions. All images were taken in the transverse XY-plane, perpendicular to the direction of ice growth. Images **(i-iii)** show the locations of images **(a-f)** respectively. The magnetic field direction is shown with blue, horizontal arrows. All micrographs were imaged at 15 mm from the bottom of the scaffolds.

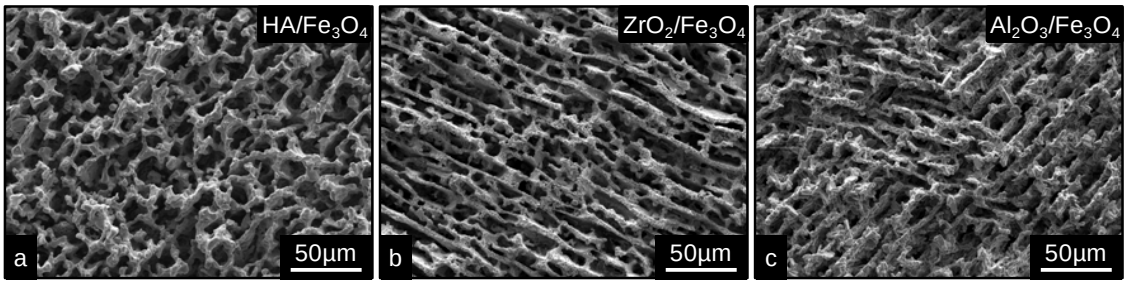

Figure 5.6. Micrographs of sintered **(a)** HA, **(b)** ZrO_2, and **(c)** Al_2O_3 scaffolds containing 3 wt% (~3 vol%) Fe_3O_4 made with no magnetic field. All micrographs were imaged at 15 mm from the bottom of the scaffolds.

Figure 5.5 contains magnified optical and SEM micrographs of the sintered HA, ZrO_2, and Al_2O_3 scaffolds made with a static magnetic field of 0.12 T. In the optical images (Figures 5.5i-iii), the distribution of color further suggests that the Fe_3O_4 (brown/purple/yellow) concentrated to the poles of the magnetic field and separated from the host ceramic (white). The microstructures of the Fe_3O_4-rich (brown/purple/yellow) and Fe_3O_4-poor (white) regions are distinctly different. The Fe_3O_4-rich HA (Figure 5.5a) has thick lamellar walls and large pores (20-50 μm), while the Fe_3O_4-poor HA (Figure 5.5b) has thin lamellar walls and small pores (10-20 μm), similar to a pure HA scaffold. The Fe_3O_4-rich ZrO_2 (Figure 5.5c) is more dense with narrow lamellar walls aligned in the direction of the magnetic field. The Fe_3O_4-poor ZrO_2 (Figure 5.5d) is a porous structure with random alignment, similar to a pure ZrO_2 scaffold. The Fe_3O_4-rich Al_2O_3 (Figure 5.5e) has a dense microstructure with larger ridges aligned in the direction of the magnetic field, while the Fe_3O_4-poor Al_2O_3 (Figure 5.5f) has a random alignment similar to a pure Al_2O_3 scaffold. This biphasic behavior was not observed in the scaffolds made with no magnetic field. Instead, the two phases were well mixed and evenly distributed throughout, resulting in the homogeneous microstructures shown in Figure 5.6a-c.

Table 5.1 lists the physical properties of the ceramic powders in the as-received condition. Although the driving forces behind the Fe_3O_4-host, particle-particle interactions observed in Figure 5.4 are not fully understood, it is known that the motion of magnetic and nonmagnetic particles in a colloidal suspension under an external magnetic field is governed by magnetic dipole, electrostatic, van der Waals, and hydrodynamic forces [358-360]. Brownian motion, which dominates collisions of colloidal particles <1 μm, is dependent on the concentration, size, and density of the

particles [358]. There seems to be no relation linking the initial particle size or molar mass to the biphasic behaviors observed in Figure 5.4a-c (compare with Table 5.1). Therefore, it may be reasonable to assume that the similar densities of the Fe_3O_4 (4.95 g/cm^3) and TiO_2 (4.26 g/cm^3) would allow for the homogeneous mixing seen in Figure 5.4d. The different crystal systems may also play a role in the particle-particle interactions observed, but this has yet to be determined (see Chapter 7). Though it may be useful to develop composite materials such as those with two distinct phases (Figure 5.5), this was not main objective of this work. Thus, the remainder of this paper focuses on the physical and mechanical properties of the TiO_2 scaffolds.

5.3.3. Magnetic alignment of TiO_2 scaffolds

X-ray diffraction patterns of TiO_2 scaffolds containing 3 wt% Fe_3O_4 (Figure 5.7) show that the crystal structure of the TiO_2 transformed from anatase before sintering to rutile after sintering at 900°C. It is also apparent in Figure 5.7 that the Fe_3O_4 initially present before sintering was absorbed into the TiO_2 scaffolds after sintering, forming a small amount of the iron titanium oxide, pseudobrookite (Fe_2TiO_5).

Figure 5.8 shows SEM micrographs of TiO_2 scaffolds containing 3 wt% Fe_3O_4 produced with no magnetic field (top), a static magnetic field (center), and a rotating magnetic field (bottom). The scaffolds made with no magnetic field showed directional alignment only in the longitudinal ice growth direction, represented by a green arrow. Figure 5.8a shows the edges and some faces of lamellar sheets oriented in the longitudinal YZ-plane. In the transverse XY-plane (Figure 5.8b), there is no uniform alignment of the micro-channels, but several small domains (~100-500 μm) of similarly

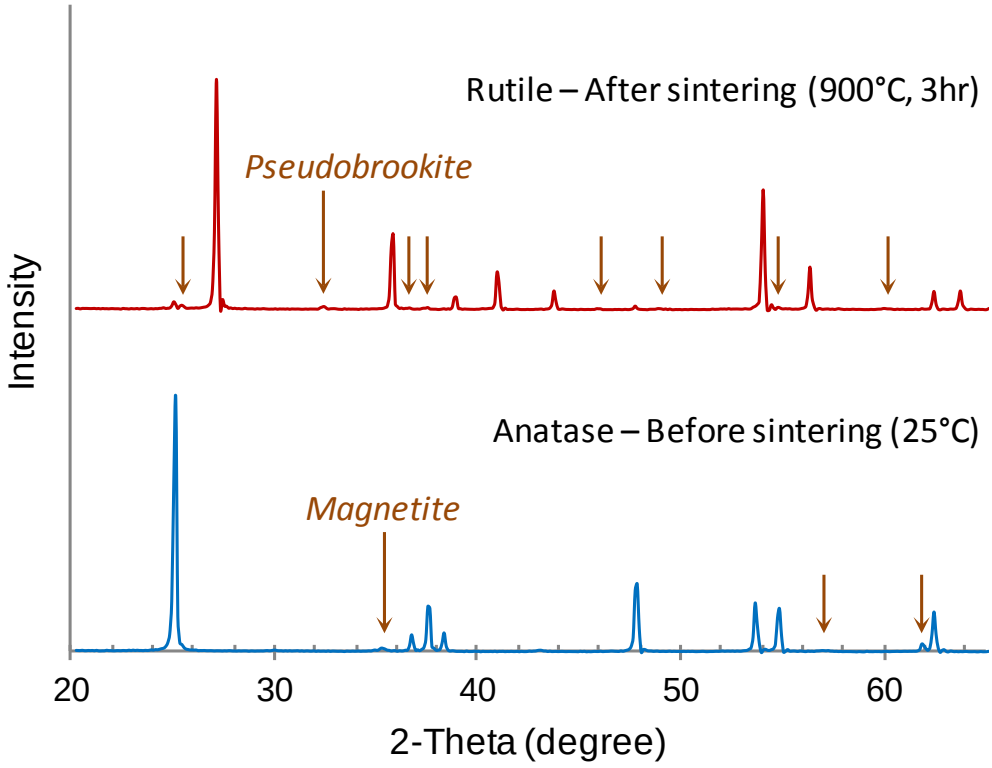

Figure 5.7. X-ray diffraction (XRD) patterns of TiO_2 scaffolds containing 3 wt% (~3 vol%) Fe_3O_4 before and after sintering at 900 °C for 3 hr. Before sintering the TiO_2 is anatase (blue) and after sintering the TiO_2 is rutile (red). Peaks corresponding to magnetite (Fe_3O_4) and pseudobrookite (Fe_2TiO_5) are marked by the arrows in the XRD patterns before and after sintering, respectively.

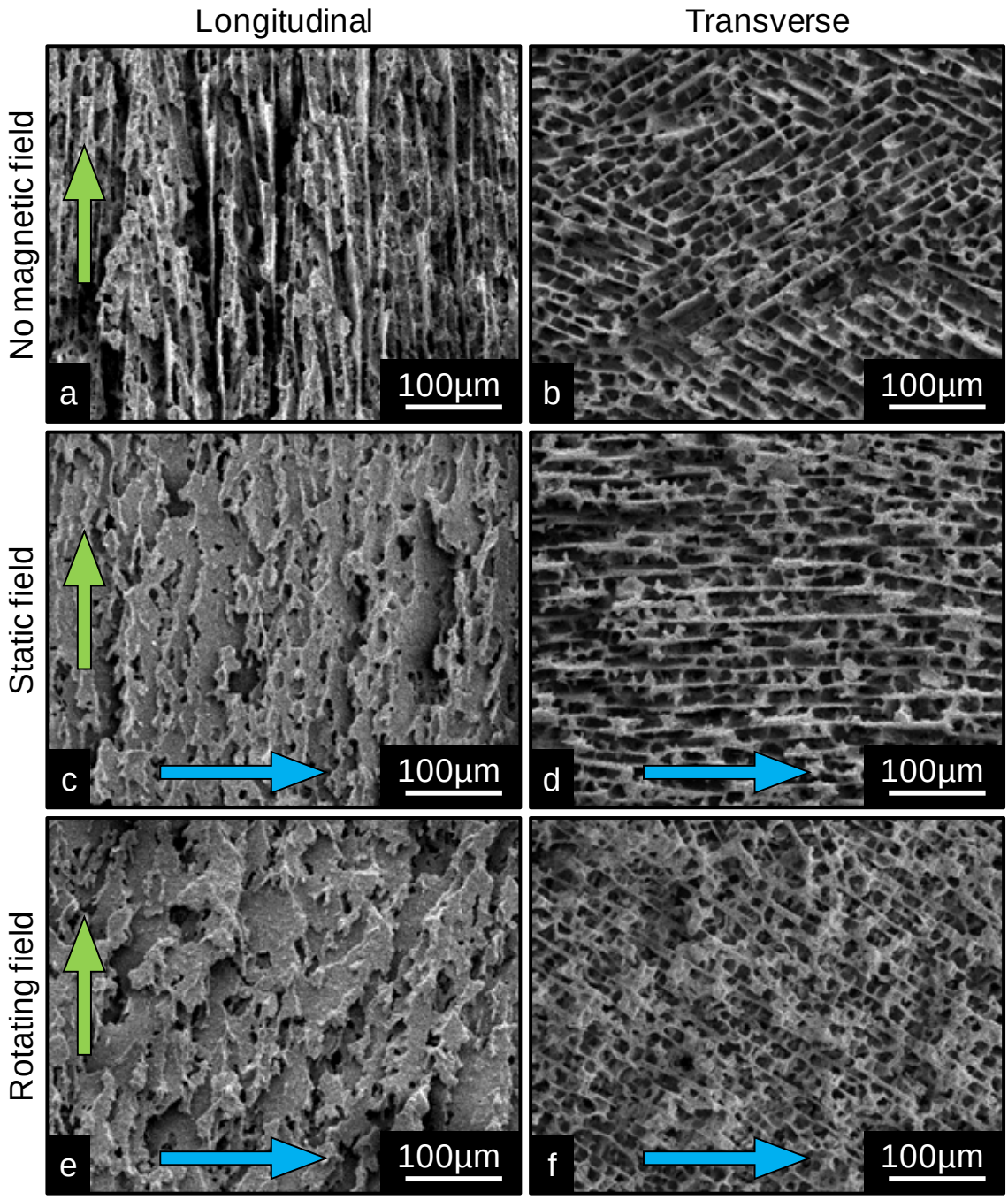

Figure 5.8. SEM micrographs of TiO_2 scaffolds containing 3 wt% (~3 vol%) Fe_3O_4 made with no magnetic field (top), a static magnetic field of 0.12 T (center), and a rotating magnetic field of 0.12 T at 0.05 rpm (bottom). Left images show microstructures in the longitudinal YZ-plane. Right images show microstructures in the transverse XY-plane. The ice growth direction is shown with green, vertical arrows. The magnetic field direction is shown with blue, horizontal arrows. All micrographs were imaged at 15 mm from the bottom of the scaffolds.

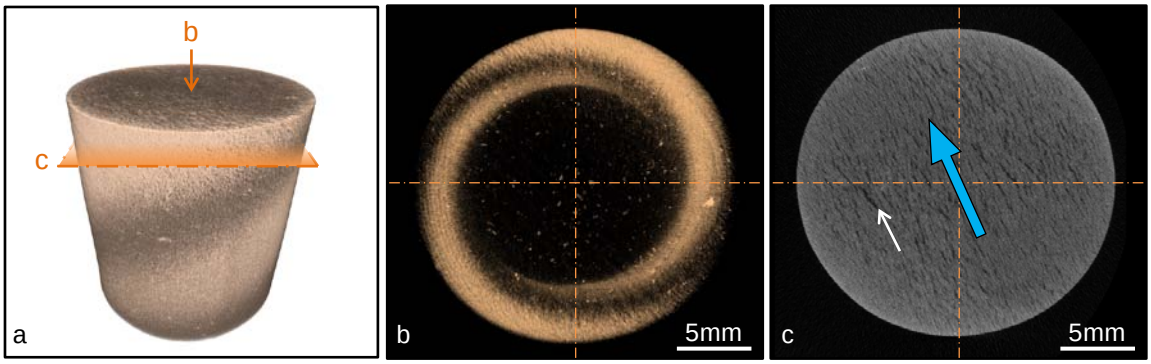

Figure 5.9. Micro-computed tomography images of a sintered TiO_2 scaffold containing 3 wt% (~3 vol%) Fe_3O_4 made with a rotating magnetic field of 0.12 T at 0.05 rpm. **(a)** 3D reconstruction of the scaffold showing the high-density (dark brown) and low-density (light brown) regions. **(b)** Top view of the scaffold with opacity adjusted to show only the high-density regions around the perimeter of the scaffold. **(c)** Image of the transverse XY-plane perpendicular to the ice growth direction at 20 mm from the bottom of the scaffold. The magnetic field direction is shown with the blue arrow. An aligned macro-channel (~50 µm wide) is noted with the white arrow.

oriented channels - an intrinsic property of most freeze-cast ceramics [289, 290, 306]. Scaffolds made with a static field of 0.12 T showed directional alignment in both the longitudinal (Figure 5.8c) and transverse (Figure 5.8d) planes. The weak magnetic field, represented by a blue arrow, introduced some order of channel alignment parallel to the field direction. Figure 5.8c shows the faces of lamellar sheets propagating along the longitudinal ice growth direction (green arrow). The magnetic field (blue arrow) forced the lamellar sheets in orientations along the field direction. Although not all the lamellar sheets were aligned throughout the entire scaffold, a vast majority of the micro-channels showed preferred alignments parallel to the field direction, resulting in large domains (>>500 µm) of similarly oriented channels, as seen in Figure 5.8d. Scaffolds made with a rotating magnetic field of 0.12 T at 0.05 rpm also showed some order of alignment in the

longitudinal (Figure 5.8e) and transverse (Figure 5.8f) planes. The lamellar sheets of the scaffolds with a rotating field seemed to be skewed by the field rotation, resulting in slanted lamellar sheets oriented ~30° off-axis from the ice growth direction (green arrow), seen in Figure 5.8e. Long-range alignment of the micro-channels (10-20 μm pores) in the transverse plane was not apparent in the scaffolds made with a rotating field. Instead, aligned macro-channels (~50 μm pores) were created by the magnetic field rotation. Figure 5.9 shows μCT images of a sintered TiO_2 scaffold containing 3 wt% Fe_3O_4 made with a rotating magnetic field. The 3D reconstruction (Figure 5.9a) and top view (Figure 5.9b) of the scaffold show a spiraling perimeter of higher density material. This helicoidal, high-density perimeter may add torsional rigidity to the scaffold. Figure 5.9c shows the larger macro-channels aligned in the direction of the magnetic field (blue arrow). Interestingly, these macro-channels did not appear in the scaffolds made with no magnetic field or a static magnetic field. It seems that the subtle movements and realignments of the Fe_3O_4 particles caused by the field rotation at the freezing front disrupted the uniformity of ice crystal growth, resulting in the macro-channels observed in Figure 5.9c. The high-density perimeter seen in Figure 5.9b, however, was similarly observed in the scaffolds made with a static field, showing a slightly higher density at the edges adjacent to the magnet poles.

5.3.4. Enhanced mechanical performance

Compression tests on the TiO_2 scaffolds were preformed on samples cut from the central region of the cylindrical scaffolds (10×10 mm^2) to avoid any edge effects from the high-density perimeters. Figure 5.10 displays the results from compression tests on

TiO_2 scaffolds with 3 wt% Fe_3O_4 made with no magnetic field (dotted lines, orange bars) and a static magnetic field of 0.12 T (solid lines, purple bars). As seen in the representative stress-strain plot (Figure 5.10a), the ultimate compressive strength of the scaffolds made with no field (dotted lines) was ~7.5 MPa in the ice growth direction (Z) and <1 MPa in the transverse plane (X, Y). When the scaffolds were fabricated under a static field (solid lines), the strength in the ice growth direction (Z) decreased slightly to ~6.5 MPa. Nevertheless, the strength and modulus in the direction of the magnetic field (Y) was more than doubled. Figure 5.10b-c show the increases in compressive strength and stiffness of the scaffolds made with a static magnetic field, respectively. The directional alignment of the micro-channels in the scaffolds made with a static field (Figure 5.8d) added significant strength and stiffness in the direction of the magnetic field.

To see the effect of Fe_3O_4 on the TiO_2 scaffolds, several samples with varying concentrations of 0-9 wt% (0-8 vol%) Fe_3O_4 were prepared and tested. Figure 5.11 contains plots of the strength and modulus in the magnetic field (Y) and ice growth (Z) directions versus initial concentration of Fe_3O_4 (wt%). As seen in Figure 5.11a-b, introducing a static magnetic field of 0.12 T doubled both the strength and modulus of the scaffolds containing 1-9 wt% Fe_3O_4 in the magnetic field direction (Y). The strength and modulus in the ice growth direction (Z), on the other hand, decreased with the introduction of a static magnetic field and increasing Fe_3O_4 (Figure 5.11c-d). Table 5.3 summarizes the physical and mechanical properties of the TiO_2 scaffolds containing 0-9 wt% Fe_3O_4. The decrease in strength and stiffness of the TiO_2 scaffolds in the ice growth direction (Z) with increasing Fe_3O_4 concentration seems to be related to the decrease in

density, and corresponding increase in porosity, of the scaffolds (Table 5.3). This trend is most likely related to the sintering characteristics of the two phases. Figure 5.12 shows SEM micrographs of the lamellar wall surfaces of TiO_2 scaffolds containing 0-9 wt% Fe_3O_4 sintered at 900°C. As seen in Figure 5.12a, the TiO_2 scaffold containing 0 wt% Fe_3O_4 is composed of small particles <<500 nm. The TiO_2 scaffolds made with 1-9 wt% Fe_3O_4 showed significant grain growth with larger rod-like particles >>500 nm (Figure 5.12b-d). This observation is consistent with the fact that iron additives may be used as sintering aids in ceramics processing to promote grain growth and agglomeration [361, 362]. Adding Fe_3O_4 to the TiO_2 scaffolds increased the strength and stiffness at low iron concentrations with and without a magnetic field (Table 5.3). In the magnetic field direction (Y), increasing the Fe_3O_4 concentration from 1 to 9 wt% had very little effect on the resulting mechanical properties (Figure 5.11a-b). Conversely, increasing the concentration of Fe_3O_4 from 1 to 9 wt% decreased the strength and stiffness of the scaffolds in the ice growth direction (Z), especially when fabricated under a static magnetic field (Figure 5.11c-d). The normal, directional alignment caused by the magnetic field seems to have disrupted some of the long-range order produced by the growing ice lamellae, which led to a decrease of mechanical integrity in the longitudinal, ice growth direction.

The unusual phenomenon of decreasing density with increasing Fe_3O_4 concentrations (Table 5.3) agrees with observations reported by Zhang *et al.* [363] that an increase in iron-doping (atom% Fe) of TiO_2 arrests nanocrystalline particle growth at increased temperatures (> 500°C). Although iron additives can promote grain growth during sintering, high concentrations of iron (>1 wt%) in the TiO_2 scaffolds may limit the

Table 5.3. Density, porosity, and compressive mechanical properties of TiO_2 scaffolds containing 1-9 wt% (0-8 vol%) Fe_3O_4 made with no magnetic field and a static field of 0.12 T. The ultimate compressive strength and Young's modulus of the scaffolds were measured in three directions: ice growth direction (Z), magnetic field direction (Y), and transverse direction (X). Sample size: N = 10.

	Density (g/cm^3)	Porosity (%)	Ultimate strength (MPa)			Young's modulus (MPa)		
			X	Y	Z	X	Y	Z
0 wt% Fe_3O_4								
No field	0.53 ± 0.01	87.6 ± 0.1	0.6 ± 0.1	0.6 ± 0.1	4.7 ± 0.6	48 ± 24	48 ± 24	144 ± 55
Static field	---	---	---	---	---	---	---	---
1 wt% Fe_3O_4								
No field	0.55 ± 0.02	87.1 ± 0.5	1.1 ± 0.3	1.1 ± 0.3	8.9 ± 0.5	58 ± 25	58 ± 25	430 ± 92
Static field	0.55 ± 0.01	87.1 ± 0.3	1.4 ± 0.2	2.0 ± 0.5	9.0 ± 0.7	45 ± 30	142 ± 57	412 ± 139
3 wt% Fe_3O_4								
No field	0.51 ± 0.01	88.0 ± 0.3	0.9 ± 0.3	0.9 ± 0.3	7.4 ± 0.2	48 ± 20	48 ± 20	459 ± 74
Static field	0.52 ± 0.01	87.7 ± 0.2	1.4 ± 0.2	2.4 ± 0.6	6.3 ± 0.7	55 ± 29	117 ± 42	332 ± 95
9 wt% Fe_3O_4								
No field	0.47 ± 0.02	89.2 ± 0.4	0.8 ± 0.2	0.8 ± 0.2	5.0 ± 0.6	33 ± 8	33 ± 8	451 ± 74
Static field	0.47 ± 0.02	89.2 ± 0.4	0.9 ± 0.1	1.8 ± 0.3	3.2 ± 0.8	34 ± 8	113 ± 43	123 ± 50

* All data reported as average ± standard deviation.

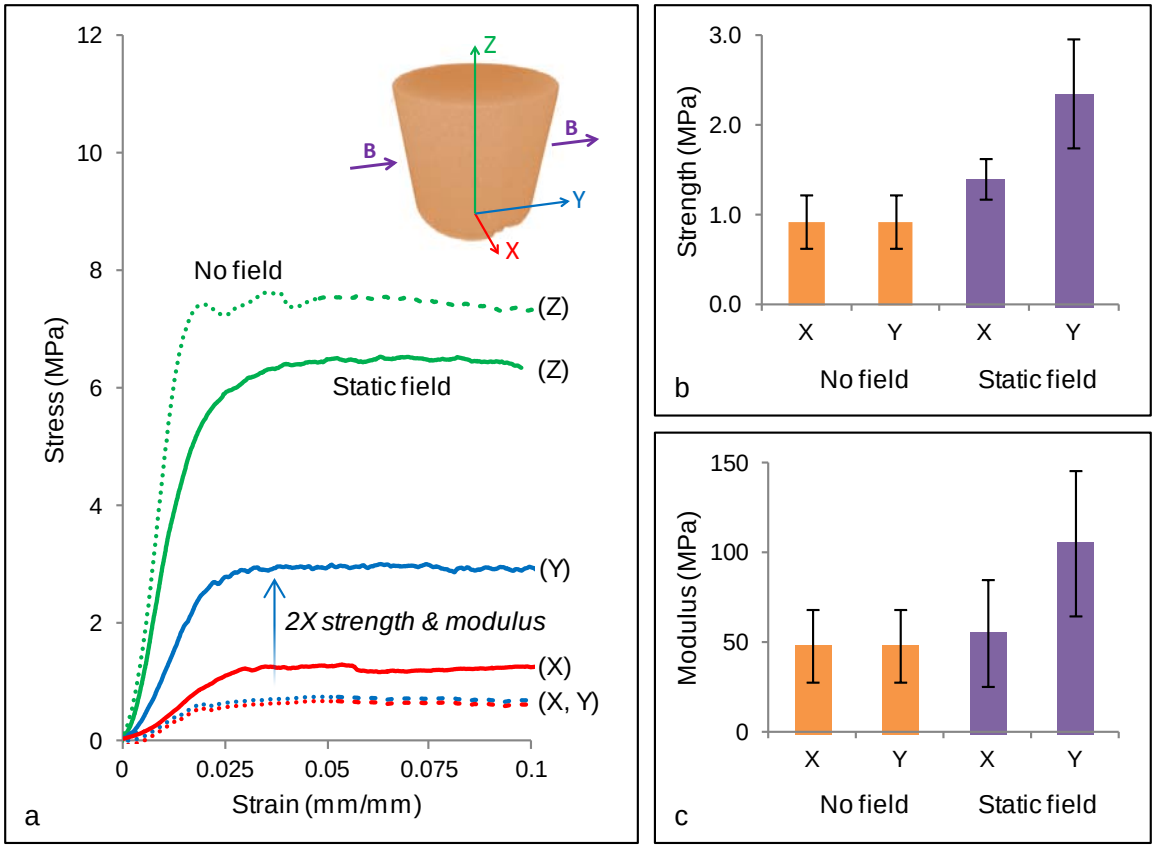

Figure 5.10. Compressive mechanical properties of TiO_2 scaffolds containing 3 wt% (~3 vol%) Fe_3O_4. **(a)** Representative stress-strain curves for the scaffolds made with no magnetic field (dotted lines) and a static magnetic field of 0.12 T (solid lines). Compression tests were performed in three directions (see top schematic): ice growth direction (Z, green), magnetic field direction (Y, blue), and transverse direction (X, red). **(b)** Ultimate compressive strength and **(c)** Young's modulus in the transverse XY-plane of the scaffolds made with no magnetic field (orange) and a static magnetic field of 0.12 T (purple).

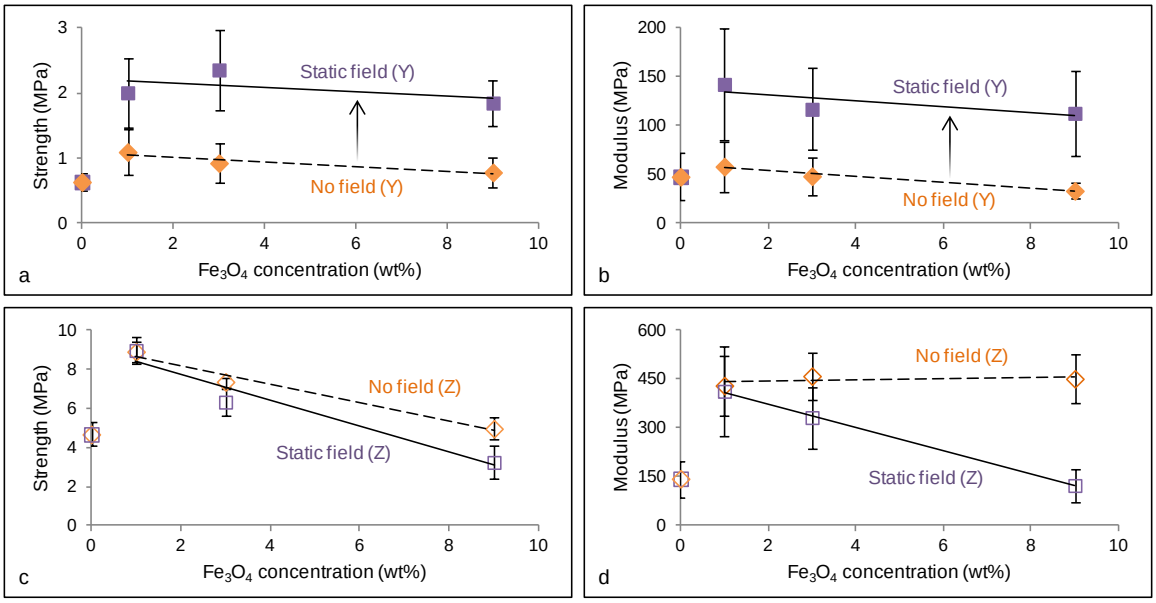

Figure 5.11. Compressive mechanical properties of TiO_2 scaffolds containing 0-9 wt% (0-8 vol%) Fe_3O_4 produced with no magnetic field (orange diamonds, dashed trend line) and a static magnetic field of 0.12 T (purple squares, solid trend line). **(a, b)** Ultimate strength and Young's modulus of scaffolds in the magnetic field direction (Y). Black arrows indicate an increase in strength and modulus in the transverse Y-direction due to the static magnetic field. **(c, d)** Ultimate strength and Young's modulus of scaffolds in the ice growth direction (Z).

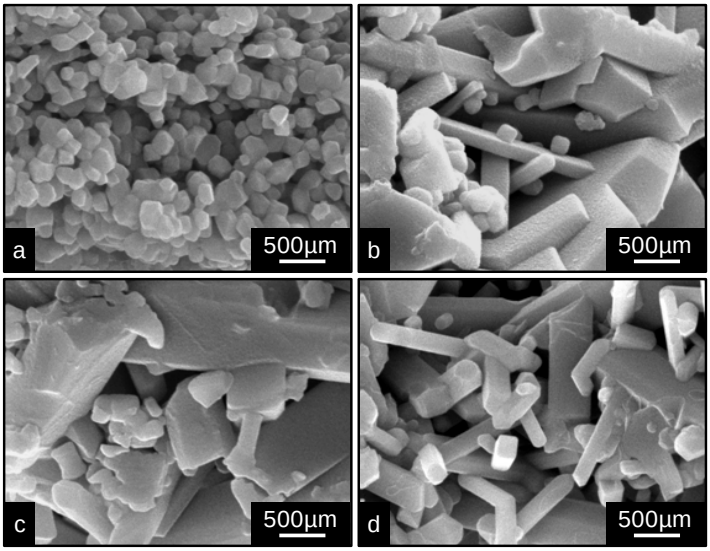

Figure 5.12. SEM micrographs of the lamellar wall surfaces of TiO_2 scaffolds sintered at 900°C, containing varying concentrations of Fe_3O_4: **(a)** 0 wt% Fe_3O_4; **(b)** 1 wt% (~1 vol%) Fe_3O_4; **(c)** 3 wt% (~3 vol%) Fe_3O_4; **(d)** 9 wt% (~8 vol%) Fe_3O_4.

size increase of nanocrystalline particles, which in turn, inhibits densification and diminishes the mechanical properties. Therefore, increasing the Fe_3O_4 concentration decreased the density, strength, and stiffness of the TiO_2 scaffolds in the ice growth direction, but not the magnetic field direction. The optimal concentration of Fe_3O_4 added to the TiO_2 scaffolds is ~1 wt%, since the mechanical properties are nearly doubled in the magnetic field direction (Y) and remain unchanged in the ice growth direction (Z) with the introduction of a static magnetic field of 0.12 T.

5.4. Conclusions

Magnetic field aligned freeze casting is a new method to fabricate anisotropic ceramic scaffolds with highly porous, directionally aligned microstructures. The addition of an external magnetic field to a conventional freeze casting unit allows the interconnected pore channels to be aligned in two directions: (1) the ice growth direction and (2) the magnetic field direction.

A variety of ceramic materials can be freeze cast into porous scaffolds. Under the influence of a weak magnetic field (0.12 T), the inter-particle interactions between the Fe_3O_4 nanoparticles and the host ceramic (hydroxyapatite (HA), ZrO_2, Al_2O_3, or TiO_2) determine the final microstructures and mechanical properties of the freeze cast scaffolds. Fe_3O_4 was well distributed throughout the TiO_2 scaffolds, but separated into distinctly different phases in the HA, ZrO_2, and Al_2O_3 scaffolds. The TiO_2 scaffolds fabricated with a static magnetic field showed channel alignment in, not only the ice growth direction, but also the magnetic field direction. The directional order induced by the static field doubled both the strength and modulus in magnetic field direction of the TiO_2 scaffolds

containing 1-9 wt% Fe_3O_4. The mechanical properties in the ice growth direction decreased by adding a magnetic field and increasing the Fe_3O_4 concentration. Even so, the loss in strength and stiffness in the ice growth direction was insignificant compared to the gain measured in the magnetic field direction at low Fe_3O_4 concentrations (1 wt%).

The concept of magnetic freeze casting may be used in a variety of future applications. The magnetic field strength and rotation speed may be adjusted to introduce varying degrees of micro-/macro-channel alignment or spiraling regions of high-density reinforced perimeters (Figure 5.9b) to make scaffolds with exceptional torsional rigidity. Scaffolds composed of feeble magnetic ceramics, such as HA or Al_2O_3, may be aligned similar the TiO_2 scaffolds reported here by coating magnetic nanoparticles before freezing. High aspect ratio nanowires or nanotubes may be added and aligned in a ceramic slurry to create "nano-bridges" between adjacent lamellae for enhanced strength and toughness. Conductive nanostructures, such as carbon nanotubes or metallic nanoparticles, may be added and aligned to improve the conductivity of scaffolds for potential electronic and energy storage devices. Finally, magnetic hybrid composites could be fabricated as high-performance, multifunctional materials for a variety of structural or medical applications.

5.5. Acknowledgements

Chapter 5, in full, is published in *Materials Science and Engineering: A* and co-authored by M. Yeh, J. Strawson, T. Goehring, S. Lujan, P. Siripasopsotorn, M.A. Meyers, and J. McKittrick of UCSD.

CHAPTER 6:

TORSIONAL PROPERTIES OF HELIX-REINFORCED COMPOSITES FABRICATED BY MAGNETIC FREEZE CASTING

6.1. Introduction

Helices are found in a variety of natural structures [364], such as the stems of woody plants [365], the skeletons of silica sponges [366], and the tusks of narwhals [367]. These naturally occurring structures grow in response to external stresses and provide reinforcement against induced torsion. Similarly, the double-helix structure of DNA governs its torsional rigidity, an important property that determines its superhelix, tertiary structure [368]. Unlike spirals that have a continuously increasing radius of curvature, such as those commonly found in mollusk shells [369, 370] and the horns and antlers of many ruminant mammals [371], helices have a constant radius of curvature and propagate along a central axis [364]. The growth, morphology, and mechanical advantage of spirals and helices observed in natural structures have fascinated scientists for decades [372, 373]. Skalak *et al* [372] and Harary and Tal [374] developed mathematical models to describe, respectively, the surface growth and morphology of several biological ultrastructures, such seashells, horns, and antlers. At the microstructural level, another form of the helix present in many natural materials is the twisted-plywood or Bouligand structure [148]. This helicoidal structure has been observed in the exoskeletons of crustaceans [51, 144, 147] and the scales of fish [55, 145]. Recently, it was reported that the twisted nature of the fibrous layers in these materials is mechanically advantageous, enhancing their impact resistance and fracture toughness [51, 55].

In modern architectural design, both spirals and helices appear in a variety of synthetic structures, primarily for their natural beauty. However, the helix is also an efficient mechanical design that provides an optimal distribution of stresses in structures subjected to torsional loading (e.g., torsion springs) [375]. Drawing inspiration from this natural design principle, engineering materials that are subjected to external torques may benefit from similar helix-reinforced architectures. Few attempts to utilize the helix for enhanced torsional rigidity in synthetic materials have been reported. Apichattrabrut and Ravi-Chandar [376] and Cheng *et al* [377] fabricated helicoidal fiber-reinforced composites that exhibited improved damage tolerance in response to tension, bending, and impact. However, the torsional rigidity of the composites was not investigated [376, 377]. Several patents [378-382] on helical reinforced materials have been filed as well. However, to the best of our knowledge, only the torsion transmitting glass shaft invented by Rodgers and Howald [382] utilizes helix-reinforced architectures to improve the torsional rigidity of cylindrical shafts.

Recently, Porter *et al* [88] invented a novel materials processing method, known as magnetic freeze casting, to fabricate ceramic scaffolds with helical architectures. This technique expands on conventional freeze casting - a popular method in which a colloidal suspension, typically composed of ceramic particles and water, is directionally frozen, then sublimated to remove the frozen solvent, and sintered to partially densify and strengthen the porous constructs [90, 121]. During solidification, the particles are pushed between and trapped within growing ice crystals, leading to lamellar pore channels that are direct replicas of the frozen solvent [90, 121]. Subsequently, the porous ceramics can be infiltrated with polymers or metals [75, 82, 84, 243], yielding hybrid composites with

hierarchical architectures that mimic the natural features of bone (e.g., osteons) or abalone nacre (e.g., brick-and-mortar structures). Although many freeze cast materials exhibit high strength and toughness [75, 80, 84], these properties are generally limited to a single direction - parallel to the direction of ice growth.

Magnetic freeze casting uses magnetic fields to manipulate magnetic nanoparticles (i.e., Fe_3O_4) during solidification. This process steers ceramic particles in the direction of the magnetic flux path. Previously, this method was shown to enhance the compressive strength and stiffness of ceramic scaffolds perpendicular to the direction of ice growth, parallel to an applied magnetic field [88]. The enhanced compressive properties obtained are due to the microstructural alignment of lamellar walls in two perpendicular directions: (1) the ice growth direction and (2) the magnetic field direction. In the same study [88], several cylindrical scaffolds with helical architectures were fabricated by rotating magnetic fields about the solidification direction. These scaffolds exhibited biphasic material properties. A circumferential helix composed of a higher-density, Fe_3O_4-rich phase surrounded an interior lower-density, Fe_3O_4-poor phase. The helix was composed of dense lamellar walls aligned parallel to the direction of the prevailing magnetic field. It was proposed that this helical architecture may act as a reinforcing structure, enhancing the torsional rigidity or shear modulus of the material [88, 90].

We show herein, both experimentally and analytically, that these helical architectures enhance the torsional rigidity of magnetic freeze cast composites. To do this, it is necessary to compare the shear modulus of composites having identical material compositions, with and without helical architectures. Although several shear test methods

currently exist [383, 384], the solid-rod torsion test was selected for this work [385]. Previous investigations show that the torsion test is best suited to induce a state of pure shear stress in cylindrical composite samples [385, 386]. The method predicts both the shear strength and stiffness of a material from a single test [385, 386]. In addition, torsion testing minimizes local material and stress concentration effects as well as unwanted bending moments due to slight misalignments of the samples [385, 386]. Experimental measurements of the torsional rigidity (i.e., shear modulus) versus the angle of helix-reinforcement were compared to determine an optimal angle of reinforcement.

6.2. Materials and Methods

6.2.1. Magnetic freeze casting setup

Helix-reinforced composite samples were prepared using a custom built freeze cast unit and rotating permanent magnet as previously described [88]. Figure 6.1 shows a picture of the magnetic freeze casting setup. Briefly, the freeze cast unit consists of a copper cold finger immersed in a liquid nitrogen bath. A band heater and thermocouple linked to a PID controller are attached to the copper cold finger in order to control the cooling rate of the copper surface at the bottom of a polyethylene (PE) mold with a 9 mm inner diameter. The rotating permanent magnet is constructed from a 1.32 T neodymium rare earth magnet, grade N42 ($2.5 \times 10 \times 10$ cm^3) (Applied Magnets, Plano, TX). Two cast iron channel arms, threaded stainless steel rods, and cast iron flux path distributors are attached to the neodymium magnet to direct and concentrate the magnetic flux path through the PE mold perpendicular to the ice growth direction (Z-axis). The magnetic field strength was kept constant for all experiments at 0.12 T. The permanent magnet

device was hung by a vertical aluminum shaft connected to a 3 V, 1.6 A, 1.65 N-m geared bipolar stepper motor (RobotShop Inc., Swanton, VT), controlled by an electronic user interface, Arduino Uno-R3 (SparkFun Electronics, Boulder, CO), capable of rotating the magnet 0.05-0.40 rpm about the *y*-axis.

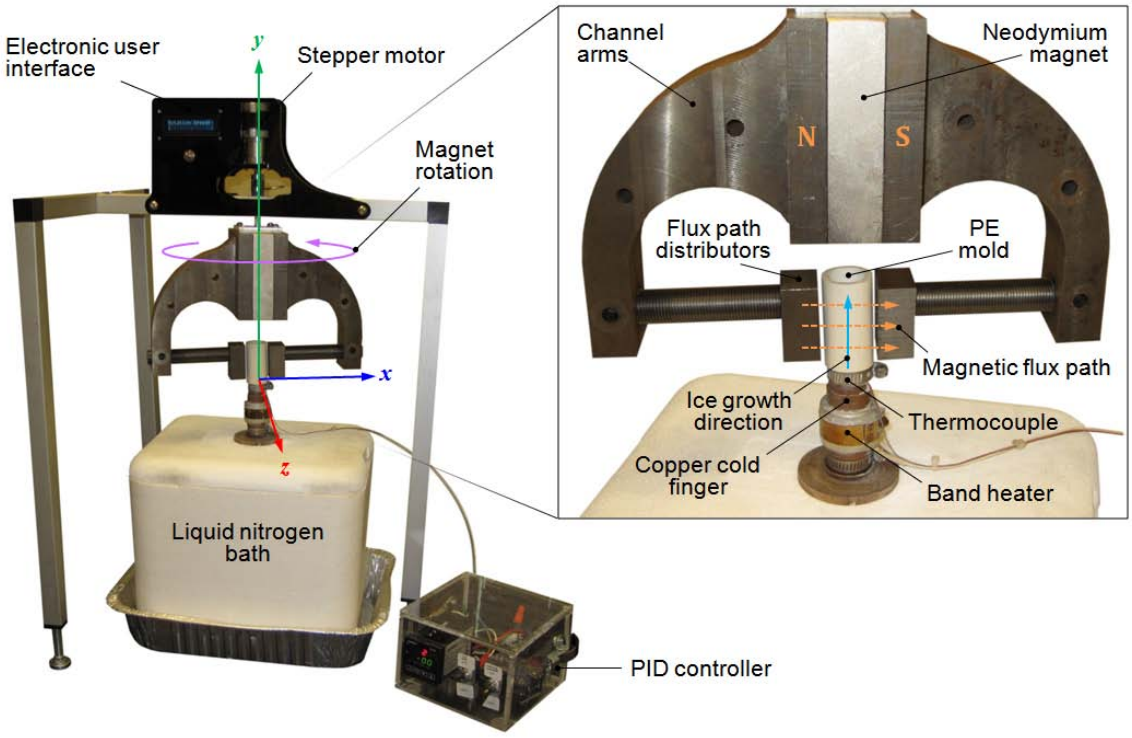

Figure 6.1. Magnetic freeze casting apparatus, illustrating the magnet rotation, ice growth, and magnetic flux path directions. The direction normal to the ice growth (*y*-axis) and magnetic flux path (*x*-axis) directions is represented by the *z*-axis.

6.2.2. Sample preparation

Aqueous slurries of 10 vol.% or 20 vol.% ZrO_2 powders (Sigma Aldrich, St. Louis, MO), with an average diameter of 0.2-0.5 μm, were mixed with 3 wt% (of the total solids) Fe_3O_4 nanoparticles (Sigma Aldrich, St. Louis, MO), with an average diameter of ~50 nm, and 1 wt% of each: organic binders, polyethylene glycol (PEG) (Alfa Aesar, Ward Hill, MA) and polyvinyl alcohol (PVA) (Alfa Aesar, Ward Hill, MA), and an ammonium polymethacrylate anionic dispersant, Darvan® 811 (R. T. Vanderbilt Company, Inc. , Norwalk, CT). The slurries were ball milled in an alumina grinding medium for 24 hr, followed by degassing under low vacuum for 10-20 min. Approximately 3 mL of the degassed slurries were poured into the PE mold and frozen at a constant rate of 10°C/min. During solidification, a magnetic field of 0.12 T was rotated about the ice growth direction (Z-axis) at 0.05 rpm, 0.20 rpm, or 0.40 rpm, resulting in the helix-reinforced architectures. After freezing, the samples were removed from the mold and lyophilized in a bench-top freeze dryer (Labconco, Kansas City, MO) at -50°C and 350 Pa for 72 hr. The porous green constructs were then sintered in an open air furnace for 3 hr at 1300°C with heating and cooling rates of ±2°C/min.

Following the sintering process, the porous scaffolds were infiltrated with epoxy (EpoxiCure Resin, Buehler, Lake Bluff, IL), resulting in ceramic-polymer composites with varying volume fractions and angles of helix-reinforcement. To infiltrate the scaffolds, the two-part epoxy solution was first mixed thoroughly for 2-3 min. Then, the porous scaffolds were immersed in the liquid epoxy solution and subjected to a low vacuum for 30 min to degas the solution and infiltrate the scaffolds. After complete infiltration, the wet samples were removed from the liquid epoxy and set at room

temperature for 24 hr, allowing the epoxy to harden and cure. For clarity, even though the ceramic phase of all the composites contains 3 wt.% Fe_3O_4, it is simply referred to as ZrO_2 throughout this study.

6.2.3. Material characterization

Scanning electron microscopy (SEM) images were taken at 15 kV on a Philips XL30 field emission environmental scanning electron microscope (FEI-XL30, FEI Company, Hillsboro, OR). For SEM preparation the samples were sputter-coated with iridium using an Emitech K575X sputter coater (Quorum Technologies Ltd., West Sussex, UK).

The thicknesses and angles of helix-reinforcement and the relative volume fractions of the ZrO_2 and epoxy phases of the composites were measured from optical images and scanning electron micrographs using ImageJ software (National Institutes of Health, Bethesda, MD). The helices were measured from optical images using the segment and angle measurements tools. The relative volume fractions were measured from the cross-sections of the composites, where the thresholds of SEM images were adjusted equally to measure the % area of each phase. Four different locations across each cross-section were measured to determine the distribution of densities caused by the rotating magnetic fields.

X-ray diffraction (XRD) was performed on a D2 Phaser X-ray diffraction tool (Bruker AXS, Madison, WI). XRD experiments confirmed that the crystal structure of the ZrO_2 phase remained monoclinic before and after sintering, while a small portion of the Fe_3O_4 phase transformed from magnetite (Fe_3O_4) before sintering to hematite (Fe_2O_3)

after sintering at 1300°C. No apparent transformation due to interactions between the ZrO_2 and Fe_3O_4 phases was observed.

6.2.4. Torsion testing

The torsional properties of the ZrO_2-epoxy composites with varying volume fractions and different angles of helix-reinforcement were compared using the solid-rod torsion test. The torsion tests were performed on a custom built torsion testing device, capable of twisting the cylindrical composites to induce a state of pure shear stress (see Appendix).

To test the samples in torsion, the cylindrical ZrO_2-epoxy composites were aligned and mounted in epoxy "grips" using a custom built mounting device. All the composite samples were fabricated such that the regions of interest have a circular cross-section of radius r_s (~7.5 mm) and length L_s (~25 mm). The epoxy grips of the samples have square cross-sections 24.5 mm x 24.5 mm with lengths of L_g (~ 25 mm), fitting neatly into the square mounts of the torsion tester. Refer to the Appendix for a complete description of the torsion testing setup and calibration.

Using an empirically derived calibration constant (C = 9.03×10^{-4}) and the measured shear modulus of the epoxy grips (G_g = 1.0 GPa), the ultimate shear stress and shear strain at the surface of the ZrO_2-epoxy composites were plotted from the experimental data (refer to Appendix). For simplicity, micromechanics describing the complex nature of the freeze-cast microstructures and the helix-reinforcements were ignored. Instead, the ZrO_2-epoxy composites were modeled as orthotropic, elastic materials with unidirectional-reinforcement, similar to that reported by Adams and

Thomas [385] and Hamed *et al* [387]. Because torsion testing a homogeneous cylinder generates stresses and strains that vary linearly from the central axis of rotation to the outer surface, the maximum shear stress and shear strain occur on the surface of the cylindrical samples. Thus, their ratio, G (shear modulus), is constant, and therefore, provides an accurate description of the torsional rigidity. These assumptions are necessary to compare the effects of ceramic content and helix-reinforcement in the cylindrical composites. Duplicates of each torsion test were run to ensure repeatability.

6.3. Results and Discussion

6.3.1. Architectural hierarchy

Figure 6.2 shows the profiles and cross-sections of eight different ZrO_2-epoxy composites fabricated by magnetic freeze casting. As seen in the figure, the two different solid loadings of ZrO_2 (10 vol.% and 20 vol.% suspensions) used during the freeze casting process resulted in two sets of composites with varying volume fractions of ZrO_2 and epoxy. For clarity, the two sets are referred to as 40:60 and 60:40 composites corresponding to the ZrO_2 and epoxy contents, respectively. That is, the 40:60 composites contain ~40 vol.% ZrO_2 and ~60 vol.% epoxy, while the 60:40 composites contain ~60 vol.% ZrO_2 and ~40 vol.% epoxy (refer to Table 6.1). The composites have four levels of structural hierarchy: (1) the helix-reinforcement due to the rotating magnetic fields (Figures 6.3a-c); (2) the microstructural alignment due to freeze casting (Figures 6.3d and 6.3e); (3) the layered ZrO_2-epoxy interface due to polymer infiltration (Figure 6.3f); (4) the ZrO_2 grain structure after sintering and polymer infiltration (Figure 6.3f).

Table 6.1. Material properties of the aluminum (Al 6061-T6), epoxy, and ZrO_2-epoxy composites, showing the rotation speed of the magnetic field and the resulting helix angle, the average ZrO_2 volume fraction and the ZrO_2 volume fractions of the helix-reinforced (A) and non-reinforced (B) regions corresponding to Figure 6.2, the twist direction, and the mechanical shear properties.

Sample type	Rotation speed (rpm)	Helix angle (degrees)	ZrO_2 fraction (vol.%)			Twist direction	Shear strength [b] (MPa)	Shear modulus [b] (GPa)
			Average [a]	A	B			
Al 6061-T6	---	---	---	---	---	CW	207 ± 6	26.0 ± 1.2
Epoxy	---	---	---	---	---	CW	48 ± 2	1.0 ± 0.1
ZrO_2-epoxy composites (40:60)	No field	---	37 ± 4	---	---	CW	36 ± 0	2.5 ± 0.5
	0.05	42	38 ± 10	47	29	CW	37 ± 2	3.1 ± 0.3
	0.20	73	36 ± 5	41	32	CW	46 ± 7	2.8 ± 0.3
	0.40	84	37 ± 6	42	32	CW	48 ± 1	2.6 ± 0.4
ZrO_2-epoxy composites (60:40)	No field	---	58 ± 4	---	---	CW	30 ± 5	2.8 ± 0.8
	0.05	42	59 ± 5	62	55	CW	51 ± 13	5.5 ± 0.7
	0.20	73	57 ± 5	61	54	CW	46 ± 3	4.8 ± 0.7
	0.40	84	59 ± 7	65	53	CW	54 ± 2	4.3 ± 0.5
	0.05	42	63 ± 2	65	61	CCW	35 ± 10	2.8 ± 0.6

[a] measurements recorded as average ± standard deviation (n = 4);
[b] measurements recorded as average ± standard deviation for Al 6061-T6 (n = 6) and epoxy (n = 6), and average ± the range of duplicates for ZrO_2-epoxy composites (n = 2).

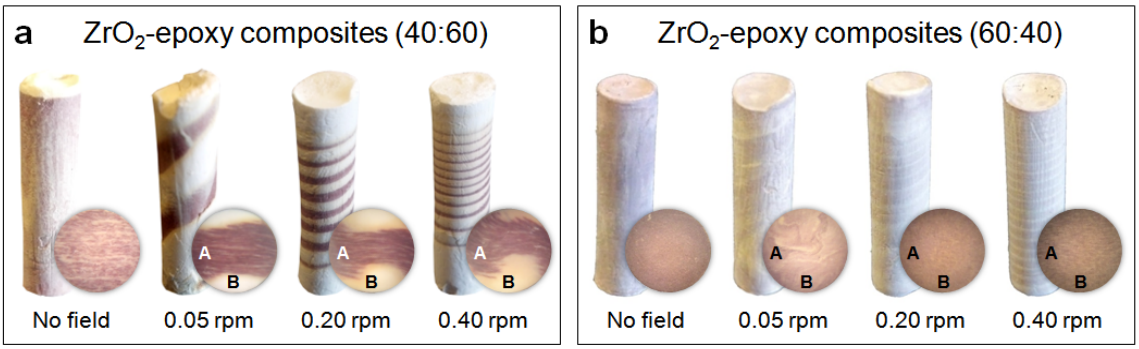

Figure 6.2. Representative images of the profiles and cross-sections of the ZrO_2-epoxy composites freeze cast under a rotating magentic field of 0.12 T at the varying rotation speeds shown. **(a)** ZrO_2-epoxy composites composed of ~40 vol.% ZrO_2 and ~60 vol.% epoxy. **(b)** ZrO_2-epoxy composites composed of ~60 vol.% ZrO_2 and ~40 vol.% epoxy. The letters "A" and "B" shown on the cross-sections represent the Fe_3O_4-rich helix-reinforced regions and Fe_3O_4-poor non-reinforced regions, respectively. The diameters of all the composites are ~7.5 mm.

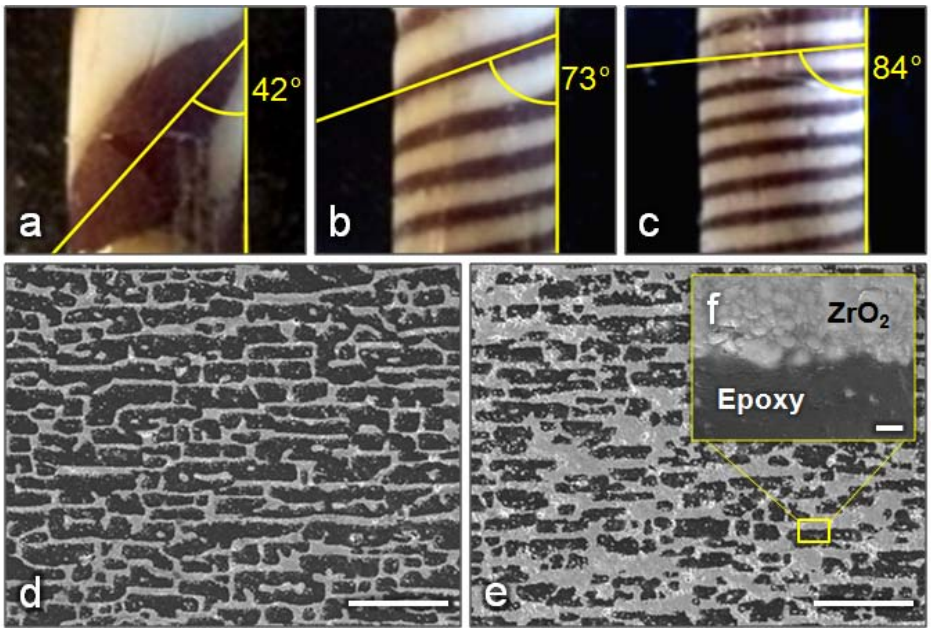

Figure 6.3. Architectural hierarchy of the ZrO_2-epoxy composites: **(a-c)** Representative images of 40:60 composites, illustrating the angle of helix-reinforcement freeze cast under a rotating magnetic field of 0.12 T at varying rotation speeds: **(a)** 0.05 rpm; **(b)** 0.20 rpm; **(c)** 0.40 rpm. **(d-f)** Representative SEM images of the composites freeze cast under a rotating magnetic field of 0.12 T at 0.20 rpm: **(d)** 40:60 composites; **(e)** 60:40 composites; **(f)** magnified image of the ZrO_2-epoxy interface. The light color is the ZrO_2 phase and the dark color is the epoxy phase. (d,e) The scale bars are 50 μm. (f) The scale bar is 1μm.

The distribution of the Fe_3O_4-rich (brown color) and Fe_3O_4-poor (white color) phases in the cross-sections of the composites varies considerably (see Figure 6.2), while the volume fractions of the two phases on the outer surface were approximately equal ($V_A = V_B = 0.5$). Figures 6.3a-c show magnified images of the 40:60 composites illustrating the different angles of helix-reinforcement. Increasing the rotation speed of the magnetic field increased the angle, but decreased the thickness of the helices. That is, the 40:60 composites fabricated with a rotating magnetic field at 0.05 rpm had helices ~4 mm thick oriented at an angle of 42°, while those at 0.20 rpm were ~1 mm thick at 73°

and those at 0.40 rpm were ~0.5 mm thick at 84°. Similar to that observed by Porter *et al* [88], the 40:60 composites showed a distinct separation of the two phases, resulting in biphasic material properties. The Fe_3O_4 phases in the 60:40 composites, on the other hand, were more homogeneously distributed. However, both sets of composites contain larger volume fractions of ZrO_2 in the helical regions. Thus, the helices are more dense and expected to reinforce the structures. Table 6.1 contains the average volume fractions of ZrO_2 in each composite as well as the distribution of ceramic content in the helix-reinforced and non-reinforced regions (respectively labeled as regions A and B, corresponding to Figure 6.2). As seen from the data in Table 6.1, the 40:60 composites contain ~10-15 vol.% more ZrO_2 in the helix-reinforced regions (A) than the non-reinforced regions (B), while the 60:40 composites contain only ~5-10 vol.% more ZrO_2 in the helix-reinforced regions (A) than non-reinforced regions (B).

Figures 6.3d-f show representative SEM images of the ZrO_2 scaffolds after infiltration with epoxy, showing the difference in microstructure and ceramic content in the Fe_3O_4-poor regions of the 40:60 composites (Figure 6.3d) and 60:40 composites (Figure 6.3e). Similarly, the microstructures of the Fe_3O_4-rich regions resemble those shown in Figure 6.3d and 6.3e, with slightly higher ceramic contents and some degree of lamellar wall alignment as previously described by Porter *et al* [88]. Figure 6.3f shows that the infiltrated epoxy is well bonded to the ZrO_2 scaffolds, completely filling the open porosity. However, the epoxy did not fill any remaining closed porosity existing in the interior of the lamellar walls after sintering the ZrO_2 scaffolds. These structural characteristics, namely the helix-reinforcement angle and the relative volume fractions of ZrO_2, affect the torsional properties of the composites.

6.3.2. Torsional properties

Because the ZrO_2-epoxy composites are reinforced by a single, continuous helix oriented in a right-handed or clockwise (CW) fashion (from the bottom up), the torsional properties of the composites are significantly different depending on the direction of applied torque and the angle of reinforcement. Similarly, the off-axis mechanical behavior of fiber-reinforced laminate composites are dependent on the direction of applied stress and the angle of fiber reinforcement [150]. Therefore, it is convenient to analyze the stress state at the outer surface of the helix-reinforced composites in an analogous fashion to that of a unidirectionally-reinforced plate.

6.3.2.1. Direction of applied torque

Figure 6.4a compares three 60:40 composites: one with no helix-reinforcement and two with identical helix-reinforcement angles of 42° twisted CW and counterclockwise (CCW) (see Table 6.1 for details). The helix-reinforced composite that was twisted in a CCW fashion shows little to no improvement over the composite without helix-reinforcement. However, when twisted in the CW direction, the 42° helix provides a significant amount of reinforcement, with nearly twice the effective shear modulus (refer to Table 6.1).

This result is due to the fact that torsion testing induces a state of pure shear stress in the cylindrical samples, as illustrated in Figures 6.4b and 6.4c. Accordingly, the maximum compressive and tensile stresses occur on the surface of the cylindrical samples at ±45° (see Figures 6.4b and 6.4c). For isotropic materials, the shear modulus

(G) is proportional to the elastic modulus (E) and Poisson's ratio (ν), according to Equation 6.1:

$$G = \frac{E}{2(1+\nu)}. \tag{6.1}$$

Hence, the composite shear modulus can be considered proportional to its elastic modulus ($G \propto E$).

To verify the experimental results observed in Figure 6.4a, the direction of applied torque was analyzed according to the schematics shown in Figures 6.4b-e, where a composite with an angle of helix-reinforcement at 45° is twisted: (a) CW and (b) CCW. Assuming the applied torque induces a state of pure shear and plane stress at the surface of the cylindrical composites, the stress elements shown can be rotated 45° such that the maximum shear stresses (τ_{max}) become maximum compressive and tensile stresses (σ_C and σ_T, respectively), as illustrated in Figures 6.4b-e. Now, it becomes convenient to apply the rule-of-mixtures to resolve the compressive and tensile elastic moduli of the composites in directions parallel and perpendicular to the helix-reinforcement [150]. Because the composites are composed of two continuously interpenetrating networks of ZrO_2 and epoxy, the compressive stiffness (E_C) is dominated by the elastic modulus of the ZrO_2 phase, while the tensile stiffness (E_T) is dominated by the ZrO_2-epoxy interfacial adhesion (i.e., interfacial shear or tensile strengths). This suggests that the compressive modulus is much greater than, and dominates, the tensile modulus, such that $E_C \gg E_T$. Therefore, according to the Voigt and Reuss models for unidirectionally-reinforced composite materials [388], and neglecting the tensile moduli, the compressive moduli of the composites can be represented as follows (refer to Figures 6.4d and 6.4e):

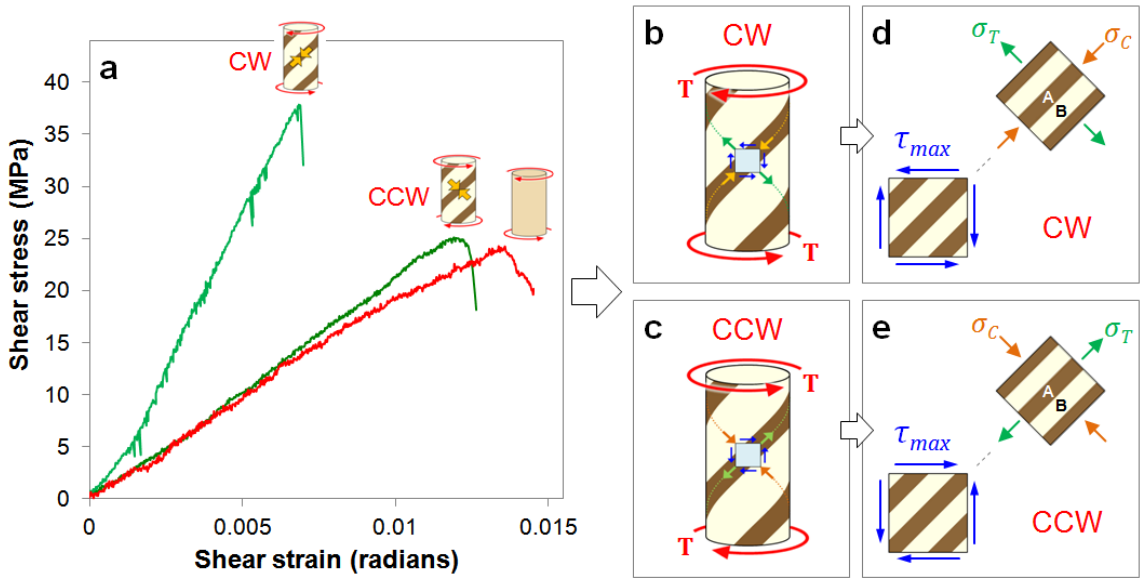

Figure 6.4. (a) Surface shear stress-strain curves illustrating the torsional behavior of ZrO_2-epoxy (60:40) composites twisted in different directions. The green curves correspond to 42° helix-reinforced composites and the red curve corresponds to a composite without helix-reinforcement. The helix-reinforced composite was nearly twice as rigid in torsion when twisted in the clockwise (CW) direction, as opposed to the counterclockwise (CCW) direction. **(b-c)** Schematics of helix-reinforced composites subjected to a torque (T) rotated: **(b)** CW and **(c)** CCW. **(d-e)** Schematics of a unidirectionally-reinforced plate, illustrative of a stress element at the outer surface of the cylindrical composites, subjected to pure shear and plane stress when twisted: **(d)** CW and **(e)** CCW. The representative stress elements are rotated such that the pure shear stresses (τ_{max}) become pure compressive and tensile stresses (σ_C and σ_T, respectively). The letters "A" and "B" represent the helix-reinforced regions (brown) and non-reinforced regions (white), respectively.

(d) The compressive modulus *parallel* to the helix-reinforcement dominates when the applied torque is in the CW direction (Voigt model):

$$E_{CW} = V_A E_A + V_B E_B \tag{6.2}$$

(e) The compressive modulus *perpendicular* to the helix-reinforcement dominates when the applied torque is in the CCW direction (Reuss model):

$$\frac{1}{E_{CCW}} = \frac{V_A}{E_A} + \frac{V_B}{E_B} \tag{6.3}$$

where E_i is the compressive elastic modulus and V_i is the volume fraction of regions A and B, referring to the helix-reinforced and non-reinforced regions, respectively. As seen in Figures 6.4b-e, depending on the direction of applied torque, the maximum compressive stresses are oriented (a) parallel or (b) perpendicular to the direction of helix reinforcement. Assuming the increased content of ZrO_2 in the helix-reinforced regions increases the elastic modulus of these regions (E_A), it is concluded that the elastic modulus of the reinforced region is greater than the non-reinforced region ($E_A > E_B$). Thus, the composite must be stiffer when twisted in the CW direction, such that $E_{CW} > E_{CCW}$. Based on the assumption from Equation 6.1, providing that $G \propto E$, the shear modulus is significantly greater when the applied torque induces a maximum compressive stress parallel to the helix-reinforcement, such that $G_{CW} > G_{CCW}$. In conclusion, the experimental observations presented in Figure 6.4a agree with the results predicted by this simplified analysis.

6.3.2.2 Angle of helix-reinforcement

In addition to the direction of applied torque, the angle of helix-reinforcement also affects the torsional properties of the composites. To verify this, three composites from each set (40:60 and 60:40) with different angles of helix-reinforcement were twisted in the CW direction. Figure 6.5 shows the shear stress-strain curves for the 60:40 composites with helix-reinforcement angles of 42°, 73°, and 84°. Comparing the slopes (i.e., shear modulus) of the stress-strain curves, it is obvious that pure epoxy (orange curve in Figure 6.5) has the lowest shear modulus (slope) followed by the composite without helix-reinforcement (red curve in Figure 6.5), while the 42° composite (green curve in Figure 6.5) has the largest shear modulus (refer to Table 6.1). Figure 6.6a contains a plot of the measured shear modulus (G_{XY}) versus the angle of helix-reinforcement for both the 40:60 and 60:40 composites. As seen in this plot, it is clear the optimal angle of helix-reinforcement is at 45°. Analogous to the trends predicted by Hamed *et al* [387] for filament wound composite tubes, the shear modulus of the 60:40 composites with a reinforcement angle of ~45° (~6 GPa) is roughly twice that of the composites with reinforcement angles of 0° and ~90° (~3 GPa) (refer to Figure 6.6a). Moreover, increasing the volume fraction of ZrO_2 increased the global shear modulus of the composites, as shown in Figure 6.6a. This is because a larger fraction of ceramic in the helical region on the outer surface of the composites carries a greater amount of the induced maximum shear stresses, since the shear modulus of ZrO_2 is ~90 GPa [389], nearly 100 times greater than that of epoxy (~1 GPa).

Again, assuming a state of pure shear and plane stress at the surface of the cylindrical composites, the results shown in Figure 6.6a are confirmed by a modified

composite laminate theory, following Hyer [150] (refer to Appendix for complete analysis). Several assumptions were made to simplify the analysis (see Appendix). Two orthogonal coordinate systems were chosen according to the schematic in Figure 6.6b. The local material coordinates (1, 2, 3) are orthogonal and oriented such that the 1-axis is parallel to the direction of helix-reinforcement. The global material coordinates (X, Y, Z) are orthogonal and oriented such that the X-axis is in the circumferential direction, the Y-axis is parallel to the cylindrical axis (ice growth direction), and the Z-axis, equivalent to the 3-axis, is in the radial direction. The angle of helix-reinforcement (φ) is expressed as the angle, rotated about the Z-axis, between the cylindrical axis (Y-axis) and the reinforcement (1-axis), such that (refer to Figure 6.6b):

$$m = \cos\left(\frac{\pi}{2} - \varphi\right); \tag{6.4}$$

$$n = \sin\left(\frac{\pi}{2} - \varphi\right). \tag{6.5}$$

According to the analysis presented in the Appendix, the normalized shear modulus (G_{XY}/G_{12}) can be expressed in terms of the angle of helix-reinforcement and the material properties in the local coordinate system [150]:

$$G_{XY}/G_{12} = \frac{1}{m^4 + n^4 + 2m^2n^2\left(2\frac{G_{12}}{E_1}(1 + 2\nu_{12}) + 2\frac{G_{12}}{E_2} - 1\right)} \tag{6.6}$$

where G_{XY} is the effective shear modulus of the composite in the XY-plane, G_{12} and ν_{12} are the shear modulus and Poisson's ratio in the 12-plane, respectively, and E_1 and E_2 are the elastic moduli of the composite parallel and perpendicular to the helix-reinforcement, respectively, which can be approximated from Equations 6.2 and 6.3, such that $E_1 \propto E_{CW}$ and $E_2 \propto E_{CCW}$. Figure 6.6b shows a plot illustrating how the global shear modulus (G_{XY})

on the outer surface of the composites varies with respect to the angle of helix-reinforcement (φ), according to Equations 6.4-6.6. This trend was plotted by ignoring the effect of Poisson's ratio ($\nu_{12} = 0$) and approximating the elastic properties in the local coordinate system as follows: $E_1 = E_{CW}$, $E_2 = E_{CCW}$, and $G_{12} = E_2/2$ (refer to Equations 6.1-6.3), where $V_A = V_B = 0.5$ and $E_A = 10 > E_B = 1$. As seen in the plot, the maximum value of the normalized shear modulus (G_{XY}/G_{12}) occurs at an angle of helix-reinforcement of 45°, in agreement with the experimental results (Figure 6.6a).

Another interesting phenomenon observed in Figure 6.5 is that the shear strength of the composites increases as the helix-reinforcement angle increases. This can be explained by the fact that brittle materials subjected to torsion fail in the direction of maximum tension, at 45° to the axis of rotation (refer to Figures 6.4b and 6.4c). Most likely, as the angle of the helix-reinforcement approaches 90°, the higher-density, helix-reinforced region deflects or redirects the tensile stresses that occur along the surface of the cylindrical samples. Accordingly, the composites with helix-reinforcement angles at 42° have the lowest shear strength because the helical interface at the Fe_3O_4-rich and Fe_3O_4-poor phases is the weakest point of the structure. When this interface is oriented perpendicular to the maximum tensile stresses, brittle failure occurs at the interface, as explained in the following section.

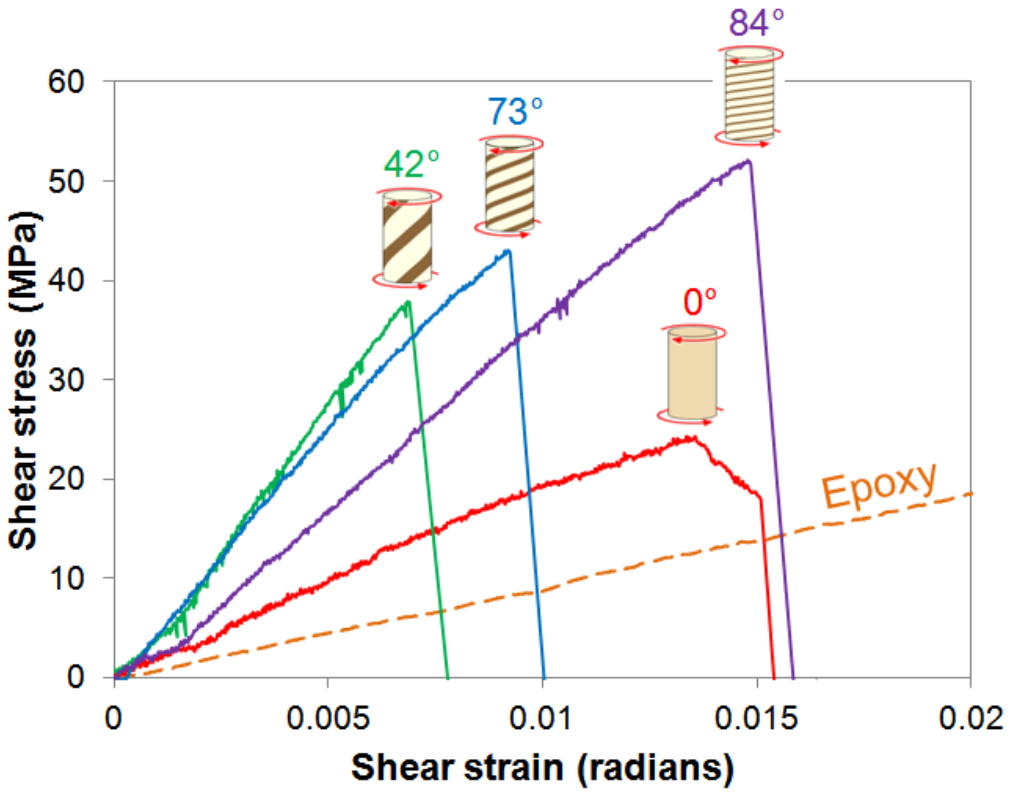

Figure 6.5. Surface shear stress-strain curves illustrating the torsional behavior of ZrO_2-epoxy (60:40) composites with different angles of helix-reinforcement. The different curves correspond to the different angles of reinforcement, illustrating that the shear modulus (slope) increases as the angle of reinforcement approaches 45°, while the shear strength (maximum stress) increases as the angle of reinforcement appraoches 90°. The dashed orange line shows the slope of pure epoxy subjected to torsion.

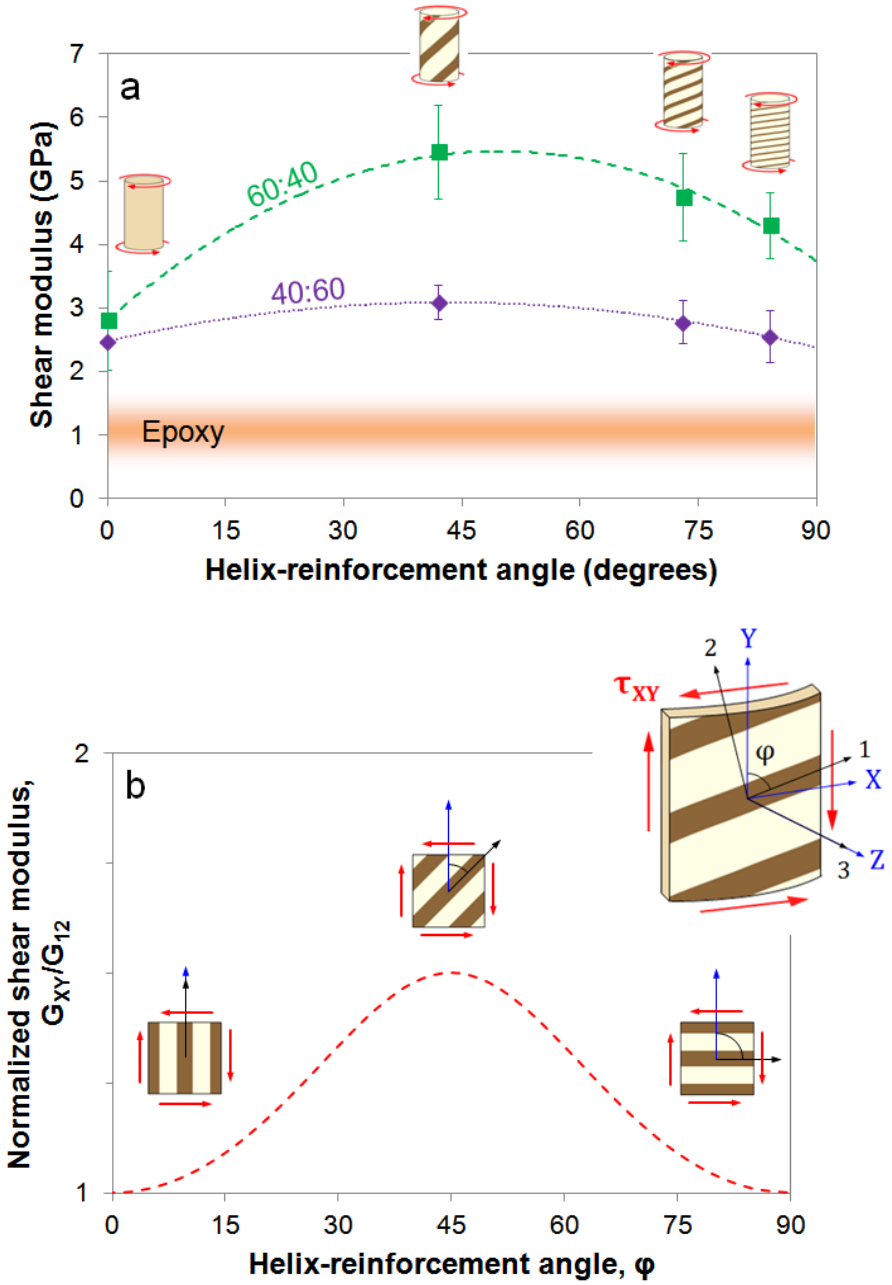

Figure 6.6. (a) Plot of the experimental average shear modulus versus the angle of helix-reinforcement for the 60:40 composites (dashed green line) and the 40:60 composites (dotted purple line). The error bars represent the range of data collected for the duplicate samples (n = 2). **(b)** Schematic of the global (X, Y, Z) and local (1, 2, 3) coordinate systems (upper righthand corner), illustrating the angle of helix-reinforcement (φ) and direction of applied shear stress (τ_{XY}). The plot shows the theoretical normalized shear modulus (G_{XY}/G_{12}, Equations 6.4-6.6) versus helix-reinforcement angle (φ), assuming the outer surface of the composites as a unidirectionally-reinforced plate subjected to pure shear and plane stress.

6.3.3. Fracture behavior

In torsion, brittle materials typically fail along a 45° angle in the direction of maximum tension (refer to Figures 6.4b and 6.4c). Ductile materials, on the other hand, typically fail in the direction of maximum shear, at an angle of 90° to the rotation axis of the applied torque. Figures 6.7a-h show the fracture surfaces of the ZrO_2-epoxy composites. Accordingly, all of the composites fractured at 45° to the rotation axis, perpendicular to the induced maximum tensile stresses (regardless of the twisting direction), suggesting brittle failure. However, upon closer observation of the crack paths (Figures 6.7i-l), it appears that some degree of brittle as well as shear failure occurs in the different composites. Most notably, Figures 6.7j and 6.7k show interesting phenomena. In the 42° helix-reinforced composites (Figure 6.7j), failure occurs at the interface between the helix-reinforced and non-reinforced regions, in the direction of the induced maximum tensile stress. Therefore, the interface separating the two phases (i.e., Fe_3O_4-rich and Fe_3O_4-poor) must be the weakest point of the structure in tension. In the 73° and 84° composites (refer to Figure 6.7k), the angle of the crack path deviates across each region. This suggests two modes of failure - brittle failure and shear failure - clearly observed in Figure 6.7k, and to a lesser extent in Figure 6.7l. As noted above, the shear strength of the composites increases as the angle of helix-reinforcement increases beyond 45°. Because the maximum tensile stresses induced by torsion are oriented at 45°, characteristic brittle failure seems to occur at the more stiff, but brittle, helix-reinforced (Fe_3O_4-rich) regions, while some instances of shear failure are observed across the non-reinforced regions (see Figure 6.7k). A possible explanation for this observed crack deflection is that brittle tensile failure in the reinforced regions occurs first and initiates post shear failure in the

non-reinforced regions, bridging the crack. This type of crack deflection is commonly observed in a variety of natural materials, such as bone and nacre [46], leading to enhanced strength and toughness.

The modes of failure observed result from mechanisms originating at the microstructural level (Figure 6.8). Tensile stresses cause delamination of the epoxy from the ZrO_2 as shown in Figure 6.8a. The debonding of the two phases concentrates local stresses through the ceramic walls, no longer allowing the epoxy to dissipate energy that accumulates between adjacent lamellae. The more prominent mode of failure observed in the composites is brittle fracture. Following delamination, the ceramic walls may be subjected to tensile or compressive stresses (depending on lamellae orientation and loading direction). In the direction of tensile loading, the lamellae exhibit brittle tensile fracture, while in the direction of compressive loading the lamellae buckle. Figure 6.8b shows a lamellar wall of ZrO_2 that has collapsed and crumbled due to brittle failure. In freeze cast ceramics, it is known that lamellar walls fail by local Euler buckling when subjected to compressive loading [89]. Therefore, after delamination, in the direction of maximum compressive stress, the ZrO_2 lamellae may buckle and collapse in a similar manner to that shown in Figure 6.8b. On the other hand, cracks that resemble shear failure (refer to Figure 6.7k) are caused by interlamellar shearing, which promotes crack propagation through the delaminated ceramic walls as they slide past each other. In conclusion, following delamination due to tensile stresses (Figure 6.8a), the brittle fracture behavior observed in the helix-reinforced composites (Figure 6.8b) is governed by two mechanisms occurring in the ceramic phase at the microstructural level: (1) brittle

fracture due to tensile or compressive loading of the lamellae and (2) interlamellar shearing of adjacent lamellae.

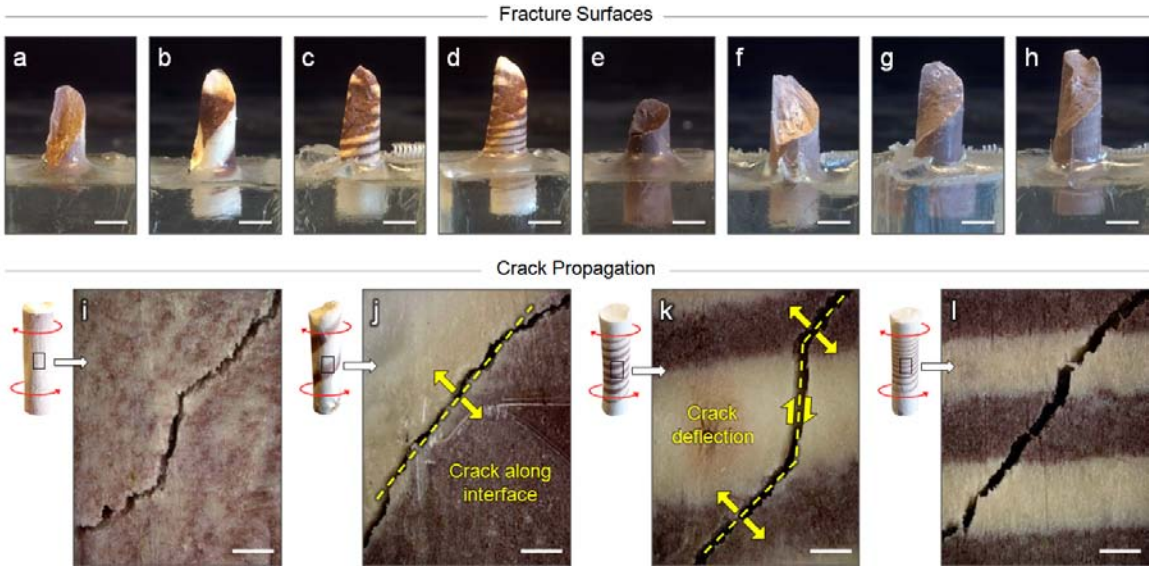

Figure 6.7. (Top) Images of the fracture surfaces of ZrO_2-epoxy composites loaded in torsion: **(a-d)** 40:60 composites; **(e-h)** 60:40 composites; **(a, e)** no magnetic field; **(b, f)** 42° helix-reinforcement; **(c, g)** 73° helix-reinforcement; **(d, h)** 84° helix-reinforcement. All scale bars are 5 mm. **(Bottom)** Representative images of the crack path and different failure mechanisms (yellow) due to the torsional loading of ZrO_2-epoxy (40:60) composites with different angles of helix-reinforcement: **(i)** no magnetic field; **(j)** 42°; **(k)** 73°; **(l)** 84°. Images of the cylindrical composites (left) show the direction of applied torque (red arrows) and magnified regions of interest (boxes). Scale bars are 500 μm.

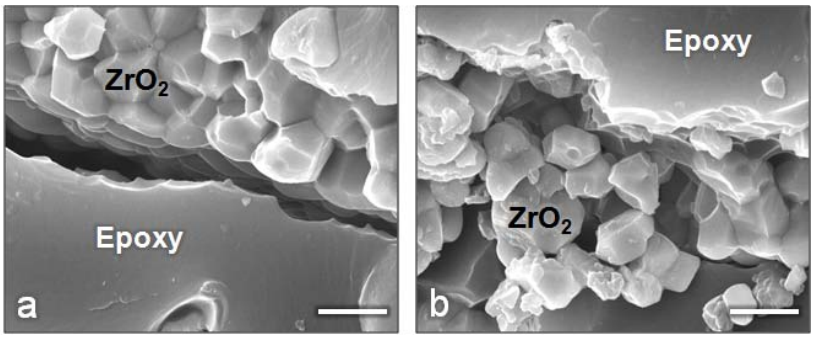

Figure 6.8. Fracture surfaces of the ZrO_2-epoxy composites, illustrating the two modes of failure: **(a)** delamination of the epoxy from the ZrO_2; **(b)** crumbling of the ZrO_2 lamellar walls due to brittle failure.

6.4. Conclusions

Helix-reinforced ZrO_2-epoxy composites fabricated by magnetic freeze casting and subsequent polymer (epoxy) infiltration exhibited exceptional torsional properties. Magnetic fields rotated at different speeds about the ice growth direction were applied to a freeze casting process to steer the magnetic nanoparticles during solidification. The composite materials had hierarchical architectures, with helices composed of higher-density ceramic regions oriented at different angles. Larger volume fractions of the ceramic phase (from ~40 vol.% to ~60 vol.%) nearly doubled the shear modulus of the composites. The helix-reinforced structures oriented at ~45° to the axis of applied torque provided the greatest torsional rigidity when twisted in the clockwise direction, such that the induced maximum compressive stresses propagated parallel to the helix-reinforcement. All of the materials exhibited brittle fracture, primarily governed by three failure mechanisms: delamination of the epoxy from the ZrO_2, brittle fracture of ZrO_2 lamellae, and interlamellar shearing of adjacent lamellae.

Hybrid composites with hierarchical architectures are promising structural materials for a variety of potential applications [84]. Introducing helix-reinforced structures, as an additional level of hierarchy, may prove beneficial for applications requiring enhanced torsional rigidity. Such applications may include cylindrical shafts used in torque converters for combustion engines and electric motors, sports equipment such as golf clubs or tennis racquets, and axles for wheeled vehicles. Other, less obvious technologies may also benefit from helix-reinforced structures. Freeze cast materials have been proposed as bone implants, having compressive strengths and stiffnesses that nearly match those of natural bone [75, 329]. For the practical use of these materials as bone

replacements, it becomes necessary to optimize all their mechanical properties, including the torsional rigidity. The method of magnetic freeze casting introduced here is an efficient means to accomplish this goal.

6.5. Appendix

6.5.1. Torsion testing and calibration

The ZrO_2-epoxy composites were tested in torsion using a custom built torsion testing device (Figure 6.9). The device was attached to the crossheads of a uniaxial Instron materials testing machine (Instron 3367, Norwood, MA) and converts the applied linear displacement of the crosshead to a rotational displacement through a rack and pinion (SR5-500 and SS5-40, Quality Transmission Components, Garden City Park, NY). The rack, attached to the upper crosshead, moves linearly with a tensile (or compressive) load (F) and displacement (d), recorded as a force and displacement by the data acquisition software (Bluehill 2, Instron, Norwood, MA). The linear motion of the rack turns the pinion, converting the applied linear motion to an applied torque (T) and angle of twist (ϕ), such that:

$$T = FR\cos\theta \tag{6.7}$$

$$\phi = \frac{d}{R} \tag{6.8}$$

where R is the pinion radius (100 mm) and θ is the pitch angle of the gear teeth (20°).

To convert the torque-rotation data to shear stress-strain data, an empirical calibration constant (C = 9.03×10^{-4}) and the shear modulus of the epoxy grips (G_g = 1.0 GPa) are determined. Therefore, to properly calibrate the torsion testing device, a series

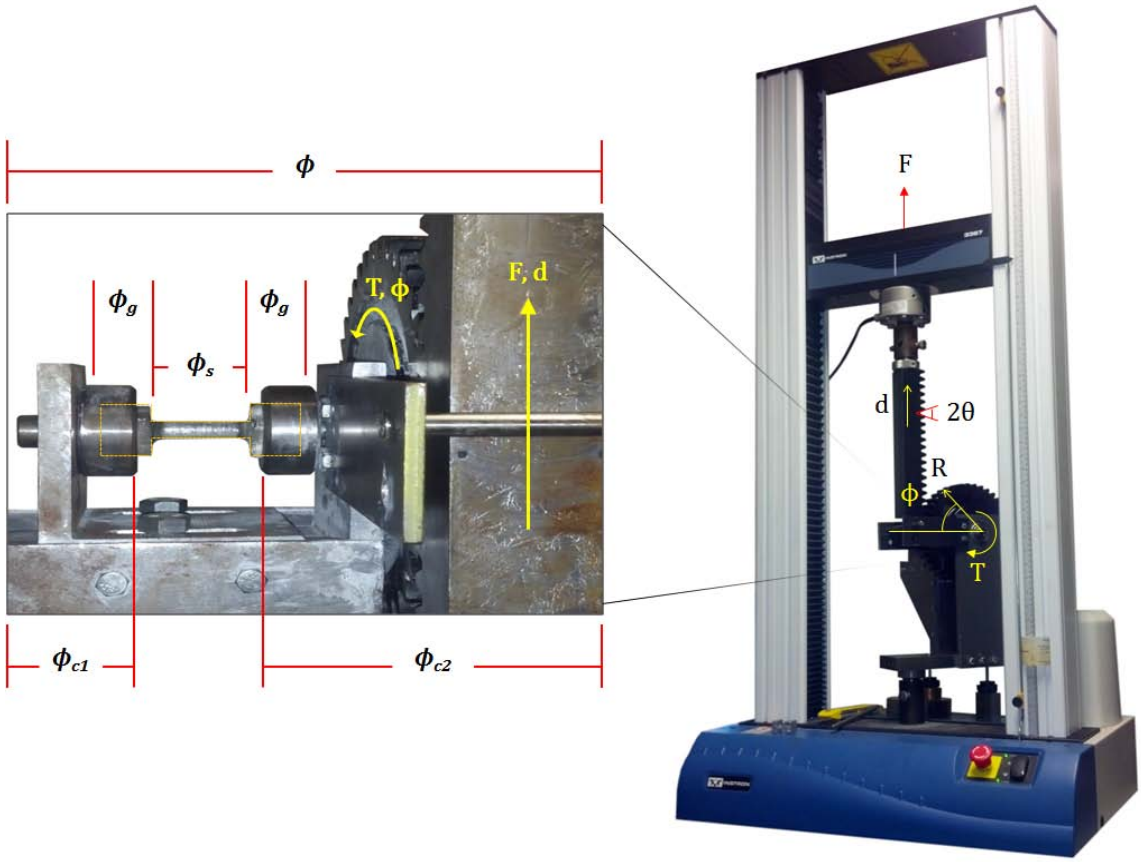

Figure 6.9. Torsion testing device, showing the rack and pinion connected to the Instron materials testing machine (right) and a typical torsion sample showing the conversion of force and displacement (F, d) to torque and rotation (T, ϕ).

of six aluminum (Al 6061-T6) samples with a known shear strength (207 MPa), shear modulus (26 GPa), lengths of approximately 40 mm and varying diameters (6 mm, 9 mm, 12 mm) were twisted in the device. The torque-rotation data collected for the aluminum samples was converted to shear stress-strain data:

$$\tau_s = \frac{T c_s}{J_s} \tag{6.9}$$

$$\gamma_s = \frac{\phi_s c_s}{L_s} \tag{6.10}$$

where τ_s is the shear stress, γ_s is the shear strain, c_s is the radial distance to the outer most surface of the composite, which is equal to the sample radius ($c_s = r_s$), J_s is the polar moment of interia of the sample (for a circular cross-section: $J_s = \frac{\pi}{2} {c_s}^4$; for a square cross-section: $J_s = \frac{b^4}{6}$, where b is the square width of the grips), and L_s is the sample length. Assuming that the total angle of twist (ϕ) is the sum of the angles of twist for all of the components subjected to a torque (T) (refer to Figure 6.9):

$$\phi = \sum_i \phi_i = \phi_s + 2\phi_g + \phi_{c1} + \phi_{c2} \tag{6.11}$$

the angle of twist of each component can be calculated as:

$$\phi_i = \frac{T L_i}{J_i G_i} \tag{6.12}$$

where ϕ_i is angle of twist, L_i is the length, J_i is the polar moment of inertia, and G_i is the shear modulus of component i - referring to the sample of interest (s), the square grips (g), and the device mounts ($c1$ and $c2$), according to Figure 6.9. Assuming that the geometry and compliance of all the components of the torsion testing device (e.g., mounts) are constant, ϕ_{c1} and ϕ_{c2} can be combined into a single constant value, such that Equation 6.12 can be rewritten as:

$$\phi = T\left(\frac{L_s}{J_s G_s} + 2\frac{L_g}{J_g G_g} + C\right) \tag{6.13}$$

where

$$C = \frac{L_{c1}}{J_{c1} G_{c1}} + \frac{L_{c2}}{J_{c2} G_{c2}}. \tag{6.14}$$

Next, Equation 6.13 is differentiated with respect to the torque to determine the shear modulus of the sample (G_s) with respect to the slope of the stress-strain curve ($\partial\phi/\partial T$) and the calibration constant (C):

$$\frac{\partial\phi}{\partial T} = \frac{\partial}{\partial T}\left[T\left(\frac{L_s}{J_s G_s} + 2\frac{L_g}{J_g G_g} + C\right)\right]. \tag{6.15}$$

Then, setting $G_g = G_s$ because the sample grips and the region of interest of the aluminum samples are composed of the same material, Equation 6.15 can be rewritten as:

$$G_s = \frac{\frac{L_s}{J_s} + 2\frac{L_g}{J_g}}{\frac{\partial\phi}{\partial T} - C} \tag{6.16}$$

where $\partial\phi/\partial T$ is the inverse of the slope of the linear regime of the torque-rotation curve, the values L_s, L_g, J_s, and J_g are all measurable parameters that describe the geometry of the sample, and C is a calibration constant that accounts for the geometry and stiffness of the torsion testing device. Therefore, the ultimate shear stress and shear strain can be plotted using Equations 6.9 and 6.10, where:

$$c_s = r_s \tag{6.17}$$

$$\phi_s = \left[\phi - T\left(2\frac{L_g}{J_g G_g} + C\right)\right]. \tag{6.18}$$

Figure 6.10a shows a plot of the calculated stress-strain curves of the six aluminum samples, using the empirically derived calibration constant:

$$C = 9.03 \times 10^{-4}.$$

As seen in the plot (Figure 6.10a), the measured shear strength and modulus of aluminum samples are nearly equal to their known values.

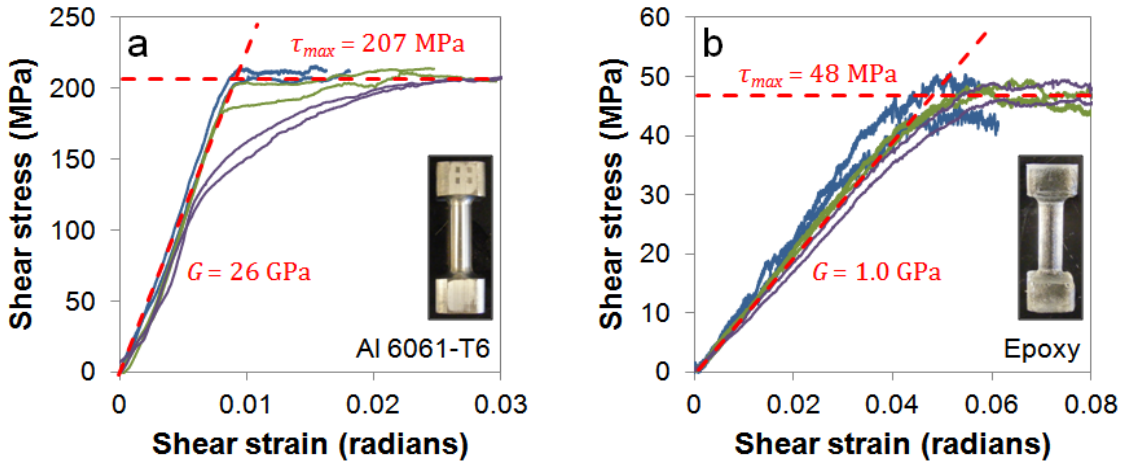

Figure 6.10. Shear stress-strain curves: **(a)** aluminum (Al 6061-T6) samples used to determine the calibration constant (C = 9.03×10^{-4}); **(b)** epoxy samples used to determine the shear modulus of the epoxy grips (G_g=1.0 GPa). The insets show representative images of the dumbbell shaped samples.

Next, to determine the torsional properties of the epoxy used as grips when testing the composites, pure epoxy samples were fabricated and tested. A two part epoxy resin (EpoxiCure Resin, Buehler, Lake Bluff, IL) was degassed under low vacuum and poured into 3D printed molds to form dumbbell shaped samples, like that shown in Figure 6.10b. Six epoxy samples with lengths of approximately 40 mm and varying diameters (6 mm, 9 mm, 12 mm) were tested in torsion. Figure 6.10b shows the shear stress-strain curves of the epoxy samples, using the above calibration constant. The shear strength and modulus of the epoxy were determined from the plot to be ~48 MPa and ~1.0 GPa, respectively.

Finally, using the empirically derived calibration constant (C = 9.03×10^{-4}) and the shear modulus of the epoxy grips (G_g = 1.0 GPa), the ultimate shear stress and shear strain of the ZrO_2-epoxy composites can be plotted from the experimental data using Equations 6.9, 6.10, 6.17, and 6.18. Accordingly, the composite maximum shear strength

(τ_{max}) and shear modulus (G_s) of the ZrO_2-epoxy composites can be calculated as follows:

$$\tau_{max} = \frac{Tr_s}{J_s} \tag{6.19}$$

$$G_s = \frac{L_s/J_s}{\frac{\partial \phi}{\partial T} - 2\frac{L_g}{J_g G_g} - C}. \tag{6.20}$$

6.5.2. Angle of helix-reinforcement analysis

Referring to Section 6.3.2.2 and Figure 6.6b, the global elastic moduli (E_X, E_Y) and shear modulus (G_{XY}) of the composites can be predicted analytically, as a function of the angle of helix-reinforcement (φ). Assuming the outer surface of the cylindrical composites is a unidirectionally-reinforced plate subjected to a state of pure shear and plane stress, as illustrated in Figure 6.6b, the stresses on the plate may be reduced as follows:

$$\sigma_X = \sigma_Y = \sigma_Z = \tau_{XZ} = \tau_{YZ} = 0 \tag{6.21}$$

and

$$\sigma_3 = \tau_{23} = \tau_{13} = 0. \tag{6.22}$$

However, it is important to note that, with the assumption of plane stress, the out-of-plane normal strain is not negligible ($\varepsilon_3 \neq 0$), while the out-of-plane shear strains are reduce to zero ($\gamma_{23} = \gamma_{13} = 0$) [150]. Now, the stresses and strains in the local coordinate system (1, 2, 3) can be expressed in terms of the global coordinate system (X, Y, Z), using the transformation matrix [150]:

$$[T] = \begin{bmatrix} m^2 & n^2 & 2mn \\ n^2 & m^2 & -2mn \\ -mn & mn & m^2 - n^2 \end{bmatrix}, \tag{6.23}$$

where $m = \cos\left(\frac{\pi}{2} - \varphi\right)$ and $n = \sin\left(\frac{\pi}{2} - \varphi\right)$, such that:

$$\begin{pmatrix} \sigma_1 \\ \sigma_2 \\ \tau_{12} \end{pmatrix} = [T] \begin{pmatrix} \sigma_X \\ \sigma_Y \\ \tau_{XY} \end{pmatrix} \tag{6.24}$$

and

$$\begin{pmatrix} \varepsilon_1 \\ \varepsilon_2 \\ \frac{1}{2}\gamma_{12} \end{pmatrix} = [T] \begin{pmatrix} \varepsilon_X \\ \varepsilon_Y \\ \frac{1}{2}\gamma_{XY} \end{pmatrix} \tag{6.25}$$

where σ_i and τ_{ij} are the normal and shear stresses, and ε_i and γ_{ij} are the normal and shear strains in the (1, 2, 3) and (X, Y, Z) directions, respectively. The relationship between the stresses and strains in the local coordinate system (1, 2, 3) can be expressed by the reduced compliance matrix [S] [150]:

$$\begin{pmatrix} \varepsilon_1 \\ \varepsilon_2 \\ \frac{1}{2}\gamma_{12} \end{pmatrix} = \begin{bmatrix} S_{11} & S_{12} & 0 \\ S_{12} & S_{22} & 0 \\ 0 & 0 & \frac{1}{2}S_{66} \end{bmatrix} \begin{pmatrix} \sigma_1 \\ \sigma_2 \\ \tau_{12} \end{pmatrix} \tag{6.26}$$

where

$$\begin{gathered} S_{11} = \frac{1}{E_1}; \\ S_{12} = -\frac{\nu_{12}}{E_1} = -\frac{\nu_{21}}{E_2}; \\ S_{22} = \frac{1}{E_2}; \\ S_{66} = \frac{1}{G_{12}}; \end{gathered} \tag{6.27}$$

and ν_{ij} is Poisson's ratio, E_i is the elastic modulus, and G_{ij} is the shear modulus in the (1, 2, 3) directions, respectively. However, it is necessary to express the global material properties, namely the elastic moduli (E_X, E_Y) and shear modulus (G_{XY}), as functions of the angle of helix-reinforcement (φ) to determine how this angle influences the overall strength and stiffness of the composites subjected to an applied torque. Thus, combining Equations 6.23-6.26 yields:

$$\begin{pmatrix} \varepsilon_X \\ \varepsilon_Y \\ \frac{1}{2}\gamma_{XY} \end{pmatrix} = [T]^{-1} \begin{bmatrix} S_{11} & S_{12} & 0 \\ S_{12} & S_{22} & 0 \\ 0 & 0 & \frac{1}{2}S_{66} \end{bmatrix} [T] \begin{pmatrix} \sigma_X \\ \sigma_Y \\ \tau_{XY} \end{pmatrix}, \tag{6.28}$$

which can be rewritten as the transformed reduced compliance matrix $[\bar{S}]$ [150]:

$$\begin{pmatrix} \varepsilon_X \\ \varepsilon_Y \\ \gamma_{XY} \end{pmatrix} = \begin{bmatrix} \bar{S}_{11} & \bar{S}_{12} & \bar{S}_{16} \\ \bar{S}_{12} & \bar{S}_{22} & \bar{S}_{26} \\ \bar{S}_{16} & \bar{S}_{26} & \bar{S}_{66} \end{bmatrix} \begin{pmatrix} \sigma_X \\ \sigma_Y \\ \tau_{XY} \end{pmatrix} \tag{6.29}$$

where

$$\begin{gathered} \bar{S}_{11} = S_{11}m^4 + (2S_{12} + S_{66})m^2n^2 + S_{22}n^4; \\ \bar{S}_{12} = (S_{11} + S_{22} - S_{66})m^2\,n^2 + S_{12}(n^4 + m^4); \\ \bar{S}_{16} = (2S_{11} - 2S_{12} - S_{66})m^3n - (2S_{22} - 2S_{12} - S_{66})mn^3; \\ \bar{S}_{22} = S_{11}n^4 + (2S_{12} + S_{66})m^2n^2 + S_{22}m^4; \\ \bar{S}_{26} = (2S_{11} - 2S_{12} - S_{66})mn^3 - (2S_{22} - 2S_{12} - S_{66})m^3n; \\ \bar{S}_{66} = 2(2S_{11} + 2S_{22} - 4S_{12} - S_{66})m^2n^2 + S_{66}(n^4 + m^4). \end{gathered} \tag{6.30}$$

By analogy (refer to Equations 6.26 and 6.27), the elastic moduli (E_X, E_Y) and shear modulus (G_{XY}) in the global coordinate system can be expressed in terms of the transformed reduced compliance matrix $[\bar{S}]$ [150]:

$$E_X = \frac{1}{\bar{S}_{11}} = \frac{E_1}{m^4 + m^2 n^2 \left(\frac{E_1}{G_{12}} - 2\nu_{12}\right) + n^4 \frac{E_1}{E_2}}; \tag{6.31}$$

$$E_Y = \frac{1}{\bar{S}_{22}} = \frac{E_2}{m^4 + m^2 n^2 \left(\frac{E_2}{G_{12}} - 2\nu_{21}\right) + n^4 \frac{E_2}{E_1}}; \tag{6.32}$$

$$G_{XY} = \frac{1}{\bar{S}_{66}} = \frac{G_{12}}{m^4 + n^4 + 2m^2 n^2 \left(2\frac{G_{12}}{E_1}(1 + 2\nu_{12}) + 2\frac{G_{12}}{E_2} - 1\right)}. \tag{6.33}$$

Finally, dividing Equation 6.33 by the local material shear modulus (G_{12}) yields the normalized shear modulus shown in Equation 6.6 and plotted in Figure 6.6b:

$$G_{XY}/G_{12} = \frac{1}{m^4 + n^4 + 2m^2 n^2 \left(2\frac{G_{12}}{E_1}(1 + 2\nu_{12}) + 2\frac{G_{12}}{E_2} - 1\right)}. \tag{6.34}$$

6.6. Acknowledgements

Chapter 6, in full, is currently under peer review for publication in *Composites Part A: Applied Science and Manufacturing*, and co-authored by L. Meraz, A. Calderon, H. Choi, A. Chouhan, L. Wang, M.A. Meyers, and J. McKittrick of UCSD.

CHAPTER 7:

MAGNETIC ALIGNMENT OF ICE TEMPLATED CERAMICS

7.1. Introduction

Methods for tailoring the microstructures of ceramic scaffolds or hybrid composites allow engineers to produce designer materials with enhanced mechanical properties for specific functions. Ice-templating (or freeze casting) has gained tremendous popularity, in recent years, as a convenient method to fabricate porous scaffolds with highly anisotropic, interconnected pore channels or hybrid composites with interpenetrating networks of two constituent phases (upon infiltration of the scaffolds with a second phase) [75, 80, 84, 89, 287, 288]. Freeze cast materials have been shown to exhibit exceptional unidirectional strength, stiffness, and toughness [75, 80, 84], mimicking many of the structural features of natural biological materials, such as the lamellar walls, mineral bridges, and surface asperities of abalone nacre or the osteonal and trabecular architectures of bone [90]. However, the mechanical properties perpendicular to the direction of ice growth are generally poor - due to a lack of microstructural alignment and uniformity in these directions [88, 306]. Although there have been many attempts to tailor the pore architectures of freeze cast scaffolds [90, 121, 222, 304], few have successfully achieved a high degree of long-range microstructural alignment perpendicular to the ice growth direction [80, 88, 306].

Recently, Porter et al. [88, 91] applied external weak magnetic fields (~0.1 T) to the ice templating process to further control the microstructural evolution of porous ceramics and ceramic-polymer composites. They showed that static and rotating

magnetic fields propagating perpendicular to the ice growth axis aligned a variety of structural features, leading to improved compressive and torsional properties, respectively. These examples [88, 91] prove that the magnetic alignment of ice templated ceramics (or magnetic freeze casting) is an excellent method to form bulk ceramic materials with tailored architectures oriented in prescribed directions.

Magnetic fields have also been used to control the microstructural alignment, and consequently improve the mechanical properties and functionality, of bulk ceramics [350-356, 390-394], alloys [395, 396], and carbon-reinforced polymers [397-401]. Using high magnetic fields up to10 T, Suzuki, Uchikoshi and coworkers [352-356] and Sassa, Asai and coworkers [392-394] successfully aligned a variety of paramagnetic and diamagnetic materials to form compact polycrystalline ceramics with magnetically controlled crystallographic orientations. Wang and coworkers [395, 396] applied high gradient magnetic fields up to 12 T to form functionally graded alloys with continuously varying morphological compositions. Several other groups [397-401] utilized strong magnetic fields (3-25 T) to align carbon nanotubes or carbon nanofibers in polymer matrices. Although these methods result in bulk materials with highly-oriented crystalline microstructures, functionally graded morphologies, aligned reinforcements, or enhanced mechanical properties, the use of strong magnetic fields (>>1 T) has several disadvantages, including high cost, high energy consumption, and safety concerns. Therefore, fabrication processes that utilize weak magnetic fields (<<1 T) to align the microstructures of ceramics or composites are advantageous for the efficient and scalable manufacturing of bulk structural materials.

A few groups have utilized weak magnetic fields (<<1 T) to fabricate ceramic composites [48, 49, 81, 83, 402-407]. Of those, Yan and coworkers [405-407] successfully demonstrated slip casting in the presence of gradient magnetic fields (0-0.15 T) to fabricate Ni-ZrO_2 composites with functionally graded microstructures and continuously varying mechanical properties. Studart and coworkers [48, 49, 81, 83, 402-404] used ultralow magnetic fields (0.001-0.01 T) to align high aspect ratio ceramic platelets and rods in polymer matrices, resulting in particulate composites with enhanced stiffness, strength, hardness, wear resistance, localized reinforcement, and shape memory effects [48, 81]. Similarly, Sommer et al. [408] developed injectable materials with aligned pores, using magnetically responsive rods as sacrificial pore formers.

In comparison to those methods [48, 49, 81, 83, 402-408], magnetic freeze casting is a more flexible method to fabricate a variety of advanced structural materials with designer architectures (i.e., porous scaffolds and hybrid composites). The continuity, interconnectivity, and directional alignment of the lamellae and other structural features enhance the performance of these materials significantly, compared to those composed of discrete elements or particles [88, 91]. These intricate structural features may be designed with great precision utilizing different magnetic materials, field orientations, and freeze casting techniques. Magnetic freeze casting may also be combined with other freezing and post processing techniques (e.g., flow freezing, infiltration, pressurized sintering) to fabricate high-performance, hierarchical materials with aligned crystals [303, 305], interpenetrating networks of different material constituents [82, 243], or high relative fractions of ceramic (>98%) [80].

Here we review three modes of magnetically induced microstructural alignment in ice templated ceramics: (1) lamellar wall alignment; (2) mineral bridge alignment; (3) biphasic reinforcement. Uniform, gradient, and rotating weak magnetic fields (< 0.12 T) were applied to colloidal mixtures of magnetite (Fe_3O_4) and paramagnetic (TiO_2) or diamagnetic (ZrO_2) particles during unidirectional freezing to compare the effects of the magnetic fields and casting materials on the resulting scaffold architectures and mechanical properties. Adding magnetic fields that propagate perpendicular to the freeze casting direction shows great potential, as a simple and convenient method, to form ceramic materials with continuous, interconnected microstructural features aligned by two mechanisms: (1) ice growth and (2) magnetic fields.

7.2. Materials and Methods

7.2.1. Magnetic freeze casting setup

The magnetic freeze cast scaffolds were prepared using a custom built freeze cast unit and rotating permanent magnet, as previously described [88]. Briefly, the freeze cast unit consists of a copper cold finger immersed in a liquid nitrogen bath. A band heater and thermocouple linked to a PID controller are attached to the copper cold finger in order to control the cooling rate of the copper surface at the bottom of polyethylene (PE) molds with 4 mm, 9 mm, and 20 mm inner diameters. A permanent magnet propagates a gradient magnetic field through the colloidal suspensions, perpendicular to the ice growth direction.

Table 7.1. Properties of ceramic powders, as received. Information reported by manufacturers unless otherwise noted.

	Magnetite (Fe_3O_4)	Titania (TiO_2)	Zirconia (ZrO_2)
Crystal system[a]	Cubic	Tetragonal	Monoclinic
Density (g/cm^3)	4.95	4.26	5.89
Molar mass (g/mol)	231.53	79.87	123.22
Particle size (μm)[c]	<0.05	0.2-0.5	0.2-0.5
Magnetic susceptibility (cm^3/mol)[b]	--- (ferrimagnetic)	$+5.9 \times 10^{-6}$ (paramagnetic)	-13.8×10^{-6} (diamagnetic)

[a] Crystal systems confirmed by XRD measurements.
[b] Magnetic molar susceptibility, taken from [409].
[c] Particle sizes measured from SEM micrographs.

7.2.2. Sample Preparation

To compare the effects of colloidal suspensions composed of Fe_3O_4 + paramagnetic (TiO_2) particles and Fe_3O_4 + diamagnetic (ZrO_2) particles, Fe_3O_4 nanoparticles (< 50 nm) (Sigma Aldrich, St. Louis, MO) were mixed in deionized water with TiO_2 (paramagnetic, Sigma Aldrich, St. Louis, MO) or ZrO_2 (diamagnetic, Sigma Aldrich, St. Louis, MO) particles of equal size (0.2-0.5 μm). All the ceramic particles investigated here are spherical. The aqueous slurries contained 10 vol.% TiO_2 or ZrO_2, 0-9 wt.% Fe_3O_4, plus 1 wt.% of each: organic binders, polyethylene glycol (PEG) (Alfa Aesar, Ward Hill, MA) and polyvinyl alcohol (PVA) (Alfa Aesar, Ward Hill, MA), and an ammonium polymethacrylate anionic dispersant, Darvan® 811 (R. T. Vanderbilt Company, Inc. , Norwalk, CT). Table 7.1 shows the physical properties of the ceramic powders, as received. As seen in the table, the major difference between the two nonmagnetic particles investigated here is that the TiO_2 is has a positive susceptibility making it paramagnetic, while the ZrO_2 has a negative susceptibility making it diamagnetic.

The slurries were ball milled in an alumina grinding medium for 24 hours, followed by degassing under low vacuum for 10-20 min. Approximately 1-10 mL of the degassed slurries were poured into the PE molds and frozen at a constant rate of 10°C/min. Several samples were frozen under four different magnetic field conditions: (1) no magnetic field; (2) uniform magnetic fields of ~0.1 T; (3) gradient magnetic fields of ~0.1 T; and (4) rotating gradient magnetic fields of ~0.1 T at 0.05 rpm. The gradient magnetic fields were achieved by placing a large mold (20 mm) in between the poles, while the uniform magnetic fields were achieved by placing smaller molds (4 mm and 9 mm) in between the poles where the fields were nearly constant (refer to Figure 7.2). After freezing, the samples were removed from the molds with a hydraulic press and lyophilized in a bench-top freeze dryer (Labconco, Kansas City, MO) at -50°C and 350 Pa for 72 hr. The porous green constructs were then sintered in an open air furnace for 3 hr at predetermined temperatures of 900°C for TiO_2 and 1300°C for ZrO_2 and with heating and cooling rates of 2°C/min. For clarity, even though the ceramic scaffolds contain 0-9 wt.% Fe_3O_4, they are simply referred to as TiO_2 (paramagnetic) or ZrO_2 (diamagnetic) scaffolds throughout this report.

7.2.3. Microscopy

Optical microscopy images were taken with a VHX-1000 digital microscope system equipped with a CCD camera (KEYENCE Corporation, Osaka, Japan). Scanning electron microscopy (SEM) images were taken at 15 kV on a Philips XL30 field emission environmental scanning electron microscope (ESEM) (FEI-XL30, FEI Company, Hillsboro, OR). For SEM preparation the samples were sputter-coated with iridium using

an Emitech K575X sputter coater (Quorum Technologies Ltd., West Sussex, UK). Energy-dispersive X-ray spectroscopy (EDX) was performed on the ESEM. Coloring of the orientation domains was performed manually, to distinguish the lamellar wall alignment angles, using Jasc Paint Shop Pro.

7.2.4. Micro-computed tomography

One TiO_2 scaffold containing 10 vol.% TiO_2 and 3 wt.% Fe_3O_4, cast in a 20 mm mold with a rotating magnetic field of ~0.1 T at 0.05rpm, was scanned on a micro-computed tomography (micro-CT) unit, Skyscan 1076 (Bruker Biospin, Kontich, Belgium). The scaffold was imaged at 9 µm isotropic voxel size, applying an electric potential of 70 kV and a current of 200 µA, using a 1 mm aluminum filter. Two TiO_2 scaffolds containing 10 vol.% TiO_2 and 5 wt.% Fe_3O_4, cast in 4 mm molds with (1) no magnetic field and (2) a uniform magnetic field of ~0.1 T, were scanned on a high resolution micro-CT unit, Skyscan 1272 (Bruker Biospin, Kontich, Belgium). The two scaffolds were imaged at 0.5 µm isotropic voxel size, applying an electric potential of 70 kV and a current of 142 µA, using a 0.5 mm aluminum filter. A beam hardening correction algorithm was applied during image reconstruction. Images and 3D rendered models were developed using Skyscan's Dataviewer and CTVox software.

7.2.5. X-ray diffraction

X-ray diffraction (XRD) on the TiO_2 scaffolds was performed with a Miniflex II XRD machine (Rigaku, The Woodlands, TX). XRD experiments confirmed that the crystal structures of all the TiO_2 scaffolds transformed from anatase before sintering to

rutile after sintering at 900°C, while a small portion of the Fe_3O_4 phase was absorbed into the TiO_2 scaffolds after sintering, forming a small amount of the iron titanium oxide, pseudobrookite (Fe_2TiO_5) [88]. XRD on the ZrO_2 scaffolds was performed on a D2 Phaser X-ray diffraction tool (Bruker AXS, Madison, WI). XRD experiments confirmed that the crystal structure of the ZrO_2 scaffolds remained monoclinic before and after sintering at 1300°C, while a small portion of the Fe_3O_4 phase transformed from magnetite (Fe_3O_4) before sintering to hematite (Fe_2O_3) after sintering [91]. No apparent transformation due to interactions between the ZrO_2 and Fe_3O_4 phases was observed [91].

7.2.6. Mechanical testing

Compression testing of the scaffolds was performed on an Instron materials testing machine (Instron 3342, Norwood, MA) with a 500 N load cell at a crosshead velocity of 0.005 mm/sec, as previously described [88]. Briefly, the scaffolds were cut into small samples of approximately $5 \times 5 \times 5$ mm^3 and compressed parallel to the ice growth or magnetic field directions. The compressive ultimate strength and Young's modulus were determined from the maximum stress and the linear slope of the stress-strain curves, respectively.

Torsion testing of the composites with different angles of helix-reinforcement were compared using the solid-rod torsion test. The torsion tests were performed on a custom built torsion testing device, capable of twisting the cylindrical composites to induce a state of pure shear stress, as previously described [91]. Briefly, the cylindrical composites were aligned and mounted in epoxy "grips" using a custom built mounting device. All the composite samples were fabricated such that the regions of interest have a

circular cross-section of radius r_s (~7.5 mm) and length L_s (~25 mm). The epoxy grips of the samples have square cross-sections 24.5 mm x 24.5 mm with lengths of L_g (~ 25 mm), fitting neatly into the square mounts of the torsion tester.

7.3. Results and discussion

7.3.1. Ice templated scaffolds

As previously discussed, ice templated scaffolds have continuously interconnected pore channels that are aligned parallel to the direction of ice growth. This unidirectional alignment is the key structural mechanism responsible for the extraordinary strength and stiffness of these highly porous ceramic materials. Figure 7.1a-b shows stress-strain curves for two scaffolds freeze cast at 10°C/min under no magnetic field. As seen in the plots, the scaffolds are approximately 10 times stronger and stiffer when compressed parallel to the ice growth direction than perpendicular (transverse direction). This is the consequence of the long-range microstructural alignment and interconnectivity of the lamellar walls in a single (ice growth) direction (see Figure 1c-d). The different compressive properties observed in these plots are due to the different material compositions (TiO_2 and ZrO_2) and sintering temperatures (900°C and 1300°C, respectively). However, these plots illustrate the fact that the compressive properties parallel to the direction of ice growth are always greater than those perpendicular, regardless of the material composition or post processing conditions.

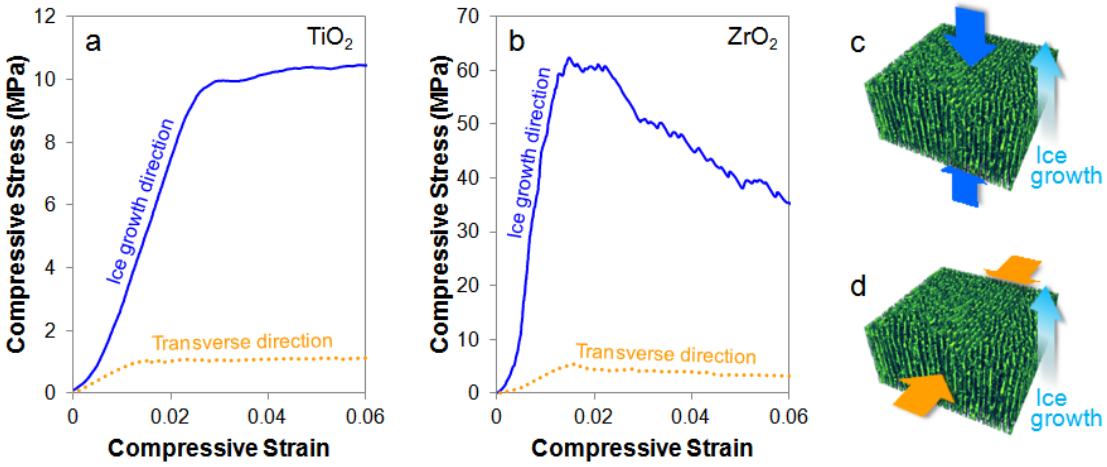

Figure 7.1. (a-b) Representative stress-strain curves illustrating the compressive behavior of (a) TiO_2 and (b) ZrO_2 scaffolds (each containing 3 wt.% Fe_3O_4) in the ice growth (blue solid line) and transverse (perpendicular to the ice growth, orange dotted line) directions. **(c-d)** Representative µCT images of a freeze cast scaffold (with no magnetic field), illustrating the direction of ice growth with respect to the different compressive loading conditions: (c) parallel and (d) perpendicular.

7.3.2. Uniform and gradient magnetic fields

Figure 7.2 shows the magnetic freeze casting setups. The flux density of the magnetic field (B_{mag}) across the separation gap (G) between the poles (N, S) can be theoretically determined by the following equation [Furlani 2001, Joshi 2013]:

$$B_{mag}(Y) = B'\left(\frac{G}{2} + Y\right) + B'\left(\frac{G}{2} - Y\right), \tag{7.1}$$

where $B'(y)$ is the flux density of each of the two poles, approximated as individual rectangular magnets with remanent flux densities (B_r), lengths ($2l$) and widths ($2w$), magnetized through the thicknesses (t), such that [Furlani 2001, Joshi 2013]:

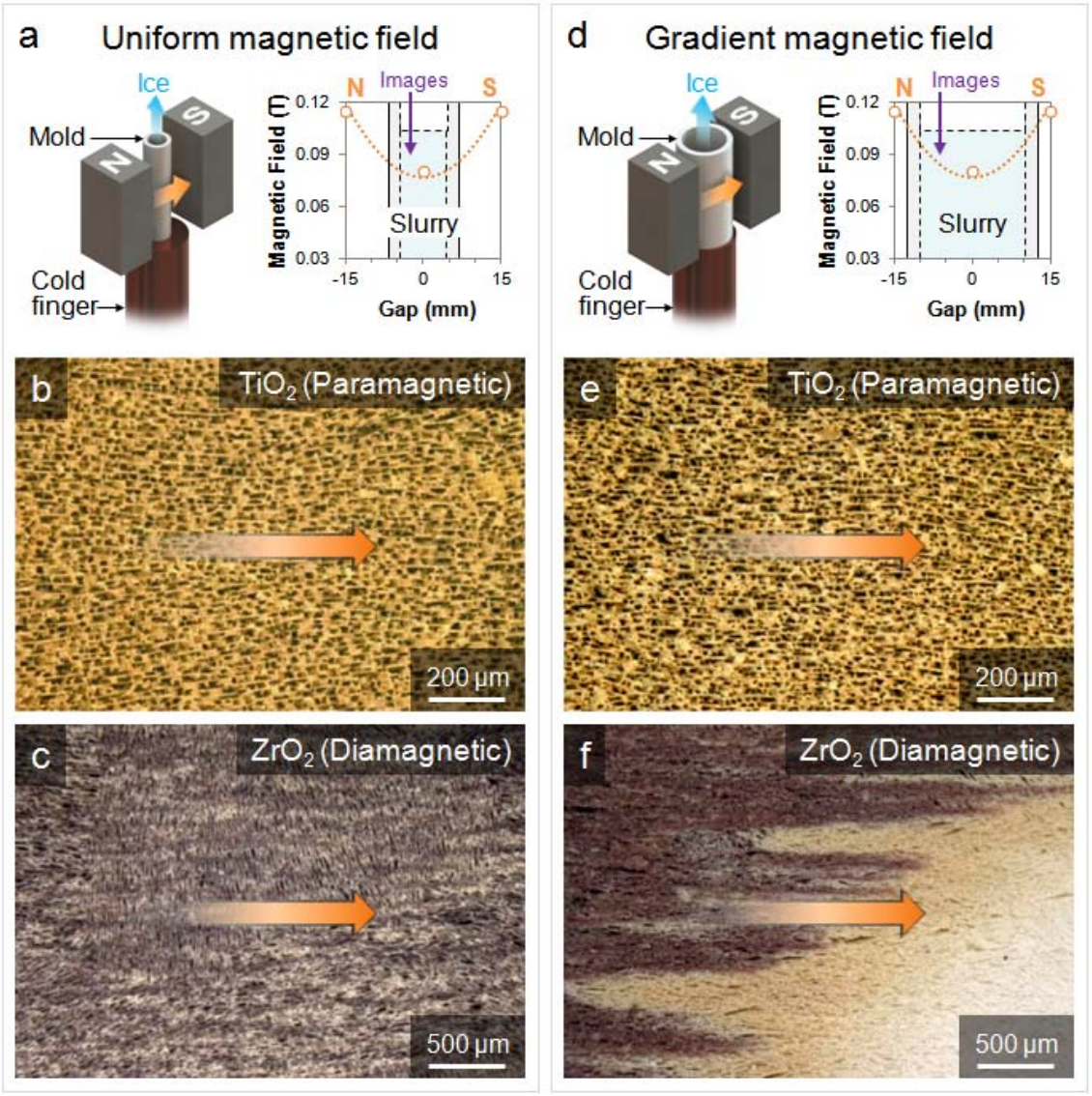

Figure 7.2. Effect of **(a-c)** uniform magnetic fields and **(d-f)** gradient magnetic fields on the distribution of Fe_3O_4 (magnetic nanoparticles) with **(b, e)** TiO_2 (paramagnetic) and **(c, f)** ZrO_2 (diamagnetic) particles during the ice templating process. **(a, d)** Schematics of the magnetic freeze casting setups in order to produce **(a)** uniform magnetic fields and **(d)** gradient magnetic fields through the colloidal slurries. The orange arrow represents the magnetic field direction and the blue arrow represents the ice growth direction. The purple arrow shows where the images of samples (b-f) were approximately taken.

$$B'(y) = \frac{B_r}{\pi}\left[\tan^{-1}\left(\frac{(y+t)\sqrt{l^2+w^2+(y+t)^2}}{lw}\right) - \tan^{-1}\left(\frac{y\sqrt{l^2+w^2+y^2}}{lw}\right)\right]. \quad (7.2)$$

Using these equations, the magnetic field strength (magnetic flux density, B_{mag}) was plotted as a function of the distance across the separation gap (Y), shown to the right of the images in Figures 7.2a and 7.2d. The dotted line represents the theoretical flux density across a gap of 30 mm, assuming the magnetic poles are rectangular magnets with remanent flux densities of 0.2 T and cross-sections 25.4 mm wide by 50.8 mm long. The thicknesses were assumed to be sufficiently large, such that $t \to \infty$, which reasonably accounts for the custom design of the magnetic flux path distributors, as previously described [88]. Also shown on the plots are the actual values of the magnetic field strength measured by a Gauss meter (hollow circles), which are in good agreement with the theoretical predictions (dotted line).

When the separation gap between the magnet poles (N, S) is 30 mm, a gradient magnetic field is produced, varying through the center from ~0.12 T near the poles (Y = ±15 mm) to ~0.08 T at the midpoint (Y = 0 mm). To compare the behavior of the different colloidal suspensions under both uniform and gradient fields, two small molds (4 mm and 9 mm inner diameters, Figure 7.2a) and a large mold (20 mm inner diameter, Figure 7.2d) were used during the freeze casting processes. Outlines of the respective molds containing the aqueous slurries are shown in the plots to illustrate the nearly uniform magnetic field that passes through a small mold (9 mm) and the steep gradient magnetic field that passes through a large mold (20 mm).

In the presence of uniform magnetic fields (~0.1 T), two different mechanisms of microstructural alignment were observed: lamellar wall alignment (Figure 7.2b) and

mineral bridge alignment (Figure 7.2c) - refer to Section 7.3.4.2 for more details. Conversely, gradient magnetic fields (0.08-0.12 T) led to a redistribution of the colloidal particles, resulting in density gradients (Figure 7.2e) and biphasic composition gradients (Figure 7.2f). Using Monte Carlo simulations, Peng et al. [359, 360] illustrated the behavior of colloidal suspensions containing magnetic and nonmagnetic particles subjected to uniform and gradient fields. Under uniform fields, magnetic particles tend to form branched clusters and linear chains aligned in the field direction [359]. Under gradient fields, magnetic particles tend to cluster and aggregate in the direction of the increasing field [360]. These behaviors are observed in the scaffolds freeze cast under the different magnetic fields (Figure 7.2). The scaffolds in Figures 7.2b-c exhibit some degree of alignment parallel to the direction of the uniform field, while the scaffolds in Figures 7.2e-f exhibit graded structures parallel to the gradient field, similar to those predicted by Peng et al. [359, 360]. Moreover, different microstructural features aligned parallel to the magnetic fields are present in all the scaffolds (Figures 7.2), which are further described in the following sections.

7.3.3. Magnetic response of paramagnetic and diamagnetic colloids

An interesting phenomenon was discovered when freeze casting the paramagnetic colloids, as compared to the diamagnetic colloids. As previously introduced by Porter et al. [88], mixtures of TiO_2 and Fe_3O_4 did not seem to separate into different phases in the presence of a gradient magnetic field (refer to Figure 7.2e). On the other hand, mixtures of ZrO_2, Al_2O_3, and hydroxyapatite (HA) with Fe_3O_4 separated into two distinct phases: Fe_3O_4-rich and Fe_3O_4-poor [88]. Figure 7.2f shows this biphasic separation of Fe_3O_4-rich

(brown) and Fe_3O_4-poor (white) phases in the ZrO_2 scaffolds freeze cast under a gradient magnetic field. Although not previously understood, this phenomenon is now realized to be due to the paramagnetic susceptibility of TiO_2, when compared to the diamagnetic susceptibilities of ZrO_2, Al_2O_3, and HA (refer to Table 7.1) [Mag Suscept, Fatemi-Ardekani Thesis 2010].

It is well known that diamagnetic materials, such as ZrO_2, do not exhibit a magnetic dipole-dipole response under weak magnetic fields (<1 T), nor do they interact with neighboring particles that do exhibit a magnetic response [405]. However, numerical simulations of paramagnetic particles in viscous fluids have demonstrated motion and clustering of the particles under uniform magnetic fields [410]. Paramagnetic particles have also been shown to flocculate with Fe_3O_4 particle clusters in the presence of weak to moderate fields [411-413]. Since Fe_3O_4 exhibits a strong magnetic response to weak external fields, aggregating into long particle chains or branched clusters [347, 349, 414-416], it is expected that these magnetic aggregates will attract neighboring paramagnetic (TiO_2) particles during the ice templating process. This attractive particle-aggregate interaction produces a more homogeneous mixture of magnetic (Fe_3O_4) and paramagnetic (TiO_2) particles, resulting in more uniform microstructural alignment throughout the scaffold cross-sections (refer to Figure 7.2b,e). On the other hand, no attractive forces between the magnetic (Fe_3O_4) and diamagnetic (ZrO_2) particles occur, leading to the biphasic separation observed in Figure 7.2f and, to a smaller degree, in Figure 7.2c.

7.3.4. Magnetic Alignment Mechanisms

7.3.4.1. Lamellar wall alignment (paramagnetic particles, uniform magnetic fields)

Figure 7.3 shows μCT and SEM images of TiO_2 (+ 5 wt.% Fe_3O_4) scaffolds freeze cast under no magnetic field (a-b) and a uniform magnetic field of ~0.1 T (c-d). Typically, ice grows in discrete orientation domains, several millimeters long, parallel to the ice growth direction, and several micrometers wide, perpendicular to the ice growth direction [289, 290]. The extraordinary mechanical properties usually reported for ice templated ceramics are due to the long-range uniformity of these domains parallel to the ice growth axis (refer to Figure 7.1). As seen in Figures 7.1c-d, it is apparent that the lamellar walls are oriented parallel to the ice growth axis, but not in the transverse direction. The random alignment of the orientation domains perpendicular to the ice growth axis generally results in a complete lack of long-range, cross-sectional uniformity.

Figures 7.3a-b illustrate the lack of uniform alignment in a TiO_2 scaffold freeze cast under no magnetic field. As seen in Figure 7.3a, the different orientation domains are colored according to their angle of directional alignment, ranging from -90° to +90°. A magnified image of the lack of cross-sectional alignment in the scaffold is shown in Figure 7.3b. In contrast, the scaffold freeze cast under a uniform field (Figures 7.3c-d) showed considerable long-range alignment parallel to both the ice growth and magnetic field (orange arrow) directions. In fact, ~75% of the scaffold cross-section is aligned within ±5° of the magnetic field (refer to Figure 7.3c). Figure 7.3d shows a magnified image of the scaffold cross-section with lamellar walls aligned parallel to the uniform magnetic field.

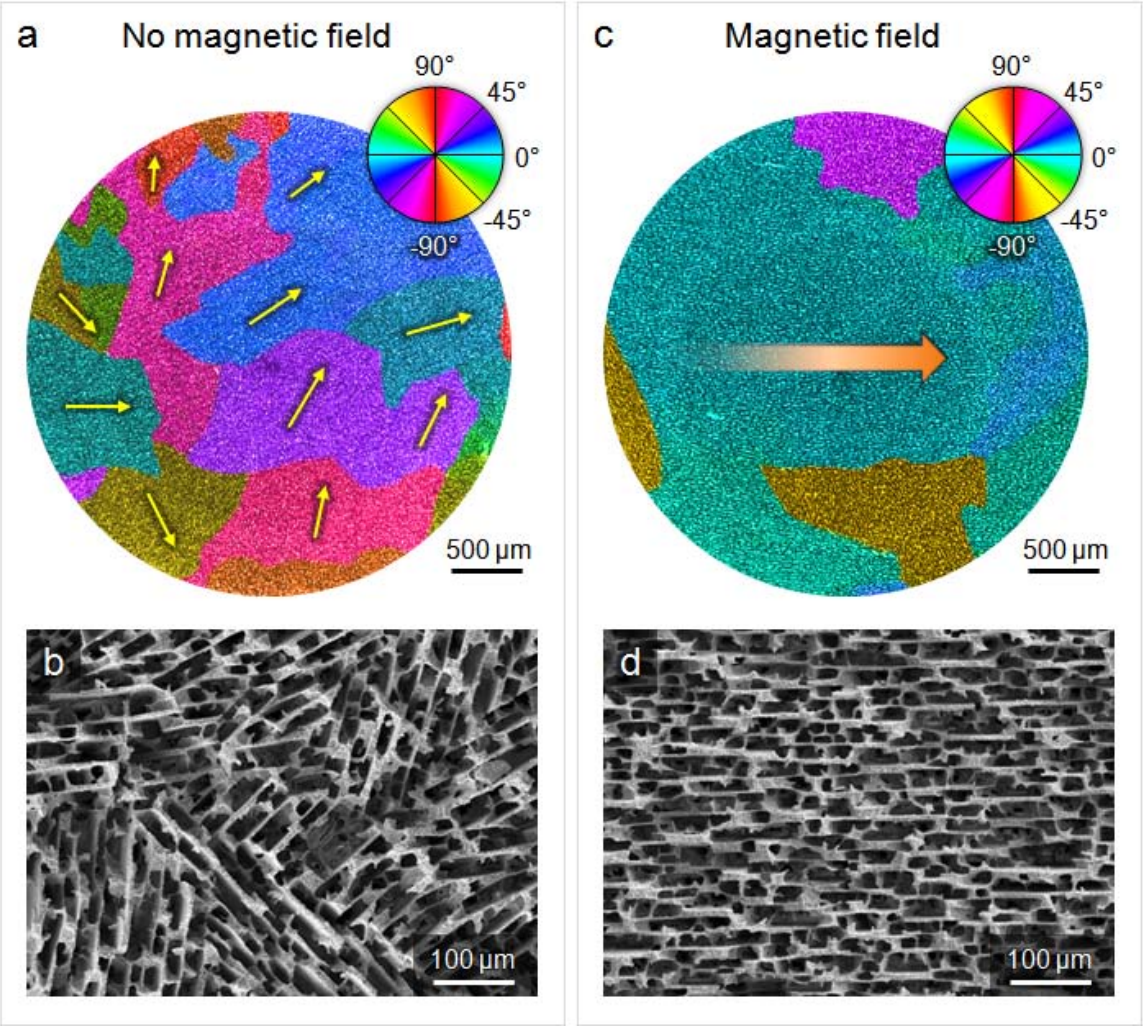

Figure 7.3. Representative images of TiO_2 (+ 5 wt.% Fe_3O_4) scaffolds freeze cast under: **(a-b)** no magnetic field and **(c-d)** a uniform magnetic field of ~0.1 T. The µCT images (top) are colored according to the parallel alignment of lamellar walls from -90° to +90°, corresponding to the color wheels (top right). The SEM micrographs show representative images of (b) randomly oriented and (d) aligned lamellar walls. The orange arrow in (c) represents the direction of the magnetic field.

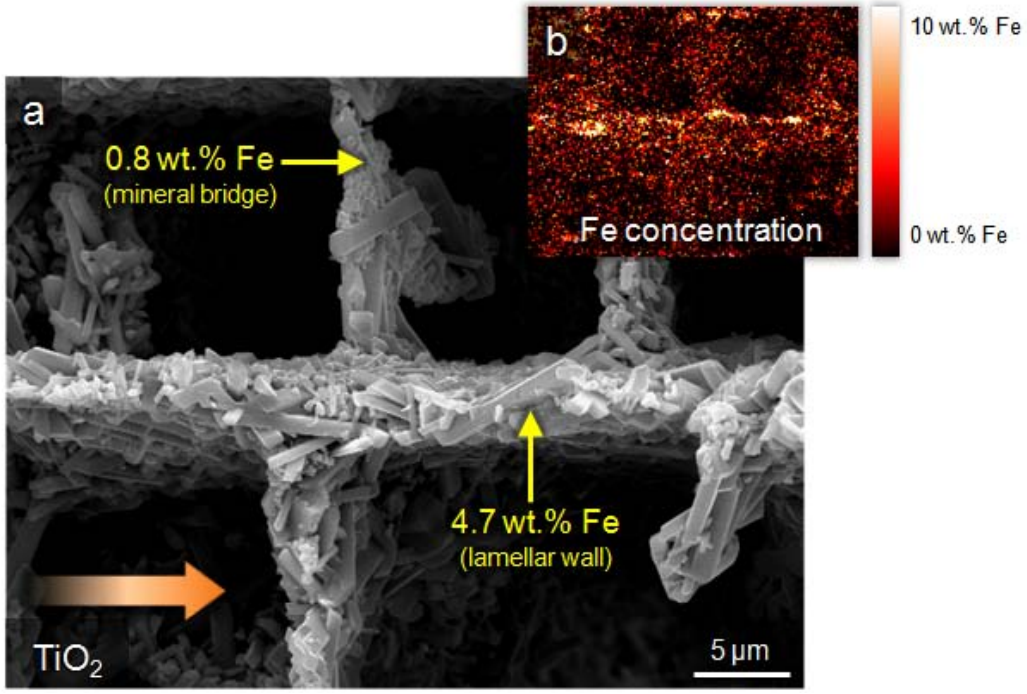

Figure 7.4. (a) Micrograph of a magnetically aligned TiO_2 (+ 3 wt.% Fe_3O_4) lamellar wall, illustrating the fractions of iron (Fe) concentrated in the lamellar wall (4.7 wt.%) and a mineral bridge (0.8 wt.%). The orange arrow represents the direction of the magnetic field. **(b)** Elemental map of the scaffold in shown in (a), illustrating the concentration distribution of Fe throughout the microstructure, according to the color scale (top right).

As previously reported [88], the alignment of lamellar walls was only observed in the TiO_2 scaffolds. This effect is due to the paramagnetic susceptibility of TiO_2 and its tendency to interact with Fe_3O_4 clusters in the presence of a magnetic field [411-413]. Figure 7.4 proves that a higher concentration of iron (Fe) is observed in the lamellar walls, as opposed to the mineral bridges. Therefore, it is reasonable to conclude that linear chains of Fe_3O_4 nanoparticles aggregate with TiO_2 particles, because of their paramagnetic susceptibility. This linear agglomeration of particles forms under the

influence of a uniform magnetic field and forces the lamellar walls to bi-align with the growing ice crystals *and* prevailing magnetic field.

It is likely that, because the colloidal particles act as nucleation sites for the growth of new ice crystals in the slurry [301], the aligned chains of colloids force the nucleation of pseudo-magnetically aligned ice crystals. However, there is a precise balance of colloidal energies that must be taken into account. Preliminary experimental observations suggest that at high freeze rates (~10 °C/min) very little magnetic alignment occurs, while at low freezing rates (<10 °C/min) a significant amount of lamellar wall alignment occurs. Thus, there should be optimal freezing rates, magnetic field strengths, and colloidal compositions that lead to the highest degree of lamellar wall alignment (the topic of ongoing research).

7.3.4.2. Mineral bridge alignment (diamagnetic particles, uniform magnetic fields)

Unlike paramagnetic particles, diamagnetic particles, such as ZrO_2, exhibit no magnetic response in weak fields. Therefore, the resulting microstructural alignment of the ZrO_2 scaffolds in the presence of uniform magnetic fields is quite different from that observed in the TiO_2 scaffolds. Figure 7.5 shows electron micrographs of ZrO_2 (+ 5 wt.% Fe_3O_4) scaffolds freeze cast under no magnetic field (a-b) and a uniform magnetic field of ~0.1 T (c-d). The scaffold freeze cast with no magnetic field shows no significant cross-sectional alignment, other than the randomly aligned orientation domains spanning several hundred micrometers (Figure 7.5a-b). On the other hand, the scaffold freeze cast under a uniform magnetic field, shows a high degree of cross-sectional alignment across the entire sample (Figure 7.5c). However, unlike the lamellar wall alignment observed for

the TiO_2 scaffolds, the ZrO_2 scaffolds exhibit a different type of magnetic alignment - mineral bridge alignment (refer to yellow arrows in Figure 7.5d).

To illustrate this order of alignment, the scaffold cross-sections are colored according to the orientation of the lamellar walls in Figure 7.5a and the mineral bridges in Figure 7.5c. Referring to Figure 7.5d, it is clear that long, continuously connected mineral bridges, aligned parallel to the magnetic field, span several lamellar walls regardless of their orientation (see yellow arrows). If fact, ZrO_2 (+ 3 wt.% Fe_3O_4) scaffolds fabricated with no magnetic field were found to have mineral bridges spanning ~2 ± 1 (average ± standard deviation, N=40) lamellar walls, while those fabricated under a uniform magnetic field of ~0.1 T had mineral bridges spanning ~5 ± 4 (average ± standard deviation, N=40) lamellar walls. In contrast to Figure 7.4, Figure 7.6 proves that a higher concentration of iron (Fe) is observed in the mineral bridges of the ZrO_2 scaffolds, as opposed to the lamellar walls. It is also obvious that the mineral bridge (~5 μm) is much thicker than the lamellar walls (~1 μm).

Experimental observations show that increasing the concentration of Fe_3O_4 nanoparticles or the field strength results in longer and thicker mineral bridges. This phenomenon is due to the distinct phase separation that occurs between the magnetic (Fe_3O_4) and diamagnetic (ZrO_2) particles during the freezing process. According to solidification theory (refer to Chapter 3), larger particles are more likely to be trapped by the approaching ice front, leading to the formation of mineral bridges [75]. That is, particle rejection (formation of lamellar walls) and entrapment (formation of mineral bridges) is governed by the critical velocity of the freezing front [78]:

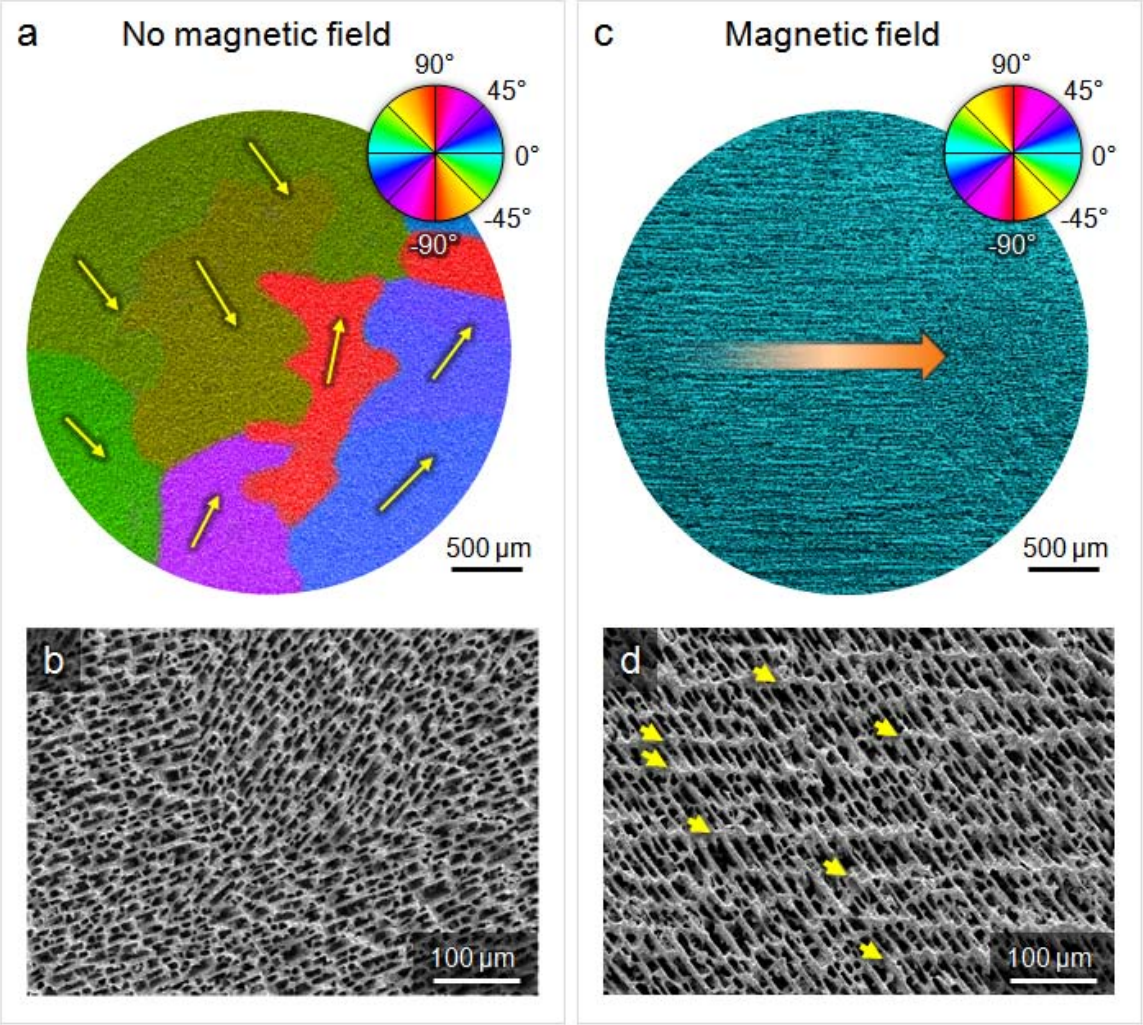

Figure 7.5. Representative images of ZrO_2 (+ 5 wt.% Fe_3O_4) scaffolds freeze cast under: **(a-b)** no magnetic field and **(c-d)** a uniform magnetic field of ~0.1 T. The SEM images (top) are colored according to the parallel alignment of **(a)** lamellar walls and **(c)** mineral bridges from -90° to +90°, corresponding to the color wheels (top right). The SEM micrographs show representative images of **(b)** randomly oriented lamellar walls and **(d)** aligned mineral bridges. The orange arrow in (c) represents the direction of the magnetic field. The yellow arrows in (d) point out several aligned mineral bridges.

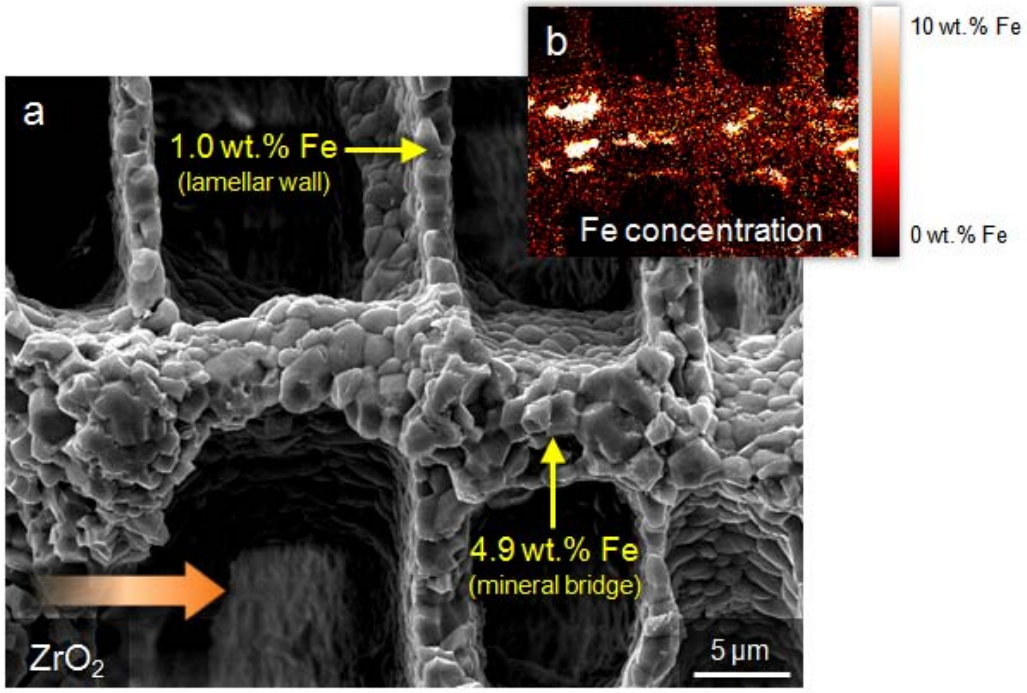

Figure 7.6. (a) Micrograph of a magnetically aligned ZrO_2 (+ 3 wt.% Fe_3O_4) mineral bridge, illustrating the fractions of iron (Fe) concentrated in the mineral bridge (4.9 wt.%) and a lamellar wall (1.0 wt.%). The orange arrow represents the direction of the magnetic field. **(b)** Elemental map of the scaffold in shown in (a), illustrating the concentration distribution of Fe throughout the microstructure, according to the color scale (top right).

$$v_{cr} = \frac{\Delta\sigma_0 d}{3\eta r}\left(\frac{a_0}{d}\right)^n \tag{7.3}$$

where $\Delta\sigma_0$ is the thermodynamic free energy of the system, d is the liquid layer thickness between the particle and the freezing front, a_0 is the mean distance between molecules in the liquid layer, n an exponential correction value, η is the dynamic viscosity of the liquid, and r is the particle radius. From this equation, it is apparent that increasing the colloid particle size ($\uparrow r$) will decrease the critical velocity for particle entrapment ($\downarrow v_{cr}$), leading to more mineral bridging. Following this theory, the magnetic aggregation of

particle chains or clusters will increase the *apparent* radii (r) of the colloids, leading to a higher degree of particle entrapment. Because these clusters (with large *apparent* radii) are linearly aligned parallel to the magnetic field, they are entrapped by the approaching ice front, regardless of the orientation and size of the growing ice crystals. The diamagnetic (ZrO_2) particles, however, are unaffected by the magnetic field and form characteristic, randomly oriented domains of parallel lamellar walls.

7.3.4.3. Biphasic reinforcement (gradient magnetic fields)

The resulting microstructural organization of scaffolds freeze cast under gradient magnetic fields is quite different from those of uniform magnetic fields. As shown in Figures 7.2 e-f, gradient magnetic fields produce biphasic density gradients in the TiO_2 scaffolds (Figure 7.2e) and biphasic composition gradients in the ZrO_2 scaffolds (Figure 7.2f). To better illustrate these structural differences, Figure 7.7 compares the structural hierarchy of two cylindrical scaffolds freeze cast under identical conditions at 10 °C/min with rotating magnetic fields of ~0.1 T at 0.05 rpm.

Again, it is obvious from the color of the TiO_2 scaffold that the Fe_3O_4 and TiO_2 (paramagnetic) particles do not separate into two distinct compositional phases (see Figures 7.7a-b). However, upon observation of a μCT scan (Figure 7.7c), it becomes apparent that there is a distinct density separation from the central region (green, corresponding to a porosity of ~65%) to the helical region (orange, corresponding to a and porosity of ~60%). This redistribution of density occurs because the magnetic particles attract and aggregate with paramagnetic particles near the poles of the magnet with higher field strengths (refer to

Figure 7.2d). Regardless of this density redistribution, the general microstructure of the TiO_2 scaffold throughout its cross-section is fairly uniform, similar to that shown in Figures 7.7d-e.

Conversely, the different colors (brown and white) of the ZrO_2 scaffolds shown in Figures 7.7f-g clearly show that there is a the distinct compositional phase separation between the helical, Fe_3O_4-rich (brown) and central, Fe_3O_4-poor (white) regions. Figures 7.7h-i show representative micrographs of these regions, respectively. Similar to the scaffolds fabricated under a uniform magnetic field (refer to Figure 7.5c-d), the cross-section of the helical region (brown) contains several long, continuously connected mineral bridges aligned parallel to the direction of the magnetic field (see Figure 7.7h). On the other hand, the central region (white) does not show any degree of magnetic alignment (Figure 7.7i). In addition, the ZrO_2 scaffold (Figure 7.7f-j) shows a large variation of porosity, from ~70% in the central (white) region to ~50% in the helical region.

Recently, Porter et al. [91] demonstrated that ZrO_2 scaffolds with similar helical architectures have a lower porosity in the helical regions (brown) than in the central region (white) as well. Utilizing this helical redistribution of material, they [91] determined that the helical perimeter acts as a type of reinforcing structure against torsional moments. By that notion, gradient magnetic fields could be used to locally redistribute ceramic particles in freeze cast scaffolds, thereby changing the localized response of particular features - a concept recently demonstrated by Erb et al. [81] for platelet-reinforced composites.

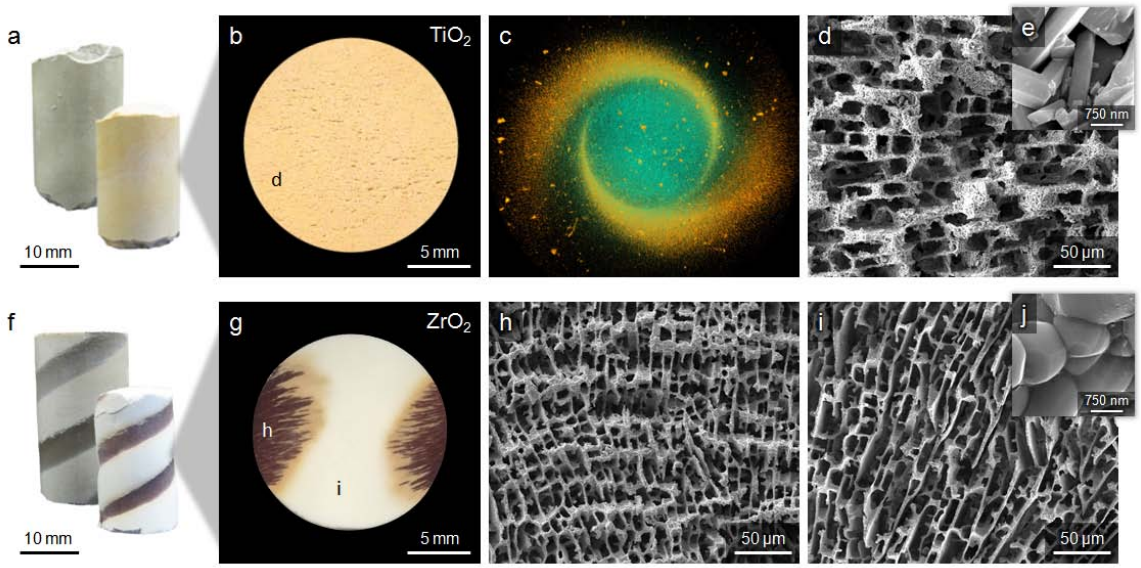

Figure 7.7. Structural hierarchy of **(a-e)** TiO_2 scaffolds and **(f-j)** ZrO_2 scaffolds, both containing 3 wt.% Fe_3O_4 and freeze cast at 10°C/min under a rotating magnetic field of ~0.1 T at 0.05 rpm: **(a, f)** macro images of the cylindrical scaffolds before (back) and after (front) sintering at predetermined temperatures of 900°C and 1300°C, respectively; **(b, g)** macro images of the scaffold cross-sections; **(c)** µCT image of the sintered TiO_2 scaffold shown in (a), where orange represents the higher-density helical region and green represents the lower-density central region; **(d, e)** representative micrographs of the TiO_2 scaffold (d) cross-section and (e) lamellar wall in the helical region; **(h-j)** representative micrographs of the ZrO_2 scaffold (h) cross-section in the helical region, (i) cross-section in the central region, and (j) lamellar wall in the helical region. The letters in (b) and (g) correspond to the imaging locations of the micrographs shown in (d), (h), and (i).

7.3.5. Enhanced mechanical performance

In summary, uniform and gradient external magnetic fields may be applied to the ice templating process to align a range of microstructures in freeze cast scaffolds: lamellar walls, mineral bridges, and biphasic reinforcements. But, how do these microstructures affect the mechanical performance?

Figure 7.8 contains plots showing how the magnetic alignment of ice templated ceramics leads to enhanced mechanical performance. Under static uniform magnetic fields, the alignment of lamellar walls (blue) and mineral bridges (red) in TiO_2 and ZrO_2 scaffolds, respectively, both lead to increased strength (Figure 7.8a) and stiffness (Figure 7.8b) when compressed parallel to the magnetic field and perpendicular to the ice growth direction. Under rotating gradient magnetic fields, ZrO_2-epoxy composites twisted along the ice growth axis showed enhanced torsional rigidity (effective shear modulus), varying with the angle of helix-reinforcement (Figure 7.8c), as previously reported [91]. Although these magnetic alignment mechanisms may slightly alter the continuity of microstructural alignment in the ice growth direction, the change in mechanical performance is negligible compared to the increase in performance experienced in the transverse (magnetic field) directions (depending on the exact processing conditions, of course) [88]. Thus, these alignment mechanisms, and several others that have yet to be discovered, are effective means to reinforce ice templated ceramics.

When comparing the mechanical effect of the lamellar wall and mineral bridge alignment mechanisms (Figures 7.8a-b), it is apparent that increasing the concentration of Fe_3O_4 in the scaffolds changes the compressive performance parallel to the magnetic field direction. Even though it seems that the mineral bridge alignment leads to better

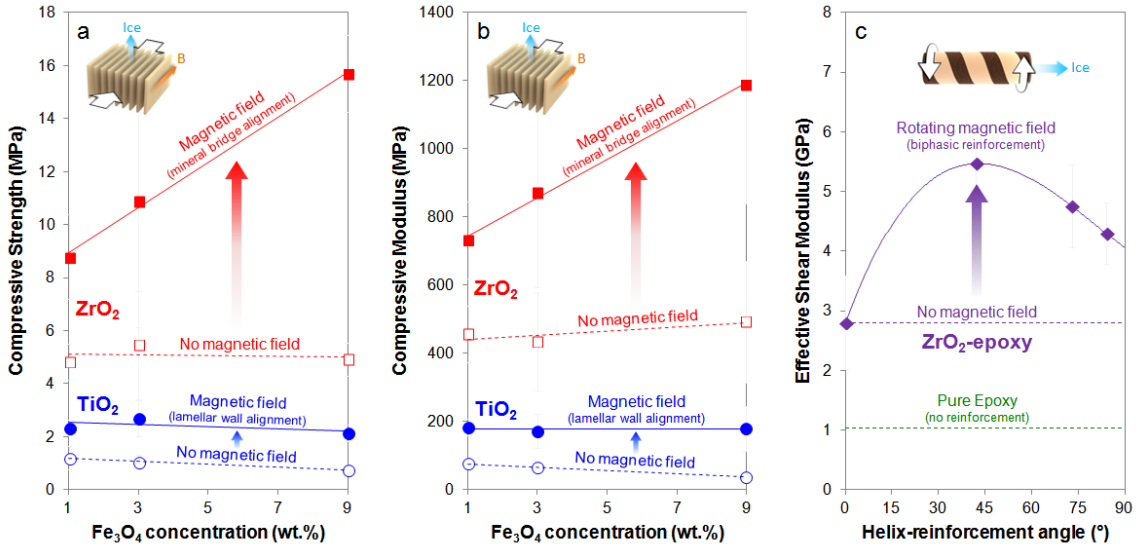

Figure 7.8. Mechanical properties of magnetically aligned ice templated ceramics: **(a-b)** Strength and modulus of TiO_2 (blue) and ZrO_2 (red) scaffolds compressed parallel the magnetic field (orange arrow), perpendicular to the ice growth direction (blue arrow). All scaffolds were freeze cast at 10°C/min under a uniform magnetic field of ~0.1 T. All scaffolds were ~90% porous. Each data point corresponds to the average of three samples (N=3). **(c)** Torsional properties of pure epoxy (green) and ZrO_2-epoxy composites (purple) with varying angles of helix reinforcement, twisted about the ice growth axis. All composites contain ~60 vol.% ZrO_2 and ~40 vol.% epoxy. The dashed purple line represents a ZrO_2-epoxy composite fabricated under no magnetic field. Data adapted from [91].

compressive properties, over the lamellar wall alignment, it should be noted that in both cases (with the addition of 3 wt.% Fe_3O_4) the compressive strength and stiffness of the scaffolds is nearly doubled when subjected to a static, uniform magnetic field (refer to Figure 7.8a-b). In the TiO_2 scaffolds, increasing the Fe_3O_4 concentration does not increase the mechanical properties any more than a small addition (1 wt.%) of Fe_3O_4 nanoparticles (blue lines, Figure 7.8a-b) [88]. This is because the compressive properties are dependent on the alignment of the lamellar walls in the scaffold. Once an optimal concentration (~1 wt.%) of Fe_3O_4 is added to the colloidal suspension, linear clusters (or

chains) of magnetic and paramagnetic particles form nucleation sites for the growth of parallel ice crystals. Increasing the concentration of Fe_3O_4 will not add any further reinforcement, as the orientation of the lamellar walls governs the mechanical behavior. In contrast, increasing the Fe_3O_4 concentration in the ZrO_2 scaffolds leads to longer and thicker aligned mineral bridges, resulting in enhanced compressive properties (red lines, Figure 7.8a-b). This is because the mechanical performance of the scaffolds in the magnetic field direction is directly dependent on the orientation, continuity, length, and thickness of the mineral bridges. Therefore, adding more Fe_3O_4 to a freezing colloidal suspension allows for the entrapment of larger particle chains that form aligned mineral bridges.

In the case of biphasic helical reinforcement (Figure 7.8c), Porter et al. [91] compared experimental results with simplified analytical theories to explain why the helical reinforcement enhanced the torsional properties of ZrO_2-epoxy composites (refer to Chapter 6). In conclusion, an optimal helix-reinforcement angle of 45° was determined to stiffen the composite cylinders in torsion, leading to an effective shear modulus nearly double that of an equivalent composite freeze cast under no magnetic field (refer to Figure 7.8c) [91]. Using gradient magnetic fields in a similar manner, different types of biphasic or localized reinforcement may also be possible (the topic of ongoing research).

7.4. Conclusions

The magnetic alignment of ice templated ceramics (or magnetic freeze casting) is an efficient means to control the microstructural orientation and mechanical properties of ceramic scaffolds and hybrid composites (upon infiltration of the scaffolds with a second

phase) in prescribed directions. Since the innovation of magnetic freeze casting in 2012 [88], three distinct types of magnetically-induced architectural alignment have been discovered: (1) lamellar wall alignment, (2) mineral bridge alignment, and (3) biphasic reinforcement. Under a static, uniform magnetic field (~0.1 T), TiO_2 (paramagnetic) particles aggregate with linear chain-like clusters of Fe_3O_4 nanoparticles, leading to the evolution of lamellar walls aligned parallel to the magnetic field. When ZrO_2 (diamagnetic) particles are freeze cast with Fe_3O_4 nanoparticles under a static, uniform magnetic field (~0.1 T), the magnetic (Fe_3O_4) and diamagnetic particles segregate into two distinct phases, leading to the formation of long, continuously aligned mineral bridges. Both the alignment of lamellar walls and mineral bridges enhance the strength and stiffness of scaffolds compressed parallel to the magnetic alignment direction. The third order of alignment discovered, biphasic reinforcement, occurs when a colloidal solution is frozen under the influence of a gradient magnetic field. In the presence of a gradient magnetic field, TiO_2 (paramagnetic) scaffolds form biphasic density gradients, while ZrO_2 (diamagnetic) scaffolds form biphasic composition gradients. After infiltration with epoxy, ZrO_2-epoxy composites with helical reinforcements, formed by a rotating, gradient magnetic field, show enhanced torsional properties [91].

7.5. Acknowledgements

Chapter 7, in part, will be revised and submitted for publication in *Materials Today*, and co-authored by A. Bahadur of Bruker Biospin and M.A. Meyers, and J. McKittrick of UCSD.

CHAPTER 8:

CONCLUDING REMARKS AND FUTURE WORK

8.1. Summary

Bioinspired design is a creative, cross-disciplinary field that shares knowledge between engineering and biology disciplines to inspire new engineering technologies and explore undiscovered biological phenomena. Research in this area has led to novel bioinspired materials that mimic the structures, properties, or functions of different natural biological materials. For instance, synthetic thin films, porous scaffolds, and bulk composites that draw inspiration from the microstructural organization and mechanical properties of bone and abalone nacre have been developed through a variety of different materials processing routes. Of those, two materials processing techniques stand out as simple and convenient methods to control the architectures and microstructural alignment of ceramic-based materials: (1) freeze casting and (2) magnetic alignment.

This dissertation introduces magnetic freeze casting, a materials processing method to fabricate ceramic scaffolds and composites that draw inspiration from the microstructural alignment of bone, nacre, and other hard biological materials. Freeze casting utilizes the unidirectional growth of ice to carve out micro-architectures in freezing colloidal suspensions. Once frozen the ice is removed via lyophilization, and different post processing techniques (sintering or infiltration) can be applied to fabricate porous scaffolds or hybrid composites with unidirectionally aligned microstructures. Adding external magnetic fields to the freeze casting process allows for controlled microstructural alignment in multiple directions: ice growth and magnetic fields.

To date, three types of architectural alignment mechanisms have been discovered in magnetically aligned ice templated scaffolds: lamellar wall alignment, mineral bridge alignment, and biphasic reinforcement. Applying static uniform magnetic fields to mixtures of magnetic and paramagnetic colloids leads to scaffolds with lamellar walls aligned parallel to the ice growth and magnetic field directions. Applying static uniform magnetic fields to mixtures of magnetic and diamagnetic colloids leads to scaffolds with mineral bridges aligned parallel to magnetic field direction, regardless of the orientation of lamellar walls. Both lamellar wall and mineral bridge alignments lead to enhanced compressive properties in the magnetic field direction, when propagated transverse to the ice growth direction. Applying rotating gradient magnetic fields to freeze cast ceramics, results in helical biphasic properties, where the helical perimeters typically have a lower porosity and higher density. This biphasic helical alignment leads to enhanced torsional properties, when freeze cast composites are fabricated under a rotating magnetic field.

The potential of magnetic freeze casting is extensive and vastly unexplored - with a variety of promising applications, ranging from bone implants to lightweight armor. Utilizing different magnetic materials, field orientations, and freezing techniques, combined with secondary post processing methods [80-82, 84, 305] to fabricate magnetically aligned ceramics may result in materials with enhanced mechanical properties for a variety of structural applications. As previously reported, magnetic freeze casting could be used to develop materials for load-bearing bone implants, lightweight composites, separation filters, insulators, catalyst supports, electronic and energy storage devices, or cylindrical shafts used in torque converters for combustion engines and electric motors, sports equipment such as golf clubs or tennis racquets, and axles for

wheeled vehicles. The science behind magnetic freeze casting may help researchers better understand the physics of ice growth and the behavior of magnetorheological fluids. Further investigation in this area may lead to new processing methods to develop magnetic nanoparticles, colloidal solutions, self-assembly processes, and next-generation materials for high-performance applications.

8.2. Where to go from here?

Research related to magnetic freeze casting is currently in progress on several fronts. Experimentally, we are developing simple processing routes to magnetize a range of colloidal particles of different compositions (TiO_2, ZrO_2, Al_2O_3, hydroxyapatite and carbon, among others), sizes (with diameters and aspect ratios ranging from several nanometers to several hundred micrometers), and morphologies (spherical particles, platelets, rods, wires and nanotubes, among others). Theoretically, we are developing a comprehensive analytical approach that incorporates theories from solidification, magnetism, and colloid sciences. Combining future experiments with theory should provide a more in depth understanding of the simultaneous freezing and magnetic alignment mechanisms leading to a wide range of unexplored architectures. To do this, we will first explore different ice growth velocities (i.e., freezing rates), different magnetic susceptiblies of colloidal particles, and different magnetic field strengths. These three parameters were recently identified as the most influential properties that control whether the colloids form aligned lamellar walls, mineral bridges, or biphasic compositions. This work may impact several fields of science and engineering related to

the freezing of colloidal suspensions (solidification) or the control of magnetic fluids (magnetorheology).

Other potential areas of research could focus on the development and optimization of different freezing techniques combined with different magnetic fields. It would be especially interesting to characterize scaffolds fabricated under a range of different magnetic field orientations and strengths. Combining magnetic fields with advanced freeze casting techniques, such as flow freezing, could lead to magnetic ice templated ceramics with multiple directions of alignment. For instance, applying a uniform magnetic field perpendicular to the ice growth direction of a flowing slurry, could lead to ceramic scaffolds with three orthogonal orientations of alignment: (1) ice growth, (2) slurry flow, and (3) magnetic field. Another area to be explored is the use of magnetic fields to create localized reinforcement, by concentrating magnetic particles locally to enhanced the material properties.

Other promising areas of future research include the investigation of secondary post processing techniques, such as polymer infiltration or pressurized sintering. These methods have already been shown to greatly enhance the mechanical performance of freeze cast scaffolds, leading to extremely stiff, strong and tough ceramic materials. Performing secondary post processing techniques after magnetic freeze casting may lead to even better ceramic materials with tailored anisotropic properties.

REFERENCES

[1] Merriam-Webster Dictionary. www.merriam-webster.com.

[2] Suddath C. A Breif History of: Velcro. TIME: Time Inc.; 2010.

[3] Jusufi A, Goldman DI, Revzen S, Full RJ. Active tails enhance arboreal acrobatics in geckos. Proc Natl Acad Sci U S A 2008;105:4215-9.

[4] Full R. Learning from the gecko's tail. TED; 2009.

[5] Jones K. English Wild Flowers. http://www.seasonalwildflowers.com/july/lesser-burdock.html 2014.

[6] Fix DS. Electron Microscope. http://www.dailysciencefix.com/electron-microscope/ 2013.

[7] Jennings P. Stickybot. https://ib.berkeley.edu/alumni/postcard_5.php UC Regents; 2014.

[8] Meyers MA, McKittrick J, Chen P-Y. Structural Biological Materials: Critical Mechanics-Materials Connections. Science 2013;339:773-9.

[9] Chen PY, McKittrick J, Meyers MA. Biological materials: Functional adaptations and bioinspired designs. Prog Mater Sci 2012;57:1492-704.

[10] Meyers MA, Chen PY, Lin AYM, Seki Y. Biological materials: Structure and mechanical properties. Prog Mater Sci 2008;53:1-206.

[11] Ortiz C, Boyce MC. Materials science - Bioinspired structural materials. Science 2008;319:1053-4.

[12] Fratzl P, Weinkamer R. Nature's hierarchical materials. Prog Mater Sci 2007;52:1263-334.

[13] Wegst UGK, Ashby MF. The mechanical efficiency of natural materials. Philos Mag 2004;84:2167-81.

[14] Aizenberg J, Sundar VC, Yablon AD, Weaver JC, Chen G. Biological glass fibers: Correlation between optical and structural properties. Proc Natl Acad Sci U S A 2004;101:3358-63.

[15] Aizenberg J, Weaver JC, Thanawala MS, Sundar VC, Morse DE, Fratzl P. Skeleton of Euplectella sp.: Structural hierarchy from the nanoscale to the macroscale. Science 2005;309:275-8.

[16] Ashby MF, Gibson LJ, Wegst U, Olive R. The Mechanical-Properties Of Natural Materials .1. Material Property Charts. Proceedings of the Royal Society-Mathematical and Physical Sciences 1995;450:123-40.

[17] Bar-Cohen Y. Biomimetics: Biologically Inspired Technologies. Boca Raton: Taylor and Francis Group; 2006.

[18] Bar-Cohen Y. Biomimetics: Nature-Based Innovation. Boca Raton, Fl: CRC Press, Taylor & Francis Group, LLC; 2012.

[19] Barthelat F. Biomimetics for next generation materials. Philos Trans R Soc A-Math Phys Eng Sci 2007;365:2907-19.

[20] Barthelat F, Mirkhalaf M. The quest for stiff, strong and tough hybrid materials: an exhaustive exploration. J R Soc Interface 2013;10.

[21] Bellamkonda RV. Biomimetic materials - Marine inspiration. Nat Mater 2008;7:347-8.

[22] Bhushan B. Biomimetics: lessons from nature - an overview. Philos Trans R Soc A-Math Phys Eng Sci 2009;367:1445-86.

[23] Bhushan B. Bioinspired Structured Surfaces. Langmuir 2012;28:1698-714.

[24] Bruet BJF, Song JH, Boyce MC, Ortiz C. Materials design principles of ancient fish armour. Nat Mater 2008;7:748-56.

[25] Chen PY, Lin AYM, Lin YS, Seki Y, Stokes AG, Peyras J, et al. Structure and mechanical properties of selected biological materials. Journal of the Mechanical Behavior of Biomedical Materials 2008;1:208-26.

[26] Currey JD, Taylor JD. Mechanical Behavior of Some Mulluscan Hard Tissues. J Zool 1974;173:395-406.

[27] Currey JD, Zioupos P, Davies P, Casinos A. Mechanical Properties of Nacre and Highly Mineralized Bone. Proceedings: Biological Sciences 2001;268:107-11.

[28] Currey JD. Bones: Structure and Mechanics. Princeton, NJ: Princeton University Press; 2002.

[29] Dunlop JWC, Fratzl P. Biological Composites. In: Clarke DR, Ruhle M, Zok F, editors. Annual Review of Materials Research, Vol 402010. p. 1-24.

[30] Easterling KE, Harrysson R, Gibson LJ, Ashby MF. On The Mechanics Of Balsa And Other Woods. Proceedings of the Royal Society of London Series a-Mathematical Physical and Engineering Sciences 1982;383:31-&.

[31] Espinosa HD, Rim JE, Barthelat F, Buehler MJ. Merger of structure and material in nacre and bone - Perspectives on de novo biomimetic materials. Prog Mater Sci 2009;54:1059-100.

[32] Fratzl P. Biomimetic materials research: what can we really learn from nature's structural materials? J R Soc Interface 2007;4:637-42.

[33] Gibson LJ, Ashby MF, Karam GN, Wegst U, Shercliff HR. The Mechanical-Properties Of Natural Materials .2. Microstructures For Mechanical Efficiency. Proceedings of the Royal Society-Mathematical and Physical Sciences 1995;450:141-62.

[34] Gibson LJ, Ashby MF. Cellular Materials in Nature. Integr Comp Biol 2011;51:E47-E.

[35] Jackson AP, Vincent JFV, Turner RM. The mechanical design of nacre. Proc R Soc Lond Ser B-Biol Sci 1988;234:415-&.

[36] Ji BH, Gao HJ. Mechanical properties of nanostructure of biological materials. Journal of the Mechanics and Physics of Solids 2004;52:1963-90.

[37] Ji BH, Gao HJ. Mechanical Principles of Biological Nanocomposites. In: Clarke DR, Ruhle M, Zok F, editors. Annual Review of Materials Research, Vol 402010. p. 77-100.

[38] Launey ME, Buehler MJ, Ritchie RO. On the Mechanistic Origins of Toughness in Bone. In: Clarke DR, Ruhle M, Zok F, editors. Annual Review of Materials Research, Vol 40. Palo Alto: Annual Reviews; 2010. p. 25-53.

[39] Lee H, Lee BP, Messersmith PB. A reversible wet/dry adhesive inspired by mussels and geckos. Nature 2007;448:338-U4.

[40] Lin AY-M, Chen P-Y, Meyers MA. The growth of nacre in the abalone shell. Acta Biomaterialia 2008;4:131-8.

[41] Mayer G. Rigid biological systems as models for synthetic composites. Science 2005;310:1144-7.

[42] McKittrick J, Chen PY, Tombolato L, Novitskaya EE, Trim MW, Hirata GA, et al. Energy absorbent natural materials and bioinspired design strategies: A review. Materials Science and Engineering: C 2010;30:331-42.

[43] Meyers MA, Chen PY, Lopez MI, Seki Y, Lin AYM. Biological materials: A materials science approach. Journal of the Mechanical Behavior of Biomedical Materials 2011;4:626-57.

[44] Nalla RK, Kinney JH, Ritchie RO. Mechanistic fracture criteria for the failure of human cortical bone. Nat Mater 2003;2:164-8.

[45] Peterlik H, Roschger P, Klaushofer K, Fratzl P. From brittle to ductile fracture of bone. Nat Mater 2006;5:52-5.

[46] Ritchie RO. The conflicts between strength and toughness. Nat Mater 2011;10:817-22.

[47] Song JH, Ortiz C, Boyce MC. Threat-protection mechanics of an armored fish. Journal of the Mechanical Behavior of Biomedical Materials 2011;4:699-712.

[48] Studart AR. Towards High-Performance Bioinspired Composites. Advanced Materials 2012;24:5024-44.

[49] Studart AR, Erb RM. Bioinspired materials that self-shape through programmed microstructures. Soft Matter 2014;10:1284-94.

[50] Vollrath F, Knight DP. Liquid crystalline spinning of spider silk. Nature 2001;410:541-8.

[51] Weaver JC, Milliron GW, Miserez A, Evans-Lutterodt K, Herrera S, Gallana I, et al. The Stomatopod Dactyl Club: A Formidable Damage-Tolerant Biological Hammer. Science 2012;336:1275-80.

[52] Weiner S, Wagner HD. The material bone: Structure mechanical function relations. Annu Rev Mater Sci 1998;28:271-98.

[53] Xia F, Jiang L. Bio-inspired, smart, multiscale interfacial materials. Advanced Materials 2008;20:2842-58.

[54] Yang W, Chen IH, Gludovatz B, Zimmermann EA, Ritchie RO, Meyers MA. Natural Flexible Dermal Armor. Advanced Materials 2013;25:31-48.

[55] Zimmermann EA, Gludovatz B, Schaible E, Dave NKN, Yang W, Meyers MA, et al. Mechanical adaptability of the Bouligand-type structure in natural dermal armour. Nature Communications 2013;4.

[56] Cheong H, Chiu I, Shu LH, Stone RB, McAdams DA. Biologically Meaningful Keywords for Functional Terms of the Functional Basis. Journal of Mechanical Design 2011;133.

[57] Chiu I, Shu LH, Asme. Bridging cross-domain terminology for biomimetic design2005.

[58] Chiu I, Shu LH. Biomimetic design through natural language analysis to facilitate cross-domain information retrieval. AI EDAM-Artif Intell Eng Des Anal Manuf 2007;21:45-59.

[59] Nagel JKS, Nagel RL, Stone RB, McAdams DA. Function-based, biologically inspired concept generation. AI EDAM-Artif Intell Eng Des Anal Manuf 2010;24:521-35.

[60] Nagel JKS, Stone RB, McAdams DA, Asme. An Engineering-To-Biology Thesaurus For Engineering Design2010.

[61] Vincent JFV, Mann DL. Systematic technology transfer from biology to engineering. Philos Trans R Soc Lond Ser A-Math Phys Eng Sci 2002;360:159-73.

[62] Vincent JFV. Biomimetic modelling. Philos Trans R Soc Lond Ser B-Biol Sci 2003;358:1597-603.

[63] Vincent JFV, Bogatyreva OA, Bogatyrev NR, Bowyer A, Pahl AK. Biomimetics: its practice and theory. J R Soc Interface 2006;3:471-82.

[64] Vincent JFV. Biomimetics - a review. Proc Inst Mech Eng Part H-J Eng Med 2009;223:919-39.

[65] Shu LH, Ueda K, Chiu I, Cheong H. Biologically inspired design. Cirp Annals-Manufacturing Technology 2011;60:673-93.

[66] asknature.org. Biomimicry 3.8; 2008-2014.

[67] Ball P. Life's lessons in design. Nature 2001;409:413-6.

[68] Feynman R. There's Plenty of Room at the Bottom. 1959.

[69] Benyus J. Biomimicry: Innovation Inspired by Nature. New York: HarperCollins Publishers Inc.; 1997.

[70] Reap J, Baumeister D, Bras B, Asme. Holism, biomimicry and sustainable engineering2005.

[71] Schuenke M, Schulte E, Schumacher U, Ross LM, Lamperti ED, Voll M. General Anatomy and Musculoskeletal System. New York: Georg Thieme Verlag; 2006.

[72] Nalla RK, Kruzic JJ, Kinney JH, Balooch M, Ager JW, Ritchie RO. Role of microstructure in the aging-related deterioration of the toughness of human cortical bone. Mater Sci Eng C-Biomimetic Supramol Syst 2006;26:1251-60.

[73] Anatomy-3D. http://www.anatomy-3d.com/skeletonmuscles-big.jpg2014.

[74] Bose S, Vahabzadeh S, Bandyopadhyay A. Bone tissue engineering using 3D printing. Materials Today 2013;16:496-504.

[75] Deville S, Saiz E, Nalla RK, Tomsia AP. Freezing as a path to build complex composites. Science 2006;311:515-8.

[76] Deville S, Saiz E, Tomsia AP. Freeze casting of hydroxyapatite scaffolds for bone tissue engineering. Biomaterials 2006;27:5480-9.

[77] Fu Q, Rahaman MN, Dogan F, Bal BS. Freeze-cast hydroxyapatite scaffolds for bone tissue engineering applications. Biomed Mater 2008;3.

[78] Wegst UGK, Schecter M, Donius AE, Hunger PM. Biomaterials by freeze casting. Philos Trans R Soc A-Math Phys Eng Sci 2010;368:2099-121.

[79] Hutmacher DW. Scaffolds in tissue engineering bone and cartilage. Biomaterials 2000;21:2529-43.

[80] Bouville F, Maire E, Meille S, Van de Moortèle B, Stevenson AJ, Deville S. Strong, tough and stiff bioinspired ceramics from brittle constituents. Nat Mater 2014.

[81] Erb RM, Libanori R, Rothfuchs N, Studart AR. Composites Reinforced in Three Dimensions by Using Low Magnetic Fields. Science 2012;335:199-204.

[82] Launey ME, Munch E, Alsem DH, Saiz E, Tomsia AP, Ritchie RO. A novel biomimetic approach to the design of high-performance ceramic-metal composites. J R Soc Interface 2010;7:741-53.

[83] Libanori R, Erb RM, Studart AR. Mechanics of platelet-reinforced composites assembled using mechanical and magnetic stimuli. ACS applied materials & interfaces 2013;5:10794-805.

[84] Munch E, Launey ME, Alsem DH, Saiz E, Tomsia AP, Ritchie RO. Tough, Bio-Inspired Hybrid Materials. Science 2008;322:1516-20.

[85] Turner JS, Soar RC. Beyond biomimicry: What termites can tell us about realizing the living building. Industrialised, integrated, intelligent sustainable construction 2008:233-48.

[86] LaVan DA, Cha JN. Approaches for biological and biomimetic energy conversion. Proceedings of the National Academy of Sciences 2006;103:5251-5.

[87] Wood RJ. The first takeoff of a biologically inspired at-scale robotic insect. Robotics, IEEE Transactions on 2008;24:341-7.

[88] Porter MM, Yeh M, Strawson J, Goehring T, Lujan S, Siripasopsotorn P, et al. Magnetic freeze casting inspired by nature. Materials Science and Engineering: A 2012;556:741-50.

[89] Porter MM, Imperio R, Wen M, Meyers MA, McKittrick J. Bioinspired scaffolds with varying pore architectures and mechanical properties. Advanced Functional Materials 2013.

[90] Porter MM, McKittrick J, Meyers MA. Biomimetic Materials by Freeze Casting. JOM 2013:1-8.

[91] Porter MM, Meraz L, Calderon A, Choi H, Chouhan A, Wang L, et al. Torsional properties of helix-reinforced composites fabricated by magnetic freeze casting. Composites Part A: Applied Science and Manufacturing 2014;(under review).

[92] Porter MM, Bahadur A, Meyers MA, McKittrick J. Magnetic Alignment of Ice Templated Ceramics. Materials Today 2014;(in progress).

[93] Meyers MA, Hodge AM, Roeder RK. Biological materials science and engineering: Biological materials, biomaterials, and biomimetics. JOM 2008;60:21-2.

[94] Lazaris A, Arcidiacono S, Huang Y, Zhou JF, Duguay F, Chretien N, et al. Spider silk fibers spun from soluble recombinant silk produced in mammalian cells. Science 2002;295:472-6.

[95] Seidel A, Liivak O, Jelinski LW. Artificial spinning of spider silk. Macromolecules 1998;31:6733-6.

[96] Xia XX, Qian ZG, Ki CS, Park YH, Kaplan DL, Lee SY. Native-sized recombinant spider silk protein produced in metabolically engineered Escherichia coli results in a strong fiber. Proc Natl Acad Sci U S A 2010;107:14059-63.

[97] Chung WJ, Oh JW, Kwak K, Lee BY, Meyer J, Wang E, et al. Biomimetic self-templating supramolecular structures. Nature 2011;478:364-8.

[98] Cui FZ, Li Y, Ge J. Self-assembly of mineralized collagen composites. Mater Sci Eng R-Rep 2007;57:1-27.

[99] Kotch FW, Raines RT. Self-assembly of synthetic collagen triple helices. Proc Natl Acad Sci U S A 2006;103:3028-33.

[100] Boesel LF, Greiner C, Arzt E, del Campo A. Gecko-Inspired Surfaces: A Path to Strong and Reversible Dry Adhesives. Advanced Materials 2010;22:2125-37.

[101] Dean B, Bhushan B. Shark-skin surfaces for fluid-drag reduction in turbulent flow: a review. Philos Trans R Soc A-Math Phys Eng Sci 2010;368:4775-806.

[102] Oeffner J, Lauder GV. The hydrodynamic function of shark skin and two biomimetic applications. The Journal of Experimental Biology 2012;215:785-95.

[103] Wainwright SA, Vosburgh F, Hebrank JH. Shark Skin - Function In Locomotion. Science 1978;202:747-9.

[104] Carman ML, Estes TG, Feinberg AW, Schumacher JF, Wilkerson W, Wilson LH, et al. Engineered antifouling microtopographies - correlating wettability with cell attachment. Biofouling 2006;22:11-21.

[105] Huang YF, Chattopadhyay S, Jen YJ, Peng CY, Liu TA, Hsu YK, et al. Improved broadband and quasi-omnidirectional anti-reflection properties with biomimetic silicon nanostructures. Nat Nanotechnol 2007;2:770-4.

[106] Li YF, Zhang JH, Zhu SJ, Dong HP, Jia F, Wang ZH, et al. Biomimetic Surfaces for High-Performance Optics. Advanced Materials 2009;21:4731-+.

[107] Parker AR, Townley HE. Biomimetics of photonic nanostructures. Nat Nanotechnol 2007;2:347-53.

[108] Vukusic P, Sambles JR. Photonic structures in biology. Nature 2003;424:852-5.

[109] Cha JN, Stucky GD, Morse DE, Deming TJ. Biomimetic synthesis of ordered silica structures mediated by block copolypeptides. Nature 2000;403:289-92.

[110] Sarikaya M, Fong H, Sunderland N, Flinn BD, Mayer G, Mescher A, et al. Biomimetic model of a sponge-spicular optical fiber - mechanical properties and structure. Journal of Materials Research 2001;16:1420-8.

[111] Li X-M, Reinhoudt D, Crego-Calama M. What do we need for a superhydrophobic surface? A review on the recent progress in the preparation of superhydrophobic surfaces. Chemical Society Reviews 2007;36:1350-68.

[112] Solga A, Cerman Z, Striffler BF, Spaeth M, Barthlott W. The dream of staying clean: Lotus and biomimetic surfaces. Bioinspir Biomim 2007;2:S126-S34.

[113] Blaiszik BJ, Kramer SLB, Olugebefola SC, Moore JS, Sottos NR, White SR. Self-Healing Polymers and Composites. In: Clarke DR, Ruhle M, Zok F, editors. Annual Review of Materials Research, Vol 402010. p. 179-211.

[114] Huiskes R, Ruimerman R, van Lenthe GH, Janssen JD. Effects of mechanical forces on maintenance and adaptation of form in trabecular bone. Nature 2000;405:704-6.

[115] White SR, Sottos NR, Geubelle PH, Moore JS, Kessler MR, Sriram SR, et al. Autonomic healing of polymer composites. Nature 2001;409:794-7.

[116] Capadona JR, Shanmuganathan K, Tyler DJ, Rowan SJ, Weder C. Stimuli-responsive polymer nanocomposites inspired by the sea cucumber dermis. Science 2008;319:1370-4.

[117] Bar-Cohen Y. Biomimetics using electroactive polymers (EAP) as artificial muscles - A review. J Adv Mater 2006;38:3-9.

[118] Ratna D, Karger-Kocsis J. Recent advances in shape memory polymers and composites: a review. Journal of Materials Science 2008;43:254-69.

[119] Jani JM, Leary M, Subic A, Gibson MA. A review of shape memory alloy research, applications and opportunities. Materials & Design 2014;56:1078-113.

[120] Behl M, Lendlein A. Shape-memory polymers. Materials Today 2007;10:20-8.

[121] Deville S. Freeze-casting of porous ceramics: A review of current achievements and issues. Advanced Engineering Materials 2008;10:155-69.

[122] Freyman TM, Yannas IV, Gibson LJ. Cellular materials as porous scaffolds for tissue engineering. Prog Mater Sci 2001;46:273-82.

[123] Ma PX. Biomimetic materials for tissue engineering. Adv Drug Deliv Rev 2008;60:184-98.

[124] Hollister SJ. Porous scaffold design for tissue engineering. Nat Mater 2005;4:518-24.

[125] Chen PY, McKittrick J. Compressive mechanical properties of demineralized and deproteinized cancellous bone. Journal of the Mechanical Behavior of Biomedical Materials 2011;4:961-73.

[126] Lee S, Porter M, Wasko S, Lau G, Chen P-Y, Novitskaya EE, et al. Potential Bone Replacement Materials Prepared by Two Methods. MRS Online Proceedings Library 2012;1418:null-null.

[127] Tian J, Tian J. Preparation of porous hydroxyapatite. Journal of Materials Science 2001;36:3061-6.

[128] Dorozhkin SV, Epple M. Biological and medical significance of calcium phosphates. Angew Chem-Int Edit 2002;41:3130-46.

[129] Ramay HR, Zhang M. Preparation of porous hydroxyapatite scaffolds by combination of the gel-casting and polymer sponge methods. Biomaterials 2003;24:3293-302.

[130] Keaveny TM, Morgan EF, Niebur GL, Yeh OC. Biomechanics of trabecular bone. Annual Review of Biomedical Engineering 2001;3:307-33.

[131] Hamed E, Novitskaya E, Li J, Chen PY, Jasiuk I, McKittrick J. Elastic moduli of untreated, demineralized and deproteinized cortical bone: Validation of a theoretical model of bone as an interpenetrating composite material. Acta Biomaterialia 2012;8:1080-92.

[132] Novitskaya E, Chen PY, Lee S, Castro-Cesena A, Hirata G, Lubarda VA, et al. Anisotropy in the compressive mechanical properties of bovine cortical bone and the mineral and protein constituents. Acta Biomaterialia 2011;7:3170-7.

[133] Chen PY, Toroian D, Price PA, McKittrick J. Minerals Form a Continuum Phase in Mature Cancellous Bone. Calcif Tissue Int 2011;88:351-61.

[134] Lin AY-M, Meyers MA. Interfacial shear strength in abalone nacre. Journal of the Mechanical Behavior of Biomedical Materials 2009;2:607-12.

[135] Lopez MI, Meza Martinez PE, Meyers MA. Organic interlamellar layers, mesolayers and mineral nanobridges: Contribution to strength in abalone (< i> Haliotis rufescence</i>) nacre. Acta Biomaterialia 2013.

[136] Gries K, Kröger R, Kübel C, Schowalter M, Fritz M, Rosenauer A. Correlation of the orientation of stacked aragonite platelets in nacre and their connection via mineral bridges. Ultramicroscopy 2009;109:230-6.

[137] Meyers MA, Lin AY-M, Chen P-Y, Muyco J. Mechanical strength of abalone nacre: Role of the soft organic layer. Journal of the Mechanical Behavior of Biomedical Materials 2008;1:76-85.

[138] Lopez MI, Chen PY, McKittrick J, Meyers MA. Growth of nacre in abalone: Seasonal and feeding effects. Mater Sci Eng C-Mater Biol Appl 2011;31:238-45.

[139] Kakisawa H, Sumitomo T. The toughening mechanism of nacre and structural materials inspired by nacre. Sci Technol Adv Mater 2011;12.

[140] Nalla RK, Kruzic JJ, Ritchie RO. On the origin of the toughness of mineralized tissue: microcracking or crack bridging? Bone 2004;34:790-8.

[141] Sun JY, Bhushan B. Hierarchical structure and mechanical properties of nacre: a review. RSC Adv 2012;2:7617-32.

[142] Novitskaya E, Chen P-Y, Lee S, Castro-Ceseña A, Hirata G, Lubarda VA, et al. Anisotropy in the compressive mechanical properties of bovine cortical bone and the mineral and protein constituents. Acta Biomaterialia 2011;7:3170-7.

[143] Weiner S, Traub W, Wagner HD. Lamellar bone: structure–function relations. J Struct Biol 1999;126:241-55.

[144] Chen PY, Lin AYM, McKittrick J, Meyers MA. Structure and mechanical properties of crab exoskeletons. Acta Biomaterialia 2008;4:587-96.

[145] Giraud MM, Castanet J, Meunier FJ, Bouligand Y. Fibrous Structure of Coelacanth Scales - Twisted Plywood. Tissue Cell 1978;10:671-86.

[146] Giraud-Guille M. Twisted plywood architecture of collagen fibrils in human compact bone osteons. Calcif Tissue Int 1988;42:167-80.

[147] Raabe D, Sachs C, Romano P. The crustacean exoskeleton as an example of a structurally and mechanically graded biological nanocomposite material. Acta Materialia 2005;53:4281-92.

[148] Bouligand Y. Twisted Fibrous Arrangements in Biological-Materials and Cholesteric Mesophases. Tissue Cell 1972;4:189-&.

[149] Lin A, Meyers MA. Growth and structure in abalone shell. Materials Science and Engineering: A 2005;390:27-41.

[150] Hyer MW. Stress Analysis of Fiber-Reinforced Composite Materials. Boston: WCB McGraw Hill; 1998.

[151] Bonderer LJ, Studart AR, Gauckler LJ. Bioinspired design and assembly of platelet reinforced polymer films. Science 2008;319:1069-73.

[152] Yao H, Gao H. Multi-scale cohesive laws in hierarchical materials. Int J Solids Struct 2007;44:8177-93.

[153] Hamed E, Jasiuk I, Yoo A, Lee Y, Liszka T. Multi-scale modelling of elastic moduli of trabecular bone. J R Soc Interface 2012;9:1654-73.

[154] Gao HJ. Application of fracture mechanics concepts to hierarchical biomechanics of bone and bone-like materials. International Journal of Fracture 2006;138:101-37.

[155] Buehler MJ, Keten S, Ackbarow T. Theoretical and computational hierarchical nanomechanics of protein materials: Deformation and fracture. Prog Mater Sci 2008;53:1101-241.

[156] Bruck HA, Evans JJ, Peterson ML. The role of mechanics in biological and biologically inspired materials. Experimental Mechanics 2002;42:361-71.

[157] Tang ZY, Kotov NA, Magonov S, Ozturk B. Nanostructured artificial nacre. Nat Mater 2003;2:413-U8.

[158] Podsiadlo P, Kaushik AK, Arruda EM, Waas AM, Shim BS, Xu JD, et al. Ultrastrong and stiff layered polymer nanocomposites. Science 2007;318:80-3.

[159] Walther A, Bjurhager I, Malho JM, Ruokolainen J, Berglund L, Ikkala O. Supramolecular Control of Stiffness and Strength in Lightweight High-Performance Nacre-Mimetic Paper with Fire-Shielding Properties. Angew Chem-Int Edit 2010;49:6448-53.

[160] Fu QA, Saiz E, Tomsia AP. Bioinspired Strong and Highly Porous Glass Scaffolds. Advanced Functional Materials 2011;21:1058-63.

[161] Estili M, Kawasaki A, Sakka Y. Highly Concentrated 3D Macrostructure of Individual Carbon Nanotubes in a Ceramic Environment. Advanced Materials 2012;24:4322-+.

[162] Walther A, Bjurhager I, Malho JM, Pere J, Ruokolainen J, Berglund LA, et al. Large-Area, Lightweight and Thick Biomimetic Composites with Superior Material Properties via Fast, Economic, and Green Pathways. Nano Letters 2010;10:2742-8.

[163] Li Y-Q, Yu T, Yang T-Y, Zheng L-X, Liao K. Bio-Inspired Nacre-like Composite Films Based on Graphene with Superior Mechanical, Electrical, and Biocompatible Properties. Advanced Materials 2012;24:3426-31.

[164] Cheng QF, Li MZ, Jiang L, Tang ZY. Bioinspired Layered Composites Based on Flattened Double-Walled Carbon Nanotubes. Advanced Materials 2012;24:1838-43.

[165] Almirall A, Larrecq G, Delgado JA, Martinez S, Planell JA, Ginebra MP. Fabrication of low temperature macroporous hydroxyapatite scaffolds by foaming and hydrolysis of an alpha-TCP paste. Biomaterials 2004;25:3671-80.

[166] Kim HW, Lee SY, Bae CJ, Noh YJ, Kim HE, Kim HM, et al. Porous ZrO2 bone scaffold coated with hydroxyapatite with fluorapatite intermediate layer. Biomaterials 2003;24:3277-84.

[167] Tampieri A, Sprio S, Ruffini A, Celotti G, Lesci IG, Roveri N. From wood to bone: multi-step process to convert wood hierarchical structures into biomimetic hydroxyapatite scaffolds for bone tissue engineering. J Mater Chem 2009;19:4973-80.

[168] Currey J. Mechanical properties of mother of pearl in tension. Proceedings of the Royal Society of London Series B Biological Sciences 1977;196:443-63.

[169] Gibson LJ. The Mechanical-Behavior Of Cancellous Bone. J Biomech 1985;18:317-&.

[170] Goldstein SA. The Mechanical-Properties Of Trabecular Bone - Dependence On Anatomic Location And Function. J Biomech 1987;20:1055-61.

[171] Koester KJ, Ager JW, Ritchie RO. The true toughness of human cortical bone measured with realistically short cracks. Nat Mater 2008;7:672-7.

[172] Menig R, Meyers M, Meyers M, Vecchio K. Quasi-static and dynamic mechanical response of< i> Haliotis rufescens</i>(abalone) shells. Acta Materialia 2000;48:2383-98.

[173] Reilly DT, Burstein AH. Review Article - Mechanical-Properties Of Cortical Bone. Journal of Bone and Joint Surgery-American Volume 1974;A 56:1001-22.

[174] Rohl L, Larsen E, Linde F, Odgaard A, Jorgensen J. Tensile And Compressive Properties Of Cancellous Bone. J Biomech 1991;24:1143-9.

[175] Corni I, Harvey TJ, Wharton JA, Stokes KR, Walsh FC, Wood RJK. A review of experimental techniques to produce a nacre-like structure. Bioinspir Biomim 2012;7.

[176] Yao HB, Ge J, Mao LB, Yan YX, Yu SH. 25th Anniversary Article: Artificial Carbonate Nanocrystals and Layered Structural Nanocomposites Inspired by Nacre: Synthesis, Fabrication and Applications. Advanced Materials 2014;26:163-88.

[177] Kleinfeld ER, Ferguson GS. Stepwise Formation Of Multilayered Nanostructural Films From Macromolecular Precursors. Science 1994;265:370-3.

[178] Wei H, Ma N, Shi F, Wang ZQ, Zhang X. Artificial nacre by alternating preparation of layer-by-layer polymer films and CaCO3 strata. Chemistry of Materials 2007;19:1974-8.

[179] Yao HB, Fang HY, Tan ZH, Wu LH, Yu SH. Biologically Inspired, Strong, Transparent, and Functional Layered Organic-Inorganic Hybrid Films. Angew Chem-Int Edit 2010;49:2140-5.

[180] Aksay IA, Trau M, Manne S, Honma I, Yao N, Zhou L, et al. Biomimetic pathways for assembling inorganic thin films. Science 1996;273:892-8.

[181] Zhang SM, Zhang JW, Zhang ZJ, Dang HX, Liu WM, Xue QJ. Preparation and characterization of self-assembled organic-inorganic nacre-like nanocomposite thin films. Materials Letters 2004;58:2266-9.

[182] Xu GF, Yao N, Aksay IA, Groves JT. Biomimetic synthesis of macroscopic-scale calcium carbonate thin films. Evidence for a multistep assembly process. Journal of the American Chemical Society 1998;120:11977-85.

[183] Chen R, Wang C-a, Huang Y, Le H. An efficient biomimetic process for fabrication of artificial nacre with ordered-nanostructure. Materials Science and Engineering: C 2008;28:218-22.

[184] Bennadji-Gridi F, Smith A, Bonnet JP. Montmorillonite based artificial nacre prepared via a drying process. Materials Science and Engineering B-Solid State Materials for Advanced Technology 2006;130:132-6.

[185] Yao HB, Tan ZH, Fang HY, Yu SH. Artificial Nacre-like Bionanocomposite Films from the Self-Assembly of Chitosan-Montmorillonite Hybrid Building Blocks. Angew Chem-Int Edit 2010;49:10127-31.

[186] Sellinger A, Weiss PM, Nguyen A, Lu YF, Assink RA, Gong WL, et al. Continuous self-assembly of organic-inorganic nanocomposite coatings that mimic nacre. Nature 1998;394:256-60.

[187] Li XQ, Zeng HC. Calcium Carbonate Nanotablets: Bridging Artificial to Natural Nacre. Advanced Materials 2012;24:6277-82.

[188] Cheng QF, Wu MX, Li MZ, Jiang L, Tang ZY. Ultratough Artificial Nacre Based on Conjugated Cross-linked Graphene Oxide. Angew Chem-Int Edit 2013;52:3750-5.

[189] Sofie SW. Fabrication of Functionally Graded and Aligned Porosity in Thin Ceramic Substrates With the Novel Freeze–Tape-Casting Process. Journal of the American Ceramic Society 2007;90:2024-31.

[190] Liu T, Chen BQ, Evans JRG. Ordered assemblies of clay nano-platelets. Bioinspir Biomim 2008;3.

[191] Lin TH, Huang WH, Jun IK, Jiang P. Bioinspired Assembly of Colloidal Nanoplatelets by Electric Field. Chemistry of Materials 2009;21:2039-44.

[192] Lin TH, Huang WH, Jun IK, Jiang P. Electrophoretic co-deposition of biomimetic nanoplatelet-polyelectrolyte composites. Electrochemistry Communications 2009;11:1635-8.

[193] Lin TH, Huang WH, Jun IK, Jiang P. Electrophoretic deposition of biomimetic nanocomposites. Electrochemistry Communications 2009;11:14-7.

[194] Lin W, Wang CA, Le HL, Long B, Huang Y. Special assembly of laminated nanocomposite that mimics nacre. Mater Sci Eng C-Biomimetic Supramol Syst 2008;28:1031-7.

[195] Long B, Wang CA, Lin W, Huang Y, Sun JL. Polyacrylamide-clay nacre-like nanocomposites prepared by electrophoretic deposition. Compos Sci Technol 2007;67:2770-4.

[196] Burghard Z, Tucic A, Jeurgens LPH, Hoffmann RC, Bill J, Aldinger F. Nanomechanical properties of bioinspired organic-inorganic composite films. Advanced Materials 2007;19:970-+.

[197] Burghard Z, Zini L, Srot V, Bellina P, van Aken PA, Bill J. Toughening through Nature-Adapted Nanoscale Design. Nano Letters 2009;9:4103-8.

[198] Glinel K, Laschewsky A, Jonas AM. Ordered polyelectrolyte "multilayers". 4. Internal structure of clay-based multilayers. J Phys Chem B 2002;106:11246-52.

[199] Liu CH, Li WZ, Li HD, He JL. Micro-assembling of carbide/metal by ion-beam sputtering process. Surface & Coatings Technology 1996;84:420-4.

[200] Volkmer D, Harms M, Gower L, Ziegler A. Morphosynthesis of nacre-type laminated CaCO3 thin films and coatings. Angew Chem-Int Edit 2005;44:639-44.

[201] Ma PX. Scaffolds for tissue fabrication. Materials Today 2004;7:30-40.

[202] Almirall A, Larrecq G, Delgado JA, Martínez S, Planell JA, Ginebra MP. Fabrication of low temperature macroporous hydroxyapatite scaffolds by foaming and hydrolysis of an α-TCP paste. Biomaterials 2004;25:3671-80.

[203] Barralet JE, Grover L, Gaunt T, Wright AJ, Gibson IR. Preparation of macroporous calcium phosphate cement tissue engineering scaffold. Biomaterials 2002;23:3063-72.

[204] Charrière E, Lemaitre J, Zysset P. Hydroxyapatite cement scaffolds with controlled macroporosity: fabrication protocol and mechanical properties. Biomaterials 2003;24:809-17.

[205] Chu TMG, Orton DG, Hollister SJ, Feinberg SE, Halloran JW. Mechanical and in vivo performance of hydroxyapatite implants with controlled architectures. Biomaterials 2002;23:1283-93.

[206] del Real RP, Wolke JGC, Vallet-Regi M, Jansen JA. A new method to produce macropores in calcium phosphate cements. Biomaterials 2002;23:3673-80.

[207] Dong J, Kojima H, Uemura T, Kikuchi M, Tateishi T, Tanaka J. In vivo evaluation of a novel porous hydroxyapatite to sustain osteogenesis of transplanted bone marrow-derived osteoblastic cells. Journal of Biomedical Materials Research 2001;57:208-16.

[208] Ioku K, Yanagisawa K, Yamasaki N, Kurosawa H, Shibuya K, Yokozeki H. Preparation and characterization of porous apatite ceramics coated with beta-tricalcium phosphate. Biomed Mater Eng 1993;3:137-45.

[209] Kawata M, Uchida H, Itatani K, Okada I, Koda S, Aizawa M. Development of porous ceramics with well-controlled porosities and pore sizes from apatite fibers and their evaluations. J Mater Sci-Mater Med 2004;15:817-23.

[210] Landi E, Celotti G, Logroscino G, Tampieri A. Carbonated hydroxyapatite as bone substitute. Journal of the European Ceramic Society 2003;23:2931-7.

[211] Liu D-M. Influence of porosity and pore size on the compressive strength of porous hydroxyapatite ceramic. Ceramics International 1997;23:135-9.

[212] Milosevski M, Bossert J, Milosevski D, Gruevska N. Preparation and properties of dense and porous calcium phosphate. Ceramics International 1999;25:693-6.

[213] Ota Y, Kasuga T, Abe Y. Preparation and Compressive Strength Behavior of Porous Ceramics with β-Ca(PO3)2 Fiber Skeletons. Journal of the American Ceramic Society 1997;80:225-31.

[214] Pilliar RM, Filiaggi MJ, Wells JD, Grynpas MD, Kandel RA. Porous calcium polyphosphate scaffolds for bone substitute applications — in vitro characterization. Biomaterials 2001;22:963-72.

[215] Ramay HRR, Zhang M. Biphasic calcium phosphate nanocomposite porous scaffolds for load-bearing bone tissue engineering. Biomaterials 2004;25:5171-80.

[216] Sous M, Bareille R, Rouais F, Clément D, Amédée J, Dupuy B, et al. Cellular biocompatibility and resistance to compression of macroporous β-tricalcium phosphate ceramics. Biomaterials 1998;19:2147-53.

[217] Tancred DC, McCormack BAO, Carr AJ. A synthetic bone implant macroscopically identical to cancellous bone. Biomaterials 1998;19:2303-11.

[218] Porter MM, Lee S, Tanadchangsaeng N, Jaremko MJ, Yu J, Meyers MA, et al. Porous Hydroxyapatite-Polyhydroxybutyrate Composites Fabricated by a Novel Method Via Centrifugation. In: Prorok BC, Barthelat F, Korach CS, Grande-Allen KJ, Lipke E, Lykofatitits G, et al., editors. Mechanics of Biological Systems and Materials. New York: Springer; 2013. p. 63-71.

[219] Wang JX, Zhao HC, Zhou SB, Lu X, Feng B, Duan CH, et al. One-step in situ synthesis and characterization of sponge-like porous calcium phosphate scaffolds using a sol-gel and gel casting hybrid process. Journal of Biomedical Materials Research Part A 2009;90A:401-10.

[220] Bauer J, Hengsbach S, Tesari I, Schwaiger R, Kraft O. High-strength cellular ceramic composites with 3D microarchitecture. Proceedings of the National Academy of Sciences 2014;111:2453-8.

[221] Rengier F, Mehndiratta A, von Tengg-Kobligk H, Zechmann CM, Unterhinninghofen R, Kauczor HU, et al. 3D printing based on imaging data: review of medical applications. Int J Comput Assist Radiol Surg 2010;5:335-41.

[222] Li WL, Lu K, Walz JY. Freeze casting of porous materials: review of critical factors in microstructure evolution. Int Mater Rev 2012;57:37-60.

[223] Gorna K, Munoz-Espi R, Grohn F, Wegner G. Bioinspired mineralization of inorganics from aqueous media controlled by synthetic polymers. Macromolecular Bioscience 2007;7:163-73.

[224] Schweizer S, Taubert A. Polymer-Controlled, Bio-Inspired Calcium Phosphate Mineralization from Aqueous Solution. Macromolecular Bioscience 2007;7:1085-99.

[225] Oaki Y, Kotachi A, Miura T, Imai H. Bridged nanocrystals in biominerals and their biomimetics: Classical yet modern crystal growth on the nanoscale. Advanced Functional Materials 2006;16:1633-9.

[226] Ludwigs S, Steiner U, Kulak AN, Lam R, Meldrum FC. Bioinspired polymer-inorganic hybrid materials. Advanced Materials 2006;18:2270-+.

[227] Nunes JK, Ertas M, Du LB, DeSimone JM. Hierarchical Control of Polymer Composite Nano- and Micro-Structure with Lithography. Chemistry of Materials 2010;22:4069-75.

[228] Schulz M, Borner M, Hausselt J, Heldele R. Polymer derived ceramic microparts from X-ray lithography - lecross-linking behavior and process optimization. Journal of the European Ceramic Society 2005;25:199-204.

[229] Ekiz OO, Dericioglu AF, Kakisawa H. An efficient hybrid conventional method to fabricate nacre-like bulk nano-laminar composites. Mater Sci Eng C-Mater Biol Appl 2009;29:2050-4.

[230] Bonderer LJ, Feldman K, Gauckler LJ. Platelet-reinforced polymer matrix composites by combined gel-casting and hot-pressing. Part I: Polypropylene matrix composites. Compos Sci Technol 2010;70:1958-65.

[231] Bonderer LJ, Feldman K, Gauckler LJ. Platelet-reinforced polymer matrix composites by combined gel-casting and hot-pressing. Part II: Thermoplastic polyurethane matrix composites. Compos Sci Technol 2010;70:1966-72.

[232] Parsons AJ, Ahmed I, Han N, Felfel R, Rudd CD. Mimicking Bone Structure and Function with Structural Composite Materials. J Bionic Eng 2010;7:S1-S10.

[233] Russias J, Saiz E, Nalla RK, Gryn K, Ritchie RO, Tomsia AP. Fabrication and mechanical properties of PLA/HA composites: A study of in vitro degradation. Mater Sci Eng C-Biomimetic Supramol Syst 2006;26:1289-95.

[234] Wang CA, Huang Y, Zan QF, Guo H, Cai SY. Biomimetic structure design - a possible approach to change the brittleness of ceramics in nature. Mater Sci Eng C-Biomimetic Supramol Syst 2000;11:9-12.

[235] Clegg WJ, Kendall K, Alford NM, Button TW, Birchall JD. A Simple Way To Make Tough Ceramics. Nature 1990;347:455-7.

[236] Martinez-Vazquez FJ, Perera FH, Miranda P, Pajares A, Guiberteau F. Improving the compressive strength of bioceramic robocast scaffolds by polymer infiltration. Acta Biomaterialia 2010;6:4361-8.

[237] de Jongh PE, Eggenhuisen TM. Melt Infiltration: an Emerging Technique for the Preparation of Novel Functional Nanostructured Materials. Advanced Materials 2013;25:6672-90.

[238] Miao X, Lim WK, Huang X, Chen Y. Preparation and characterization of interpenetrating phased TCP/HA/PLGA composites. Materials Letters 2005;59:4000-5.

[239] Peroglio M, Gremillard L, Gauthier C, Chazeau L, Verrier S, Alini M, et al. Mechanical properties and cytocompatibility of poly(epsilon-caprolactone)-infiltrated biphasic calcium phosphate scaffolds with bimodal pore distribution. Acta Biomaterialia 2010;6:4369-79.

[240] Sharifi S, Shafieyan Y, Mirzadeh H, Bagheri-Khoulenjani S, Rabiee SM, Imani M, et al. Hydroxyapatite scaffolds infiltrated with thermally crosslinked polycaprolactone fumarate and polycaprolactone itaconate. Journal of Biomedical Materials Research Part A 2011;98A:257-67.

[241] Zou H, Wu S, Shen J. Polymer/Silica Nanocomposites: Preparation, Characterization, Properties, and Applications. Chemical Reviews 2008;108:3893-957.

[242] Chen R, Johnson MB, Plucknett KP, White MA. Thermal conductivity of tunable lamellar aluminum oxide/polymethyl methacrylate hybrid composites. Journal of Materials Research 2012;27:1869-76.

[243] Launey ME, Munch E, Alsem DH, Barth HB, Saiz E, Tomsia AP, et al. Designing highly toughened hybrid composites through nature-inspired hierarchical complexity. Acta Materialia 2009;57:2919-32.

[244] Pezzotti G, Asmus SMF, Ferroni LP, Miki S. In situ polymerization into porous ceramics: a novel route to tough biomimetic materials. J Mater Sci-Mater Med 2002;13:783-7.

[245] Chen H-Y, Elkasabi Y, Lahann J. Surface Modification of Confined Microgeometries via Vapor-Deposited Polymer Coatings. Journal of the American Chemical Society 2005;128:374-80.

[246] Elkasabi Y, Chen HY, Lahann J. Multipotent polymer coatings based on chemical vapor deposition copolymerization. Advanced Materials 2006;18:1521-+.

[247] Jang J, Lim B. Facile Fabrication of Inorganic-Polymer Core–Shell Nanostructures by a One-Step Vapor Deposition Polymerization. Angewandte Chemie International Edition 2003;42:5600-3.

[248] Fratzl P. A Composite Matter of Alignment. Science 2012;335:177-8.

[249] Yang TY, Lee JM, Yoon SY, Park HC. Hydroxyapatite scaffolds processed using a TBA-based freeze-gel casting/polymer sponge technique. J Mater Sci-Mater Med 2010;21:1495-502.

[250] Lee JH, Choi HJ, Yoon SY, Kim BK, Park HC. Porous mullite ceramics derived from coal fly ash using a freeze-gel casting/polymer sponge technique. J Porous Mat 2013;20:219-26.

[251] Young Yang T, Young Kim W, Young Yoon S, Chae Park H. Macroporous silicate ceramics prepared by freeze casting combined with polymer sponge method. Journal of Physics and Chemistry of Solids 2010;71:436-9.

[252] Lee J-H, Wang L, Boyce MC, Thomas EL. Periodic Bicontinuous Composites for High Specific Energy Absorption. Nano Letters 2012;12:4392-6.

[253] Munch E, Franco J, Deville S, Hunger P, Saiz E, Tomsia AP. Porous ceramic scaffolds with complex architectures. JOM 2008;60:54-8.

[254] Seitz H, Rieder W, Irsen S, Leukers B, Tille C. Three-dimensional printing of porous ceramic scaffolds for bone tissue engineering. J Biomed Mater Res Part B 2005;74B:782-8.

[255] Gutiérrez MC, Ferrer ML, del Monte F. Ice-Templated Materials: Sophisticated Structures Exhibiting Enhanced Functionalities Obtained after Unidirectional Freezing and Ice-Segregation-Induced Self-Assembly†. Chemistry of Materials 2008;20:634-48.

[256] Qian L, Zhang HF. Controlled freezing and freeze drying: a versatile route for porous and micro-/nano-structured materials. J Chem Technol Biotechnol 2011;86:172-84.

[257] Lottermoser A. Über das Ausfrieren von Hydrosolen. Berichte der deutschen chemischen Gesellschaft 1908;41:3976-9.

[258] Bobertag O, Feist K, Fischer HW. Über das Ausfrieren von Hydrosolen. Berichte der deutschen chemischen Gesellschaft 1908;41:3675-9.

[259] Maxwell WA, Gurnick RS, Francisco AC. Preliminary investigation of the freeze-casting method for forming refractory powders. NACA Research Memorandum. Lewis Flight Propulsion Laboratory1954.

[260] Fukasawa T, Ando M, Ohji T, Kanzaki S. Synthesis of porous ceramics with complex pore structure by freeze-dry processing. Journal of the American Ceramic Society 2001;84:230-2.

[261] Fukasawa T, Deng ZY, Ando M, Ohji T, Goto Y. Pore structure of porous ceramics synthesized from water-based slurry by freeze-dry process. Journal of Materials Science 2001;36:2523-7.

[262] Fu Q, Rahaman MN, Dogan F, Bal BS. Freeze casting of porous hydroxyapatite scaffolds. I. Processing and general microstructure. J Biomed Mater Res Part B 2008;86B:125-35.

[263] Pekor C, Groth B, Nettleship I. The Effect of Polyvinyl Alcohol on the Microstructure and Permeability of Freeze-Cast Alumina. Journal of the American Ceramic Society 2010;93:115-20.

[264] Pekor CM, Kisa P, Nettleship I. Effect of Polyethylene Glycol on the Microstructure of Freeze-Cast Alumina. Journal of the American Ceramic Society 2008;91:3185-90.

[265] de Hazan Y. Porous Ceramics, Ceramic/Polymer, and Metal-Doped Ceramic/Polymer Nanocomposites via Freeze Casting of Photo-Curable Colloidal Fluids. Journal of the American Ceramic Society 2012;95:177-87.

[266] Fu Q, Rahaman MN, Dogan F, Bal BS. Freeze casting of porous hydroxyapatite scaffolds. II. Sintering, microstructure, and mechanical behavior. J Biomed Mater Res Part B 2008;86B:514-22.

[267] Azami M, Moztarzadeh F, Tahriri M. Preparation, characterization and mechanical properties of controlled porous gelatin/hydroxyapatite nanocomposite through layer solvent casting combined with freeze-drying and lamination techniques. J Porous Mat 2010;17:313-20.

[268] Blindow S, Pulkin M, Koch D, Grathwohl G, Rezwan K. Hydroxyapatite/SiO2 Composites via Freeze Casting for Bone Tissue Engineering. Advanced Engineering Materials 2009;11:875-84.

[269] Fu Q, Rahaman M, Bal BS, Brown R. Proliferation and function of MC3T3-E1 cells on freeze-cast hydroxyapatite scaffolds with oriented pore architectures. J Mater Sci: Mater Med 2009;20:1159-65.

[270] Jung H-D, Yook S-W, Kim H-E, Koh Y-H. Fabrication of titanium scaffolds with porosity and pore size gradients by sequential freeze casting. Materials Letters 2009;63:1545-7.

[271] Kim JH, Lee JH, Yang TY, Yoon SY, Kim BK, Park HC. TBA-based freeze/gel casting of porous hydroxyapatite scaffolds. Ceramics International 2011;37:2317-22.

[272] Lee E-J, Koh Y-H, Yoon B-H, Kim H-E, Kim H-W. Highly porous hydroxyapatite bioceramics with interconnected pore channels using camphene-based freeze casting. Materials Letters 2007;61:2270-3.

[273] Li JC, Dunand DC. Mechanical properties of directionally freeze-cast titanium foams. Acta Materialia 2011;59:146-58.

[274] Lin Y-S, Meyers MA, Olevsky EA. Microchannelled hydroxyapatite components by sequential freeze drying and free pressureless spark plasma sintering Advances in Applied Ceramics 2012;111:269-74.

[275] Macchetta A, Turner IG, Bowen CR. Fabrication of HA/TCP scaffolds with a graded and porous structure using a camphene-based freeze-casting method. Acta Biomaterialia 2009;5:1319-27.

[276] Mallick KK. Freeze Casting of Porous Bioactive Glass and Bioceramics. Journal of the American Ceramic Society 2009;92:S85-S94.

[277] Mallick KK, Winnett J, van Grunsven W, Lapworth J, Reilly GC. Three-dimensional porous bioscaffolds for bone tissue regeneration: Fabrication via adaptive foam reticulation and freeze casting techniques, characterization, and cell study. Journal of Biomedical Materials Research Part A 2012;100A:2948-59.

[278] Moritz T, Richter H-J. Ceramic Bodies with Complex Geometries and Ceramic Shells by Freeze Casting Using Ice as Mold Material. Journal of the American Ceramic Society 2006;89:2394-8.

[279] Moritz T, Richter HJ. Ice-mould freeze casting of porous ceramic components. Journal of the European Ceramic Society 2007;27:4595-601.

[280] Song J-H, Koh Y-H, Kim H-E, Li L-H, Bahn H-J. Fabrication of a Porous Bioactive Glass–Ceramic Using Room-Temperature Freeze Casting. Journal of the American Ceramic Society 2006;89:2649-53.

[281] Soon YM, Shin KH, Koh YH, Lee JH, Kim HE. Compressive strength and processing of camphene-based freeze cast calcium phosphate scaffolds with aligned pores. Materials Letters 2009;63:1548-50.

[282] Yoon BH, Koh YH, Park CS, Kim HE. Generation of large pore channels for bone tissue engineering using camphene-based freeze casting. Journal of the American Ceramic Society 2007;90:1744-52.

[283] Zhang Y, Zhou K, Bao Y, Zhang D. Effects of rheological properties on ice-templated porous hydroxyapatite ceramics. Materials Science and Engineering: C 2013;33:340-6.

[284] Deng Z-Y, Fernandes HR, Ventura JM, Kannan S, Ferreira JMF. Nano-TiO2-Coated Unidirectional Porous Glass Structure Prepared by Freeze Drying and Solution Infiltration. Journal of the American Ceramic Society 2007;90:1265-8.

[285] Dutta A, Tekalur SA. Synthetic staggered architecture composites. Materials & Design 2013;46:802-8.

[286] Dutta A, Vanderklok A, Tekalur SA. High strain rate mechanical behavior of seashell-mimetic composites: Analytical model formulation and validation. Mechanics of Materials 2012;55:102-11.

[287] Zhang H, Hussain I, Brust M, Butler MF, Rannard SP, Cooper AI. Aligned two- and three-dimensional structures by directional freezing of polymers and nanoparticles. Nat Mater 2005;4:787-93.

[288] Deville S, Maire E, Bernard-Granger G, Lasalle A, Bogner A, Gauthier C, et al. Metastable and unstable cellular solidification of colloidal suspensions. Nat Mater 2009;8:966-72.

[289] Deville S, Maire E, Lasalle A, Bogner A, Gauthier C, Leloup J, et al. In Situ X-Ray Radiography and Tomography Observations of the Solidification of Aqueous Alumina Particle Suspensions-Part I: Initial Instants. Journal of the American Ceramic Society 2009;92:2489-96.

[290] Deville S, Maire E, Lasalle A, Bogner A, Gauthier C, Leloup J, et al. In Situ X-Ray Radiography and Tomography Observations of the Solidification of Aqueous Alumina Particles Suspensions. Part II: Steady State. Journal of the American Ceramic Society 2009;92:2497-503.

[291] Deville S, Bernard-Granger G. Influence of surface tension, osmotic pressure and pores morphology on the densification of ice-templated ceramics. Journal of the European Ceramic Society 2011;31:983-7.

[292] Lasalle A, Guizard C, Maire E, Adrien J, Deville S. Particle redistribution and structural defect development during ice templating. Acta Materialia 2012;60:4594-603.

[293] Shanti NO, Araki K, Halloran JW. Particle redistribution during dendritic solidification of particle suspensions. Journal of the American Ceramic Society 2006;89:2444-7.

[294] Zou JL, Zhang Y, Li RX. Effect of Suspension State on the Pore Structure of Freeze-Cast Ceramics. Int J Appl Ceram Technol 2011;8:482-9.

[295] Körber C, Rau G, Cosman MD, Cravalho EG. Interaction of particles and a moving ice-liquid interface. Journal of Crystal Growth 1985;72:649-62.

[296] Uhlmann DR, Chalmers B, Jackson KA. Interaction between particles and a solid-liquid interface. Journal of Applied Physics 1964;35:2986-93.

[297] Deville S, Saiz E, Tomsia AP. Ice-templated porous alumina structures. Acta Materialia 2007;55:1965-74.

[298] Araki K, Halloran JW. Porous ceramic bodies with interconnected pore channels by a novel freeze casting technique. Journal of the American Ceramic Society 2005;88:1108-14.

[299] Araki K, Halloran JW. Room-temperature freeze casting for ceramics with nonaqueous sublimable vehicles in the naphthalene-camphor eutectic system. Journal of the American Ceramic Society 2004;87:2014-9.

[300] Guo R, Wang CA, Yang AK. Piezoelectric Properties of the 1-3 Type Porous Lead Zirconate Titanate Ceramics. Journal of the American Ceramic Society 2011;94:1794-9.

[301] Deville S, Maire E, Lasalle A, Bogner A, Gauthier C, Leloup J, et al. Influence of Particle Size on Ice Nucleation and Growth During the Ice-Templating Process. Journal of the American Ceramic Society 2010;93:2507-10.

[302] Bouville F, Maire E, Deville S. Lightweight and stiff cellular ceramic structures by ice templating. Journal of Materials Research 2014;29:175-81.

[303] Bouville F, Maire E, Deville S. Self-Assembly of Faceted Particles Triggered by a Moving Ice Front. Langmuir 2014.

[304] Deville S. Ice-templating, freeze casting: Beyond materials processing. Journal of Materials Research 2013;28:2202-19.

[305] Hunger PM, Donius AE, Wegst UGK. Platelets self-assemble into porous nacre during freeze casting. Journal of the Mechanical Behavior of Biomedical Materials 2013;19:87-93.

[306] Munch E, Saiz E, Tomsia AP, Deville S. Architectural Control of Freeze-Cast Ceramics Through Additives and Templating. Journal of the American Ceramic Society 2009;92:1534-9.

[307] Deville S, Viazzi C, Guizard C. Ice-Structuring Mechanism for Zirconium Acetate. Langmuir 2012;28:14892-8.

[308] Koh YH, Lee EJ, Yoon BH, Song JH, Kim HE, Kim HW. Effect of polystyrene addition on freeze casting of ceramic/camphene slurry for ultra-high porosity ceramics with aligned pore channels. Journal of the American Ceramic Society 2006;89:3646-53.

[309] Zuo KH, Zhang Y, Zeng Y-P, Jiang D. Pore-forming agent induced microstructure evolution of freeze casted hydroxyapatite. Ceramics International 2011;37:407-10.

[310] Zhang YM, Hu LY, Han JC. Preparation of a Dense/Porous BiLayered Ceramic by Applying an Electric Field During Freeze Casting. Journal of the American Ceramic Society 2009;92:1874-6.

[311] Preiss A, Su B, Collins S, Simpson D. Tailored graded pore structure in zirconia toughened alumina ceramics using double-side cooling freeze casting. Journal of the European Ceramic Society 2012;32:1575-83.

[312] Waschkies T, Oberacker R, Hoffmann MJ. Control of Lamellae Spacing During Freeze Casting of Ceramics Using Double-Side Cooling as a Novel Processing Route. Journal of the American Ceramic Society 2009;92:S79-S84.

[313] Moon JW, Hwang HJ, Awano M, Maeda K. Preparation of NiO-YSZ tubular support with radially aligned pore channels. Materials Letters 2003;57:1428-34.

[314] Chen Y, Bunch J, Li TS, Mao ZP, Chen FL. Novel functionally graded acicular electrode for solid oxide cells fabricated by the freeze-tape-casting process. J Power Sources 2012;213:93-9.

[315] Ren LL, Zeng YP, Jiang DL. Fabrication of gradient pore TiO2 sheets by a novel freeze-tape-casting process. Journal of the American Ceramic Society 2007;90:3001-4.

[316] Deville S. The making of a paper – A praise for Slow Science. http://sylvaindevillenet/blog/2014.

[317] Hong C, Du J, Liang J, Zhang X, Han J. Functionally graded porous ceramics with dense surface layer produced by freeze-casting. Ceramics International 2011;37:3717-22.

[318] Koh Y-H, Jun I-K, Sun J-J, Kim H-E. In situ Fabrication of a Dense/Porous Bi-layered Ceramic Composite using Freeze Casting of a Ceramic–Camphene Slurry. Journal of the American Ceramic Society 2006;89:763-6.

[319] Akkouch A, Zhang Z, Rouabhia M. A novel collagen/hydroxyapatite/poly(lactide-co-ε-caprolactone) biodegradable and bioactive 3D porous scaffold for bone regeneration. Journal of Biomedical Materials Research Part A 2011;96A:693-704.

[320] Han J, Hu L, Zhang Y, Zhou Y. Fabrication of Ceramics with Complex Porous Structures by the Impregnate–Freeze-Casting Process. Journal of the American Ceramic Society 2009;92:2165-7.

[321] William D. Callister J. Materials Science and Engineering: An Introduction. 6th ed. Hoboken, NJ: John Wiley & Sons, Inc; 2003.

[322] Olevsky EA, Froyen L. Impact of Thermal Diffusion on Densification During SPS. Journal of the American Ceramic Society 2009;92:S122-S32.

[323] Olevsky EA, Kandukuri S, Froyen L. Consolidation enhancement in spark-plasma sintering: Impact of high heating rates. Journal of Applied Physics 2007;102.

[324] Pawelec KM, Husmann A, Best SM, Cameron RE. Ice-templated structures for biomedical tissue repair: From physics to final scaffolds. Applied Physics Reviews 2014;1:-.

[325] Lu J, Flautre B, Anselme K, Hardouin P, Gallur A, Descamps M, et al. Role of interconnections in porous bioceramics on bone recolonization in vitro and in vivo. J Mater Sci Mater Med 1999;10:111-20.

[326] Hulbert SF, Young FA, Mathews RS, Klawitter JJ, Talbert CD, Stelling FH. Potential of ceramic materials as permanently implantable skeletal prostheses. Journal of Biomedical Materials Research 1970;4:433-56.

[327] Nudelman F, Gotliv BA, Addadi L, Weiner S. Mollusk shell formation: Mapping the distribution of organic matrix components underlying a single aragonitic tablet in nacre. J Struct Biol 2006;153:176-87.

[328] Hunger PM, Donius AE, Wegst UGK. Platelets self-assemble into porous nacre during freeze casting. J Mech Behav Biomed Mater.

[329] Lee S, Porter M, Wasko S, Lau G, Chen P-Y, Novitskaya EE, et al. Potential Bone Replacement Materials Prepared by Two Methods. MRS Online Proceedings Library 2012;1418.

[330] Hunger PM, Donius AE, Wegst UGK. Structure–property-processing correlations in freeze-cast composite scaffolds. Acta Biomaterialia 2013;9:6338-48.

[331] Ren L, Zeng Y-P, Jiang D. Preparation of porous TiO2 by a novel freeze casting. Ceramics International 2009;35:1267-70.

[332] Ren L, Zeng Y-P, Jiang D. The improved photocatalytic properties of P-type NiO loaded porous TiO2 sheets prepared via freeze tape-casting. Solid State Sciences 2010;12:138-43.

[333] Jackson KA, Hunt JD. Lamellar and rod eutectic growth. Transactions of the Metallurgical Society of Aime 1966;236:1129-&.

[334] Glicksman ME. Principles of Solidification. New York, NY, USA: Springer; 2011.

[335] Aladko LS, Manakov AY, Ogienko AG, Ancharov AI. New data on phase diagram and clathrate formation in the system water–isopropyl alcohol. J Incl Phenom Macrocycl Chem 2009;63:151-7.

[336] Murthy SSN. Detailed Study of Ice Clathrate Relaxation: Evidence for the Existence of Clathrate Structures in Some Water−Alcohol Mixtures. The Journal of Physical Chemistry A 1999;103:7927-37.

[337] Beer FP, E. Russell Johnston J, DeWolf JT. Mechanics of Materials. New York: McGraw-Hill; 2002.

[338] Li J, Forberg S, Hermansson L. Evaluation Of The Mechanical-Properties Of Hot Isostatically Pressed Titania And Titania Calcium-Phosphate Composites. Biomaterials 1991;12:438-40.

[339] Li XD, Chang WC, Chao YJ, Wang RZ, Chang M. Nanoscale structural and mechanical characterization of a natural nanocomposite material: The shell of red abalone. Nano Letters 2004;4:613-7.

[340] Fukasawa T, Deng ZY, Ando M, Ohji T, Kanzaki S. Synthesis of porous silicon nitride with unidirectionally aligned channels using freeze-drying process. Journal of the American Ceramic Society 2002;85:2151-5.

[341] Lee SH, Jun SH, Kim HE, Koh YH. Piezoelectric properites of PZT-based ceramic with highly aligned pores. Journal of the American Ceramic Society 2008;91:1912-5.

[342] Koh YH, Song JH, Lee EJ, Kim HE. Freezing dilute ceramic/camphene slurry for ultra-high porosity ceramics with completely interconnected pore networks. Journal of the American Ceramic Society 2006;89:3089-93.

[343] Correa-Duarte MA, Grzelczak M, Salgueirino-Maceira V, Giersig M, Liz-Marzan LM, Farle M, et al. Alignment of carbon nanotubes under low magnetic fields through attachment of magnetic nanoparticles. J Phys Chem B 2005;109:19060-3.

[344] Horton M, Hong HP, Li C, Shi B, Peterson GP, Jin SH. Magnetic alignment of Ni-coated single wall carbon nanotubes in heat transfer nanofluids. Journal of Applied Physics 2010;107.

[345] Mashkour M, Tajvidi M, Kimura T, Kimura F, Ebrahimi G. Fabricating Unidirectional Magnetic Papers using Permanent Magnets to Align Magnetic Nanoparticle Covered Natural Cellulose Fibers. BioResources 2011;6:4731-8.

[346] Tumpane J, Karousis N, Tagmatarchis N, Norden B. Alignment of carbon nanotubes in weak magnetic fields. Angew Chem-Int Edit 2008;47:5148-52.

[347] Wang H, Chen QW, Sun LX, Qi HP, Yang X, Zhou S, et al. Magnetic-Field-Induced Formation of One-Dimensional Magnetite Nanochains. Langmuir 2009;25:7135-9.

[348] Xu YY, Yuan JY, Fang B, Drechsler M, Mullner M, Bolisetty S, et al. Hybrids of Magnetic Nanoparticles with Double-Hydrophilic Core/Shell Cylindrical Polymer Brushes and Their Alignment in a Magnetic Field. Advanced Functional Materials 2010;20:4182-9.

[349] Yamaguchi K, Matsumoto K, Fujii T. Magnetic-Anisotropy by Ferromagnetic Particles Alignment in a Magnetic-Field. Journal of Applied Physics 1990;67:4493-5.

[350] Akiyama J, Hashimoto M, Takadama H, Nagata F, Yokogawa Y, Sassa K, et al. Formation of c-axis aligned hydroxyapatite sheet by simultaneous imposition of high magnetic field and mold rotation during slip casting process. In: Nakamura T, Yamashita K, Neo M, editors. Bioceramics 18, Pts 1 and 22006. p. 53-6.

[351] Sakka Y, Suzuki TS. Textured development of feeble magnetic ceramics by colloidal processing under high magnetic field. J Ceram Soc Jpn 2005;113:26-36.

[352] Suzuki TS, Uchikoshi T, Sakka Y. Control of texture in alumina by colloidal processing in a strong magnetic field. Sci Technol Adv Mater 2006;7:356-64.

[353] Suzuki TS, Uchikoshi T, Sakka Y. Texture development in anatase and rutile prepared by slip casting in a strong magnetic field. J Ceram Soc Jpn 2011;119:334-7.

[354] Tang FQ, Uchikoshi T, Suzuki TS, Sakka Y. Alignment of TiO2 particles by electrophoretic deposition in a high magnetic field. Mater Res Bull 2004;39:2155-61.

[355] Uchikoshi T, Suzuki TS, Iimura S, Tang FQ, Sakka Y. Control of crystalline texture in polycrystalline TiO2 (anatase) by electrophoretic deposition in a strong magnetic field. Journal of the European Ceramic Society 2006;26:559-63.

[356] Uchikoshi T, Suzuki TS, Okuyama H, Sakka Y, Nicholson PS. Electrophoretic deposition of alumina suspension in a strong magnetic field. Journal of the European Ceramic Society 2004;24:225-9.

[357] Ficai D, Ficai A, Vasile BS, Ficai M, Oprea O, Guran C, et al. Synthesis of Rod-Like Magnetite by Using Low Magnetic Field. Dig J Nanomater Biostruct 2011;6:943-51.

[358] Chin CJ, Lu SC, Yiacoumi S, Tsouris C. Fractal dimension of particle aggregates in magnetic fields. Sep Sci Technol 2004;39:2839-62.

[359] Peng XL, Min Y, Ma TY, Luo W, Yan M. Two-dimensional Monte Carlo simulations of structures of a suspension comprised of magnetic and nonmagnetic particles in uniform magnetic fields. J Magn Magn Mater 2009;321:1221-6.

[360] Peng X, Min Y, Ma T, Yan M. Two-dimensional Monte Carlo simulations of a suspension comprised of magnetic and nonmagnetic particles in gradient magnetic fields. J Magn Magn Mater 2009;321:3250-5.

[361] Einarsrud MA, Hagen E, Pettersen G, Grande T. Pressureless sintering of titanium diboride with nickel, nickel boride, and iron additives. Journal of the American Ceramic Society 1997;80:3013-20.

[362] Filho FP, Nogueira R, Graca MYF, Valente MA, Sombra ASB, Silva CC. Structural and mechanical study of the sintering effect in hydroxyapatite doped with iron oxide. Physica B 2008;403:3826-9.

[363] Zhang YH, Reller A. Nanocrystalline iron-doped mesoporous titania and its phase transition. J Mater Chem 2001;11:2537-41.

[364] Thompson DAW. On Growth and Form. Cambridge: Cambridge University Press; 1917.

[365] Skatter S, Kucera B. Spiral grain - An adaptation of trees to withstand stem breakage caused by wind-induced torsion. Holz Als Roh-und Werkst 1997;55:207-13.

[366] Weaver JC, Aizenberg J, Fantner GE, Kisailus D, Woesz A, Allen P, et al. Hierarchical assembly of the siliceous skeletal lattice of the hexactinellid sponge Euplectella aspergillum. J Struct Biol 2007;158:93-106.

[367] Kingsley MCS, Ramsay MA. The Spiral in the Tusk of the Narwhal. Arctic 1988;41:236-8.

[368] Frankkamenetskii MD, Lukashin AV, Anshelevich VV, Vologodskii AV. Torsional and Bending Rigidity of the Double Helix from Data on Small DNA Rings. J Biomol Struct Dyn 1985;2:1005-12.

[369] Wada K. Spiral Growth of Nacre. Nature 1966;211:1427-&.

[370] Yao N, Epstein A, Akey A. Crystal growth via spiral motion in abalone shell nacre. Journal of Materials Research 2006;21:1939-46.

[371] Bubenik GA, Bubenik AB. Horns, Pronghorns, and Antlers: Evolution, Morphology, Physiology, and Social Significance. New York: Springer; 1990.

[372] Skalak R, Farrow DA, Hoger A. Kinematics of surface growth. J Math Biol 1997;35:869-907.

[373] Wherry G. Direction of spirals in horns. Nature 1901;63:348-.

[374] Harary G, Tal A. The Natural 3D Spiral. Computer Graphics Forum 2011;30:237-46.

[375] Kees Jr G, Worrick III CB, Santangelo JA. Torsion spring. United States: Codman & Shurtleff, Inc.; 1990.

[376] Apichattrabrut T, Ravi-Chandar K. Helicoidal composites. Mech Adv Mater Struct 2006;13:61-76.

[377] Cheng LA, Thomas A, Glancey JL, Karlsson AM. Mechanical behavior of bio-inspired laminated composites. Compos Pt A-Appl Sci Manuf 2011;42:211-20.

[378] Antal S, Arvai M, Bartha Z, Gorgenyi P, Meitzen N. Rubber hose with spiral fiber reinforcing core. United States: Taurus Gumiipari Vallalat; 1980.

[379] Brussee RC. Method of making a filament reinforced pressure vessel. United States: Structural Fibers; 1966.

[380] Folsom MF. Fiber-reinforced plastic springs with helical fiber wind. United States: Folsom; Mark F.; 1997.

[381] Mead GNJ. Helical reinforced materials and method of making same. United States: George N J Mead; 1969.

[382] Rodgers JJL, Howald AM. Torsion transmitting glass shaft and method of manufacture. United States: Libbey Owens Ford Glass Co; 1951.

[383] Adams D. A comparison of shear test methods. High-Performance Composites 2005:9-10.

[384] Chiao CC, Moore RL, Chiao TT. Measurement of shear properties of fibre composites: Part 1. Evaluation of test methods. Composites 1977;8:161-9.

[385] Adams DF, Thomas RL. The Solid-Rod Torsion Test for the Determination of Unidirectional Composite Shear Properties. Textile Research Journal 1969;39:339-45.

[386] Davalos JF, Qiao P, Wang J, Salim HA, Schlussel J. Shear moduli of structural composites from torsion tests. Journal of composite materials 2002;36:1151-73.

[387] Hamed AF, Megat MH, Sapuan SM, Sahari BB. Theoretical Analysis for Calculation of the Through Thickness Effective Constants for Orthotropic Thick Filament Wound Tubes. Polymer-Plastics Technology and Engineering 2008;47:1008-15.

[388] Park J, Lakes RS. Biomaterials: An Introduction. New York: Springer; 2007.

[389] Liu Q-J, Liu Z-T, Feng L-P. Elasticity, electronic structure, chemical bonding and optical properties of monoclinic ZrO2 from first-principles. Physica B: Condensed Matter 2011;406:345-50.

[390] Sakka Y, Suzuki TS, Uchikoshi T. Fabrication and some properties of textured alumina-related compounds by colloidal processing in high-magnetic field and sintering. Journal of the European Ceramic Society 2008;28:935-42.

[391] Uchikoshi T, Suzuki TS, Tang F, Okuyama H, Sakka Y. Crystalline-oriented TiO2 fabricated by the electrophoretic deposition in a strong magnetic field. Ceramics International 2004;30:1975-8.

[392] Cao ZP, Sassa K, Asai S. The orientation mechanism of (Ca,Sr)Bi4Ti4O15 ceramics prepared by slip casting in high magnetic field and subsequent sintering. Journal of the European Ceramic Society 2007;27:2591-6.

[393] Akiyama J, Hashimoto M, Takadama H, Nagata F, Yokogawa Y, Iwai K, et al. Formation of c-axis aligned polycrystal hydroxyapatite using a high magnetic field with mechanical sample rotation. Journal of the Japan Institute of Metals 2006;70:412-4.

[394] Li SQ, Sassa K, Asai S. Preferred orientation of Si3N4 ceramics by slip casting in a high magnetic field. Ceramics International 2006;32:701-5.

[395] Liu T, Wang Q, Gao A, Zhang C, Wang CJ, He J. Fabrication of functionally graded materials by a semi-solid forming process under magnetic field gradients. Scripta Materialia 2007;57:992-5.

[396] Wang Q, Liu T, Gao A, Zhang C, Wang CJ, He JC. A novel method for in situ formation of bulk layered composites with compositional gradients by magnetic field gradient. Scripta Materialia 2007;56:1087-90.

[397] Camponeschi E, Vance R, Al-Haik M, Garmestani H, Tannenbaum R. Properties of carbon nanotube-polymer composites aligned in a magnetic field. Carbon 2007;45:2037-46.

[398] Choi ES, Brooks JS, Eaton DL, Al-Haik MS, Hussaini MY, Garmestani H, et al. Enhancement of thermal and electrical properties of carbon nanotube polymer composites by magnetic field processing. Journal of Applied Physics 2003;94:6034-9.

[399] Garmestani H, Al-Haik MS, Dahmen K, Tannenbaum R, Li DS, Sablin SS, et al. Polymer-mediated alignment of carbon nanotubes under high magnetic fields. Advanced Materials 2003;15:1918-+.

[400] Kimura T, Ago H, Tobita M, Ohshima S, Kyotani M, Yumura M. Polymer composites of carbon nanotubes aligned by a magnetic field. Advanced Materials 2002;14:1380-3.

[401] Shi DL, He P, Lian J, Chaud X, Bud'ko SL, Beaugnon E, et al. Magnetic alignment of carbon nanofibers in polymer composites and anisotropy of mechanical properties. Journal of Applied Physics 2005;97.

[402] Erb RM, Cherenack KH, Stahel RE, Libanori R, Kinkeldei T, Munzenrieder N, et al. Locally Reinforced Polymer-Based Composites for Elastic Electronics. ACS applied materials & interfaces 2012;4:2860-4.

[403] Erb RM, Sander JS, Grisch R, Studart AR. Self-shaping composites with programmable bioinspired microstructures. Nature Communications 2013;4.

[404] Libanori R, Erb RM, Reiser A, Le Ferrand H, Suess MJ, Spolenak R, et al. Stretchable heterogeneous composites with extreme mechanical gradients. Nature Communications 2012;3.

[405] Peng XL, Yan M, Shi WT. A new approach for the preparation of functionally graded materials via slip casting in a gradient magnetic field. Scripta Materialia 2007;56:907-9.

[406] Shi WT, Peng XL, Ma TY, Luo W, Yan M. Fabrication of ZrO2/Ni functionally graded materials based on components distinct different magnetic properties. Wuji Cailiao Xuebao/Journal of Inorganic Materials 2007;22:1183-6.

[407] Yan M, Peng XL, Ma TY. Microstructures of Ni-ZrO2 functionally graded materials fabricated via slip casting under gradient magnetic fields. Journal of Alloys and Compounds 2009;479:750-4.

[408] Sommer MR, Erb RM, Studart AR. Injectable Materials with Magnetically Controlled Anisotropic Porosity. ACS applied materials & interfaces 2012;4:5086-91.

[409] Magnetic susceptibility of the elements and inorganic compounds.

[410] Suh YK, Kang S. Motion of paramagnetic particles in a viscous fluid under a uniform magnetic field: benchmark solutions. Journal of Engineering Mathematics 2011;69:25-58.

[411] Ebner AD, Ploehn HJ, Ritter JA. Magnetic field orientation and spatial effects on the retention of paramagnetic nanoparticles with magnetite. Sep Sci Technol 2002;37:3727-53.

[412] Ebner AD, Ritter JA. Retention of paramagnetic particles by magnetite particle clusters with multifunctional character. Sep Sci Technol 2004;39:2785-808.

[413] Ebner AD, Ritter JA, Ploehn HJ. Magnetic hetero-flocculation of paramagnetic colloidal particles. Journal of Colloid and Interface Science 2000;225:39-46.

[414] Climent E, Maxey MR, Karniadakis GE. Dynamics of self-assembled chaining in magnetorheological fluids. Langmuir 2004;20:507-13.

[415] Hendriksen PV, Christiansen G, Morup S. Magnetization Reversal In Chain-Like Clusters Of Interacting Particles. J Magn Magn Mater 1994;132:207-18.

[416] Trohidou KN, Blackman JA. Aggregation And Segregation In A Mixture Of Magnetic And Nonmagnetic Particles. Physical Review B 1995;51:11521-6.